



National Technical University of Athens
School of Naval Architecture and Marine Engineering
Ship Design Laboratory

**Numerical Simulation of Large Amplitude Ship Motions
and Applications to Ship Design and Safe Operation**

by

Shukai Liu

Doctoral Thesis

Athens, April 2011



National Technical University of Athens
School of Naval Architecture and Ocean Engineering
Ship Design Laboratory

**Numerical Simulation of Large Amplitude Ship Motions
and Applications to Ship Design and Safe Operation**

by

Shukai Liu

Doctoral Thesis

Advisory Committee:

Apostolos D. Papanikolaou,	Professor (<i>Supervisor</i>)
Konstantinos J. Spyrou,	Professor
Georgios Zaraphonitis,	Associate Professor

about ship design...

This is how you are to make it: the length of the ark three hundred cubits, its width fifty cubits, and its height thirty cubits. Make a roof for the ark, and finish it to a cubit above; and put the door of the ark in its side; make it with lower, second, and third decks.

-- *Genesis 6:15-6:16*

ABSTRACT

Numerical Simulation of Large Amplitude Ship Motions and Applications to Ship Design and Safe Operation

by

Shukui Liu

In this thesis, a time domain hybrid method is developed to study the seakeeping behavior of ships and floating structures in waves (at zero and nonzero forward speed). The thesis deals with three different basic solution approaches to the set problem, namely, a time domain transient Green function solver and alternatively a time domain *hybrid* solver for zero speed problems, whereas the time domain hybrid solver has been adopted for the nonzero forward speed seakeeping problem. Basic constituents of all above approaches are the developed time domain transient Green function method, the time domain hybrid method plus a motion simulation model, which is capable of simulating both small and large amplitude motions of ships and floating structures.

For the time domain transient Green function method, the constant panel method is used to find a numerical solution to the set Boundary value Problem of potential theory. It is validated by numerous examples of submerged bodies and floating bodies, either without or with forward speed. Obtained results include added mass and damping coefficients, diffraction force amplitudes, wave making resistance (steady problem), drift forces and added resistance.

For the numerical implementation of the time domain hybrid method, the GMRES solver is used to solve the resulting set equations, while two different motion models are integrated. For the zero speed case, the validation cases cover both simple, mathematical geometries and practical ship hulls. Obtained numerical results show that the method is robust and of satisfactory accuracy. For the nonzero speed case, the Chimera grid concept is introduced to increase the accuracy and efficiency. Whereas all above theoretical approaches have been formulated and solved in an earthbound system, an alternative approach that is based on a body fixed coordinate system has been also investigated, exhibiting higher computational efficiency with a reduced number panel. Validation results include the wave making resistance (steady problem), small amplitude ship motions, large amplitude ship motions and added resistance of ships in waves.

It is proved in this thesis that by properly selecting a solver, the developed package of methods is capable of simulating large amplitude motions of ships or floating structures in waves and it can serve as an advanced tool for the assessment of ship design and ship operation.

Acknowledgement

Six years ago in 2004, when the NTUA-Harbin Engineering University ASIA LINK project “*Knowledge transfer on ship design, production and operation*” was initialized, I made up my mind to come to NTUA-Athens for pursuing scientific progress and finally made the trip late of 2005. Five years later, at this moment, while I am ready for the examination by my PhD committee, I look back on these years’ experience and notice that there are many people I am grateful to during this route.

My special thanks go to Professor A. Papanikolaou who has been a great supervisor, not only on my study but also on my life. From the night I arrived to Athens until now, he has been continuously guiding and supporting me, either scientifically or financially, to progress in the right direction.

I also like to thank the other two members in my advisory committee, Professor K. Spyrou and Assoc. Professor G. Zaraphonitis, for their encouragement and scientific contributions through many discussions during these years.

My gratitude also goes to Professor Wenyang Duan from Harbin Engineering University, who led me to the scientific world of naval architecture. Though not guiding me face-to-face, he has contributed a lot to my development and enabled me to progress in Greece peacefully.

I would like also to thank Dr. D. Spanos, Dr. E. Boulougouris and Mr. D. Mourkoyianis from the Ship Design laboratory of NTUA for their willingness to help me in my research; thanks, also to George Papatzanakis, Nancy Trikalioti, and Dina Stamataki for their help with my living in Greece.

I would like to thank also Nikos, Yiannis, Panagiotis, Manoulis, and Stavros for their company in the office during these years.

I take this chance to thank Dr. M. Sant and Ms. Lili Kong for their company. It was these two persons that made my life in Greece very colorful and enjoyable.

At last I have to admit that I am indebted to my sister Lihui Liu; it is because of her unconditional contribution to our family that enabled me to stay in a foreign country without much worries about my parents.

This PhD study has been initially financially supported by the EU funded ASIA LINK programme ASI/B7-301/98/679-044 (072433) and thereafter by a stipend of NTUA’s Research Committee and funding of the Ship Design Laboratory of NTUA.

Contents

List of Figures.....	xi
List of Tables.....	xv
Chapter 1 Introduction.....	1
1.1 Review of the State-of-Art.....	1
1.2 Overview, Objectives and Innovations.....	4
1.3 Chapters of This Thesis.....	6
Chapter 2 Time Domain Transient Green Function Method.....	9
2.1 Definition of the Boundary Value Problem.....	9
2.2 Integral Equations.....	9
2.3 Hydrodynamic Forces.....	11
2.4 The Quasi-Second Order Problem - Calculation of Added Resistance.....	12
2.5 Numerical Scheme.....	13
2.6 Numerical Results and Discussion.....	14
2.6.1 Radiation Problem of a Floating Hemisphere.....	14
2.6.2 Radiation Problem of a Submerged Sphere.....	15
2.6.3 Radiation Problem of a Wigley Hull.....	16
2.6.4 Diffraction Problem of a Submerged Sphere.....	17
2.6.5 Diffraction Problem of a Wigley Hull.....	18
2.6.6 Resistance of a Submerged Spheroid.....	21
2.6.7 Resistance of a Wigley Hull.....	23
2.6.8 Added Resistance of a Submerged Spheroid.....	26
2.7 Summary and Conclusions.....	30

Chapter 3	Time Domain Hybrid Method for Modeling Seakeeping Problems	33
3.1	Problem Formulation	33
3.2	Integral Equations	35
3.3	Free-Surface Condition.....	36
3.4	Body Boundary Condition and m_j Term Calculation	38
3.4.1	Neumann-Kelvin Simplification	38
3.4.2	Direct Calculation.....	38
3.5	Large Amplitude Ship Motions in Regular Waves with Six Degrees of Freedom	39
3.5.1	Radiation Forces	41
3.5.2	Diffraction Forces.....	42
3.5.3	Incidental Wave Forces and Hydrostatic Forces	42
3.6	Numerical Scheme	43
3.7	Summary and Conclusions	45
Chapter 4	Simulation of Ship Motions at Zero Speed by Time-Domain Hybrid Method	47
4.1	Small Amplitude Ship Motions in Regular Waves with Six Degrees of Freedom	47
4.1.1	The Simplified Head-Sea Case.....	50
4.1.2	Beam-Sea Case	51
4.2	Large Amplitude Head Seas Condition	52
4.2.1	Diffraction Forces and Radiation Forces.....	53
4.2.2	Incidental Wave Forces and Hydrostatic Forces	53
4.3	Numerical Procedure for Time-Domain Ship Motions' Simulation	54
4.4	Results of Small Amplitude Radiation and Diffraction Problems.....	55
4.4.1	Rectangular Barge	55
4.4.2	Hemisphere Case	58
4.4.3	Wigley Case.....	62

4.4.4 Series 60 Case.....	65
4.4.5 Diffraction and Radiation Problems of S175 Ship.....	67
4.5 Motion Simulation under Small Amplitude Incident Waves.....	68
4.5.1 Wigley Case, Head Seas Condition.....	68
4.5.2 Series60 Case, Head Seas Condition.....	71
4.5.3 Roll Motion of a Barge.....	71
4.5.4 S-175 Ship Case.....	74
4.6 Large Amplitude Ship Motion Simulation in Head Seas.....	76
4.6.1 Wigley Hull Case.....	77
4.6.2 Series60 ($C_b=0.6$) Case.....	81
4.6.3 S175 Ship Case.....	83
4.6.4 Modified Wigley Hull Case.....	85
4.7 Conclusions.....	87
Chapter 5 Simulation of Motions of Ships Advancing in Waves by the Time-Domain Hybrid Method.....	89
5.1 Hydrodynamic Forces.....	89
5.2 Calculation of Added Resistance in Short Waves.....	89
5.3 Consideration on Time Stepping and the Overlapping Grid Concept.....	91
5.4 Numerical Scheme.....	93
5.5 Results and Discussions.....	94
5.5.1 Wave Resistance of a Wigley Hull.....	94
5.5.2 Diffraction Problem of S175 Ship at $Fn=0.275$	97
5.5.3 Motion Simulation of S175 Ship at $Fn=0.275$ with Different Wave Conditions.....	97
5.5.4 Added Resistance of S175 Ship at $Fn=0.275$	99
5.6 Conclusions.....	100
Chapter 6 Further Development of the Time Domain Hybrid Method.....	101

6.1	Free Surface Condition	101
6.2	Discretization of Free Surface Condition	103
6.3	Integral Equations	105
6.4	Numerical Results and Discussions	105
6.4.1	Forced Motion Problem of S175 Ship at $F_n=0.275$	105
6.4.2	Motion Simulation of S175 Ship at $F_n=0.275$ with Different Wave Conditions	107
6.4.3	Motion of a Wigley Hull with Different Above-Water Hull Shapes	110
6.5	Computational Time	114
Chapter 7	Summary of the Research and Recommendations for Future Development	117
	Bibliography	119
	Appendix-1 Time-domain hybrid method for radiation problems, with impulsive function	127
	Curriculum Vitae	133

List of Figures

Figure 2.1 Comparison on added-masses and damping coefficients	15
Figure 2.2 Panelization of the Sphere and its motion $Z=Z_0+A\cos\omega t$	15
Figure 2.3 Comparison on added masses and damping coefficients	16
Figure 2.4 Comparison on added masses and damping coefficients	17
Figure 2.5 Results at different heaving amplitude for $k=0.1$	17
Figure 2.6 Comparison on wave load F_1 and F_3	18
Figure 2.7 Panels used to represent the Wigley hull	18
Figure 2.8 Calculated results of wave load F_1 , F_3 and F_5 , $Fn=0.0$, head seas	19
Figure 2.9 Calculated results of wave load F_1 , F_3 and F_5 , $Fn=0.2$, head seas	20
Figure 2.10 Panelization of the Ellipsoid	21
Figure 2.11 Wave making resistance $Fn=0.45$ $d=0.252c$	21
Figure 2.12 Wave making resistance $Fn=0.45$ $d=0.5c$	22
Figure 2.13 Wave making resistance $d=0.252c$ $Fn=0.35$	22
Figure 2.14 Wave making resistance $d=0.252c$, $Fn=0.6$	22
Figure 2.15 Perspective view of the Wigley hull with 320 improved progressional panels	24
Figure 2.16 Wave making resistance C_W results, hull fixed	25
Figure 2.17 Wave making resistance C_W results, with sinkage/trim correction	25
Figure 2.18. Wave making resistance calculation of a steadily moving Wigley hull, $Fn=0.4$	26
Figure 2.19 Unsteady wave numbers of two wave systems	27
Figure 2.20 Weighting function of k_2 wave system	27
Figure 2.21 Kochin function of a submerged spheroid	27
Figure 2.22 Integrand in Maruo's formula	28
Figure 2.23 Horizontal drift force on a submerged spheroid at $Fn=0$, $d=0.75B$	29
Figure 2.24 Added resistance on a submerged spheroid, $Fn=0.2$, $d=0.75B$	29
Figure 2.25 Added resistance on a submerged spheroid, $Fn=0.3$, $d=0.75B$	29
Figure 2.26 Horizontal drift force on a submerged spheroid at $Fn=0$, $d=1.25B$	30
Figure 2.27 Added resistance on a submerged spheroid, $Fn=0.2$, $d=1.25B$	30
Figure 3.1 Coordinate system Definition and Decomposition of the fluid domain	33
Figure 3.2 Ship crossing free surface panels	37
Figure 4.1 Perspective view of the panelization scheme	56
Figure 4.2 Force histories on a barge with different free-surface panelization, $T=10s$	57
Figure 4.3 Froude-Krylov moment and wave exciting moment of a barge at <i>beam seas</i>	58
Figure 4.4 Panelization for the simulation of the hemisphere	59
Figure 4.5 Panelization for the Wigley case, with 1215 panels in total	63
Figure 4.6 Added mass and damping coefficient results of the Wigley hull, $Fn=0.0$	63
Figure 4.7 Roll added mass and damping coefficient of the Wigley hull, $Fn=0.0$	64

Figure 4.8 Froude-Krylov moment and total wave exciting moment of the Wigley hull, $F_n=0.0$	64
Figure 4.9 Panelization for the SERIES60 case, with 1224 panels in total.	65
Figure 4.10 Added masses and damping coefficients of Series 60 hull, $C_b = 0.60$, $F_n=0.0$	66
Figure 4.11 Panelization for S175 ship computation; with 3394 panels in total	67
Figure 4.12 Roll added mass and damping coefficient of S175 ship, $F_n=0.0$	68
Figure 4.13 Froude-Krylov moment and wave exciting moment of S175 Ship, $F_n=0.0$	68
Figure 4.14 Motions' histories of Wigley III at zero speed, $\lambda/L=1.0$	69
Figure 4.15 Motions' histories of Wigley IV at zero speed, $\lambda/L=1.0$	69
Figure 4.16 Prediction of heave and pitch motions of Wigley III at zero speed	70
Figure 4.17 Prediction of heave and pitch motions of Wigley IV at zero speed	70
Figure 4.18 Comparison for heave and pitch motions of Series60 at zero speed	71
Figure 4.19 Linear motion history of the barge with an incident wave $\lambda=60m$	72
Figure 4.20 Linear motion history of the barge with an incident wave $\lambda=90m$	72
Figure 4.21 Linear motion history of the barge with an incident wave $\lambda=135m$	72
Figure 4.22 Linear motion results from NEWDRIFT and the hybrid method	73
Figure 4.23 Displacement of the barge, small amplitude incident wave, $\lambda=60m$	73
Figure 4.24 Prediction of heave and pitch motions of S175 ship at zero speed	74
Figure 4.26 Roll displacement of S175 ship with an incident wave $\lambda=400m$	75
Figure 4.27 Roll displacement of S175 ship with an incident wave $\lambda=169m$	76
Figure 4.28 Nondimensional time varying restoring moment of S175 ship at beam seas	76
Figure 4.29 Panelization for Froude-Krylov force computation	78
Figure 4.30 Results on heave and pitch motions of Wigley-III, $F_n=0.0$	78
Figure 4.31 Nondimensionalized heave motion at $\lambda/L=1.5$ at different wave amplitudes	79
Figure 4.32 Nondimensionalized pitch motion at $\lambda/L=1.5$ at different wave amplitudes	79
Figure 4.33 Nondimensionalized heave motion, $\lambda/L=1.0$, with different computation setting	79
Figure 4.34 Nondimensionalized pitch motion, $\lambda/L=1.0$. with different computation setting	80
Figure 4.35 Nondimensionalized nonlinear heave and pitch motion, $\lambda/L=1.0$, $H/\lambda=0.04$	80
Figure 4.36 Wetted surface at $t/T=6$ for Froude-Krylov force calculation ($\lambda/L=1.5$, $H/\lambda=0.04$)	80
Figure 4.37 Wetted surface at $t/T=6.25$ for Froude-Krylov force calculation ($\lambda/L=1.5$, $H/\lambda=0.04$)	80
Figure 4.38 Wetted surface at $t/T=6.5$ for Froude-Krylov force calculation ($\lambda/L=1.5$, $H/\lambda=0.04$)	81
Figure 4.39 Wetted surface at $t/T=6.75$ for Froude-Krylov force calculation ($\lambda/L=1.5$, $H/\lambda=0.04$)	81
Figure 4.40 Results of Series60 heave and pitch motions at zero speed	82
Figure 4.41 Nondimensionalized nonlinear heave and pitch motion at $\lambda/L=1.0$ with $H/\lambda=0.04$ by setting the bottom of control surface at $d/\lambda=0.9$	82
Figure 4.42 Series60 pitch motion in a wave $\lambda/L=0.5$, small amplitude and large amplitude	83
Figure 4.43 Comparison for heave and pitch motions of S175, $F_n=0.0$	84
Figure 4.44 Nondimensionalized nonlinear heave and pitch motion at $\lambda/L=1.25$, head seas, $F_n=0.0$	84
Figure 4.45 Body plan of the modified Wigley hull	86
Figure 4.46 Comparison for heave and pitch motions of Modified Wigley Hull at zero speed	86
Figure 4.47 Nondimensionalized nonlinear heave and pitch motion at $\lambda/L=1.0$, head seas	87

Figure 5.1 Coordinate system for the short waves range added resistance calculation methods	90
Figure 5.2 Overview of the different zones of free-surface panelization	91
Figure 5.3 Example of free-surface panelization	92
Figure 5.4 Flowchart of the HYBRID method program, with forward speed	94
Figure 5.5 Example of runtime panelization	95
Figure 5.6 Downstream potential results along longitudinal direction, $Fn=0.275$	96
Figure 5.7 Wave making resistance of a Wigley hull, without sinkage/trim correction	96
Figure 5.8 Time history of the wave making resistance of a Wigley hull, $Fn=0.25$	97
Figure 5.9 Wave exciting force of S175 ship at $Fn=0.275$	97
Figure 5.10 Motion amplitude of S175 ship at $Fn=0.275$	98
Figure 5.11 Added resistance on S-175 ship at $Fn=0.275$	99
Figure 6.1 Wetted free surface panels' simulation	103
Figure 6.2 Added masses and damping coefficients due to forced heave motion, S175, $Fn = 0.275$	106
Figure 6.3 Added masses and damping coefficients due to forced pitch motion, S175, $Fn = 0.275$	106
Figure 6.4 Heave motion amplitude calculation of S175 ship, $Fn=0.275$	107
Figure 6.5 Pitch motion amplitude calculation of S175 ship, $Fn=0.275$	108
Figure 6.6 Heave and pitch motion histories calculation of S175 ship, $\lambda/L=1.4$, $Fn=0.275$	109
Figure 6.7 Wave exciting force in heave direction of S175 ship, $Fn=0.275$	109
Figure 6.8 Heave and pitch motion of Wigley III hull, $Fn=0.2$, small amplitude	111
Figure 6.9 Panelization of the Modified Wigley III hull	111
Figure 6.9 Heave amplitude of three different Wigley hulls, $Fn=0.2$, $Amp/L=0.01$	112
Figure 6.10 Pitch amplitude of three different Wigley hulls, $Fn=0.2$, $Amp/L=0.01$	112
Figure 6.11. Heave amplitude of three different Wigley hulls, $Fn=0.2$, $Amp/L=0.02$	113
Figure 6.12. Pitch amplitude of three different Wigley hulls, $Fn=0.2$, $Amp/L=0.02$	113

List of Tables

Table 2.1 Wave resistance coefficient of the Wigley hull at $Fr=0.3$	24
Table 2.2 Wave resistance coefficient of the Wigley hull at $Fr=0.4$	24
Table 2.3 List of studies cases	31
Table 4.1 Hydrodynamic coefficients of the barge with different free-surface panelization, $T=10s$	56
Table 4.2 Hydrodynamic coefficients of the barge with different control-surface penalization, $T=10s$	58
Table 4.3 Added mass and damping results of a barge, $k=1.5$	60
Table 4.4 Added mass and damping results of a barge, $k=3.0$	60
Table 4.5 Added mass and damping results of a barge, $k=6.0$	61

Chapter 1 Introduction

1.1 Review of the State-of-Art

The reliable prediction of the seakeeping behavior of ships in real seas is a demanding task for naval architects and of great practical interest to ship owners/users, as it affects both the design and operation of ships.

Nowadays, Computational Fluid Dynamics (CFD) products based on solving Reynolds-Averaged-Navier-Stokes (RANS) equations have demonstrated their capabilities in almost every aspect of ship hydrodynamic problems, but they are still very time-consuming and even with the most advanced computational power they are still not able to conduct seakeeping assessments with proper accuracy and within desirable time. Thus the development of alternative methods based on *potential theory* is still attractive and necessary as they are much more efficient to implement.

Since the early 50ties, many hydrodynamicists addressed the problem of a surface ship sailing in waves by approximate analytical and simplified or more advanced numerical methods in the framework of linear ship motion theories. The strip theory was the first one which delivered accurate enough results for practical applications to ship motions' prediction and enjoy a wide application even today. Grim (1953) and Korvin-Kroukovsky (1955) did the pioneering work on strip theory, whereas Gerritsma & Beukelman (1967) and Salvesen et al. (1970) further improved this theory for practical applications. But due to some inherent limitations of strip theory (linearity of responses, quasi 2D approach, slender body, low speed and high frequency assumptions), its application is confined to a certain extent. Note, however, that an exact 2D second-order theory for the loads and motion responses of arbitrarily shaped 2D sectional forms was presented by Papanikolaou in the late 70ties (1977, 1980).

With the rapid advance of computer technology in the 70ties, various frequency domain 3D approaches were successfully developed for the zero speed problems (Faltinsen et al., 1975; Chang et al., 1976; Garrison, 1978; Papanikolaou, 1985). Zaraphonitis (1990) solved the exact second-order problem of loads and motions of arbitrarily 3D bodies at zero speed in waves. For the nonzero speed 3D problem, Chang (1977) was the first to present a numerical solution on the basis of the Green function method, while Inglis & Price (1981) and Guevel & Bougis (1982) later followed further improving relevant theory for practical applications. Although results of these theories appear closer to relevant experimental data, some intricate numerical problems related to the significantly more complex corresponding Green function and the treatment of the singularity at the intersection of the body boundary and the free-surface hindered their wide

application. Iwashita & Ohkusu (1992) appear to have developed a satisfactory numerical solution to the 3D, nonzero speed problem based on the Green function method.

Another approach is the so-called Rankine source method (Yeung, 1973), which use a distribution of simple $1/r$ term over the body surface as well as on a carefully-chosen part of the free surface. Many researchers, including Bertram (1990), Nakos & Sclavounos (1990), further developed this method to practical utility. The results show improvement over results from strip theory based methods due to taking into account of 3D flow effect and forward speed effect. But still they cannot be applied to study large amplitude motions of modern ships with strong flare due to their inherent linear character. Kashiwagi (1997, 2009) presented an Enhanced Unified Theory and showed good improvement by accounting the forward speed effect properly.

An alternative to the formulation and solution of the problem in the frequency domain is to work in the time domain, enabling the address of large amplitude ship motion problems which is very important for the design and the assessment of safe operation of modern ships operating in a variety of adverse environmental conditions. Following the pioneering work of Finkelstein (1957) and Cummins (1960), many researchers investigated seakeeping problems by different time domain approaches and showed promising results for both the linear problem and nonlinear problems of different level. Beck & Liapis (1987) and Korsmeyer (1988) investigated the linearized radiation problem at zero speed, while King et al. (1988) studied the linearized diffraction problem with forward speed. Beck & Magee (1990) and Ferrant (1990) presented convincing results on submerged bodies undergoing large-amplitude motions, while Lin & Yue (1990), Lin et al. (1994) and Shin et al. (1997) showed the applicability of the method to large amplitude ship motions. The time dependent change of ship's wetted surface and of ship's hull displacement due to the incident waves and ship motions could be modeled accurately. But this method proved not satisfactory in some practical cases. When it was applied to floating bodies with a flare of their sections at the waterline, which is very common to modern ship designs, numerical problems may arise and computations fail. Duan and Dai (1999) found that the common panel method using transient Green function for a non-wall-sided floating body does not satisfy the *mean-value theorem of definite integrals* for the near water surface panels. More recently Duan and Dai (2007) presented their study on an improved scheme for integration of the Green function, which shows that by their method the highly oscillatory performance of the Green function can be reduced. Further validation of this scheme is not available yet.

In addition to these alternative time domain Green function methods, the Rankine source methods have also been implemented in time domain. Sclavounos, et al. (1997) and Song, et al. (2011) developed different approaches, which showed very promising results. The difficulties of this method lies in the treatment of the radiation condition in the far-field, which is sometimes

approximated by some ‘damping beach scheme’ at certain distance from the body; one fundamental problem with this is that for the irregular seas case its application is very questionable. In all these approaches, the discretized free surface area is quite large so that a large number of panels are needed; thus, it is not easy to implement numerically.

In view of the pros and cons of these two schools of methods, a *new hybrid method* concept has been formulated. The fluid domain is decomposed into an inner and an outer part. The Rankine source method is applied in the inner domain to find the dominant equation so that there should be not any problem with body’s flare, while the transient Green function method is used in the outer domain to obtain a relationship between the velocity potential and its normal derivative on each panel, which forms a boundary condition for the inner domain solution. Duan *et al.* (1999) introduced an imaginary vertical surface which starts from the waterplane, projects downwards and encloses the hull surface in the fluid domain. This method works fine unless the body has some bulb-like hull form which exceeds the projection of the water plane. Zhang *et al.* (1998) developed a similar scheme, but introduced a matching surface which is located at some distance away from the body and moving at the same speed as the ship. He used an extrapolation scheme to simulate the free surface condition and a pre-corrected Fast Fourier Transform scheme (Kring, et al., 2000) to speed up the simulation.

Yasukawa (2003) presented a similar scheme for Numerical Wave Tank (NMT) simulation purpose. A damping beach is imposed on the tank side opposing the wave maker. The near field free surface panels are arbitrarily shaped and moving with the ship. They are treated as additional unknown panels whereas the source strengths of the fixed panels on the same position are set to zero. Kataoka and Iwashita (2004) also developed a similar scheme to solve the seakeeping problem. Besides the similarity with the other methods in the theoretical formulation, at every time step the nodes of time-varying free surface panels are shifted only in y-direction and the corresponding matrices’ elements are updated. Also in this formulation the solution domain is fixed so that the radiation condition on the matching surface can be obtained exactly. The difference between these methods basically lies in the different ways of treatment of the boundary condition in the far field, in simulating the free surface and the numerical schemes. More recently, there is a trend of integrating CFD techniques into the hybrid method so as to study highly nonlinear phenomena. Iafrati, et al. (2003) presented a hybrid method combining a CFD scheme using conventional grids and the BEM for potential-flow free-surface problems. Sueyoshi et al. (2007) uses particle methods in the inner domain and a boundary element method in the outer domain to study various wave-free surface problems. Lin et al. (2009) presented recently a paper where they combined a viscous flow solver in the inner domain and potential

flow solver in the outer domain. There is a slight overlap between the two introduced domains, which creates a matching domain.

The approaches adopted in the present thesis are believed to continue above introduced hybrid concept developments and will be elaborated in the following.

1.2 Overview, Objectives and Innovations

The main objective of this thesis is to develop in the frame of potential theory a time domain, numerical simulation method, which is capable of predicting large amplitude motions of ships and floating structures in response to incoming waves. Addressed shiplike bodies are assumed with zero or nonzero constant forward speed. Developed method(s) and related software tool(s) should be applicable to ship design and the assessment of ships and offshore structures in seaways.

In the course of this thesis, the author proceeded with the development of a Time Domain transient Green Function method (TDGF) and demonstrated its implementation by applications to the fundamental hydrodynamic problems (Liu *et al.*, 2007). Due to the inherent limitation of the method, it is not applicable to the study of realistic ships with flares. Thus the hybrid method concept is adopted for the calculation of hydrodynamic forces acting on ships advancing with constant speed in waves. In this method, the fluid domain is decomposed into an inner and an outer part. The Rankine source method is applied in the inner domain while the transient Green function method is used in the outer domain. This hybrid method works efficiently with a relatively small number of panels compared to a pure Rankine source method, for the free surface panelization is restricted between the body boundary and the control surface. A double integration algorithm with respect to time, originally developed by Wang (2003) and validated on diffraction forces' calculation, is herein adopted to simulate the free-surface boundary condition.

For the simulation of the motions, the calculation of the force components is based on the following assumptions: if the incident wave amplitude is small (quasi-linear case), then the Froude-Krylov forces and hydrostatic restoring forces are calculated based on ships' geometric/hydrostatic data, whereas, if the incident wave amplitude is large, then both above force components are calculated exactly up to the undisturbed incident wave surface. The diffraction forces and radiation forces, however, are calculated up to the mean wetted surface by the developed hybrid method in all incident wave amplitude cases. Calculated force components are introduced into the equations of motions to predict ship motions in the time domain.

Developed theoretical time domain simulation method was numerically implemented by use of the Boundary Element Method (BEM). The boundary of the inner domain is discretized in to

quadratic or triangular panels. On each panel the potential value or source strength is assumed to be constant. The Generalized Minimum RESidual (GMRES) method is adopted to obtain a solution for the equations. After the potentials and its spatial partial derivatives on the panels are obtained, the pressure is calculated by Bernoulli's equation. Then the hydrodynamic forces can be obtained by integrating the pressure over the wetted hull surface. Then the motions of the ship are simulated by using an iterative prediction-correction scheme. After the converged value is arrived, the simulated will march to next step. In order to yield stable and accurate prediction, the Chimera grid concept is introduced so that two panel systems are set up in the beginning of the simulation. There will be simultaneous information exchange between the two grid systems. In order to validate the developed theoretical method and numerical scheme (computer code), many characteristic case studies on the hydrodynamic forces and motions of standard type ships have been conducted. Results are compared with those of other authors and available experimental data. An important outcome of the presented method is its successful application to the assessment of the ITTC standard ship S175, which has non-wall-sided sections at the ends, while moving with forward speed in head seas. Good agreement has been observed for all studied cases between the results of the present method, other numerical codes and experimental data. Thus, the method proves promising regarding its applicability to the more general large amplitude motion problem of ships, advancing in waves of arbitrary heading.

In the course of the conducted research, the hybrid method has also been applied to study the seakeeping performance of a basic Wigley hull with different above-water shape, both at zero speed and nonzero speed. Obtained results clearly show the effect of different above-waterplane shape on motions, thus they prove that the developed method can be used for ship design optimization and the assessment of ships' performance in high seas. Meanwhile the added resistance of ships can also be calculated in the framework of the present method. This capability will support the increased importance of this type of tools in ship design, when selecting ship's engine/propulsion system and considering ship's performance in terms of sustainable service speed in realistic sea conditions. It also affects ship's operation when optimizing the sailing route for minimum fuel consumption and green-sailing considerations.

The main objectives and innovations of this thesis refer to the following:

- Development and numerical implementation of a hybrid, nonlinear time-domain method for the prediction of forces exerted on the ship calm water and in waves (wave making resistance, radiation and diffraction forces, added resistance in waves) and of large amplitude ship motions in response to incoming small or large amplitude waves. The introduced method accounts for the above still water level hull form.

-
- The developed method is called *hybrid* in the sense of dividing the fluid flow domain into an inner domain and an outer domain and using different approach in each domain but matching the solution of each domain on the matching surface. Furthermore, the force components in motion simulation are calculated based on different assumptions, which is also *hybrid*.
 - Numerical implementation of the GMRES method in the solution of the large scale set of equations, which seems not to have been adopted by other authors before.
 - Introduction of the *Chimera* grid concept to account for the accurate description of fluid domain geometry with limited number of panels and to allow small time-step simulation which is necessary for accurate time-domain simulations.
 - Simulation of the free surface boundary condition by integration of the linearized free surface condition. Though this method was introduced by another author before, its validation was limited to the calculation of the diffraction forces only.
 - Introduction of the far field added resistance calculation method into a time domain solver and validation thereof in a large variety of study cases.

1.3 Chapters of This Thesis

The present thesis describes the development and validation of a time domain hybrid method and a suit of software tools for simulating large amplitude motions of ships advancing in waves with constant forward speed. It consists of the following contents:

In Chapter 2, the potential theory boundary value problem is formulated and the time domain Green function method is introduced to solve the problem. Numerical scheme is briefly described and validation results are presented on the calculation of hydrodynamic forces.

In Chapter 3, the hybrid method is introduced and motion prediction method is elaborated. Specific problems, such as free surface condition simulation and m_j term calculation, are explained.

In Chapter 4, validation results for zero speed case are presented, including diffraction problem, forced motion problem, free motion problem under the excitation of both small amplitude and large amplitude incident waves. Based on the numerical tests, preliminary conclusions are drawn on how to determine the optimal matching surface and corresponding panelization. A variety of hull forms are used to validate the linear hydrodynamic coefficients, exciting forces, and some discussion of large amplitude motions.

In Chapter 5, validation results for non-zero speed case are presented, including wave making resistance problem, diffraction problem, forced motion problem, free motion problem under the

excitation of both small amplitude and large amplitude incident waves, also the quasi second quantity, added resistance, is calculated.

In Chapter 6, the formulation is reconsidered in a body-fixed coordinate system so as to use a fixed free surface area to improve the computational efficiency. Validation results include the forced motion problem and free motion problem of a container ship. By studying a mathematical Wigley type hull with different above water shapes it is shown that the developed scheme is capable of evaluating the seakeeping character from the design point of view.

Chapter 2 Time Domain Transient Green Function Method

2.1 Definition of the Boundary Value Problem

Consider an arbitrary 3D body floating on the free surface and undergoing 6-DOF motions. An earth-fixed Cartesian coordinate system is chosen with the x-y plane coincident with the undisturbed free surface and z-axis pointing upwards through the ship's mass centroid. The origin O is located on the undisturbed free-surface. Ship's forward speed U_0 is in x-axis direction. The fluid is assumed to be homogeneous, incompressible, inviscid and its motion irrotational. The water depth is infinite. The unsteady flow field can be described by a velocity potential:

$$\Phi_T(x,y,z,t) = \Phi_0(x,y,z,t) + \Phi(x,y,z,t) \quad (2-1)$$

where Φ_0 is the incident wave potential, $\Phi = \Phi_T - \Phi_0$ is the disturbed flow potential, t is time, and $p(x, y, z)$ is a point in the flow field. In the fluid domain $\Omega(t)$, which is bounded by the free surface $S_f(t)$, the body surface $S_b(t)$ and the control surface S_c at far field, $\Phi(p, t)$ satisfies Laplace's equation:

$$\nabla^2 \Phi(p, t) = 0 \quad (2-2)$$

The body boundary condition is applied on the instantaneously wetted body boundary $S_b(t)$:

$$\partial \Phi / \partial n = v_n - \partial \Phi_0 / \partial n \quad (\text{on } S_b(t), t > 0) \quad (2-3)$$

\mathbf{n} is the unit normal vector pointing out of the fluid domain $\Omega(t)$, and v_n is the instantaneous velocity of the body surface. The *linearized* condition is imposed on the free surface $S_f(t)$:

$$\frac{\partial^2 \Phi}{\partial t^2} + g \frac{\partial \Phi}{\partial z} = 0 \quad (\text{on } S_f(t), t > 0) \quad (2-4)$$

where g is the gravitational acceleration. The initial conditions at $t=0$ are:

$$\Phi = \frac{\partial \Phi}{\partial t} = 0 \quad (\text{on } S_f(t), t=0) \quad (2-5)$$

For finite time, the conditions on the control surface at infinite are:

$$\Phi, \nabla \Phi, \frac{\partial \Phi}{\partial t} \rightarrow 0 \quad (\text{on } S_c, t > 0) \quad (2-6)$$

2.2 Integral Equations

The time-domain transient Green function (TDGF) which satisfies the linearized free-surface condition is defined as following:

$$G(p,t; q,\tau) = \left(\frac{1}{r_{pq}} - \frac{1}{r_{pq'}} \right) + \tilde{G}(p,t; q,\tau) \quad (2-7)$$

where $\tilde{G}(p,t; q,\tau)$ represents the free-surface memory part:

$$\tilde{G}(p,t; q,\tau) = 2 \int_0^\infty \sqrt{gk} e^{k(z+\zeta)} J_0(kR) \sin \left[\sqrt{gk} (t-\tau) \right] dk \quad (2-8)$$

where $p(x,y,z)$ and $q(\xi,\eta,\zeta)$ are the field and source points respectively, $R = \sqrt{(x-\xi)^2 + (y-\eta)^2}$
 $r_{pq} = \sqrt{R^2 + (z-\zeta)^2}$, $r_{pq'} = \sqrt{R^2 + (z+\zeta)^2}$, and J_0 is the zero-order Bessel function.

Suppose that p is in the fluid domain $\Omega(t)$, we apply Green's Theorem to $\Phi(q,\tau)$ and $\tilde{G}(p,t; q,\tau)$. After certain transformations, we get the integral equation for the disturbed potential $\Phi(p,t)$ as following:

$$2\pi\Phi(p,t) + \iint_{S_b(t)} \left[\Phi(q,t) \frac{\partial}{\partial n_q} \left(\frac{1}{r_{pq}} - \frac{1}{r_{pq'}} \right) - \left(\frac{1}{r_{pq}} - \frac{1}{r_{pq'}} \right) \frac{\partial \Phi}{\partial n_q} \right] ds_q = \int_0^t d\tau \left\{ \iint_{S_b(\tau)} \left(\tilde{G} \frac{\partial \Phi}{\partial n_q} - \Phi \frac{\partial \tilde{G}}{\partial n_q} \right) ds_q + \frac{1}{g} \int_{wl(\tau)} \left(\tilde{G} \frac{\partial \Phi}{\partial \tau} - \Phi \frac{\partial \tilde{G}}{\partial \tau} \right) V_N dl_q \right\} \quad (2-9)$$

where $p \in S_b(t)$, $wl(\tau)$ is the intersection line of the instant ship surface and XOY plane and \mathbf{N} is the normal vector of $wl(\tau)$, and V_N is the velocity of $wl(\tau)$ on \mathbf{N} direction. This integral equation features a *mixed distribution* of dipoles and sources over the body surface and it leads directly to solutions of velocity potential on the body surface. An alternative integral equation which features a *source distribution* takes the following form:

$$\Phi(p,t) = \frac{1}{4\pi} \iint_{S_b(t)} \sigma(q,t) \left(\frac{1}{r_{pq}} - \frac{1}{r_{pq'}} \right) ds_q + \frac{1}{4\pi} \int_0^t d\tau \left[\iint_{S_b(\tau)} \sigma(q,\tau) \tilde{G}(p,t; q,\tau) ds_q + \frac{1}{g} \int_{wl(\tau)} \sigma(q,\tau) \tilde{G}(p,t; q,\tau) V_N v_n dl_q \right] \quad (2-10)$$

where $\sigma(q,t)$ is the source strength and $p \in \Omega_b(t)$. Notice that $v_n = (\mathbf{N} \cdot \mathbf{n}) V_N$ and apply the body boundary condition for p so we obtain the equation for σ :

$$\frac{\partial \Phi}{\partial n_p} = v_n(p,t) - \frac{\partial \Phi_I}{\partial n_p} = \frac{1}{2} \sigma(p,t) + \frac{1}{4\pi} \iint_{S_b(t)} \sigma(q,t) \frac{\partial}{\partial n_p} \left(\frac{1}{r} - \frac{1}{r'} \right) ds_q + \frac{1}{4\pi} \int_0^t d\tau \left[\iint_{S_b(\tau)} \sigma(q,\tau) \frac{\partial \tilde{G}}{\partial n_p} ds_q - \frac{1}{g} \int_{wl(\tau)} \sigma(q,\tau) \frac{\partial \tilde{G}}{\partial n_p} V_N v_n dl_q \right] \quad p \in S_b(t) \quad (2-11)$$

After finding the solution of σ , Φ and $\partial \Phi / \partial x_i$ can be easily evaluated.

2.3 Hydrodynamic Forces

The unsteady pressure exerting on the body is given by Bernoulli's equation:

$$p = -\rho \left(\frac{\partial \Phi}{\partial t} + \frac{1}{2} \nabla \Phi \cdot \nabla \Phi \right) \quad (2-12)$$

Integrating the above equation over the instantaneous wetted surface $S_b(t)$ we can obtain the hydrodynamic forces acting on the body:

$$\vec{F} = -\rho \iint_{S_b(t)} p \vec{n} ds \quad (2-13)$$

$\frac{\partial \Phi}{\partial t}$ is usually evaluated by introducing the material derivative of the potential on the body as:

$$\frac{\partial \Phi}{\partial t} = \frac{D\Phi}{Dt} - \vec{V} \cdot \nabla \Phi \quad (2-14)$$

The material derivative is obtained by finite-differencing of the potential on the body panels to time (Lin et al. 1990; Yasukawa, 2003). V includes both the forward speed and wave induced motion speed. In the present work, only the forward speed part is accounted. In fact, with some transformations (Duan, 1995), we can obtain a more convenient expression for numerical computation, especially when studying a floating body whose instantaneous wet surface is varying with time:

$$\begin{aligned} \vec{F} &= -\rho \frac{d}{dt} \iint_{S_b(t)} \Phi \vec{n} ds + \rho \iint_{S_b(t)} \left[\frac{\partial \Phi}{\partial n} \cdot \nabla \Phi - \frac{1}{2} (\nabla \Phi)^2 \vec{n} \right] ds - \rho \int_{\Gamma(t)} \Phi V_N \vec{k} dl \\ \vec{M} &= -\rho \frac{d}{dt} \iint_{S_b(t)} \Phi (\vec{r} \times \vec{n}) ds \\ &+ \rho \iint_{S_b(t)} \left[(\nabla \Phi) \frac{\partial \Phi}{\partial n} \vec{r} - \frac{1}{2} (\nabla \Phi)^2 (\vec{r} \times \vec{n}) \right] ds - \rho \int_{\Gamma(t)} \Phi V_N (\vec{r} \times \vec{k}) dl \end{aligned} \quad (2-15)$$

For a submerged body undergoing large amplitude motions, the waterline integral term vanishes. Once the time varying forces are obtained, we can conduct a harmonic analysis as below:

$$F_{ij}(t) = \sum_{n=0}^{\infty} (A_{ij}(n) \cos n\omega t + B_{ij}(n) \sin n\omega t) \quad (2-16)$$

in which $A_{ij}(I)$ and $B_{ij}(I)$ correspond to the *linear* frequency domain concepts of added mass and damping coefficient.

2.4 The Quasi-Second Order Problem - Calculation of Added Resistance

As a physical phenomenon, the added resistance is a steady force of second-order with respect to the incident wave amplitude, occurring when a ship advancing with certain speed in a seaway and which is acting opposite to ship's forward speed in longitudinal direction, thus increasing ship's calm water resistance. The prediction of added resistance is of high practical interest recently due to economic and operation considerations, thus it grasps many researchers' interest. For a time domain method, the direct way for obtaining the added resistance is to calculate both the wave making resistance in calm water and total resistance in waves and then subtract the difference between them; but it basically needs two runs and the accurate and robust calculation of partial derivatives, which is not easy. In the present study, Maruo's far field theory (1963) based on the Kochin function concept is adopted for added resistance prediction and the corresponding scheme is imbedded into the present code for validation purpose.

The complex function $H(k_j, \theta)$, known as *Kochin* function, describing the elementary waves radiated from the ships is given by:

$$H(k_j, \theta) = \iint_S \left(\phi \frac{\partial}{\partial n} - \frac{\partial \phi}{\partial n} \right) G_j(\theta) ds \quad (2-17)$$

where:

$$G_j(\theta) = \exp \left[k_j(\theta) z + i k_j(\theta) (x \cos \theta + y \sin \theta) \right] \quad (2-18)$$

and $k_j(\theta)$, $j = 1, 2$ are the unsteady wave numbers:

$$k_j(\theta) = \frac{K_0}{2} \frac{1 - 2\Omega \cos \theta \pm \sqrt{1 - 4\Omega \cos \theta}}{\cos^2 \theta} \quad \begin{matrix} (+ : j=1 \\ - : j=2 \end{matrix}$$

In the above equations, θ is the angle of elementary waves generated by the body, $\Omega = \omega_e V / g$ is the *Hanaoka* parameter and $K_0 = g / V^2$ is the steady wave number. From the above expression the following expressions may be derived for $k_1(\theta)$ and $k_2(\theta)$:

$$k_1(\theta) = K_0 \sec^2 \theta \left(\frac{1 + \sqrt{1 - 4\Omega \cos \theta}}{4} \right)^2; \quad k_2(\theta) = k \left(\frac{2}{1 + \sqrt{1 - 4\Omega \cos \theta}} \right)^2$$

Following Maruo (1963), the added resistance may be expressed by the above Kochin function as:

$$\begin{aligned} R_{AW} = & \frac{\rho}{8\pi} \left\{ \int_{-\frac{\pi}{2}}^{-\alpha_0} + \int_{\alpha_0}^{\frac{\pi}{2}} - \int_{\frac{\pi}{2}}^{\frac{3\pi}{2}} \right\} |H(k_1, \theta)|^2 \frac{k_1 [k_1 \cos \theta - k \cos \chi]}{\sqrt{1 - 4\Omega \cos \theta}} d\theta + \\ & + \frac{\rho}{8\pi} \int_{\alpha_0}^{2\pi - \alpha_0} |H(k_2, \theta)|^2 \frac{k_2 [k_2 \cos \theta - k \cos \chi]}{\sqrt{1 - 4\Omega \cos \theta}} d\theta \end{aligned} \quad (2-19)$$

where ρ is the density of sea water and α_0 is the critical angle ($\alpha_0 = \arccos(1/(4\Omega))$) for $\Omega > 1/4$ and $\alpha_0 = 0$ for $\Omega \leq 1/4$. When $V=0$ then $\Omega=0$, $k_1(\theta) \rightarrow \infty$ and $k_2(\theta)=k$. Thus the wave systems are reduced to the ring wave only. For the zero speed case, the drift force may be expressed as following (Maruo, 1960):

$$R_{AW} = \frac{\rho k^2}{8\pi} \int_0^{2\pi} |H(\theta)|^2 (\cos \theta - \cos \chi) d\theta \quad (2-20)$$

where $H(\theta) = \iint_S \exp[kz + ik(x \cos \theta + y \sin \theta)] \left[\phi k (n_z + i \cos \theta \cdot n_x + i \sin \theta \cdot n_y) - \frac{\partial \phi}{\partial n} \right] ds$

2.5 Numerical Scheme

To solve the above integral equations, the normal panel method (Hess and Smith, 1964) is used. The wetted body surface is divided into N^b quadrilateral panels and the waterline intersection is divided into N^w segments. The velocity potential and its derivatives on each panel and segment are assumed to be constant while the equations are satisfied on the geometrical center. Take Eq. (2-9) as an example, the discretized form is:

$$\sum_{j=1}^{N^b} \{C_{ij} \Phi_{nj}^M + D_{ij} \Phi_i^M\} = MM_i \quad i = 1, 2, \dots, N^b \quad (2-21)$$

the influence matrices are:

$$C_{ij} = -\iint_{\Delta s_j} \left(\frac{1}{r} - \frac{1}{r'} \right) ds, \quad D_{ij} = \begin{cases} 2\pi + \iint_{\Delta s_j} \frac{\partial}{\partial n_j} \left(-\frac{1}{r} \right) ds & i = j \\ \iint_{\Delta s_j} \frac{\partial}{\partial n_j} \left(\frac{1}{r} - \frac{1}{r'} \right) ds & i \neq j \end{cases}$$

$$MM_i = \Delta t \sum_{m=0}^{M-1} \left\{ \sum_{j=1}^{N^b} \left(\Phi_{nj}^m \iint_{\Delta s_j} \tilde{G}_j^m ds - \Phi_j^m \iint_{\Delta s_j} \tilde{G}_{nj}^m ds \right) + \frac{1}{g} \sum_{k=1}^{N^w} \left(\tilde{G}_k^m \int_{\Delta l_k} \Phi_{\tau k}^m V_{Nk}^m dl_k - \Phi_k^m \int_{\Delta l_k} \tilde{G}_{\tau k}^m V_{Nk}^m dl_k \right) \right\}$$

where m, M are the indices of history time τ and present time t ; i, j and k are the indices for field point p , source point q and waterline segment Δl . For instance, \tilde{G}_{nj}^m means the normal velocity

$\frac{\partial \tilde{G}}{\partial n}$ on j -th panel at time τ .

In the computation, the body surface is usually discretized by 100~400 panels (for added resistance calculation, finer panels will be absolutely necessary) so that the influence matrices are not large. A Gaussian Elimination method is a good choice to find the solution. But as MM_i is a convolutional integration, the solution must be done with a time-marching technique thus burdens the calculation. After mapping the quadrilateral elements into standard unit squares the integration

of the memory-related terms may be obtained by one-point or four-point Gauss quadrature. The computation of \tilde{G} related terms is based on Huang's work (1991). As to the submerged case or floating bodies at zero speed, the waterline integral vanish automatically. For the cases with floating bodies, the waterline integral is not included in the present work.

For added resistance problem, the calculation of Kochin functions is of first importance. In head waves for the symmetric potentials ϕ_1, ϕ_3, ϕ_5 and the symmetric part of the diffraction potential ϕ_{7c} , the Kochin function takes the following form:

$$H_m(k_j, \theta) = 2 \iint_{S/2} e^{k_j(\theta)z + ik_j(\theta)x \cos \theta} \cos(k_j(\theta)y \sin \theta) \cdot \left[k_j(\theta)(\phi_{mc}n_z - \phi_{ms} \cdot \cos \theta \cdot n_x) - \frac{\partial \phi_{mc}}{\partial n} + i \cdot k_j(\theta)(\phi_{ms}n_z + \phi_{mc}n_x \cos \theta) - i \frac{\partial \phi_{ms}}{\partial n} \right] ds \quad (2-22)$$

$$- 2 \iint_{S/2} e^{k_j(\theta)z + ik_j(\theta)x \cos \theta} \sin(k_j(\theta)y \sin \theta) \cdot (\phi_{mc} + i\phi_{ms})k_j(\theta) \cdot \sin \theta \cdot n_y ds$$

where, $m= 1, 3, 5, 7c$. For the anti-symmetric potentials, i.e. ϕ_2, ϕ_4, ϕ_6 and ϕ_{7s} , the Kochin function takes the following form:

$$H_m(k_j, \theta) = 2i \iint_{S/2} e^{k_jz + ik_jx \cos \theta} \sin(k_j(\theta)y \sin \theta) \cdot \left[k_j(\theta)(\phi_{mc}n_z - \phi_{ms} \cos \theta \cdot n_x) - \frac{\partial \phi_{mc}}{\partial n} + i \cdot k_j(\theta)(\phi_{ms}n_z + \phi_{mc}n_x \cos \theta) - i \frac{\partial \phi_{ms}}{\partial n} \right] ds \quad (2-23)$$

$$+ 2 \iint_{S/2} e^{k_j(\theta)z + ik_j(\theta)x \cos \theta} \cos(k_j(\theta)y \sin \theta) (\phi_{mc} + i\phi_{ms})k_j(\theta) \cdot i \cdot \sin \theta \cdot n_y ds$$

where, $m= 2, 4, 6, 7s$.

2.6 Numerical Results and Discussion

2.6.1 Radiation Problem of a Floating Hemisphere

The first set of numerical results obtained include added-mass and damping coefficients for a floating hemisphere studied by Hulme (1982). At this stage, we use the linearized body boundary condition. Starting from rest, the hemisphere is undergoing a sinusoidal motion $z=A \sin \omega t$ in deep water. Results from present method, obtained by use of 256 panels and 40 time steps per period, are compared with those of the frequency domain code NEWDRIFT (Papanikolaou, 1985; Papanikolaou & Zaraphonitis, 1987; Papanikolaou, et al. 1990) with 100 panels and of Hulme's semi-analytical method. Figure 2.1 shows the comparison of the added-mass and damping coefficient in heave, noting that A_{33} is divided by $2\pi\rho R^3/3$ and B_{33} by $2\pi\rho\omega R^3/3$ non-dimensionalization. The agreement between all methods over the entire frequency range is very

good, except for the irregular frequencies problem appearing in the results of the frequency domain code NEWDRIFT that is herein not treated.

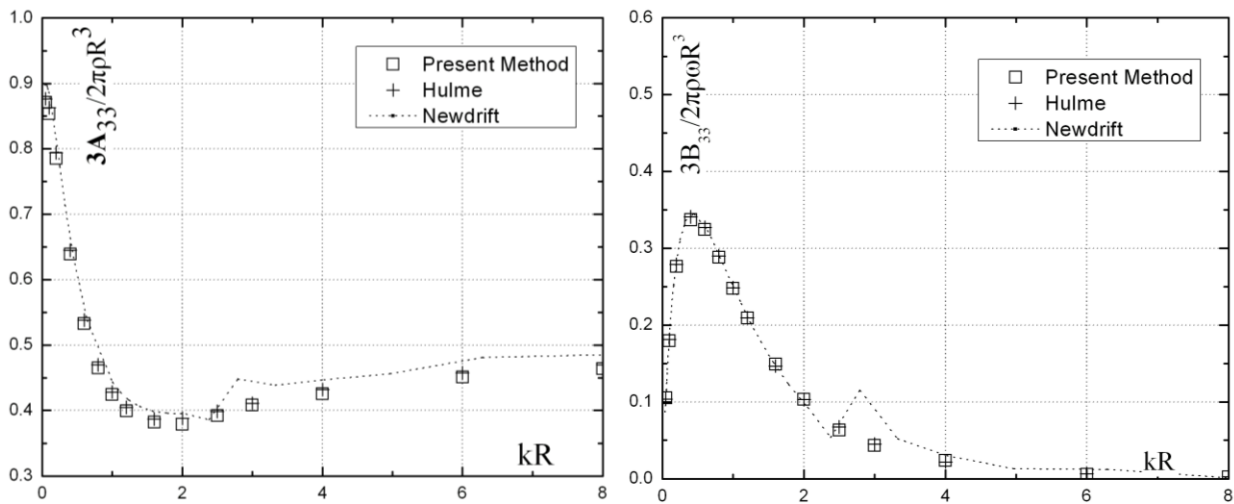


Figure 2.1 Comparison on added-masses and damping coefficients

2.6.2 Radiation Problem of a Submerged Sphere

Ferrant (1990) presented results on the heaving problem of a submerged sphere, with a mean depth of submergence equal to the diameter ($z_0/R=2.0$, Figure 2.2). In order to compare with Ferrant’s results, the same number of discrete panels, which is 200 on the whole surface, is used by NEWDRIFT and present method. Figure 2.3 shows the comparison on heave induced added-mass and damping coefficient, noting that results are divided by $4\pi\rho R^3/3$ for A_{33} , and $2\pi\rho\omega R^3/3$ for B_{33} for non-dimensionalization. The agreement among the various methods is good, despite that depending on the methods used (linear or body-exact) a clear deviation is observed.

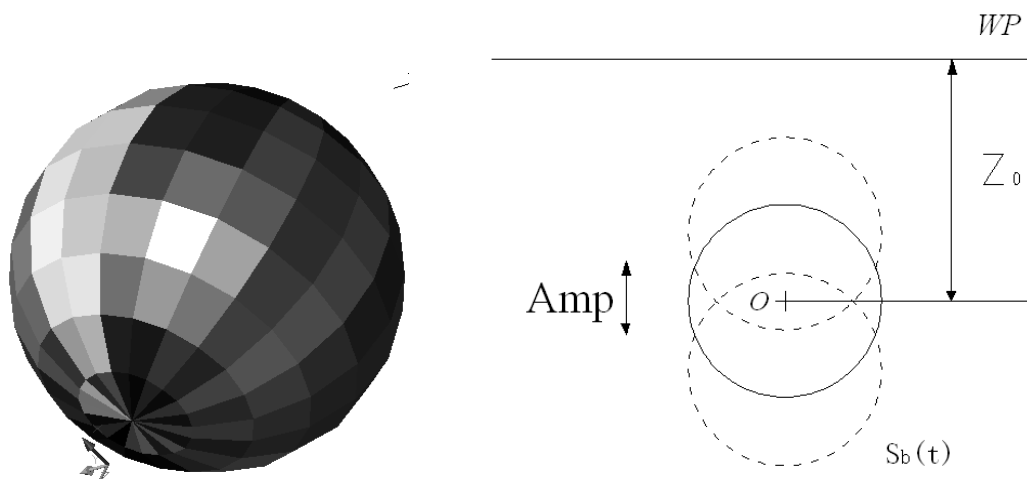


Figure 2.2 Panelization of the Sphere and its motion $Z=Z_0+A\cos\omega t$

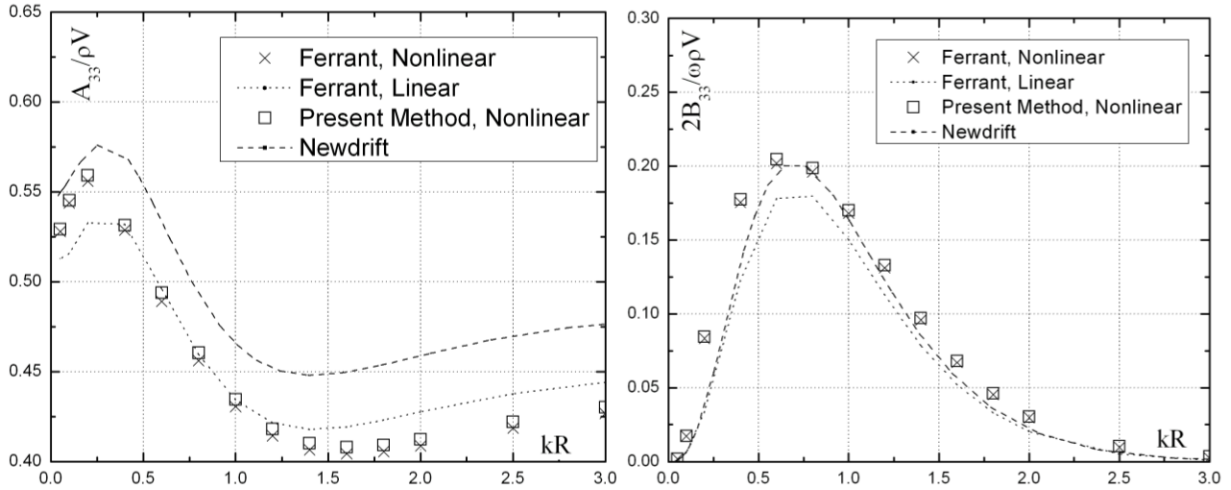


Figure 2.3 Comparison on added masses and damping coefficients

2.6.3 Radiation Problem of a Wigley Hull

A Wigley hull is defined as: $y/B_0 = [1 - (2x/L)^2][1 - (z/H)^2]$ where the beam-to-length ratio $2B_0/L = 0.1$ and draft-to-length ratio $H/L = 0.0625$. Here a hull with $L = 50.0m$ is investigated.

First, the linear case, that is, small-amplitude heaving about the equilibrium position so that the hydrodynamic force is simulated up to the mean wetted surface, is studied. 240 quadrilateral panels are used to represent the hull and the time step is determined by $\Delta t = 2\pi/40\omega$. The results are plotted against the results from NEWDRIFT in Figure 2.4.

Secondly, the large-amplitude heaving induced “added-mass” and “damping coefficient” are calculated and plotted. We choose the case $k = 0.1$ and change the amplitude of the heaving motion. After obtaining the velocity potential, two different methods, the so called differential method (noted as DIF) and the integral method (noted as ITG), are used to calculate the forces and then the same procedure is carried out to get the added-mass and damping coefficients. Figure 2.5 shows the results from this calculation. For comparison purpose, the linear results of NEWDRIFT are also plotted.

From Figure 2.5 it is clear that if the amplitude is relatively small, added mass and damping coefficients don’t change significantly. But after the amplitude arrives some value, say $Amp/B_0 = 0.3$, the effect of the amplitude becomes very clear. Similar trend has also been observed by other researchers (Kataoka et al, 2002). What’s more, the deviation between the results from traditional differential method and integral method is obvious, which indicated the necessity to employ the concept of integrating form expression (2-15) when dealing with the large-amplitude problems.

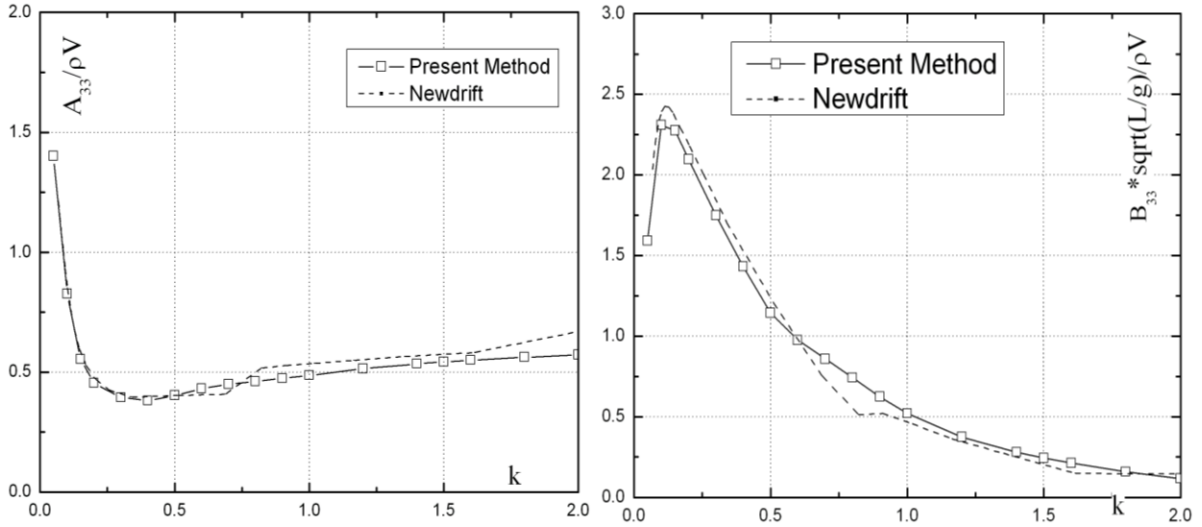


Figure 2.4 Comparison on added masses and damping coefficients

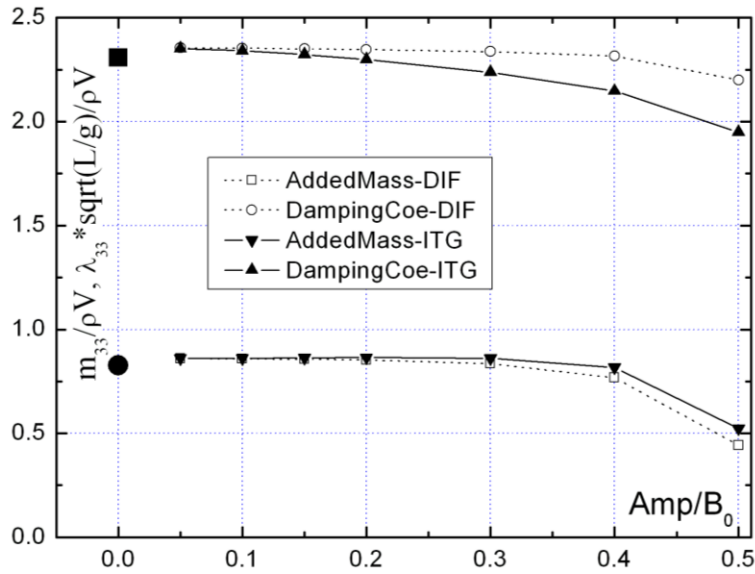


Figure 2.5 Results at different heaving amplitude for $k=0.1$, the linear results are denoted by ■ & ●

2.6.4 Diffraction Problem of a Submerged Sphere

A submerged sphere advancing in regular deep-water head waves at constant forward speed has been analyzed by Wu et al. (1988) with a linearized potential method. A distribution of sources over the surface of the sphere is expanded into a series of Legendre functions, which is an extension of the method used by Farell (1973) in analyzing the wave resistance on a submerged ellipsoid. Wu's calculation was in frequency domain, while present calculation is in time domain. In order to compare the force amplitude results, a harmonic analysis of the diffraction forces is performed:

$$F(t) = (F_{real} \cos \omega t + F_{imag} \sin \omega t) / A \rho g \pi r^3 k$$

F_{real} and F_{imag} are the so-called non-dimensional real part and imaginary parts of the wave exciting forces. The results from present TDGF method are obtained with a 100-panel meshing of the semi-hull and 52 time steps' calculation per period. Good agreement among results from different numerical methods is observed. The abscissas in Figure 2.6 are the reduced wave number kR .

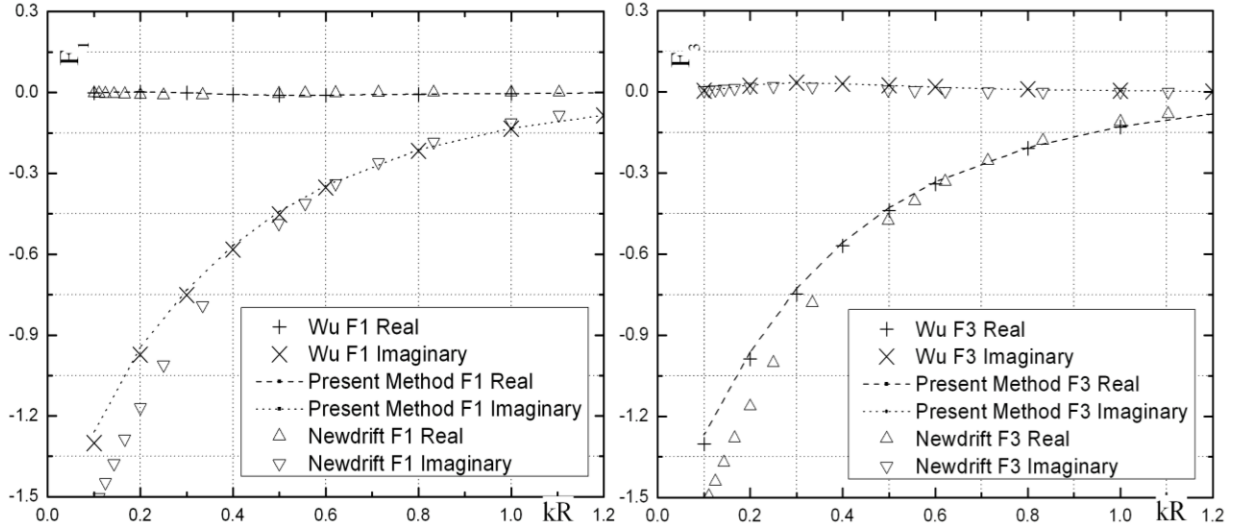


Figure 2.6 Comparison on wave load F_1 and F_3

2.6.5 Diffraction Problem of a Wigley Hull

The experiment data of a Wigley-hull form with a mid-ship section coefficient $C_m = 2/3$ and length-breadth ratio $L/B = 10$ were published by J.M.J. Journée (1992). A perspective view of the Wigley hull discretized with 250 panels is shown in Figure 2.7. The test results refer to hydrodynamic coefficients for heave and pitch, vertical motions, wave loads and added resistance in head waves. In order to validate the code, calculations are carried out herein on the wave loads acting on this Wigley hull. The dimensionless results are defined in accordance to Journée as:

$$F_1 = \frac{F_1^0}{k\zeta_a \rho g \nabla}, F_3 = \frac{F_3^0}{C_{33}\zeta_a}, F_5 = \frac{F_5^0}{kC_{55}\zeta_a}. \text{ Results obtained from present method are shown from}$$

Figure 2.8 and Fig 2.9, compared with results from the frequency domain code NEWDRIFT.

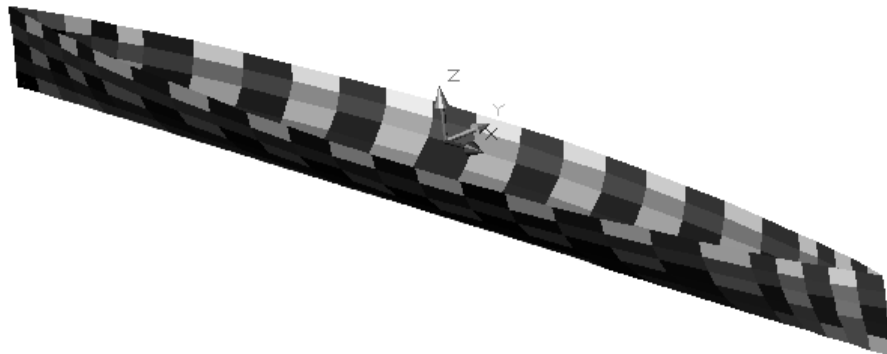


Figure 2.7 Panels used to represent the Wigley hull

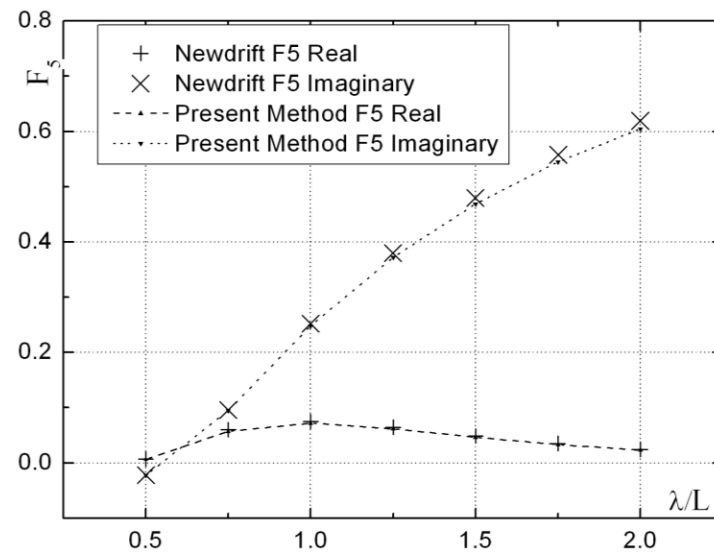
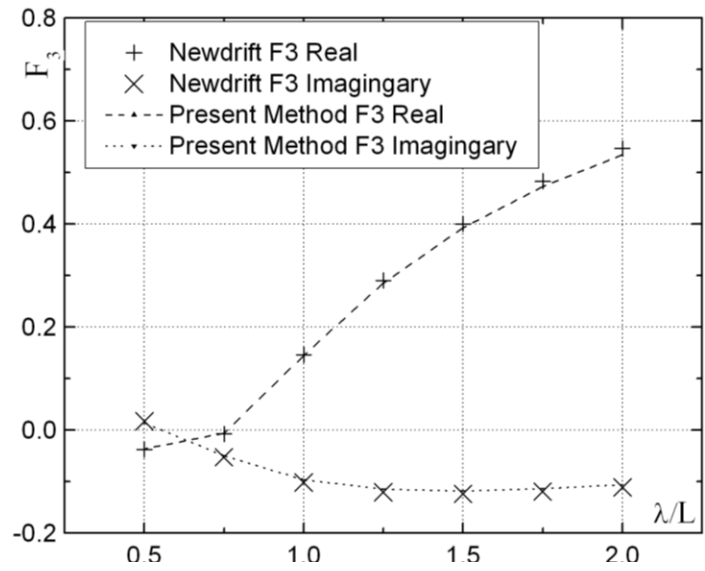
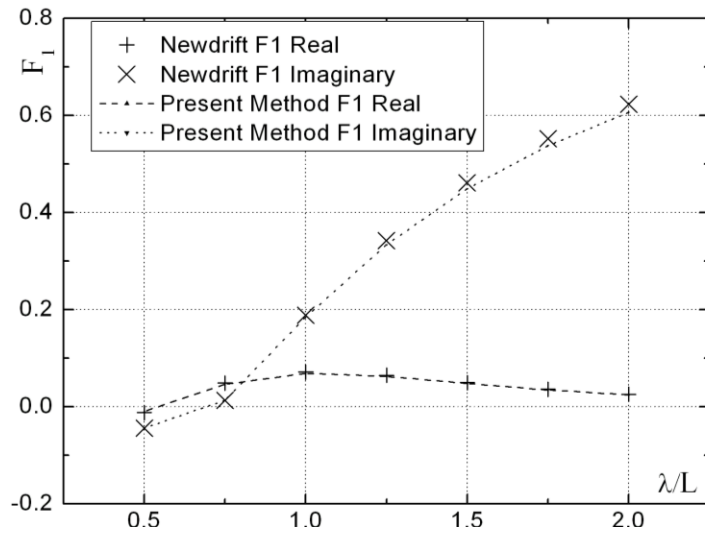


Figure 2.8 Calculated results of wave load F_1 , F_3 and F_5 , $F_n=0.0$, head seas

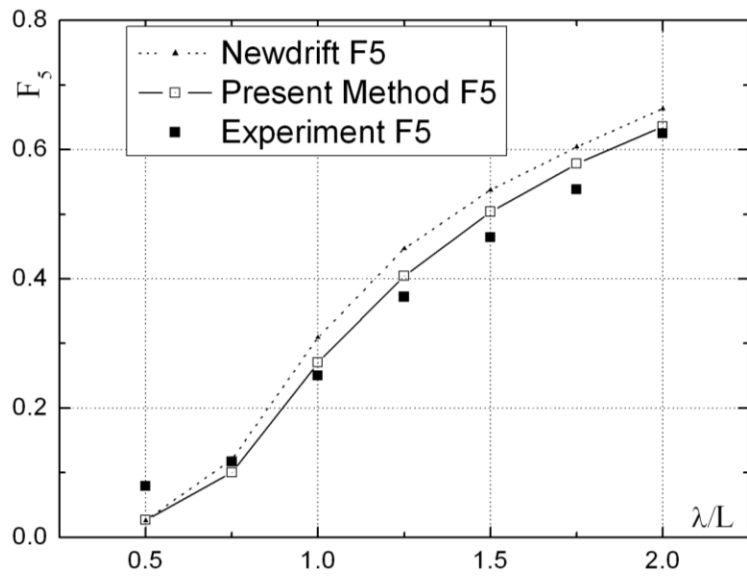
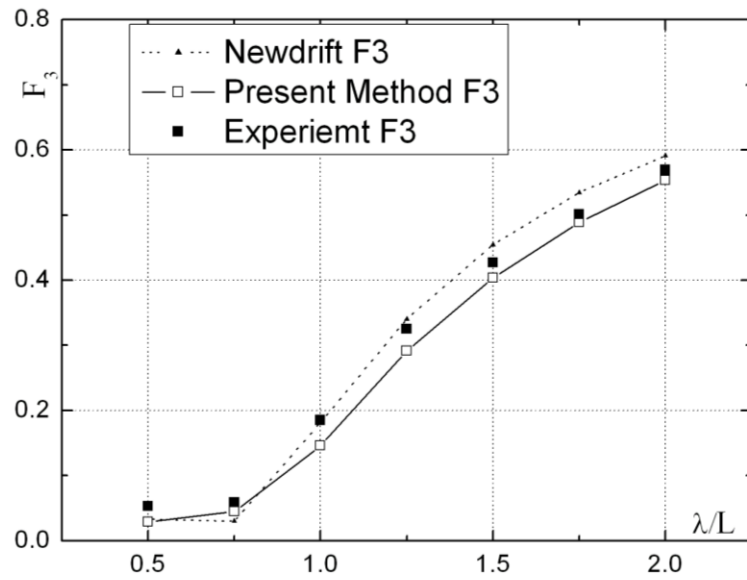
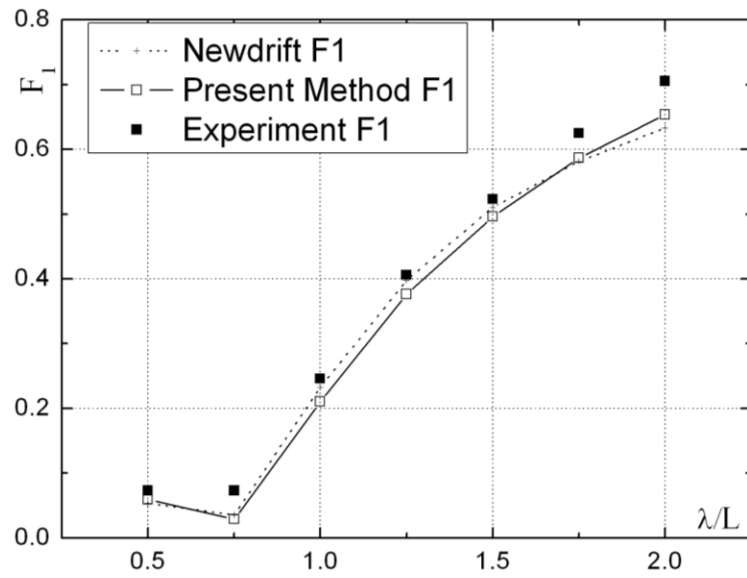


Figure 2.9 Calculated results of wave load F_1 , F_3 and F_5 , $F_n=0.2$, head seas

2.6.6 Resistance of a Submerged Spheroid

An ellipsoid with its major axis parallel to the free surface and moving with forward speed has been studied by Farell (1973) and Chen et al. (2000). In this paper we present results in comparison to those of Chen for an ellipsoid with the lengths of major and small axes $2a=2.3$ and $2b=0.4$ respectively, and different submergences and speeds.

The cosine-panel scheme is used to approximate geometrically the ellipsoid's ends more precisely. A perspective view of the semi-ellipsoid with a mesh of 288 panels is shown in Figure 2.10. The Froude number and wave making resistance coefficients are defined respectively as: $Fn = \sqrt{2gc}$, $C_w = -1000F_1/\pi\rho gc^3$, where focal distance is $c=1.132475$. Calculated results for different speeds and different submergences are shown in Figure 2.11 to Figure 2.14.

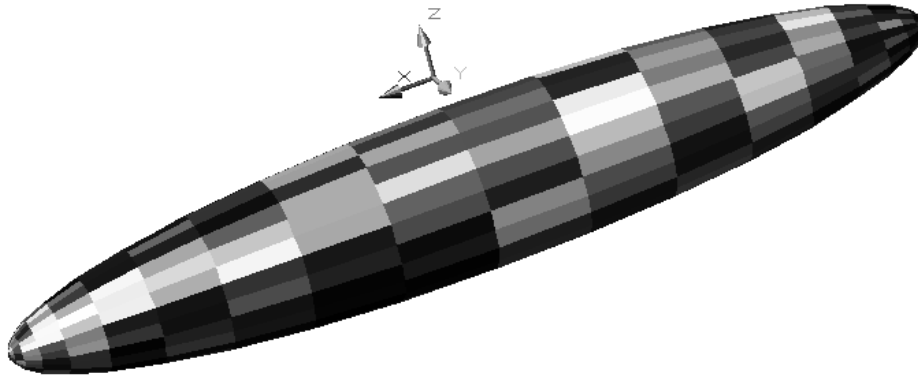


Figure 2.10 Panelization of the Ellipsoid

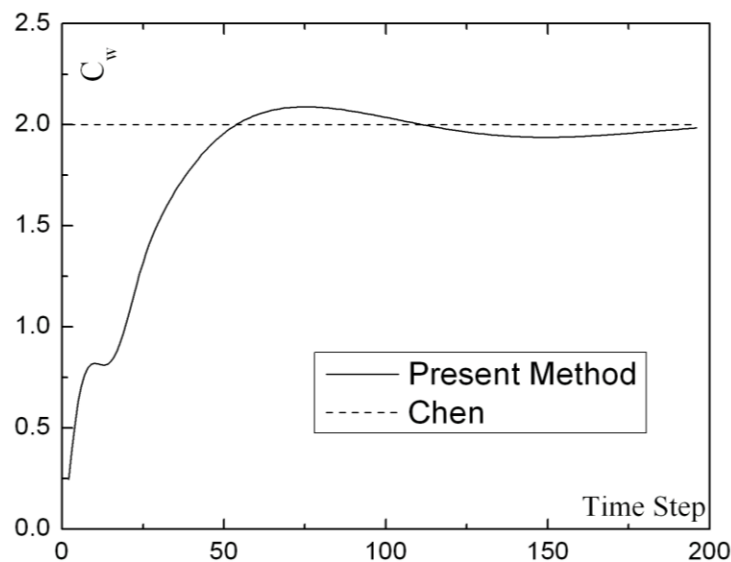


Figure 2.11 Wave making resistance $Fn=0.45$ $d=0.252c$

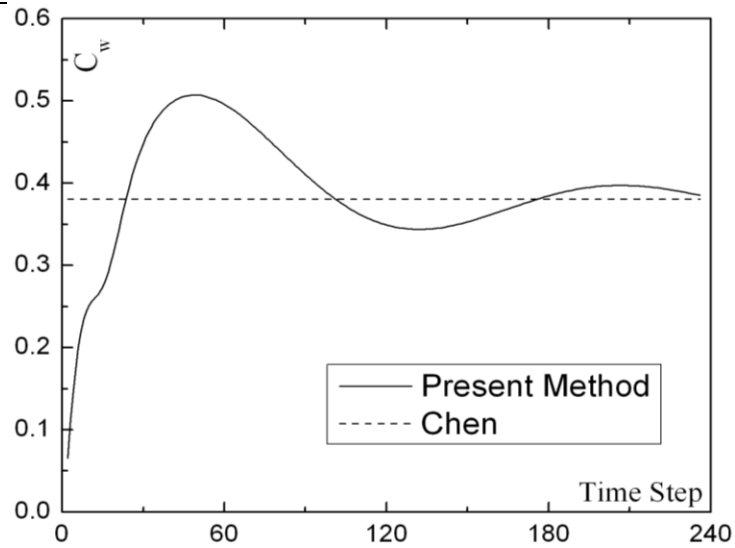


Figure 2.12 Wave making resistance $F_n=0.45$ $d=0.5c$

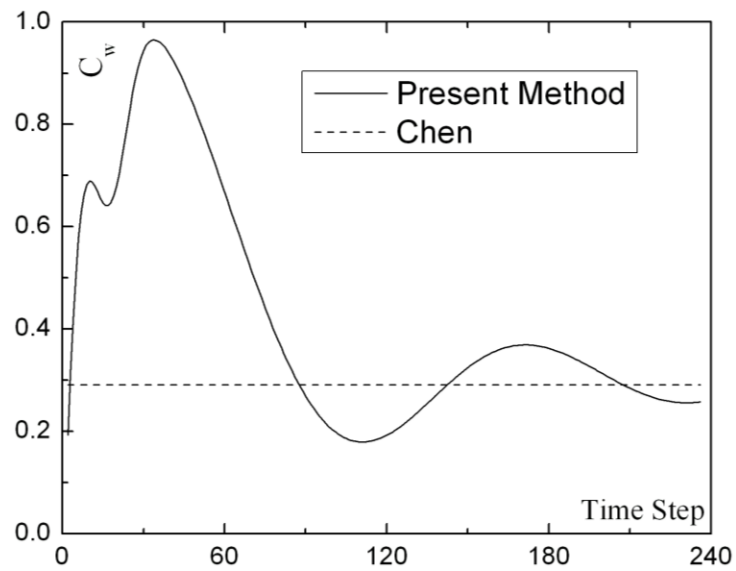


Figure 2.13 Wave making resistance $d=0.252c$ $F_n=0.35$

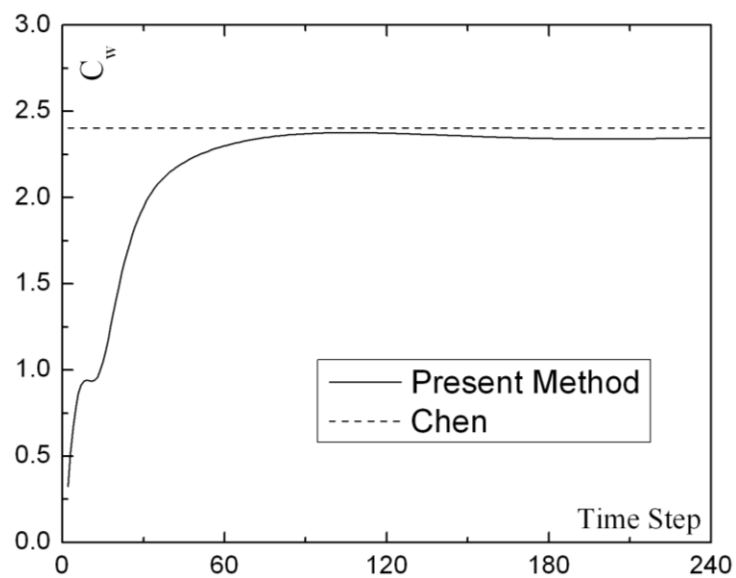


Figure 2.14 Wave making resistance $d=0.252c$, $F_n=0.6$

2.6.7 Resistance of a Wigley Hull

The Wigley hull is defined as: $y/B=[1-(2x/L)^2][1-(z/H)^2]$, where the beam-to-length ratio $2B/L=0.1$ and draft-to-length ratio $H/L=0.0625$. The Froude number is defined as $Fn=U/\sqrt{gL}$. Here a hull with $L=50.0m$ will be investigated.

An impulsive start-up mode is used in the present study with the expression of $V(t)=U_0, t>0$. Wehausen (1964) gave some general conclusions on the effect of the initial acceleration upon wave resistance problem based on his study with an asymptotic expansion scheme. From his study the decaying period takes a time of $T_0=8\pi U_0/g$, which is also confirmed by Lin&Yue (1990). Thus in the present study, we average the forces over the last T_0 time to get the resistance value.

The panel size is determined according to two principals. The first is from length of ship generated waves length $\lambda=2\pi U^2/g$. In order to describe a wave profile (assuming a sinusoidal form), there should be at least 5 control-points in one wave-length, which means 5 panels. The second principle is related to taking into account the memory effect. From a physical view, the distance the ship travels on the advancing direction in a time interval should be less than the panel-length on the same direction. Generally the first criterion is easy to meet. So we mainly use the second as our criterion. If Δl and Δt denote the panel-size and time interval respectively, the choice for $\Delta l / \Delta t U_0 \approx 2 \sim 3$ generally yields good results according to our experiences.

A convergence study is carried out regarding to time intervals and panel sizes which are shown in Table 2.1 and Table 2.2 for $Fn=0.3$ and 0.4 respectively. At last 320 panels on the whole hull (which is shown in Fig 2.15) and $\Delta t=2\pi/80$ are chosen for the calculation. This choice also meets the condition $\Delta t U_0 < \Delta l$, which is considered as the necessary condition for time-domain calculations. Figure 2.16 is a comparison among results from the present code for a fixed body, the average experimental results from Chen, et al. (1983) and SHIPFLOW (2005) results by using the standard “linear” “fixed” option. Clear deviations from experimental data and high oscillatory behaviors are observed, especially for $Fn>0.3$. This may be due to the neglect of the integration term on the water line, which appear in Equations (2-9) and (2-10).

The free-mode resistance results, which takes into account the sinkage and trim effect, is plotted in Figure 2.17 against the experimental data and SHIPFLOW results by using the standard “nonlinear” “free” option. During the calculation, it is assumed that sinkage and trim due to the steady motion are small thus a correction is performed by the following formula after a run:

$$\Delta T = F_3 / \rho g A_0^w, \quad \alpha = M_2 / \rho g A_2^w \quad (\text{assuming } GM_L \approx BM_L)$$

Here ΔT is the sinkage at the center at mid-ship and α is the trim angle, F_3 and M_2 are the heave force and pitch moment respectively. A_0^w is the water-plane area while A_2^w the corresponding

moment of inertia about y -axis. Theoretically, the correction should be performed iteratively after each calculation until an equilibrium condition, which means net vertical force F_3 and pitch moment M_2 equal to zero. In the computation, it is observed that the resistance results arrive a practically converged state after 3 times' iterative, as shown in Figure 2.18.

Table 2.1 Wave resistance coefficient of the Wigley hull at Fr=0.3

	$N^b=240$	$N^b=280$	$N^b=320$
$\Delta t = 2\pi/40$	0.23432312E-02	0.25856605E-02	0.22632792E-02
$\Delta t = 2\pi/60$	0.22777479E-02	0.21452351E-02	0.22144091E-02
$\Delta t = 2\pi/80$	0.22542330E-02	0.21653600E-02	0.21444915E-02

Table 2.2 Wave resistance coefficient of the Wigley hull at Fr=0.4

	$N^b=240$	$N^b=280$	$N^b=320$
$\Delta t = 2\pi/40$	0.51212753E-02	0.49944389E-02	0.50244194E-02
$\Delta t = 2\pi/60$	0.46899258E-02	0.50901936E-02	0.50283135E-02
$\Delta t = 2\pi/80$	0.47532834E-02	0.47532834E-02	0.49778008E-02

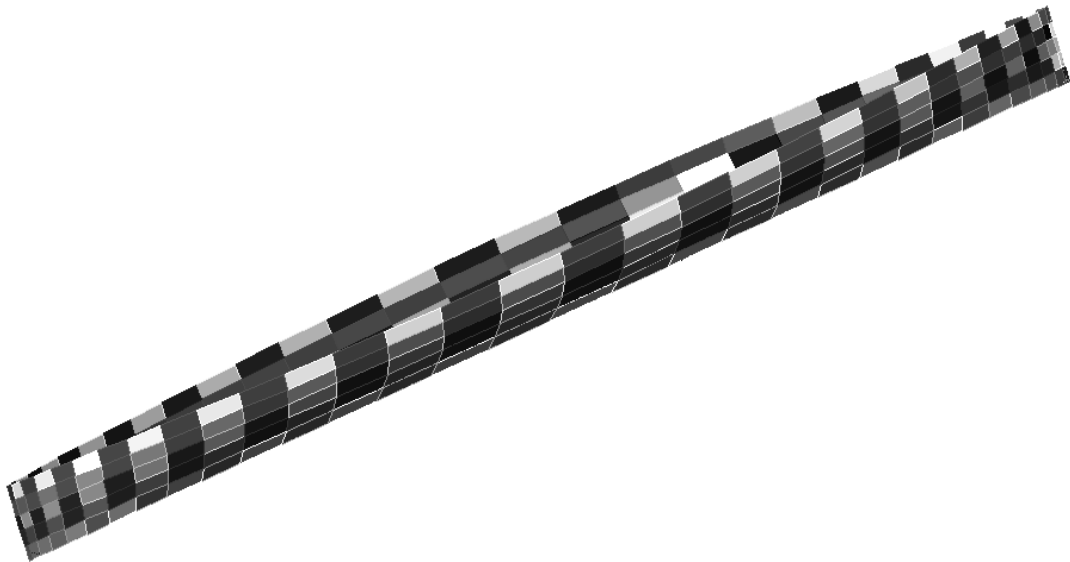


Figure 2.15 Perspective view of the Wigley hull with 320 improved progressional panels

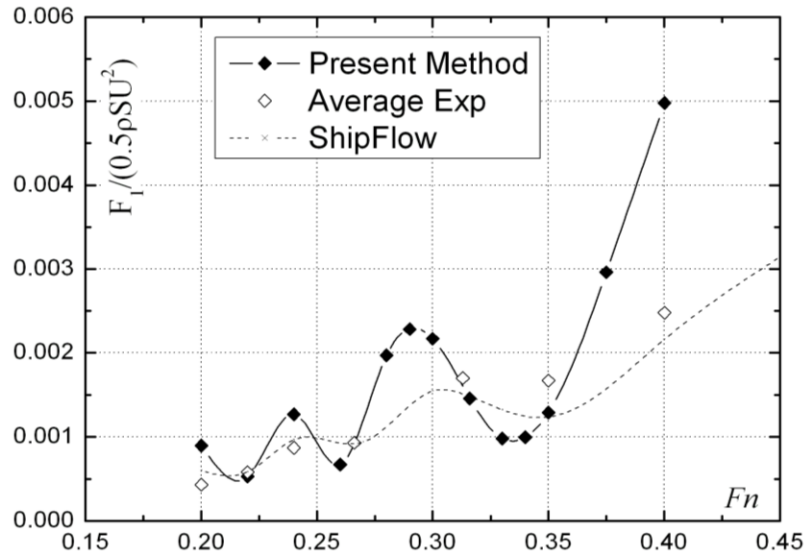


Figure 2.16 Wave making resistance C_W results, hull fixed

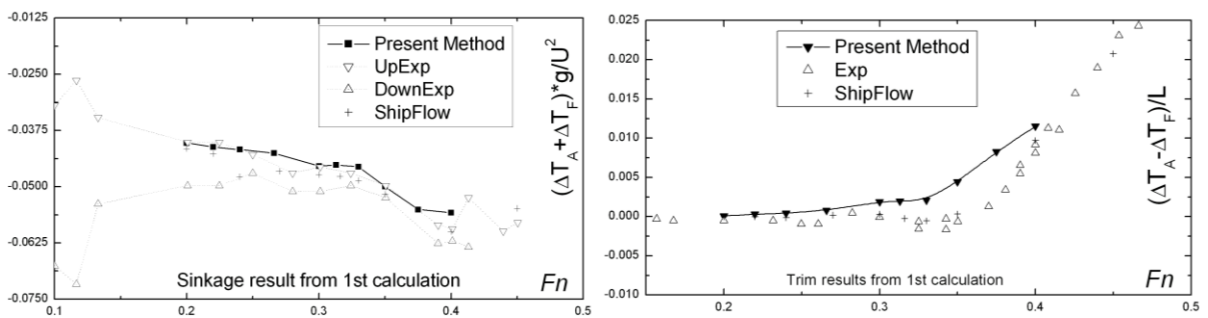
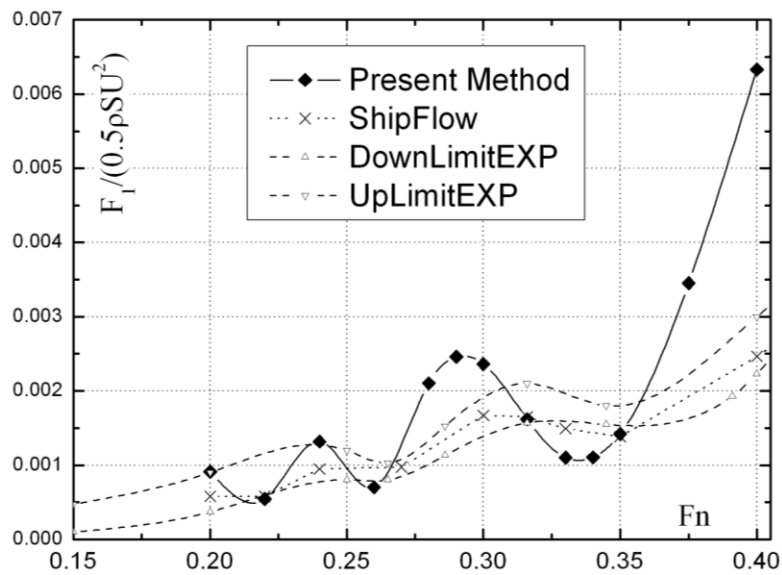


Figure 2.17 Wave making resistance C_W results, with sinkage/trim correction

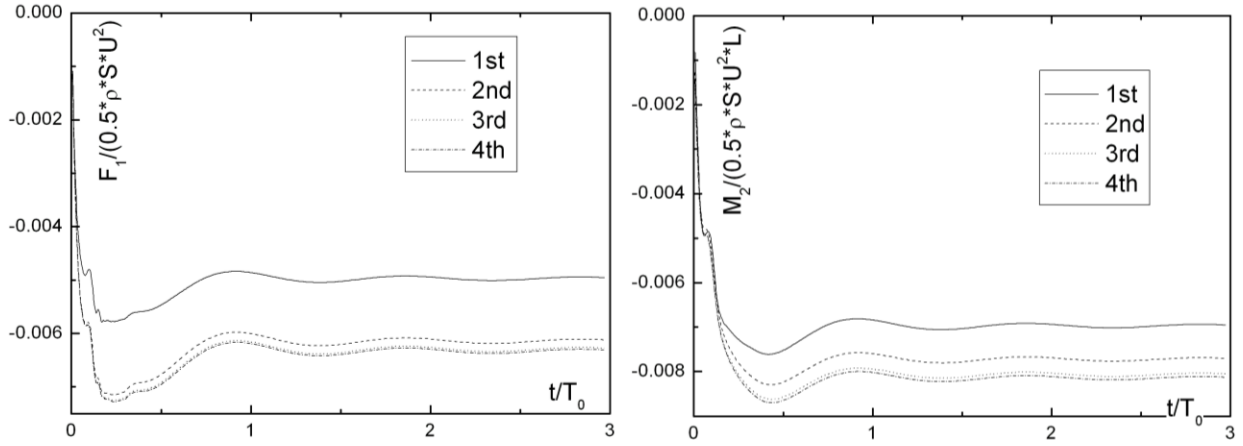


Figure 2.18. Wave making resistance calculation of a steadily moving Wigley hull, $F_n=0.4$

2.6.8 Added Resistance of a Submerged Spheroid

Iwashita et al. (1992) studied a shallowly submerged spheroid with a length to breadth ratio $L/B=5$ and draught to breadth ratio $d/B=0.75$, where the draught d is measured from the free surface to body center. In the following, we investigate the behavior of the wave systems created by this spheroid with $F_n=0.2$, $k=2.5\text{m}^{-1}$, $\omega_e \approx 7.14\text{sec}^{-1}$ in head waves. The corresponding values of Hanaoka parameter, steady wave number and critical angle are: $\Omega \approx 0.64$, $K_0 \approx 12.7\text{m}^{-1}$, $\alpha_0 \approx 67^\circ$. The unsteady wave numbers of two wave systems are plotted in Figure 2.19. From this graph it may be observed that the wave number k_1 approaches infinite when $\theta \rightarrow \pi/2$, while the wave number k_2 grows larger (although still remains bounded) as the wave direction approaches the critical angle. It has been found that the wave number k_1 is much larger than k_2 , indicating that k_1 waves are very small and can be neglected in the calculation of added resistance in head waves. Figure 2.20 shows the weighting functions in added resistance formulation. Since k_1 wave system is neglected, only the weighting functions for k_2 wave system have been shown. The weighting functions are defined by the following expressions:

$$WF2(1) = \frac{k_2(\theta)^2 \cos \theta}{\sqrt{1 - 4\Omega \cos \theta}} \quad (2-24)$$

$$WF2(2) = \frac{-k_2(\theta) k \cos \chi}{\sqrt{1 - 4\Omega \cos \theta}} \quad (2-25)$$

Figure 2.21 shows the non-dimensional Kochin function amplitude in the range $\alpha_0 < \theta < \pi$ and Figure 2.22 shows the integrand of the second term in expression (2-19). A more detailed analysis can be seen in Naito, et al. (1988).

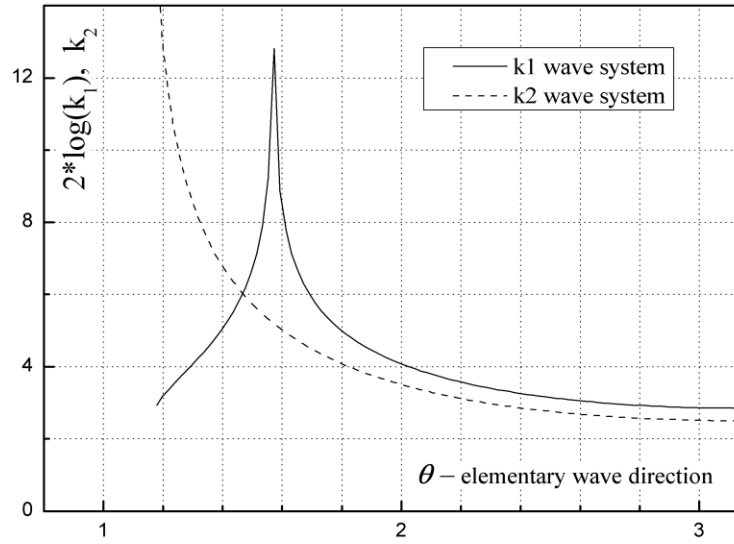


Figure 2.19 Unsteady wave numbers of two wave systems

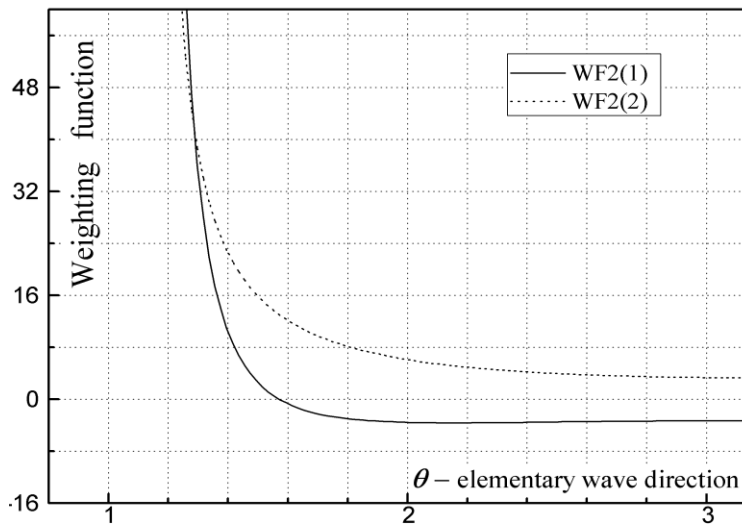


Figure 2.20 Weighting function of k_2 wave system

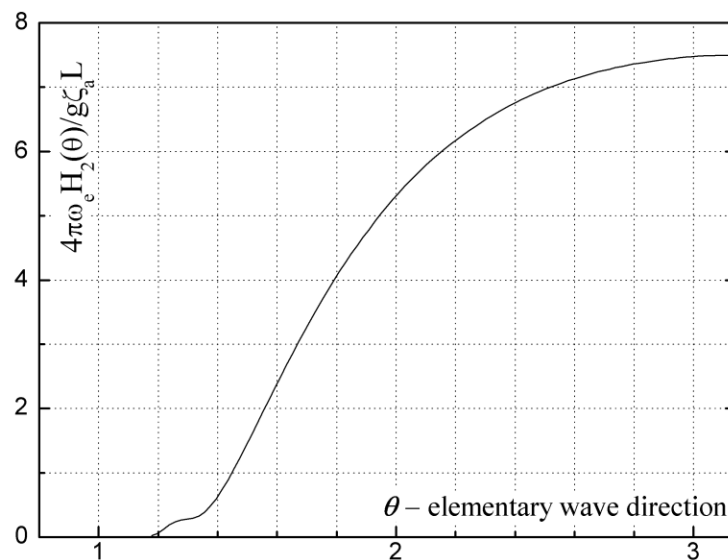


Figure 2.21 Kochin function of a submerged spheroid

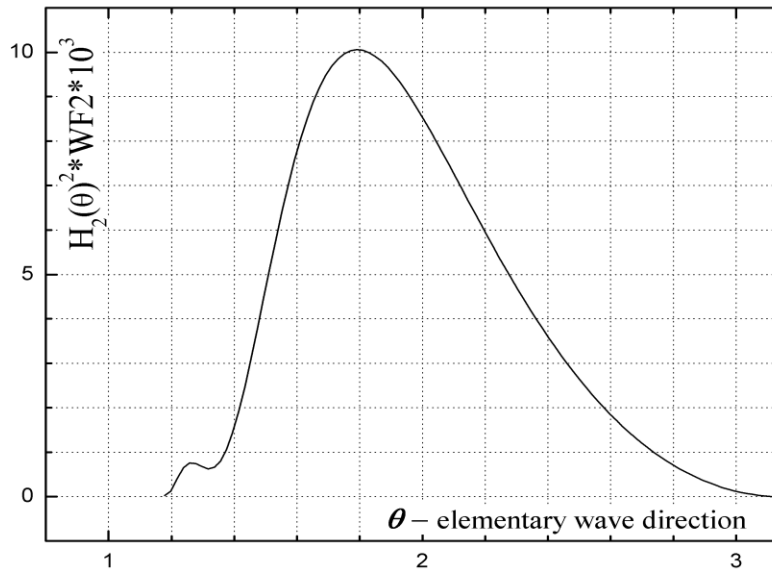


Figure 2.22 Integrand in Maruo's formula

This case has been addressed with two different approaches: The first one is using the present time-domain Green function method presented for the calculation of the first-order potential. The second approach is based on a frequency domain 3D panel method NEWDRIFT for the solution of potential calculation. The deduced first-order results either from the time-domain or the frequency domain approach are introduced in equations (2-22) and (2-23) for the calculation of the Kochin functions, from which the added resistance is calculated according to equation (2-19). In addition to the above, the drift forces and added resistance are calculated also by applying the near-field, direct pressure integration approach (Pinkster, 1979; Faltinsen, 1980), implemented in the NEWDRIFT code (denoted as NDnear in the graphs). Results from the first approach (denoted as LIUfar in the graphs) for the drift force at zero speed, and for the added resistance when the body is moving at forward speed in incident waves are presented in Figure 2.23 to Figure 2.25. Good agreement may be observed between the present results and the results of Iwashita and Ohkusu (1992), denoted as Iwashita in the graphs, both for the zero speed and nonzero speed calculations.

The same spheroid has been also tested at a deeper submergence of $d/B=1.25$. Comparisons have been herein made between the two time- and frequency domain potential solvers at zero and at a forward speed corresponding to $Fn=0.2$. Good agreement between both solvers has been obtained, when using the far-field method, noting that the 3D panel method corresponding to the NEWDRIFT code is essentially based on a zero speed Green function and forward speed effects are taken into account in an approximate way by exploiting slender body theory assumptions. These results are shown in Figure 2.26 and Figure 2.27.

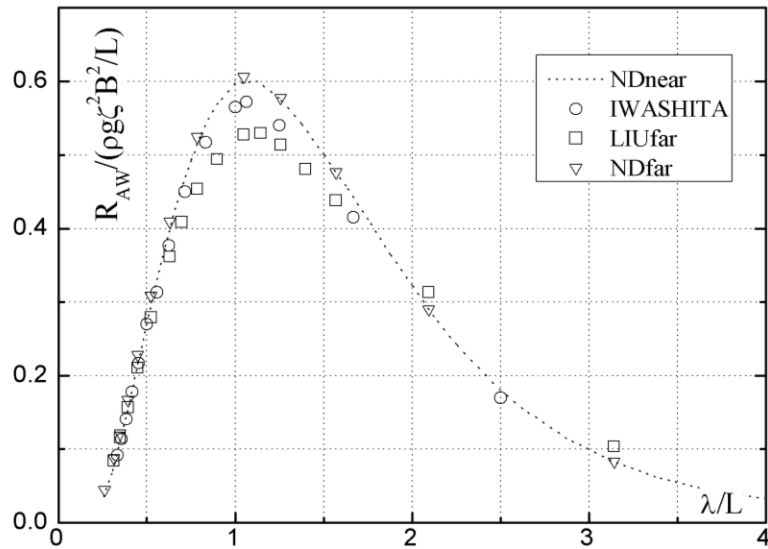


Figure 2.23 Horizontal drift force on a submerged spheroid at $Fn=0, d=0.75B$

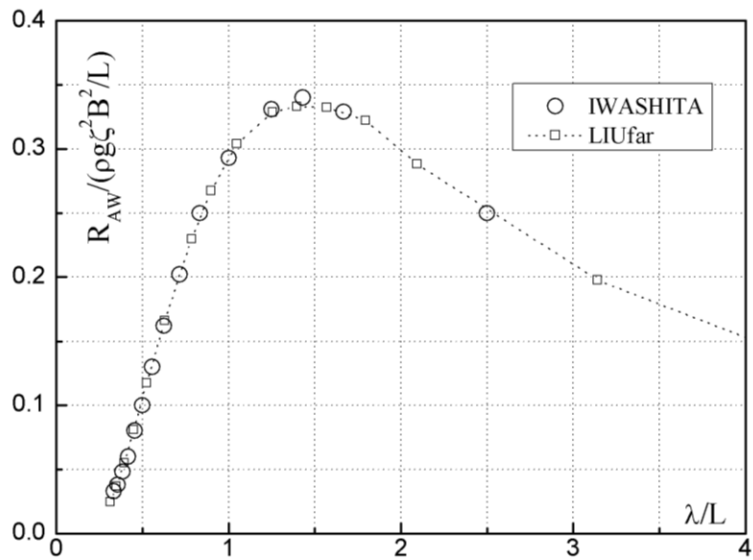


Figure 2.24 Added resistance on a submerged spheroid, $Fn=0.2, d=0.75B$

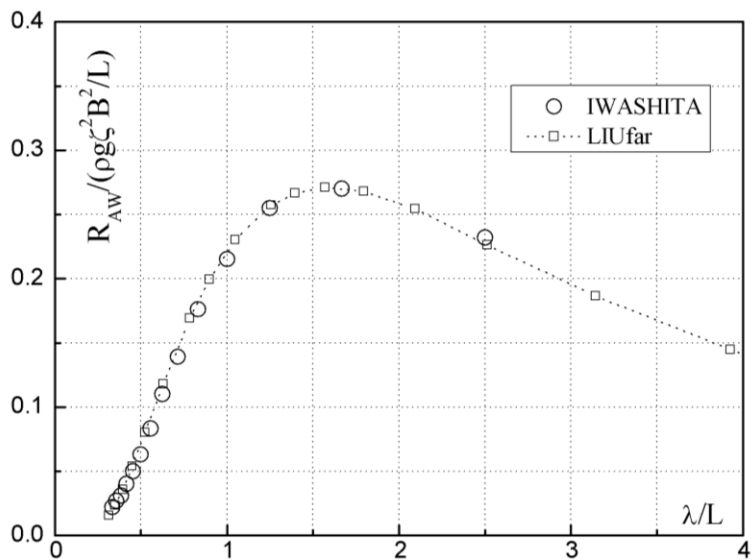


Figure 2.25 Added resistance on a submerged spheroid, $Fn=0.3, d=0.75B$

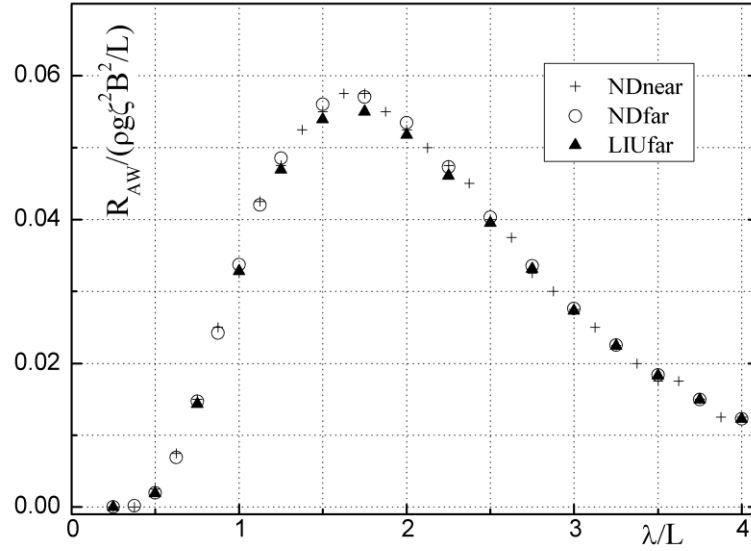


Figure 2.26 Horizontal drift force on a submerged spheroid at $Fn=0$, $d=1.25B$

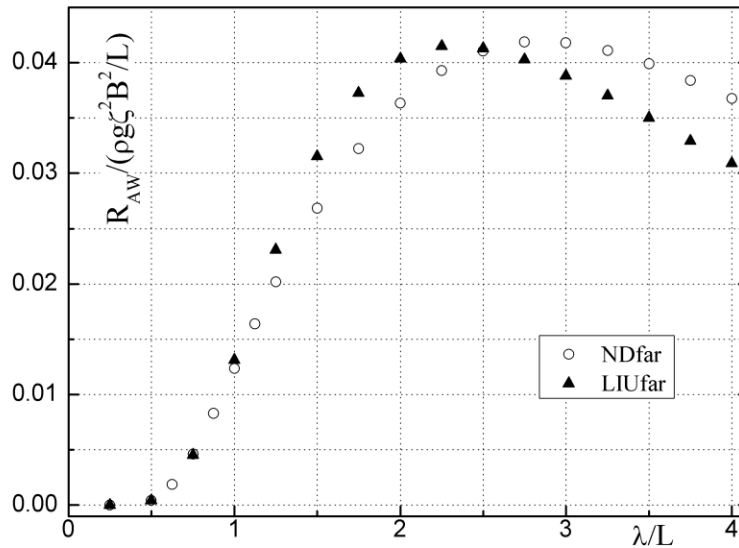


Figure 2.27 Added resistance on a submerged spheroid, $Fn=0.2$, $d=1.25B$

2.7 Summary and Conclusions

A potential flow theory based time domain transient Green function method is formulated and numerically implemented by using a constant panel method. It is validated by applications to wave making resistance problems, diffraction problems and radiation problems of simply bodies and ship-like bodies undergoing small amplitude motions or large amplitude motions. Furthermore, it is also validated by calculating the quasi-second order force – drift force or added resistance. Good agreement has been achieved when compare with the results from other well established numerical methods and experimental data, showing the method and numerical scheme are correct and promising.

But there are also some problems being brought into attention, as indicated in Table 2.3:

Table 2.3 List of studies cases

	$\omega=0$, steady case		$\omega \neq 0$	
V=0	--		Floating hemisphere, linear solution	✓
			Wigley hull, linear solution	✓
			Series 60, linear solution	×
			Submerged sphere, large-amplitude solution	✓
			Wigley hull, Large-amplitude solution	✓
V \neq 0	Submerged ellipsoid	✓	submerged sphere, in body-fixed system	✓
	Wigley hull	✓	submerged sphere, in earth-fixed system	×
	Series 60	×	Wigley hull	✓

As we see here, the problems lie in two categories. The first category refers to those applications to non-wall-sided bodies and the second are to those of floating (surface piercing) bodies with a forward speed. Further investigation shows that the first problem arises because of the transient Green function's problematic performance with this kind of bodies, which has also been noted by other researchers (Zhang *et al.*, 1998; Duan *et al.*, 1999; Kataoka *et al.*, 2004). The second problem appears to be due to the neglect of the numerically intricate waterline integral term that appears in Equations (2-10) or (2-11).

Overall, in this chapter we have shown the development and validation of a robust solver for submerged or surface piercing bodies with vertical-walls at the waterline and at zero forward speed.

Chapter 3 Time Domain Hybrid Method for Modeling Seakeeping Problems

In order to better treat the problem when dealing with non-wall-sided bodies by the Time Domain transient Green Function (TDGF) method, we decompose the fluid domain by introducing an imaginary vertical matching surface which is located away from hull; in this way the TDGF method can be better applied to practical shiplike bodies, thus introducing the idea of the “hybrid” method.

In the hybrid method, the fluid domain is decomposed into an inner domain and an outer domain. In the inner domain, the Rankine source method, which does not have problem with applications to non-wall-sided body or the waterline integral problem in the forward speed case, is used. In the outer domain, the time domain transient Green function method (TDGF) is used to find a relationship between the outer domain potential and its normal derivative, which is a boundary condition for inner domain equation. On the free surface, a double integration regarding to time t is performed to numerically simulate the linearized free-surface condition. The validated TDGF method is used to find the matching surface condition, which is a precious heritage from the first step in this thesis study. Furthermore, the matching is fixed in space, i.e., $v_n=0$ in equation (2-10) and equation (2-11), so that the difficult-to-treat waterline integral term trivially vanishes.

3.1 Problem Formulation

Consider a 3D body floating on the free water surface, advancing at constant forward speed and

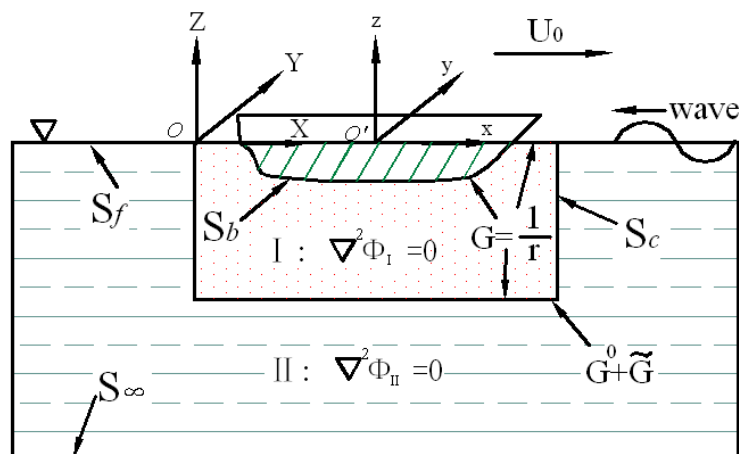


Figure 3.1 Coordinate system Definition and Decomposition of the fluid domain

undergoing 6-DOF motions in response to an incident wave. An earth-fixed Cartesian coordinate system O-XYZ is chosen with the X-Y plane coincident with the undisturbed free surface and Z-axis pointing upwards through the ship's mass centroid, as shown in Figure 3.1. The origin O is located on the undisturbed free-surface. Ship's forward speed U_0 is in X-axis direction.

Potential theory is used to determine the flow field. The fluid is assumed to be idealized and the water depth infinite. First, the flow field is decomposed into two parts, i.e. the inner domain denoted as I , bounded by the wetted body surface S_b , the control surface S_c and a part of the free surface S_f , namely between S_b and S_c ; and the outer domain denoted as II , enclosed by the control surface S_c , the remaining free surface and the boundary surface at infinity.

Let $\eta_k (k=1,2,\dots,6)$ represent the displacement of the oscillating motion on k -th direction, i.e. the translating displacement $\xi=(\eta_1,\eta_2,\eta_3)$ and the rotary displacement $\theta=(\eta_4,\eta_5,\eta_6)$, then the velocity are expressed as:

$$\vec{u} = \frac{d\vec{\xi}}{dt}, \quad \vec{\omega} = \frac{d\vec{\theta}}{dt} \quad (3-1)$$

Thus the linear displacement on the wetted surface is:

$$\mathbf{d} = \xi + \theta \times \mathbf{r} \quad (3-2)$$

where \mathbf{r} is the position vector of a point (x,y,z) .

In the framework of small amplitude hydrodynamic problems, the velocity potential Φ describing the whole flow field can be divided into the incidental wave potential, steady wave potential and unsteady disturbed wave potential:

$$\Phi_T = \Phi_0(x,y,z,t) + \Phi_s(x,y,z,t) + \Phi(x,y,z,t) \quad (3-3)$$

On the instantaneous wetted surface, the total velocity potential satisfies the following boundary condition:

$$\frac{\partial \Phi_T}{\partial n} = \sum_{j=1}^3 \dot{\eta}_j (\vec{e}_j \cdot \vec{n}) + \sum_{j=4}^6 \dot{\eta}_j (\vec{e}_{j-3} \times \vec{r}) \cdot \vec{n} \quad (3-4)$$

where \mathbf{n} is the normal vector of the ship body pointing inward of the body and $\vec{e}_j (j=1,2,3)$ are the unit vector of the x, y, z axes. The expression (3-4) can be rewritten as:

$$\frac{\partial \Phi}{\partial n} = -\frac{\partial \Phi_s}{\partial n} - \frac{\partial \Phi_0}{\partial n} + \sum_{j=1}^3 \dot{\eta}_j \vec{e}_j \cdot \vec{n} + \sum_{j=4}^6 \dot{\eta}_j \vec{e}_{j-3} \cdot (\vec{r} \times \vec{n}) \quad (\text{on } S(t)) \quad (3-5)$$

where $\mathbf{n}=(n_1,n_2,n_3)$ and $\mathbf{r} \times \mathbf{n}=(n_4,n_5,n_6)$.

The body boundary condition is satisfied on the exact instantaneous wetted surface. If we further expand it with respect to terms on the mean body surface S_0 and neglect the higher order terms, we get the linearized body boundary condition:

$$\frac{\partial \Phi}{\partial n} = -\frac{\partial \Phi_0}{\partial n} + \sum_{j=1}^6 [\dot{\eta}_j(t)n_j + U_0\eta_j(t)m_j] \quad (\text{on } S_0) \quad (3-6)$$

where $(m_1, m_2, m_3) = -(\mathbf{n} \cdot \nabla) \nabla \Phi_s / U_0$ and $(m_4, m_5, m_6) = -(\mathbf{n} \cdot \nabla) [\mathbf{r} \times \nabla \Phi_s] / U_0$. This boundary condition works fine when the motion amplitude is relatively small. For the large amplitude case of those geometries that vary much around the water-plane, it's important to take into account the nonlinearity effects associated with the geometry.

3.2 Integral Equations

As elaborated in Chapter 1, the boundary value problem will be solved by a time domain hybrid method which is a combination of Rankine source method and transient Green function method. As the Rankine source method has been interpreted thoroughly by other authors and the time domain transient Green function method has been explained in Chapter 2, in this chapter we will not elaborate the mathematic modeling of these two methods but use directly the resulting control equations.

In the inner domain I , the Rankine source method is used to solve the flow field. The integral equation takes the form of:

$$\iint_{S_c + S_b + S_f} [\Phi_I(q, t) \frac{\partial}{\partial n_q} \left(\frac{1}{r_{pq}} \right) - \frac{1}{r_{pq}} \frac{\partial}{\partial n_q} \Phi_I(q, t)] ds_q = -4\pi \Phi_I(p, t) \quad (p \in I) \quad (3-7)$$

where \mathbf{n} is the unit normal vector pointing outward of the inner domain. Let p approach the boundary then we will get:

$$\iint_{S_c + S_b + S_f} [\Phi_I(q, t) \frac{\partial}{\partial n_q} \left(\frac{1}{r_{pq}} \right) - \frac{1}{r_{pq}} \frac{\partial}{\partial n_q} \Phi_I(q, t)] ds_q = -2\pi \Phi_I(p, t) \quad (p \in S_I) \quad (3-8)$$

where $q(\xi, \eta, \zeta, \tau)$ is the source point, $p(x, y, z, t)$ is the field point; $\mathbf{r}_{pq} = (x-\xi)\mathbf{i} + (y-\eta)\mathbf{j} + (z-\zeta)\mathbf{k}$; the denotation S_b , S_c and S_f represent respectively the body surface, the control surface and the free surface.

In the outer domain II , the transient time-domain Green function is employed to solve the disturbed potential on S_c . The integral equation is expressed as:

$$\begin{aligned} & 2\pi \Phi_{II}(p, t) + \iint_{S_c} \left[\Phi_{II}(q, t) \frac{\partial}{\partial n_q} \left(\frac{1}{r_{pq}} - \frac{1}{r_{pq'}} \right) - \left(\frac{1}{r_{pq}} - \frac{1}{r_{pq'}} \right) \frac{\partial \Phi_{II}}{\partial n_q} \right] ds_q \\ & = \int_0^t d\tau \iint_{S_c} \left(\tilde{G} \frac{\partial \Phi_{II}}{\partial n_q} - \Phi_{II} \frac{\partial \tilde{G}}{\partial n_q} \right) ds_q + \frac{1}{g} \int_0^t d\tau \int_{wl(\tau)} V_N \left(\tilde{G} \frac{\partial \Phi_{II}}{\partial \tau} - \Phi_{II} \frac{\partial \tilde{G}}{\partial \tau} \right) dl_q \end{aligned} \quad (p \in S_c) \quad (3-9)$$

In the present formulation, the matching surface is fixed, thus V_N is essentially zero and the last integration term on the waterline vanishes.

On the control surface, the potential solutions from the inner domain model and the outer domain model should match each other. Considering the definitions of the normal vectors in different domains we have:

$$\Phi_I = \Phi_{II}, \frac{\partial \Phi_I}{\partial n} = -\frac{\partial \Phi_{II}}{\partial n} \quad (\text{on } S_c) \quad (3-10)$$

The velocity potential in the inner domain can also be expressed by a simple source distribution, namely as:

$$4\pi\Phi(p, t) = \iint_{S_c+S_b+S_f} \sigma(q, t) \frac{1}{r_{pq}} ds_q \quad (3-11)$$

Having obtained Φ through the aforementioned hybrid solver, the source density σ can be obtained by solving Equation (3-11). Thus the spatial derivatives can be evaluated as:

$$\frac{\partial \Phi(p, t)}{\partial x_k} = \frac{1}{4\pi} \iint_{S_c+S_b+S_f} \sigma(q, t) \frac{\partial}{\partial x_k} \frac{1}{r_{pq}} ds_q \quad (3-12)$$

3.3 Free-Surface Condition

The linearized free-surface condition can be expressed in earth fixed coordinate system as:

$$\frac{\partial^2 \Phi}{\partial t^2} + g \frac{\partial \Phi}{\partial z} = 0 \quad (3-13)$$

Integrating the above equation with respect to time t twice and taking into account the initial conditions, we will get the following expression:

$$\Phi = -g \int_0^t (t-\tau) \frac{\partial \Phi(p, \tau)}{\partial n} d\tau \quad (3-14)$$

This formulation, initially developed by Wang (2003), is simple and also proved to be a robust free-surface numerical simulator (Liu *et al.*, 2009).

It should be noted in relation to the development and implementation of the above expression, that the integration with respect to time is from moment 0 to moment t and the initial condition is set $\Phi|_{t=0} = \frac{\partial \Phi}{\partial t}|_{t=0} = 0$. This is valid only for the area that is free from disturbance/occupation

by the advancing ship hull, or the whole free surface area for zero speed problems. In case of forward speed for the area that is in the wake of the hull or the area which is occupied by the

hull at the very beginning but gradually becomes free, special treatment of the free surface boundary condition and corresponding panels is needed (Figure 3.2).

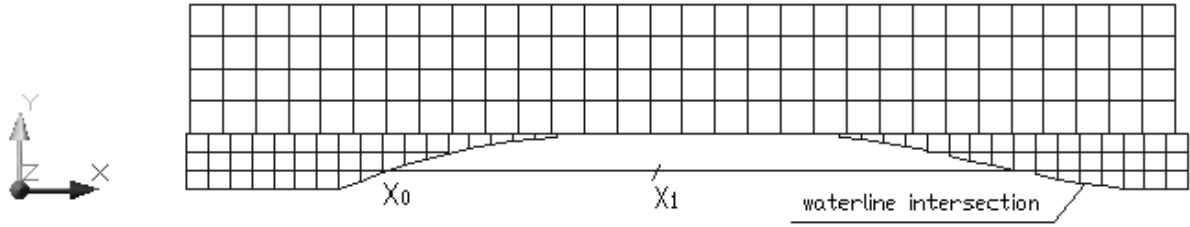


Figure 3.2 Ship crossing free surface panels

As shown in Figure 3.2, if the intersection point between the ship's waterline WL and some $y=const$ line is $x=x_0$ at moment t_0 , then for a point at $x=x_1$ which is occupied by the hull at the moment, it will take some time, $(x_1 - x_0)/U_0$, for this point to become active (wetted). The free surface condition on this point is simulated as following:

1. Do the 1st integration of the expression regarding to time $\tau \in (t_0, t)$:

$$\left. \frac{\partial \Phi(p, t)}{\partial t} - \frac{\partial \Phi(p, \tau)}{\partial \tau} \right|_{\tau=t_0} = -g \int_{t_0}^t \frac{\partial \Phi(p, \tau)}{\partial n} d\tau$$

2. Integrating the above expression with respect to time for a second time, we obtain the following expression:

$$\Phi(p, t) = \Phi(p, t_0) + \left. \frac{\partial \Phi(p, \tau)}{\partial \tau} \right|_{\tau=t_0} (t - t_0) - g \int_{t_0}^t (t - \tau) \frac{\partial \Phi(p, \tau)}{\partial n} d\tau \quad (3-15)$$

The initial conditions on this point, i.e. $\Phi(p, t_0)$ and $\left. \frac{\partial \Phi(p, \tau)}{\partial \tau} \right|_{\tau=t_0}$, can be approximated by the

corresponding values on the adjacent hull panel or by the value on its adjacent panel in the downstream. Similar procedure is followed for reference points and panels being at some time instant upfront the hull, then for some period of time being occupied by the hull, until the ship hull passes by.

This formulation is different from other similar schemes. In Zhang's formulation (Zhang et al., 1998), a fourth order Adams-Bashforth-Moulton formula is used for the time integration and the second order upwind finite difference for the gradient calculations to solve the resulting hyperbolic equations for the disturbance velocity potential and the disturbance free surface elevation. In Kataoka and Iwashita's scheme (2005), the near field free surface panels' nodes are shifted only in y-direction and the corresponding influence matrices' elements are then updated.

The free surface condition is simulated by using a Milne finite-difference method which has second-order accuracy. Finally, in Yasukawa's method (Yasukawa, 2003), the wave height and velocity potential on the free-surface are integrated by Newmark's β method.

3.4 Body Boundary Condition and m_j Term Calculation

Following the formulation in Section 3.1, m_j term which appears in the boundary condition (3-6) is expressed as following:

$$\begin{aligned} \begin{bmatrix} m_1 \\ m_2 \\ m_3 \end{bmatrix} &= -\frac{1}{U_0} \begin{bmatrix} n_1 \Phi_{sxx} + n_2 \Phi_{sxy} + n_3 \Phi_{sxz} \\ n_1 \Phi_{syx} + n_2 \Phi_{syy} + n_3 \Phi_{syx} \\ n_1 \Phi_{sxx} + n_2 \Phi_{sxy} + n_3 \Phi_{sxz} \end{bmatrix} \\ \begin{bmatrix} m_4 \\ m_5 \\ m_6 \end{bmatrix} &= \begin{bmatrix} ym_3 - zm_2 - \frac{n_2}{U_0} \Phi_{sz} + \frac{n_3}{U_0} \Phi_{sy} \\ zm_1 - xm_3 - \frac{n_3}{U_0} (\Phi_{sx} - U_0) + \frac{n_1}{U_0} \Phi_{sz} \\ xm_2 - ym_1 + \frac{n_2}{U_0} (\Phi_{sx} - U_0) - \frac{n_1}{U_0} \Phi_{sy} \end{bmatrix} \end{aligned} \quad (3-16)$$

It is clear that during the procedure of linearizing the body boundary condition of radiation problems to the mean wetted surface, the contribution of the steady potential results in this m_j term which requires the computation of the second gradients of the basic steady potential. It has been shown by other researchers (Zhao et al., 1989; Duan et al., 2002) that it is difficult to obtain good results by the direct computations. Two different methods for m_j term calculation are implemented in the present study, as elaborated in the following.

3.4.1 Neumann-Kelvin Simplification

According to the Salvesen-Tuck-Faltinsen (S.T.F.) method's simplification, the basic flow corresponds to an undisturbed stream $-U_0x$, thus

$$(m_1, m_2, m_3) = -(\mathbf{n} \cdot \nabla) \nabla (-U_0x) / U_0 = (0, 0, 0) \quad (3-16)$$

$$(m_4, m_5, m_6) = -(\mathbf{n} \cdot \nabla) [\mathbf{r} \times \nabla (-U_0x)] / U_0 = (0, n_3, -n_2) \quad (3-17)$$

This is consistent with Neumann-Kelvin linearization and easy to implement.

3.4.2 Direct Calculation

There are research groups who compute the m_j term on the basis of a double-body linearization (Chen et al., 2000). However, as extra integral equations will have to be solved, it is not adapted

in the present study. Instead, the procedure which is proposed by Wu (1991) and followed by Chen et al. (1996) and Kim (2005) is implemented in the present hybrid method's framework. The velocity potential in the inner domain can be expressed in the source distribution form as:

$$4\pi\Phi_s(p,t) = \iint_{S_c+S_b+S_f} \sigma(q,t) \frac{1}{r_{pq}} ds_q \quad (3-18)$$

Since we got Φ_s through the aforementioned hybrid solver, the source density σ can be evaluated by the above expression. Afterwards, the spatial derivatives can be evaluated as:

$$\frac{\partial\Phi_s(p,t)}{\partial x_k} = \frac{1}{4\pi} \iint_{S_c+S_b+S_f} \sigma(q,t) \frac{\partial}{\partial x_k} \frac{1}{r_{pq}} ds_q \quad (3-19)$$

The partial derivative of the velocity potential in the inner domain can also be expressed in the source distribution form as:

$$4\pi \frac{\partial\Phi_s(p,t)}{\partial x_k} = \iint_{S_c+S_b+S_f} \sigma_k(q,t) \frac{1}{r_{pq}} ds_q \quad (3-20)$$

Since $\frac{\partial\Phi_s(p,t)}{\partial x_k}$ has been obtained through the previous calculation, the source density σ_k can be evaluated by the above expression. Afterwards, the second order spatial derivatives can be evaluated as:

$$4\pi \frac{\partial^2\Phi_s(p,t)}{\partial x_k \partial x_j} = \iint_{S_c+S_b+S_f} \sigma_k(q,t) \frac{\partial}{\partial x_j} \left(\frac{1}{r_{pq}} \right) ds_q \quad (3-21)$$

3.5 Large Amplitude Ship Motions in Regular Waves with Six Degrees of Freedom

The general *ship motion formulation* has been addressed by many researchers in the past. In the present work, Jan Otto de Kat's methodology (1990) is followed to model the ship motion.

In order to study the motion of a ship advancing in wave, three coordinate systems are defined. The *OXYZ* system is earth-fixed, with *Z-axis* pointing positive upwards and *X-Y* plane coincident with the calm water free-surface. The *X-axis* is set in the centre plane pointing to FP. The origin is in the center plane, in the calm waterplane and at some convenient for-and-aft location. The *OXYZ* axis system is also used to define the incident wave system. The second coordinate system *O'xyz* coincides with *OXYZ* at the beginning but travels with the body at speed U_0 . It doesn't move with the motions of the ship. These two systems are shown in Figure 3.1.

The third coordinate system $Gx'y'z'$ is body-fixed, thus moves with all the motions of the ship. The initial position of $x'-y'$ plane is parallel to ship's calm water plane, with z' -axis normal to it and x' -axis pointing to the bow. The origin of this system is fixed to the gravity centre G. In present work it is assumed that the ship has and only has port/starboard symmetry about the $x'-z'$ plane.

The motions of the ship are determined by the orientation of system $Gx'y'z'$ relative to $Oxyz$ system. A total of six components are needed to uniquely define the motion, typically three translations, i.e. surge, sway and heave, and three rotations, i.e. roll, pitch and yaw. The six degrees of freedom motion of a rigid body in space is determined by the following two equations:

$$\begin{aligned}\frac{d\vec{P}}{dt} &= \Delta \cdot \frac{d\vec{v}}{dt} = \vec{F} = \vec{F}_{HS} + \vec{F}_I + \vec{F}_R + \vec{F}_D \\ \frac{d\vec{L}}{dt} &= I \cdot \frac{d\vec{\omega}}{dt} + \vec{\omega} \times (I \cdot \vec{\omega}) = \vec{M} = \vec{M}_{HS} + \vec{M}_I + \vec{M}_R + \vec{M}_D\end{aligned}\quad (3-22)$$

where $\mathbf{P}=m\mathbf{v}$, $\mathbf{L}=I\cdot\boldsymbol{\omega}$. \mathbf{F} and \mathbf{M} are the total force on the body and the total moment about a suitable point, Δ is the mass and \mathbf{v} is the absolute velocity vector of the gravity center in the $Oxyz$ system, and I and $\boldsymbol{\omega}$ are the inertia tensor and angular velocity about the rotating point, which is assumed to be ship's gravity center G. The moments and products of inertia in I are constants in the moving and rotating system $Gx'y'z'$. In this thesis, the conservation of linear momentum equations will be solved in the earth-fixed reference system, while the conservation of angular momentum will be expressed in the local body-fixed system. The location of a rigid body in space is fully determined by the position of G in the fixed system $O'xyz$ and the angular orientation of the $Gx'y'z'$ system with respect to the earth fixed system. In order to solve these quantities, first the position of the mass centre in the earth fixed system is defined by the vector $\mathbf{x}_G(t)=[x_G, y_G, z_G]^T$, and the velocity of the mass center is expressed by a time derivative: $\mathbf{v}(t)=d\mathbf{x}_G(t)/dt$. The rotation of the ship coordinate system is uniquely defined by the following order of rotations, characterized by the Euler angles: first rotate by the roll angle η_4 , followed by the pitch angle η_5 , and finally by the yaw angle η_6 . The Euler angles are represented by the vector $\boldsymbol{\theta}=[\eta_4, \eta_5, \eta_6]^T$.

In order to express a vector in the system $Gx'y'z'$ with respect to $OXYZ$ system, the transformation matrices associated with Euler angles are needed. The angular velocities about the body coordinate system axes given by $\boldsymbol{\omega}$ can be related to the time derivatives of the Euler angles, $\dot{\boldsymbol{\chi}}$, as follow: $B\dot{\boldsymbol{\chi}} = \vec{\omega}$ where B is also a function of the Euler angles. It is noted that with large motion simulations the Euler angles must be retained, so that the various transformation matrices are time dependent.

The translational position of the gravity centre in earth-fixed system $\mathbf{x}_G(t)$ can be obtained by integrating the velocity vector $\mathbf{v}(t)$. The velocity vector is related to the linear acceleration vector by the following expression:

$$\frac{d}{dt}\vec{v} = \vec{a} = \vec{F}/\Delta \quad (3-23)$$

$[\dot{v}_1, \dot{v}_2, \dot{v}_3]^T$ can be obtained by solving the motion equations; and then $[v_1, v_2, v_3]^T$ can be obtained by an integration regarding to time. $\mathbf{x}(t)$ can be calculated afterwards by integrating $[v_1, v_2, v_3]^T$ regarding to time. The rotational velocities of the body with respect to earth-fixed system, $\dot{\theta}$, can be related to those corresponding velocities in the body system by the following expressions with transformation matrices:

$$\begin{bmatrix} \dot{\eta}_4 \\ \dot{\eta}_5 \\ \dot{\eta}_6 \end{bmatrix} = [B]^{-1} \begin{bmatrix} \omega_1 \\ \omega_2 \\ \omega_3 \end{bmatrix} = \begin{bmatrix} 1 & s_1 t_2 & c_1 t_2 \\ 0 & c_1 & -s_1 \\ 0 & s_1 / c_2 & c_1 / c_2 \end{bmatrix} \begin{bmatrix} \omega_1 \\ \omega_2 \\ \omega_3 \end{bmatrix} \quad (3-24)$$

$[\dot{\omega}_1, \dot{\omega}_2, \dot{\omega}_3]^T$ can be obtained by solving the motion equations; and then $[\omega_1, \omega_2, \omega_3]^T$ can be obtained by an integration regarding to time. θ can be obtained afterwards by using the above expressions. Transformation for a vector between the two coordinate systems is straightforward:

$$\mathbf{x} = \mathbf{x}_G(t) + [T]\mathbf{x}' \quad (3-25)$$

where $[T]$ is the transformation matrix given by the product of the individual transformation matrices in the sequence of the Euler angles (Spanos, 2002).

On the right-hand side of the motion Equations (3-22), there are force components due to diffraction, radiation, incident wave, and restoring. Basically these forces/moments are calculated by integrating the pressure expressed by Bernoulli's equation on the body surface. Since an exact, fully nonlinear model is quite time-consuming and complicated for numerical computation, we restrict ourselves in this thesis to the consideration of some of the more important and tractable nonlinear effects. In particular, in this thesis for simulating small amplitude ship motions, all the force terms in the motion equation will be calculated up to mean wetted surface. For simulating large amplitude ship motions, the incident wave forces (Froude-Krylov) and restoring forces will be calculated up to undisturbed wavy surface and transferred into the motion equations.

3.5.1 Radiation Forces

The determination of the radiation forces is based on the developed time domain hybrid method which is valid for arbitrary motions. In the simulations, the radiation forces are calculated

system by assuming the vessel to be upright at each time. Another possible approach is to assume that the radiation force is exerting on the hull at the instantaneous position which is consistent with the motion formulation but inconsistent with radiation problem formulation. The forces are computed up to the mean wetted surface by using the velocity and acceleration information relative to the earth-fixed coordinate system. Since in this work, the conservation of linear momentum equations will be solved in the earth-fixed reference system, these forces will be converted into the equations of translational motions without any transformation. After the linear and angular accelerations in OXYZ system have been determined, assume the vessel to be positioned in the upright position when calculating the radiation forces and moments in OXYZ. The moments in local $Gx'y'z'$ system are assumed to be equal to the moments in OXYZ system.

3.5.2 Diffraction Forces

The diffraction force can be estimated by considering the vessel fixed in its mean position and the waves impinging upon it. The hybrid method is applied to determine also the diffraction forces. The ship is considered in its upright position and the body boundary condition is determined by using the incidental wave defined in the earth-fixed coordinate system. Taking a similar approach to which is used for the radiation forces, the force components given in the OXYZ system are considered as dependent on the instantaneous angles of rotation, while it is assumed that the vessel's gravity center is located at O' , thereby neglecting the linear displacements due to surge, heave and sway. The time dependence is affected through the transformation matrix [T].

3.5.3 Incidental Wave Forces and Hydrostatic Forces

It has been observed in experiments and numerical studies that the nonlinear forces due to incident waves and buoyancy have large magnitudes relative to other components such as radiation forces. Thus it is important to include these effects in the motion simulation as accurately as possible.

The Froude-Krylov forces are the forces associated with the pressure in the *undisturbed* incoming wave; in the classical linear seakeeping theory the pressure is integrated over *the mean wetted surface of the vessel*. In this work the wave pressure is calculated up to the instantaneous, undisturbed wave surface, so that the Froude-Krylov force is obtained by integrating the pressures over the instantaneous wetted surface. It should be noted that in the evaluations the wavy surface is based on the *undisturbed* incident wave. Thus, free surface changes caused by waves generated by the hull due to forward speed or motions or body-wave interactions

(diffraction), are neglected. Thus, what are called accurate Froude-Krylov forces in this work, are *not* the exact hydrodynamic wave forces since these would depend on the actual free surface. By neglecting the quadratic term in Bernoulli's equation, the wave pressure is given by:

$$p = -\rho \frac{\partial \Phi_I}{\partial t} - \rho g z = p_s + p_d \quad (3-26)$$

where p_s and p_d are the "static" and "dynamic" pressure respectively. The force associated with p_s is the static part of the Froude-Krylov force or the vertical hydrostatic force. The vector comprising the static force and moment components is given by

$$f_{FK,s}(t) = -\rho g \iint_{s(t)} z \bar{\mathbf{n}} ds \quad -\infty < z < \eta(x, y, t) \quad (3-27)$$

\mathbf{n} is the generalized six-component outward normal as *defined in the local system*. $\mathbf{n}_{4,5,6} = \mathbf{r}' \times \mathbf{n}_{1,2,3}$. At each time instant, the wetted hull surface is determined by using ship's position data at previous time step and the wave position at the present step. Then the total hydrostatic force and moment components are calculated by integration. Theoretically it is good to use iterative scheme so that a more exact motion data of current time step is ensured, however, if the time step is small this delay will not play a dominant role in the computation.

For the gravitational effects, the mass of the vessel is given by $\Delta = \rho V$, where V is the displacement of the vessel in calm water. The resulting static balance in the static vertical force is given by subtraction of the weight from the vertical component of the static Froude-Krylov force. It should be borne in mind that what is called the static Froude-Krylov force for heave is actually the change in vertical static force with respect to the still water equilibrium condition. For momentum calculation, it is simply the direct integration effect.

The dynamic Froude-Krylov forces associated with the pressure p_d in the wave field is

$$f_{FK,d}(t) = -\rho g \iint_{s(t)} \frac{\partial \Phi_I}{\partial t} \bar{\mathbf{n}} ds \quad (3-28)$$

In the present thesis the integration is carried out over the instantaneous wetted surface at each time instant, so what are called herein the dynamic Froude-Krylov forces are in fact *the exact*

forces associated with $\frac{\partial \Phi_I}{\partial t}$ term of the incident wave.

3.6 Numerical Scheme

The Boundary Element Method (BEM) is adopted to numerically solve the formulated integral equations. The potential value over each panel is assumed constant.

The discretized form of the linearized free-surface condition is:

$$\Phi_j^M = -g(\Delta t)^2 \sum_{m=1}^{M-1} (M-m) \frac{\partial \Phi_j^m}{\partial n_j} \quad (j=1,2,3,\dots,N_f) \quad (3-29)$$

Here j is the free-surface panel index while $M\Delta t$ and $m\Delta t$ denote for the present moment t and the historical moment τ respectively, $\frac{\partial \Phi_j^m}{\partial n_j}$ is $\frac{\partial \Phi}{\partial n}$ on j -th panel at time τ .

The discretized form of the integral equation in the outer domain is:

$$\sum_{j=1}^{N^c} A_{ij} \Phi_j^M = Memo_i + \sum_{j=1}^{N^c} B_{ij} \Phi_{nj}^M \quad (i=1,2,\dots,N^c) \quad (3-30)$$

$$\text{where } A_{ij} = \begin{cases} 2\pi + \iint_{\Delta s_j^M} \frac{\partial}{\partial n_j} \left(-\frac{1}{r_{ij}} \right) ds_j & (i=j) \\ \iint_{\Delta s_j^M} \frac{\partial}{\partial n_j} \left(\frac{1}{r_{ij}} - \frac{1}{r_{ij}'} \right) ds_j & (i \neq j) \end{cases}, \quad B_{ij} = \iint_{\Delta s_j^M} \left(\frac{1}{r_{ij}} - \frac{1}{r_{ij}'} \right) ds_j,$$

$Memo_i = \Delta t \sum_{m=1}^{M-1} \varepsilon_m \sum_{j=1}^{N^c} \left(\Phi_{nj}^m \iint_{\Delta s_j^m} \tilde{G}_j^m ds_j - \Phi_j^m \iint_{\Delta s_j^m} \tilde{G}_{nj}^m ds_j \right)$ where the integration on water-line is neglected due to numerical reasons. Thus we have

$$\Phi_j^M = [A_{ij}]^{-1} \left[Memo_i + \sum_{j=1}^{N^c} B_{ij} \Phi_{nj}^M \right] \quad (i=1,2,\dots,N^c) \quad (3-31)$$

The discretized form of the integral equation in the inner domain is:

$$\sum_{j=1}^{N^{c+f+b}} (C_{ij} \Phi_j^M - D_{ij} \Phi_{nj}^M) = 0 \quad (i=1,2,3,\dots,N^{c+f+b}) \quad (3-32)$$

$$\text{where } C_{ij} = \begin{cases} 2\pi & i=j \\ \int_{\Delta s_j} \frac{\partial}{\partial n_j} \left(\frac{1}{r_{ij}} \right) ds_j & i \neq j \end{cases} \text{ and } D_{ij} = \int_{\Delta s_j} \left(\frac{1}{r_{ij}} \right) ds_j. \quad N^c, N^f \text{ and } N^b \text{ denote for}$$

the panel numbers on control surface, free-surface and mean wetted surface respectively. The boundary condition is known on body boundary; from the free-surface condition we know that Φ_f is a function of $\frac{\partial \Phi_f}{\partial n}$; from Equation (3-31) we get the relationship between Φ_c and $\frac{\partial \Phi_c}{\partial n}$;

then for the inner domain integral equation, we will have $N^c + N^f + N^b$ unknowns and

$N^c + N^f + N^b$ equations. Substitute Equation (3-31) into Equation (3-32), taking into account matching condition (3-10), we get:

$$\begin{aligned} & \sum_{j,k=1}^{N^c} \left\{ -C_{ij} [A_{jk}]^{-1} [B_{kj}] - D_{ij} \right\} \Phi_{nj}^M - \sum_{j=N^c+1}^{N^{c+f}} D_{ij} \Phi_{nj}^M + \sum_{j=N^{c+f}+1}^{N^{c+f+b}} C_{ij} \Phi_j^M \\ & = - \sum_{j=1}^{N^c} C_{ij} \left\{ [A_{ij}]^{-1} [Memo_j]_o \right\} - \sum_{j=N^c+1}^{N^{c+f}} C_{ij} \Phi_j^M + \sum_{j=N^{c+f}+1}^{N^{c+f+b}} D_{ij} \Phi_{nj}^M \quad (3-33) \\ & \quad (i=1,2,3,\dots,N^{c+f+b}) \end{aligned}$$

where the subscript o indicates “outer domain”. This equation, which is formulated on the control surface, body surface and free-surface, features much larger influence matrices. In consideration of the matrix’s structure, the Generalized Minimum Residual method (GMRES) is chosen to solve the equation. After finding the solution of the equations, we get the velocity potential and the normal derivatives on control surface, free-surface and mean wetted hull surface.

For the zero speed small amplitude problems, once the panelization is set up, there will not be any update, thus the matrices are constant. For nonzero speed problem or large amplitude problems, the panelization needs to be updated at every time step, thus it results in time-dependent matrices which need to be updated at every time instant.

3.7 Summary and Conclusions

The large amplitude ship motion problem is formulated in this chapter and the hybrid method for calculating radiation and diffraction potentials is elaborated. This time domain hybrid method, which is a combination of time-domain transient Green function method and Rankine source method, is formulated to investigate the hydrodynamic forces. It is a further development of the time domain transient Green function method, as introduced in Chapter 2, in the sense that it still uses it to form the boundary condition on the matching surface but overcomes its main shortcoming on dealing with floating bodies with flared sections in the near field. Furthermore, it does not need so many panels over such a large free-surface area, as when applying the Rankine source method, since a robust boundary condition can be obtained on the control surface with the previously elaborated Green function method. The matching surface is fixed in space so that the difficult-to-treat waterline integral term vanishes. During the formulation, a free-surface simulator which is based on the linear free-surface condition is adopted. A systematic study will be needed to see the validity of this scheme in practical applications, which is also necessary for determining the position where to locate the matching surface.

The GMRES method is adopted to solve the resulting equations with large scale influence matrices. For the calculation of m_j terms, a multi-step method is chosen so that to avoid the problem on calculating second order spatial derivatives of the velocity potential on body surface.

Chapter 4 Simulation of Ship Motions at Zero Speed by Time-Domain Hybrid Method

4.1 Small Amplitude Ship Motions in Regular Waves with Six Degrees of Freedom

The large amplitude ship motion in waves theory has been formulated in the last chapter. Traditionally the ship motion is studied based on small amplitude assumption where the motion is assumed small so that when integrating Bernoulli's equation for calculating forces/moments, the contributions from the difference between the calm water level and the instantaneous wavy water surface will be of a higher order. Thus the calculation can be done up to the calm water level, which results in a fixed panelization on the mean wetted body surface.

As elaborated in the last chapter, the equations of six degrees of freedom motion are based on Newton's second law, which is written in an inertial coordinate system. But the moments acting on the body are conveniently defined in a body-fixed coordinate system, thus transformations are necessary in order to write the equations of motion in the body-fixed system. These transformations lead to the so-called *Euler equations of motion* for a rigid body, which are exact and fully nonlinear. For small amplitude motions, such a complicated system is not preferred and a linearized system of equations is more suitable for attempting a solution. The theory of linear (small amplitude) ship motions in regular waves is briefly reviewed here (Lewis, 1988).

The general form of the linearized equations in six degrees of freedom *using body axes* is,

$$\sum_{k=1}^6 \Delta_{jk} \ddot{\eta}_k(t) = \vec{F}_j(t) \quad (j=1,2,\dots,6) \quad (4-1)$$

where Δ_{jk} are the components of the generalized inertia matrix for the ship, in which the mass and moment of inertia terms, Δ and I , and all possible couplings are included. $\ddot{\eta}_k$ are the accelerations in mode k ; \vec{F}_j represent the total forces or moments acting on the body in direction j . In linearizing the equations many of the terms in Δ_{jk} become zero, and Abkowitz (1969) has shown that for a ship with lateral symmetry (4-1) reduces to the following six explicit equations:

$$\begin{aligned} \Delta(\ddot{\eta}_1 + z_c \ddot{\eta}_5) &= \vec{F}_1 & -\Delta z_c \ddot{\eta}_2 + I_{44} \ddot{\eta}_4 - I_{46} \ddot{\eta}_6 &= \vec{F}_4 \\ \Delta(\ddot{\eta}_2 - z_c \ddot{\eta}_4 + x_c \ddot{\eta}_6) &= \vec{F}_2 & \Delta(z_c \ddot{\eta}_1 - x_c \ddot{\eta}_3) + I_{55} \ddot{\eta}_5 &= \vec{F}_5 \\ \Delta(\ddot{\eta}_3 - x_c \ddot{\eta}_5) &= \vec{F}_3 & \Delta x_c \ddot{\eta}_2 - I_{64} \ddot{\eta}_4 + I_{66} \ddot{\eta}_6 &= \vec{F}_6 \end{aligned} \quad (4-2)$$

where

$F_j(t), j=1,2,3$ are the total forces in the x, y, z directions respectively;

$F_j(t)$, $j=4,5,6$ are the total moments acting about the x , y , z axes respectively;

Δ is the total mass of the ship and I_{jj} , $j=4,5,6$ are moments of inertia around the x , y , z axes respectively;

I_{46} is roll-yaw product of inertia and vanishes if the ship has fore-and-aft symmetry; $I_{46}=I_{64}$;

$(x_c, 0, z_c)$ is the coordinate of gravity centre of the ship in the $O'xyz$ system;

$\ddot{\eta}_j(t)$ is the acceleration in j -th degree of freedom, where $j=1,2,\dots,6$ refers to surge, sway, heave, roll, pitch and yaw.

Comparing (4-1) and (4-2), the generalized inertia matrix can be obtained as:

$$\Delta_{jk} = \begin{bmatrix} \Delta & 0 & 0 & 0 & \Delta z_c & 0 \\ 0 & \Delta & 0 & -\Delta z_c & 0 & \Delta x_c \\ 0 & 0 & \Delta & 0 & -\Delta x_c & 0 \\ 0 & -\Delta z_c & 0 & I_{44} & 0 & -I_{46} \\ \Delta z_c & 0 & -\Delta x_c & 0 & I_{55} & 0 \\ 0 & \Delta x_c & 0 & -I_{64} & 0 & I_{66} \end{bmatrix} \quad (4-3)$$

This matrix can be readily evaluated in any specific case. If the origin is vertically in line with the gravity centre, all terms related to x_c will be zero.

As presented in Equation (4-1), $F_j(t)$ represent the total forces or moments acting on the ship in body-fixed system. Likewise, $\ddot{\eta}_j(t)$ are the accelerations resolved in body-fixed coordinate system. In the formulation and solving of the hydrodynamic problems associated with ship motion it is usually more convenient to work in earth fixed system. As far as the linearized equations of motion are concerned, the resolution of the forces, moments and motion amplitudes into one system or the other does not matter. The distinction between the two systems has been lost in the linearization.

The forces on the right hand of Equation (4-2) can be subdivided into the gravitational and fluid forces:

$$\vec{F}_j(t) = \vec{F}_{Gj}(t) + \vec{F}_{Hj}(t) \quad (j=1,2,\dots,6) \quad (4-3)$$

Here the gravitational forces are due to the weight of the ship applied at gravity center and are usually combined with the hydrostatic part of the fluid forces as to give the *net* hydrostatic forces. The fluid forces acting on the ship, which contain the hydrostatic and hydrodynamic parts, are obtained by integrating the fluid pressure over the underwater portion of the hull. Thus the components of the fluid forces acting in each of the six DOF are given as

$$\vec{F}_{Hj}(t) = \iint_{S_b} P \vec{n}_j ds \quad (j=1,2,\dots,6) \quad (4-4)$$

where \vec{n}_j is generalized normal vector of the hull, P is the fluid pressure and S_b is the wetted hull surface.

Assuming the flow is inviscid and irrotational, the pressure on the body can be found by Bernoulli's equation as $P = -\rho \frac{\partial \Phi}{\partial t} - 0.5\rho(\nabla\Phi)^2 - \rho gz$, where the first two terms are the hydrodynamic contributions to the pressure and the third term represents the hydrostatic contribution. When this expression is substituted into Equation (4-4), the fluid forces may be divided into two parts as:

$$\vec{F}_{Hj}(t) = -\rho \iint_{S_b} \left(\frac{\partial \Phi}{\partial t} + gz \right) \vec{n}_j ds = \vec{F}_{HSj}(t) + \vec{F}_{HDj}(t) \quad (j=1,2,\dots,6) \quad (4-5)$$

where

$$\vec{F}_{HSj}(t) = -\rho g \iint_{S_b} z \vec{n}_j ds \quad (4-6)$$

$$\vec{F}_{HDj}(t) = -\rho \iint_{S_b} \frac{\partial \Phi}{\partial t} \vec{n}_j ds \quad (4-7)$$

In order to find expressions for the above to insert into the equations of motion, the hydrostatic and hydrodynamic forces will be considered separately.

To find the hydrostatic forces we must calculate the integral in Equation (4-6). The z value must be replaced by its equivalent values in the $Gx'y'z'$ system and the integrals evaluated over the instantaneous wetted hull surface. In linear theory the contributions from the area between calm water level and the actual wavy water surface are of a higher order, thus the integral is evaluated up to the calm water level.

The details of the integral evaluation have been explained in last chapter. Since the mean hydrodynamic forces are cancelled by the mean gravitational forces, the two are combined to give the *net* hydrodynamic forces. The final results for a vessel with port/starboard symmetry are given in a matrix notation as follows:

$$\vec{F}_{HSj}^*(t) = \vec{F}_{HSj}(t) + \vec{F}_{Gj}(t) = -\sum_{k=1}^6 C_{jk} \eta_k(t) \quad (j=1,2,\dots,6) \quad (4-8)$$

where $\vec{F}_{HSj}^*(t)$ is the net hydrostatic force on the body in j th direction, C_{jk} are the hydrodynamic restoring force coefficients and $\eta_k(t)$ the arbitrary motions.

The hydrodynamic restoring force coefficients C_{jk} give the net hydrostatic force acting on the vessel in j th direction due to a unit displacement in k th mode of motion. C_{jk} may be evaluated as following:

$$\begin{aligned}
C_{jk} &= 0 \quad \text{except for the values} \\
C_{33} &= \rho g \int B(x) dx \\
C_{35} &= C_{53} = -\rho g \int xB(x) dx \\
C_{44} &= \rho g \nabla \overline{GM}_T \\
C_{55} &= \rho g S_{11} + \rho g \nabla (\overline{KB} - \overline{KG})
\end{aligned} \tag{4-9}$$

The calculation of hydrodynamic forces acting on the vessel has been discussed separately in previous chapter, thus we will assume them as solved here and no further details will be given. Substituting the forces expressions into Equation (4-2), we finally get the governing equations of motions:

$$\sum_{k=1}^6 \Delta_{jk} \ddot{\eta}_k(t) + C_{jk} \dot{\eta}_k(t) = \vec{F}_j^I(t) + \vec{F}_j^R + \vec{F}_j^D \quad (j=1,2,\dots,6) \tag{4-10}$$

The components on the right-hand side, i.e. $\vec{F}_j^I(t)$, \vec{F}_j^R and \vec{F}_j^D , represent incident wave forces, radiation forces and diffraction forces.

Equations (4-10) are the linearized equations of motions for an unrestrained vessel. There are six coupled, linear equations for the six unknown motions. They have been extensively used during the years and proved to be robust for studying ship motions under small amplitude waves' excitement. For an arbitrarily shaped vessel the six equations must be solved simultaneously. However, for the case of an unrestrained ship with port/starboard symmetry the six equations may be uncoupled into two sets of three equations. The vertical-plane or longitudinal motions (surge, heave and pitch) are uncoupled from the horizontal-plane or transverse motions (sway, roll and yaw). It should be noted that the lack of coupling between the vertical and horizontal modes is a consequence of linear theory. In nonlinear theory such cross-coupling will be present.

4.1.1 The Simplified Head-Sea Case

As illustrated in the preceding section, the longitudinal (vertical plane) motions of a symmetric ship in regular waves can be studied separately from the transverse motions. For longitudinal motions, we have the equations

$$\begin{aligned}
\Delta(\ddot{\eta}_1 + \bar{z}_c \ddot{\eta}_5) &= \vec{F}_1 \\
\Delta(\ddot{\eta}_3 - \bar{x}_c \ddot{\eta}_5) &= \vec{F}_3 \\
\Delta(\bar{z}_c \ddot{\eta}_1 - \bar{x}_c \ddot{\eta}_3) + I_{55} \ddot{\eta}_5 &= \vec{F}_5
\end{aligned} \tag{4-11}$$

Furthermore, it has been found that for most comparatively long and slender ships surge has a minor effect and can be neglected. Mathematically, this can be achieved by removing the first

equation ($\eta_l \equiv 0$) and setting $z_c = 0$. If we further set $x_c = 0$, which means that the origin is vertically in line with the gravity centre, the equations of motion will be simplified to:

$$\begin{aligned}\Delta \ddot{\eta}_3 &= \vec{F}_3 \\ I_{55} \ddot{\eta}_5 &= \vec{F}_5\end{aligned}\quad (4-12)$$

Substituting the forces components into the above equation, we finally get the governing equations of motion for simplified head-sea case:

$$\begin{cases} \Delta \ddot{\eta}_3(t) + C_{33} \eta_3(t) + C_{35} \eta_5(t) = F_{30}(t) + F_{33}(t) + F_{35}(t) + F_{37}(t) \\ I_{55} \ddot{\eta}_5(t) + C_{53} \eta_3(t) + C_{55} \eta_5(t) = F_{50}(t) + F_{53}(t) + F_{55}(t) + F_{57}(t) \end{cases}\quad (4-13)$$

Note that in this simplified case, the origin of the coordinate system is at the gravity (mass) center of the body, which is assumed to lie on the calm waterplane. Solving the above equations in the time domain, we will get the time histories of the longitudinal motions. Then the steady-state part can be taken for a harmonic analysis:

$$\eta_k(t) = \frac{A_k^0}{2} + \sum_{n=1}^{\infty} A_k^n \cos(n\omega t) + B_k^n \sin(n\omega t)\quad (4-14)$$

Actually, for *linear* case, A_k^0, A_k^n and B_k^n ($n \in N, n \neq 1$) are zero, thus the expression (4-14) becomes

$$\eta_k(t) = A_k^1 \cos(\omega t) + B_k^1 \sin(\omega t)\quad (4-15)$$

So the motions' amplitudes and phase angles with respect to the incident wave are extracted as:

$$|\eta_k| = \sqrt{(A_k^1)^2 + (B_k^1)^2}\quad (4-16)$$

$$\varepsilon_{k\zeta} = \arg(A_k^1, -B_k^1)\quad (4-17)$$

4.1.2 Beam-Sea Case

The transverse motions' equations are expressed as:

$$\begin{aligned}\Delta(\ddot{\eta}_2 - z_c \ddot{\eta}_4 + x_c \ddot{\eta}_6) &= \vec{F}_2 \\ -\Delta z_c \ddot{\eta}_2 + I_{44} \ddot{\eta}_4 - I_{46} \ddot{\eta}_6 &= \vec{F}_4 \\ \Delta x_c \ddot{\eta}_2 - I_{64} \ddot{\eta}_4 + I_{66} \ddot{\eta}_6 &= \vec{F}_6\end{aligned}\quad (4-18)$$

Under small amplitude beam seas condition, if we assume $I_{46} = 0$, then further simplification can be applied. There is still coupling terms between sway and roll. For sway motion, its prediction is often involved with maneuvering problems which is not in the scope of the present study.

Thus in the present study for validation purpose it is assumed $z_c=0$. Then we have a very simplified model for roll motion:

$$I_{44}\ddot{\eta}_4 = \bar{F}_4$$

Furthermore, it is well known that in roll motion the viscous effect is very important for a good prediction. Mathematically, this is taken into account by introducing the viscous damping term (Ikeda et al., 1978). Substituting the forces components into the above equation, we finally get the simplified equations for simulating roll motion at beam-seas:

$$I_{44}\ddot{\eta}_4(t) + C_{44}\dot{\eta}_4(t) = F_{40}(t) + F_{44}(t) + F_{47}(t) + F_{4dp}(t) \quad (4-19)$$

where $F_{4dp}(t)$ is the force component related to viscous damping term and estimated as:

$$F_{4dp}(t) = -B_{dp} * \dot{\eta}_4(t)$$

where B_{dp} is the viscous damping coefficient.

4.2 Large Amplitude Head Seas Condition

Following the discussion in Section 3.5, we continue our study on large amplitude ship motions under head waves' excitement. As the ship is port/starboard symmetric, we assume that for sway, roll or yaw: $\dot{v}_2 = 0, \dot{\omega}_1 = 0, \dot{\omega}_3 = 0$. Thus the aforementioned motion equations can be further simplified. If we neglect the surge motion, then the above equation becomes

$$\begin{aligned} \Delta \dot{v}_3 &= F_3 \\ I_{55} \dot{\omega}_2 &= F_5 \end{aligned} \quad (4-20)$$

Here it is assumed that $I = \begin{bmatrix} I_{44} & 0 & 0 \\ 0 & I_{55} & 0 \\ 0 & 0 & I_{66} \end{bmatrix}$

This is very similar to the linear equation (4-12) in head-sea case, but it is important to notice that the equation is formulated in *the body-fixed coordinate system*.

The transformation matrices in head seas condition become:

$$\begin{aligned} [T] &= \begin{bmatrix} c_2 c_3 & -c_1 s_3 + s_1 s_2 c_3 & s_1 s_3 + c_1 s_2 c_3 \\ c_2 s_3 & c_1 c_3 + s_1 s_2 s_3 & -s_1 c_3 + c_1 s_2 s_3 \\ -s_2 & s_1 c_2 & c_1 c_2 \end{bmatrix} = \begin{bmatrix} c_2 & 0 & s_2 \\ 0 & 1 & 0 \\ -s_2 & 0 & c_2 \end{bmatrix} \\ [T_\theta] &= \begin{bmatrix} 1 & s_1 t_2 & c_1 t_2 \\ 0 & c_1 & -s_1 \\ 0 & s_1 / c_2 & c_1 / c_2 \end{bmatrix} = \begin{bmatrix} 1 & 0 & t_2 \\ 0 & 1 & 0 \\ 0 & 0 & 1 / c_2 \end{bmatrix} \end{aligned} \quad (4-21)$$

The transformation between two systems turns to:

$$\begin{bmatrix} \dot{\eta}_4 \\ \dot{\eta}_5 \\ \dot{\eta}_6 \end{bmatrix} = \begin{bmatrix} 1 & 0 & t_2 \\ 0 & 1 & 0 \\ 0 & 0 & 1/c_2 \end{bmatrix} \begin{bmatrix} \omega_1 \\ \omega_2 \\ \omega_3 \end{bmatrix} = \begin{bmatrix} \omega_1 + t_2 \omega_3 \\ \omega_2 \\ \omega_3 / c_2 \end{bmatrix} \Rightarrow \dot{\eta}_5 = \omega_2 \quad (4-22)$$

$[\dot{v}_1, \dot{v}_2, \dot{v}_3]^T$ and $[\dot{\omega}_1, \dot{\omega}_2, \dot{\omega}_3]^T$ can be solved by the motion equations; then $[v_1, v_2, v_3]^T$ and $[\omega_1, \omega_2, \omega_3]^T$ can be obtained by an integration regarding to time. Afterwards r_G and θ can be obtained by using the above expressions.

$$z_G \approx \int_0^t v_3 dt, \quad \eta_5 = \int_0^t \omega_2 dt$$

4.2.1 Diffraction Forces and Radiation Forces

The forces and moments in the motion equations are defined in *the body-fixed system*, while the forces and moments arising from the disturbance wave-field are solved over the mean wetted body surface. These forces are computed as though the ship is undergoing small amplitude sinusoidal motions in calm water. The radiation problem is solved by using the velocity and acceleration information relative to the earth-fixed coordinate system. The diffraction problem is solved by using the incidental wave defined in earth-fixed coordinate system.

These forces/moments are exerting on the hull at the actual position under instantaneous wave profile, though the computation will be done up to ship's mean wetted surface at upright position to reduce computational burden. In the present work, these forces need transforming into body-fixed system by using the transformation matrix.

$$\begin{aligned} F_3^R &= f_3^R & F_5^R &= f_5^R \\ F_3^D &= f_3^D & F_5^D &= f_5^D \end{aligned}$$

This treatment is consistent with the hydrodynamic force simulation in the present study.

4.2.2 Incidental Wave Forces and Hydrostatic Forces

The calculation of the Froude-Krylov force component is explained as following:

- Update the panel information (geometric centre coordinates and normal direction) according to the motion results

$$\begin{aligned} x &= x_G(t) + (c_2 x' + s_2 z') = x_G(t) + s_2 z' \\ y &= y' \\ z &= z_G(t) + (-s_2 x' + c_2 z') = z_G(t) + c_2 z' \end{aligned}$$

- Determine those panels under the instantaneous wave profile by $z \leq \zeta(x, y)$ for the computation;

- Calculate the incidental wave forces in *body-fixed* system

$$\vec{f}^l(t) = -\rho \iint_{S_b(t)} \frac{\partial \Phi_l(x_p, y_p, z_p)}{\partial t} \vec{n} ds$$

- Transform the forces into *earth-fixed* system and insert them into the motion equation;

$$F_3^l = c_2 f_3^l \quad F_5^l = f_5^l$$

The hydrostatic forces computation is similar.

4.3 Numerical Procedure for Time-Domain Ship Motions' Simulation

As explained in the previous chapter, the formulated boundary value problems are solved by using the ordinary panel method. Since the forces are assumed calculated by integration of the time dependent pressures, the motions are now simulated as following:

- 1) Arrange the panelization for hydrodynamic computation;
- 2) Set up the influence matrices;
- 3) Calculate panel characters and arrange the mass matrix;
- 4) SOLVE SMALL AMPLITUDE MOTION PROBLEM;
- 5) Arrange the panels for calculating Froude-Krylov forces;
- 6) SOLVE LARGE AMPLITUDE MOTION PROBLEM;
- 7) Output the results.

Regarding *Step 4*), the numerical scheme is explained by an application to the head-sea case as following:

- The initial conditions are set as: $t=0$: $\eta_k(0), \dot{\eta}_k(0)$ (for $k=3,5$), thus $\ddot{\eta}_k(0)$ can be calculated as:

$$\begin{cases} \ddot{\eta}_3(0) = [F_{30}(0) - C_{33}\eta_3(0) - C_{35}\eta_5(0)] / \Delta \\ \ddot{\eta}_5(0) = [F_{50}(0) - C_{53}\eta_3(0) - C_{55}\eta_5(0)] / I_{22} \end{cases}$$

- First prediction of displacement and velocity at the end of i -th step:

$$\begin{cases} \dot{\eta}_k^1(i) = \dot{\eta}_k(i-1) + \ddot{\eta}_k(i-1) \cdot \Delta t \\ \eta_k^1(i) = \eta_k(i-1) + \frac{\dot{\eta}_k(i-1) + \dot{\eta}_k^1(i)}{2} \cdot \Delta t \end{cases}$$

- Update free surface condition and matching surface condition by using historical information, $\varphi^l(i)$ is calculated; then $F_{jk}^l(i)$ are obtained. Using Equation (4-13), we get the first estimation of $\ddot{\eta}_k^1(i)$ as:

$$\begin{cases} \ddot{\eta}_3^1(i) = [F_{30}^1(i) + F_{33}^1(i) + F_{35}^1(i) + F_{37}^1(i) - C_{33}\eta_3^1(i) - C_{35}\eta_5^1(i)] / \Delta \\ \ddot{\eta}_5^1(i) = [F_{50}^1(i) + F_{53}^1(i) + F_{55}^1(i) + F_{57}^1(i) - C_{53}\eta_3^1(i) - C_{55}\eta_5^1(i)] / I_{22} \end{cases}$$

- The displacement and velocity at the end of the i -th time interval are re-estimated as:

$$t = i * \Delta t, \quad \begin{cases} \dot{\eta}_k^2(i) = \dot{\eta}_k(i-1) + \frac{\Delta t}{2} \cdot [\ddot{\eta}_k(i-1) + \ddot{\eta}_k^1(i)] \\ \eta_k^2(i) = \eta_k(i-1) + \frac{\Delta t}{2} \cdot [\dot{\eta}_k(i-1) + \dot{\eta}_k^2(i)] \end{cases}$$

- If the difference between $\dot{\eta}_k^2(i)$ and $\dot{\eta}_k^1(i)$ are small enough, we store $\dot{\eta}_k^2(i)$ as $\dot{\eta}_k(i)$.

Then the displacement and acceleration at the end of the i -th time interval are set as:

$$t = i * \Delta t, \quad \begin{cases} \eta_k(i) = \eta_k^2(i) \\ \ddot{\eta}_k(i) = \ddot{\eta}_k^1(i) \end{cases}$$

Otherwise, by setting these results as first prediction and returning to previous steps, the calculation is repeated until converged results are obtained.

- The calculation will march to the next step and be returned to step 2.

For the large amplitude motion simulation, the main difference is to calculate the hydrostatic and Froude-Krylov forces and moments on the instantaneous wetted surface.

4.4 Results of Small Amplitude Radiation and Diffraction Problems

In order to validate the hybrid method and the implemented numerical scheme, numerical tests have been carried out for small amplitude forced motion and diffraction problems of different bodies. The results from present method have been compared with available experimental data, numerical results of NEWDRIFT (3D frequency domain panel method code, Papanikolaou, 1985) and other well-established methods.

4.4.1 Rectangular Barge

The first test has been done with a rectangular barge, which has been also investigated by NEWDRIFT as an example case and is known from previously published work of O. Faltinsen et al (1974). The results for the barge, which is $90m \times 90m \times 40m$, are obtained by NEWDRIFT with 4×153 panels. In the present stage, since it is the very beginning of numerical test, we do not want to burden the work with many panels. So at first we use 150 panels on the control surface (CNP), 150 panels on half of the body (BNP) and the panel number on the free surface (FNP) changes as the enclosed free surface changes. Figure 4.1 is the view for 1600 panels on a

$3L \times 1.5L$ free-surface area. The results from different free-surface settings are shown in the following tables.

As can be seen from Table 4.1, the results reach a converged state as we increase the size of the free-surface. On vertical direction, the results are quite stable and agree well with NEWDRIFT. On horizontal direction, the results approach to NEWDRIFT results as we increase the density of grids on free surface, which indicates that the accuracy of free surface simulation is important for the simulation. It should be noticed that due to the fact that the velocity potential decays on vertical direction exponentially and the contribution on vertical forces are from the panels on the bottom only, the free surface simulation has much less influence on A_{33} and B_{33} than on A_{11} and B_{11} .

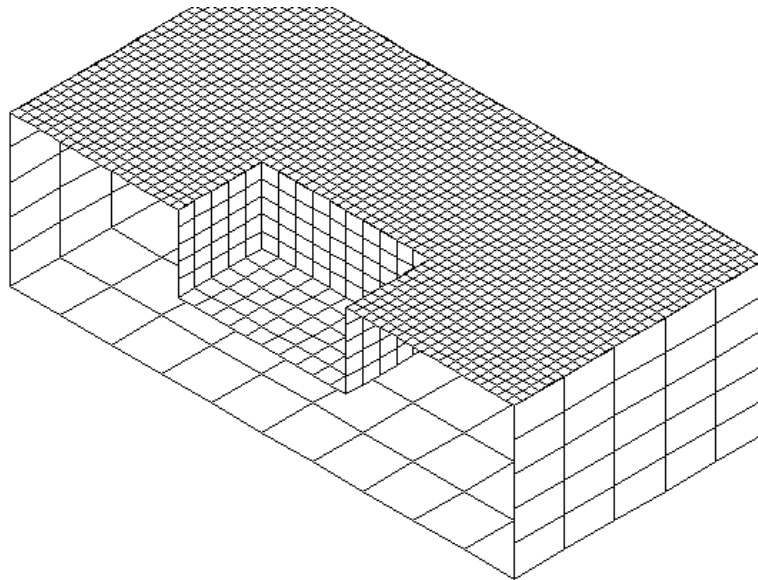


Figure 4.1 Perspective view of the panelization scheme

Table 4.1 Hydrodynamic coefficients of the barge with different free-surface panelization, $T=10s$

		Added Mass		Damping Coe.	
		A_{11}	A_{33}	B_{11}	B_{33}
PRESENT STUDY	FNP= 800	0.12719	0.66537	0.40587	0.00854
BNP=150	FNP=1600	0.21525	0.67236	0.46757	0.01405
CNP=150	FNP=2112	0.18837	0.67156	0.48862	0.01357
NEWDRIFT RESULTLS		0.17724	0.66787	0.47024	0.01672

In order to see the influence of the free-surface size, the force histories from different settings are also compared, shown in the following. From Figure 4.2 we observe that the results from using 1600 panels is very close to the results from using 2112 panels on free surface. Considering the seriously increased computing burden due to the increase of panel numbers, we may say that 1600 panels on a $3L \times 3L$ free-surface area can be used to yield good results for the present case.

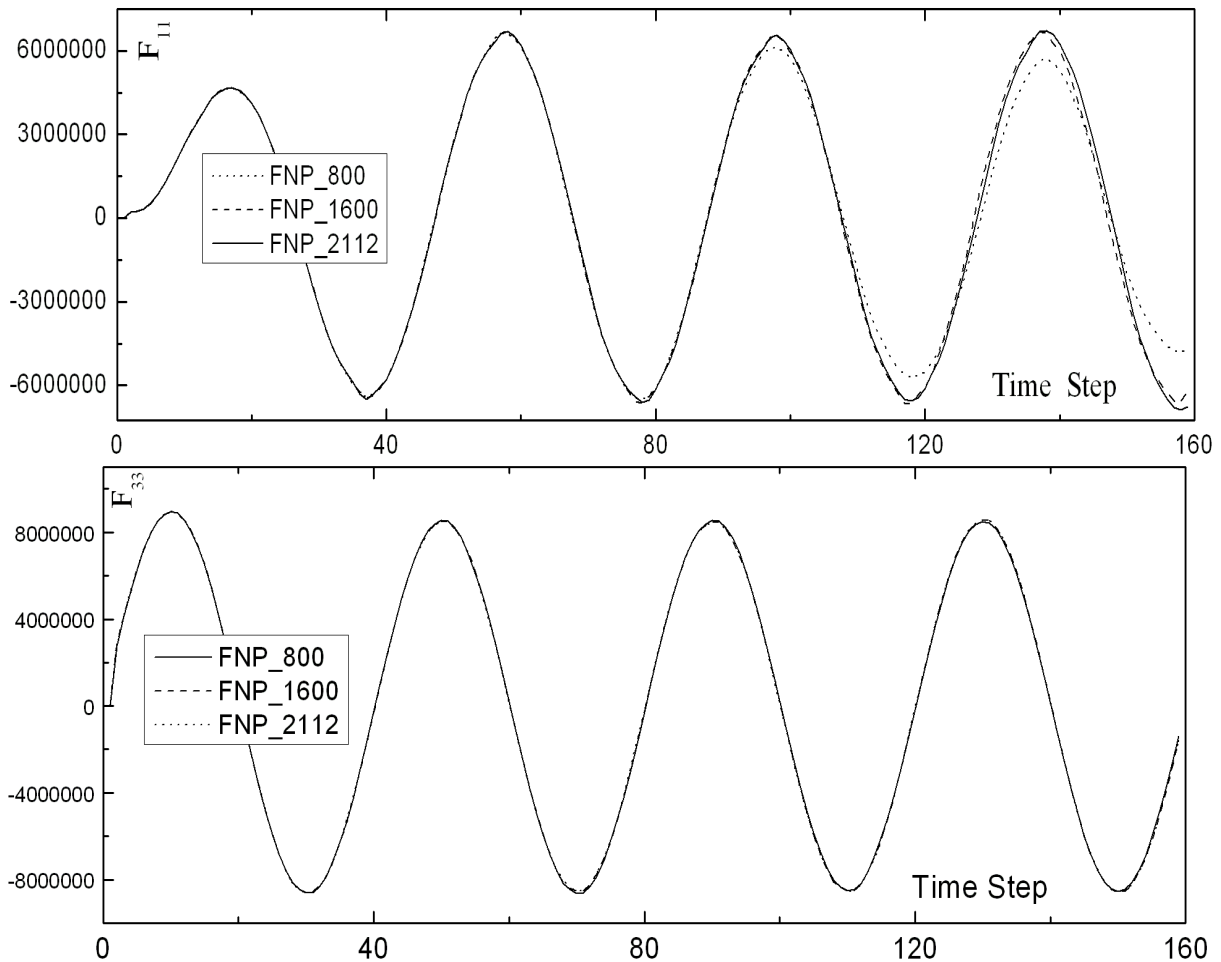


Figure 4.2 Force histories on a barge with different free-surface panelization, $T=10s$

The next step is to investigate the influence of the panels on the matching surface, in other words, to check if 150 panels are enough or not. For this reason, we employ another meshing plan, in which we increase the number of panels on the vertical boundary but retain the same meshing on the bottom (assuming that memory effects decrease exponentially with depth). The hydrodynamic coefficients' results are shown in Table 4.2. Although very limited, we do observe some improvement from using more panels on the matching surface meshing.

For this case, since the body has a double symmetric character, there is not any essential difference between head seas condition and beam seas condition. Yet though, an attempt has

been done for “beam seas condition” without using any symmetric/antisymmetric character, which means the full fluid domain is panelized and simulated. Results on diffraction problem are shown as following in Figure 4.3. The Froude Krylov moment amplitude from both the present method and NEWDRIFT are identical, proves that the integration process is correct. The agreement on exciting force is also good, which indicates that the results for diffraction problems agree well.

Table 4.2 Hydrodynamic coefficients of the barge with different control-surface penalization, T=10s

		Added Mass		Damping Coe.	
		A ₁₁	A ₃₃	B ₁₁	B ₃₃
BNP=150	CNP=150	0.21525	0.67236	0.46757	0.01405
FNP=1600	CNP=210	0.20082	0.67181	0.47085	0.01399
NEWDRIFT RESULTLS		0.17724	0.66787	0.47024	0.01672

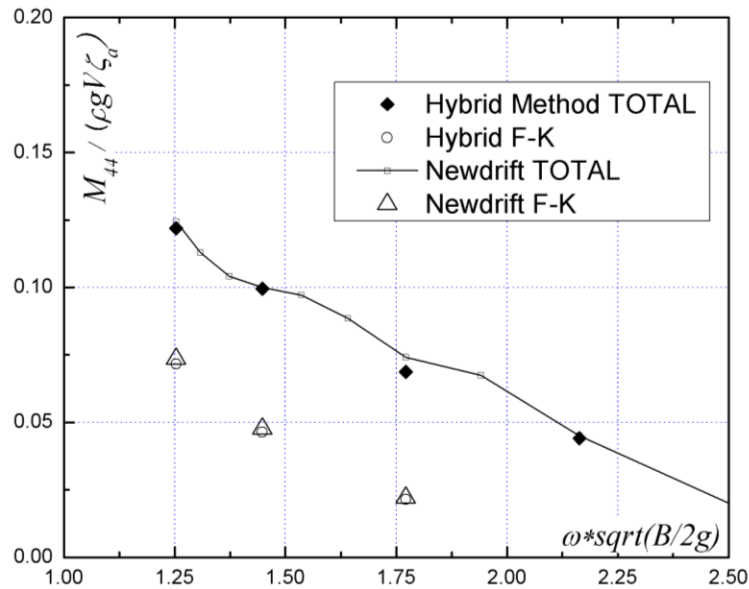


Figure 4.3 Froude-Krylov moment and wave exciting moment of a barge at beam seas

4.4.2 Hemisphere Case

The second application has been done to a floating hemisphere with radius $R=1.0m$ to test the quality of free surface simulation. This case has been also studied by the TDGF method in

Chapter 2. The panels are distributed on the matching surface, free surface and body boundary. Figure 4.4 is a perspective view of the case $k=3.0$. The matching surface is placed one wave-length away from the body boundary and 8 panels are used in a wave length on radial direction.

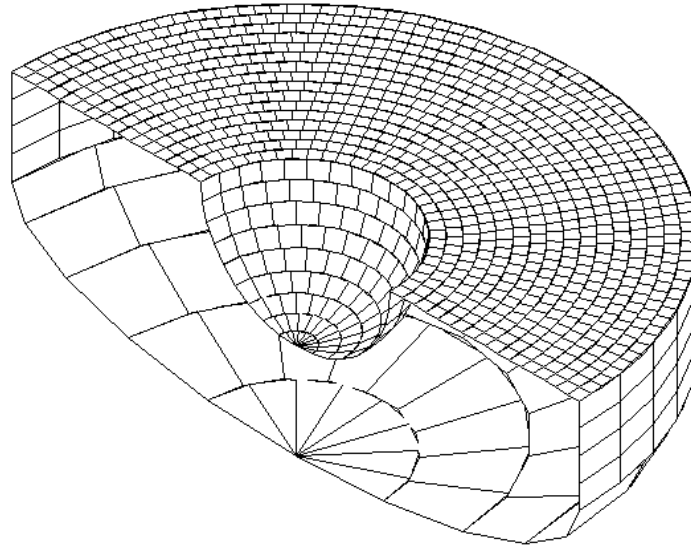


Figure 4.4 Panelization for the simulation of the hemisphere

On the matching surface fixed numbers of panels are used. The matching surface is a combination of a vertical cylinder $x^2+y^2=R_M^2$ ($-R \leq z \leq 0$) and a semi ellipsoid

$$\frac{x^2 + y^2}{R_M^2} + \frac{(z + R)^2}{R^2} = 1 \quad (-2R \leq z \leq -R).$$

Here R_M is the radius of the matching surface. As can be

seen, the panels on the ellipsoid are rather rough because it is believed that the influence is very limited due to its depth. According to our experience, 126 panels are far more enough for a quarter of the sphere surface. The panels here are fixed and distributed kind of evenly. On the free surface, different schemes are used. In the present study, the length of free-surface panel's edge is set so that $\Delta l \approx \lambda/N$, ($N=4, 8, \text{ or } 12$) and the distance between matching surface and body boundary is set as 0.5λ , 1.0λ and 2.0λ respectively. The hydrodynamic coefficients' results from different cases are shown in the tables (Table 4.3 to 4.5).

From the first two tables we see that, when the matching surface is half wave-length away, which is case $R_M=R+0.5\lambda$, the final results is not stable, especially when the panel size is large; When the matching surface is one wave-length away, which is case $R_M=R+\lambda$, the final results is not only stable, but also a convergence trend is observed when we decrease the size of the panel. When the matching surface is two wave-lengths away, which is case $R_M=R+2,0\lambda$, the final results is stable and convergent but it's clear that more panels are preferred. Similar phenomenon is observed from the results of $k=3.0$ case. In general, to set $R_M=R+0.5\lambda$ does not

yield satisfactory results while the other two can give stable results if the suitable panel size is used.

Table 4.3 Added mass and damping results of a barge, $k=1.5$

	$R_M = R + 0.5\lambda$		$R_M = R + \lambda$		$R_M = R + 2.0\lambda$	
	A ₁₁	B ₁₁	A ₁₁	B ₁₁	A ₁₁	B ₁₁
N=4	0.3393	0.3799	0.2830	0.3413	0.2554	0.3355
N=8	0.3353	0.3968	0.3419	0.3851	0.3323	0.3783
N=12	0.3299	0.3968	0.3584	0.3862	0.3512	0.3837
Chen's results	0.3687	0.4019	0.3687	0.4019	0.3687	0.4019
	A ₃₃	B ₃₃	A ₃₃	B ₃₃	A ₃₃	B ₃₃
N=4	0.4027	0.1827	0.3877	0.1543	0.3716	0.1379
N=8	0.3895	0.1657	0.3826	0.1688	0.3794	0.1575
N=12	0.3866	0.1599	0.3848	0.1687	0.3847	0.1579
Chen's results	0.3894	0.1605	0.3894	0.1605	0.3894	0.1605

Table 4.4 Added mass and damping results of a barge, $k=3.0$

	$R_M = R + 0.5\lambda$		$R_M = R + \lambda$		$R_M = R + 2.0\lambda$	
	A ₁₁	B ₁₁	A ₁₁	B ₁₁	A ₁₁	B ₁₁
N=4	0.1829	0.2050	0.1613	0.1843	0.1493	0.1764
N=8	0.1793	0.1926	0.1752	0.2136	0.1728	0.2100
N=12	0.1806	0.1878	0.1807	0.2161	0.1796	0.2149
Chen's results	0.1718	0.2234	0.1718	0.2234	0.1718	0.2234
	A ₃₃	B ₃₃	A ₃₃	B ₃₃	A ₃₃	B ₃₃
N=4	0.4162	0.0577	0.4073	0.0441	0.4061	0.0412
N=8	0.4113	0.0503	0.4009	0.0479	0.4039	0.0475
N=12	0.4109	0.0494	0.4015	0.0493	0.4054	0.0484
Chen's results	0.4115	0.0454	0.4115	0.0454	0.4115	0.0454

The first impression of $k=6.0$ case will be that, stable added mass results can be obtained by any of these settings, although the converged added mass results deviate a little from the “standard results” while the damping coefficient results oscillate obviously. This might be due to the fact that the disturbed-wave length is relatively short so that an accurate simulation of the wave is more difficult. But the shorter the wave length becomes, the less will be our interest.

Table 4.5 Added mass and damping results of a barge, $k=6.0$

	$R_M = R + 0.5\lambda$		$R_M = R + \lambda$		$R_M = R + 2.0\lambda$	
	A ₁₁	B ₁₁	A ₁₁	B ₁₁	A ₁₁	B ₁₁
N=4	0.2034	0.0636	0.1802	0.0655	0.1787	0.0667
N=8	0.2057	0.0489	0.1852	0.0786	0.1845	0.0807
N=12	0.2065	0.0467	0.1869	0.0791	0.1864	0.0828
Chen's results	0.1784	0.0779	0.1784	0.0779	0.1784	0.0779
	A ₃₃	B ₃₃	A ₃₃	B ₃₃	A ₃₃	B ₃₃
N=4	0.4475	0.0076	0.4483	0.0079	0.4484	0.0084
N=8	0.4462	0.0056	0.4468	0.0089	0.4485	0.0098
N=12	0.4460	0.0055	0.4467	0.0090	0.4482	0.0097
Chen's results	0.4575	0.0065	0.4575	0.0065	0.4575	0.0065

If we examine all the results together, we will see that for $N=4$ cases, the results are not stable. And the longer the wave length is (smaller wave number), the worse the results become. This is an indication that for very long waves, more panels in a wave length are preferred.

From the comparison among the results of those three cases, we may draw some preliminary conclusions. For the case $R_M=R+0.5\lambda$, the results are not very stable. But if we use smaller panel size, this setting can still produce some acceptable results. For the case $R_M=R+\lambda$, the results are generally stable. They are not very sensitive to the change of panel size, which is usually preferred in the calculation. For the last case $R_M=R+2.0\lambda$, it gives, if not better, as good results as the second would do. But since the free-surface area is much larger than the second case, it's not the optimal choice.

The optimal setting which is recommended here for a good simulation of the free-surface is to set $R_M=R+\lambda$ and $\Delta l \approx \lambda/N$, ($N=8$).

4.4.3 Wigley Case

A Wigley type ship model, the hull form of which has the mathematic description of $y/b=[1-(2x/L)^2][1-(z/D)^2][1+0.2(2x/L)^2]$ where $2b/L=0.1$ and $D/L=0.0625$, is studied.

For this hull 256 panels are distributed on the half-body. On the matching surface 148 panels are used. On the free surface, which is a wave length far away from the hull border, different schemes are employed. Figure 4.5 shows a perspective view of a case for $L=2m$ and wave number $k=7$. Notice that the panels on the vertical matching surface are not evenly distributed.

The added masses and damping coefficients of forced surge and heave motions are plotted in Figure 4.6. Results include those from the present hybrid method, NEWDRIFT and the linear version TDGF method.

A good agreement is observed throughout all the studied range except some deviation at low non-dimensional wave numbers for the vertical direction motion. This might be due to the fact that, at low wave-number, which means a long wave, the present free-surface penalization is not sufficient for yielding accurate results. For the longitudinal direction surge motion, although the trend is exactly the same, the deviation is more obvious. This is partly due to that the Wigley hull is very narrow in this direction so that it is more difficult to obtain very accurate results, because the resulting pressure gradient in the longitudinal direction is very small. As indicated in the box-barge case study, indeed the longitudinal direction results are more sensitive with respect to the free surface panelization. Recalling to the panelization used in that case, we may note that the panelization in the present case is comparatively rough. It should be expected the results can be improved if a denser panelization is used.

The results from forced roll motion are plotted Figure 4.7. Although the Wigley hull still has the left/right (bow/stern) symmetric character in beam seas condition, this is in general not the case for a real ship, thus we did not use this advantage in the computation. Instead, the whole fluid domain is panelized so that the panel number is actually doubled compared to the head seas condition.

From the comparison with respect to the added mass and damping coefficients (wave making part), we observe that in high frequency range, as the wave length is quite small (comparable to ship beam), it is difficult to reach a converged value. It is recommended that the free surface width should be at least $2B+2\lambda$.

The diffraction problem has been also studied. In Figure 4.8 we have the RAOs of both Froude-Krylov force and total wave exciting force. The Froude Krylov RAOs from both the present procedure and NEWDRIFT are identical, proves that the integration process is correct. But there

Numerical Simulation of Large Amplitude Ship Motions and Applications to Ship Design and Safe Operation
 is some slight deviation in the exciting force results, which indicates differences in the results
 for the diffraction problem.

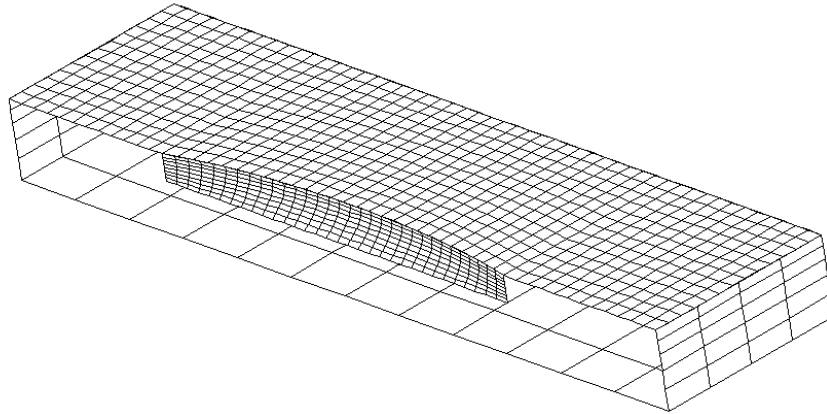


Figure 4.5 Panelization for the Wigley case, with 1215 panels in total

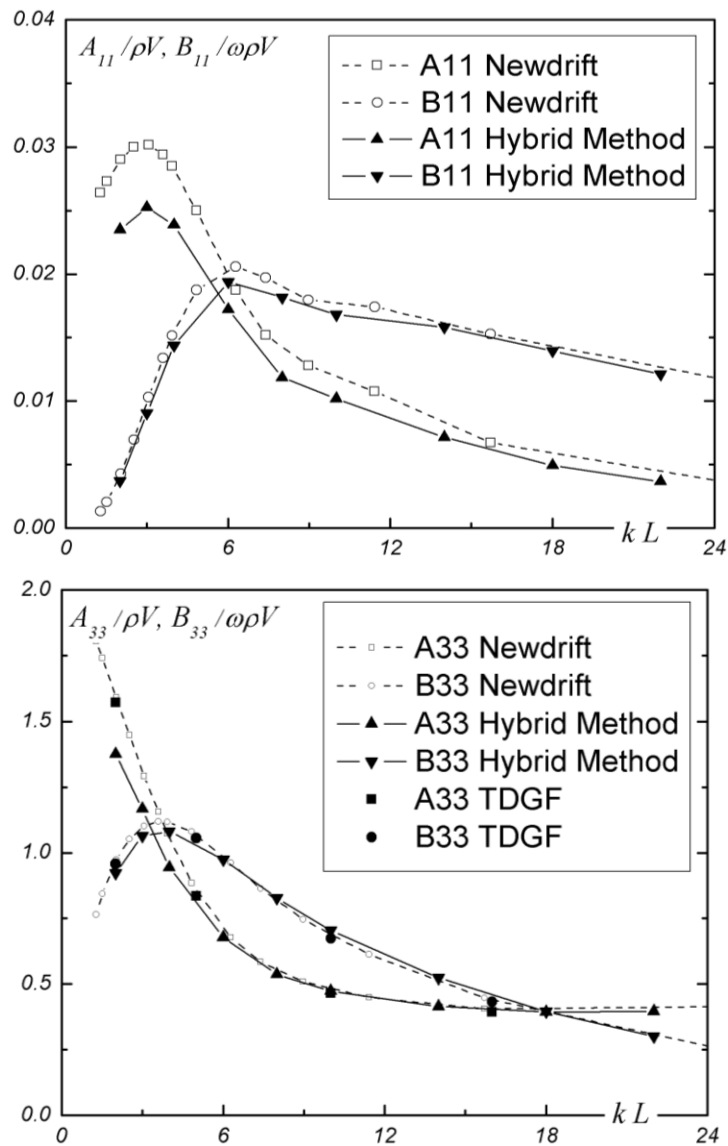


Figure 4.6 Added mass and damping coefficient results of the Wigley hull, $F_n=0.0$

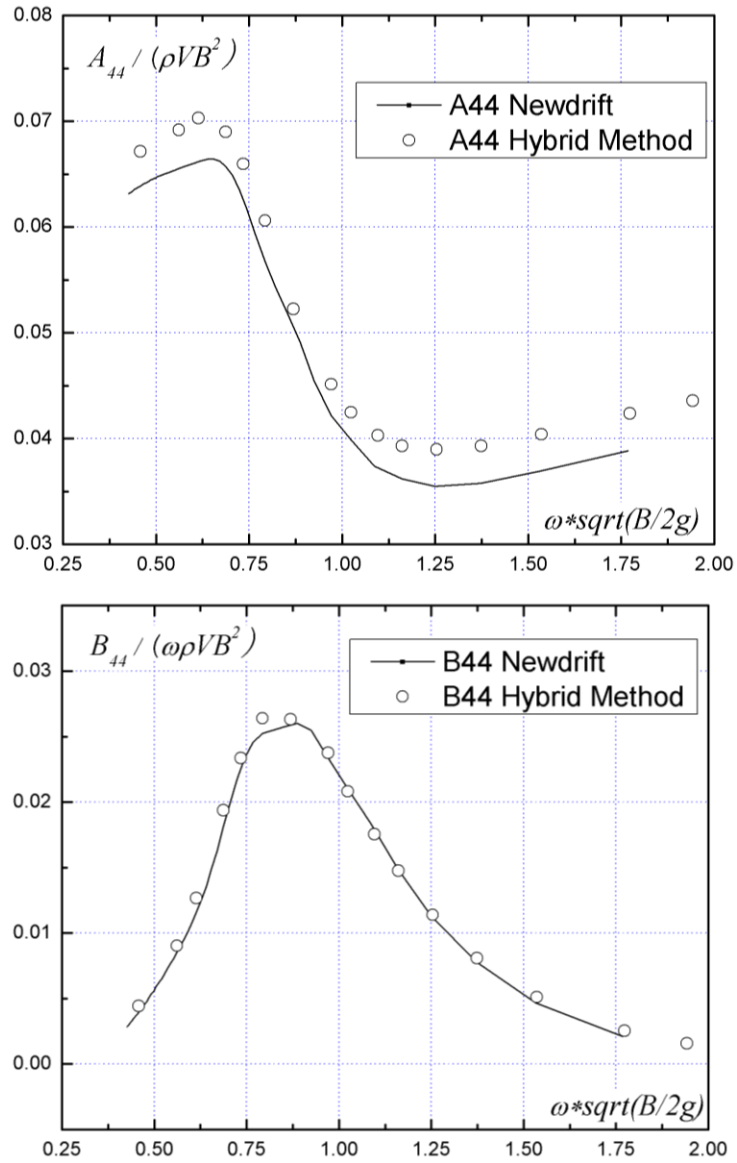


Figure 4.7 Roll added mass and damping coefficient of the Wigley hull, Fn=0.0

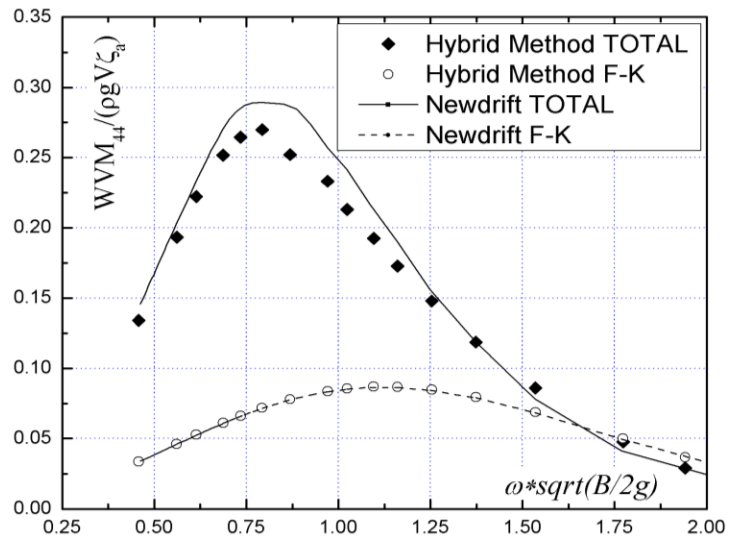


Figure 4.8 Froude-Krylov moment and total wave exciting moment of the Wigley hull, Fn=0.0

4.4.4 Series 60 Case

The model to be studied is a Series 60 hull with block coefficient $C_B=0.6$ (hull form data taken from *SHIPFLOW example cases*, 2005). The general dimensions are $1.0158 \times 0.1333 \times 0.0533$. On the matching surface 148 panels are distributed while on the half-body 238 panels are distributed. On the free surface, different schemes are used. Fixed panels are used near the hull in a very limited area in order to minimize the panelizing work. Figure 4.9 is the perspective view of a case with wave number $k=10$.

The added masses and damping coefficients are plotted in Figure 4.10. Results include those from the present hybrid method and NEWDRIFT. A good agreement is observed for every motion mode throughout all the studied range. Considering that the previous TDGF method, which uses the transient Green function, cannot deal with hulls that have flared sections at the waterline due to numerical problems, the hybrid method presently developed has a definite advantage at this point.

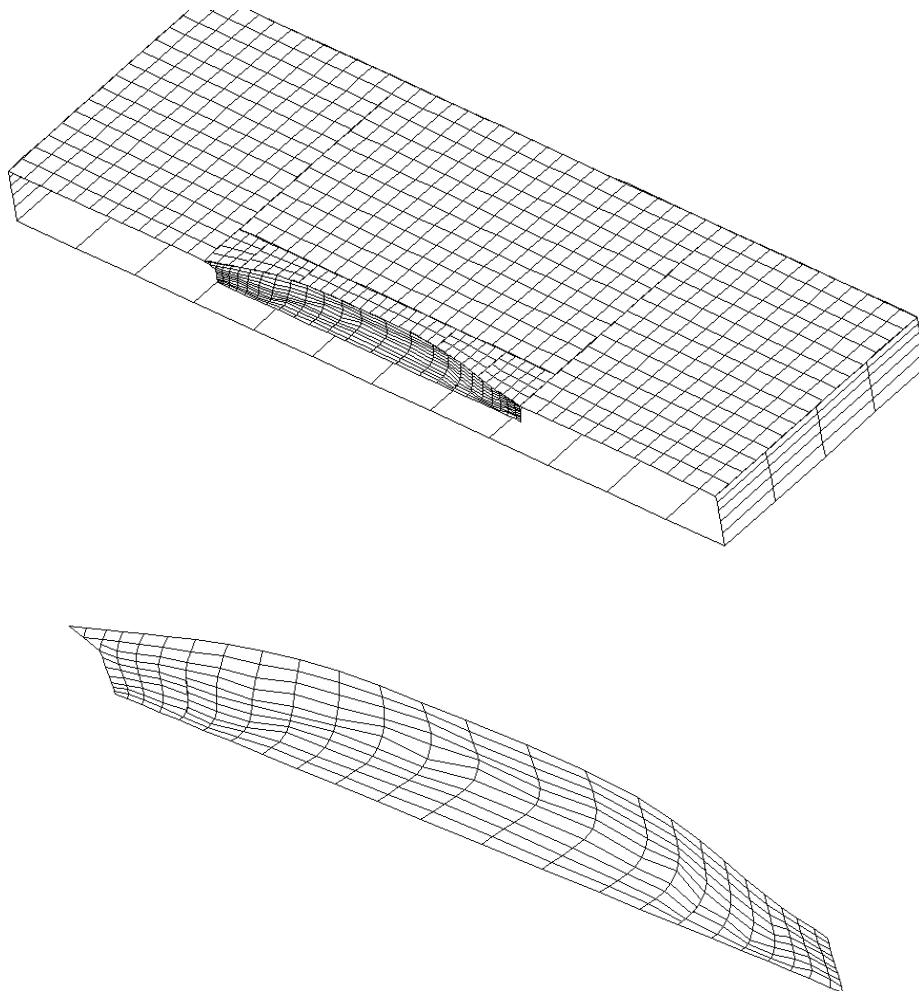


Figure 4.9 Panelization for the Series 60 case, with 1224 panels in total.

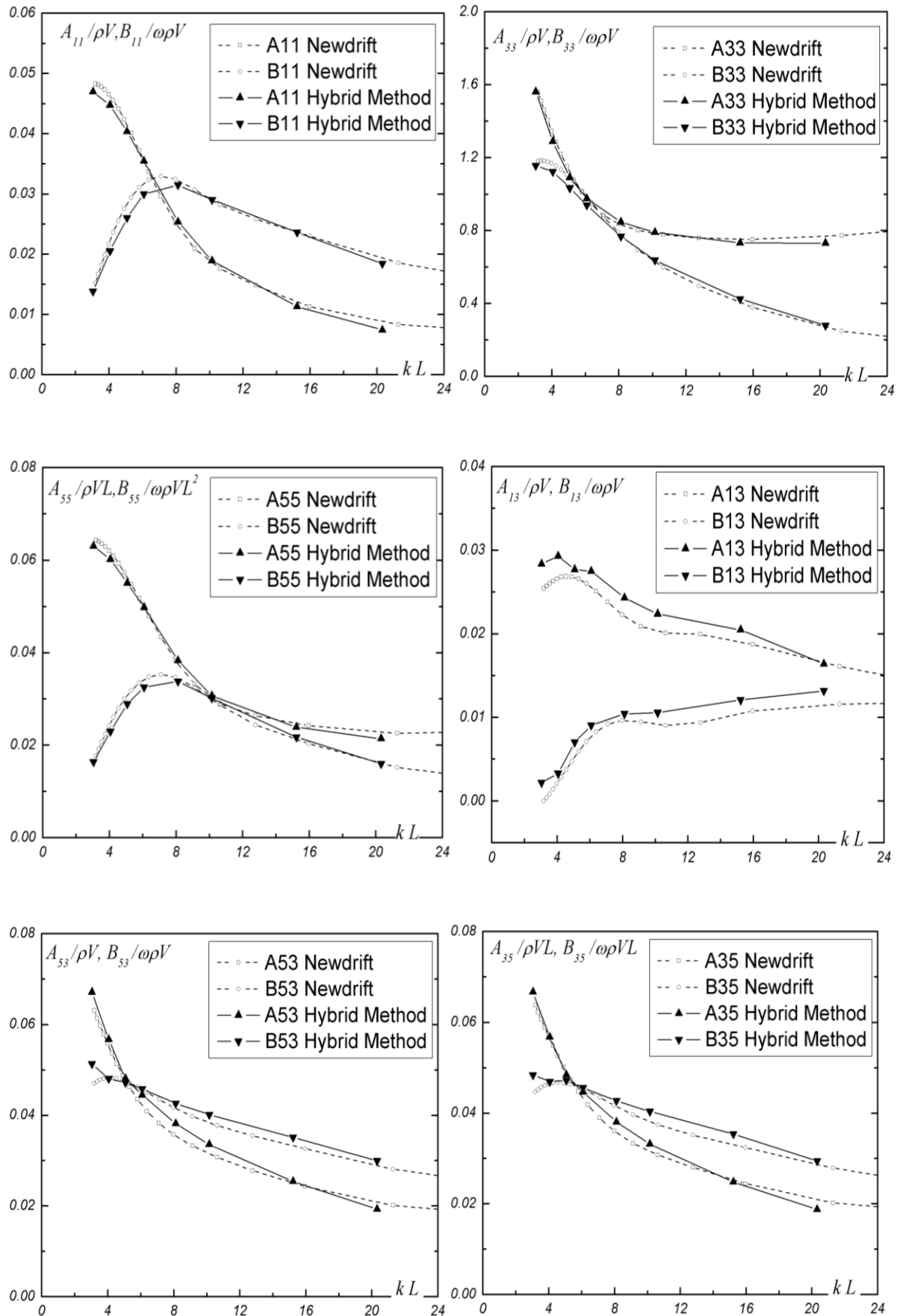


Figure 4.10 Added masses and damping coefficients of Series 60 hull, $C_b = 0.60$, $Fn = 0.0$

4.4.5 Diffraction and Radiation Problems of S175 Ship

Exploiting the experience and knowledge gained from the preparatory studies, reported earlier, the diffraction and forced motion problem of the ITTC benchmark containership S175 (ITTC Seakeeping Committee Report, 1978) in beam seas condition is studied in this section. During the computational analysis of the S175 ship, the width of the free surface area is set about $2B+2\lambda$ (e.g. as shown in Figure 4.11) except for the very short wave range. Obtained results for the added mass and damping coefficients, are shown in Figure 4.12 and for the diffraction moment amplitude in Figure 4.13, plotted against the results of the panel code NEWDRIFT; good agreement between the results is generally observed.

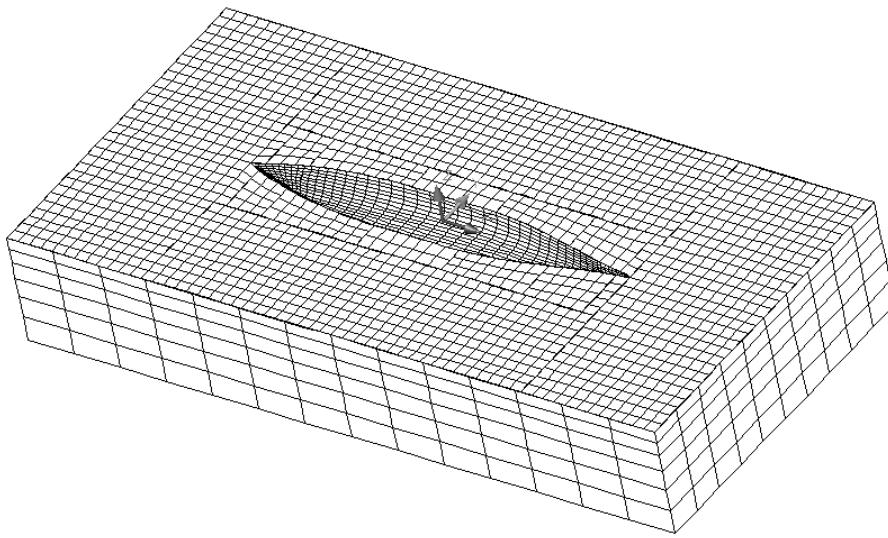
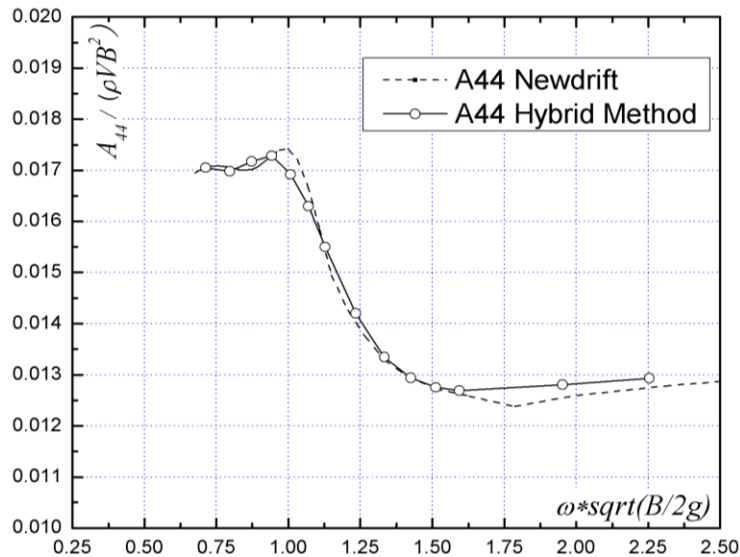


Figure 4.11 Panelization for S175 ship computation; with 3394 panels in total



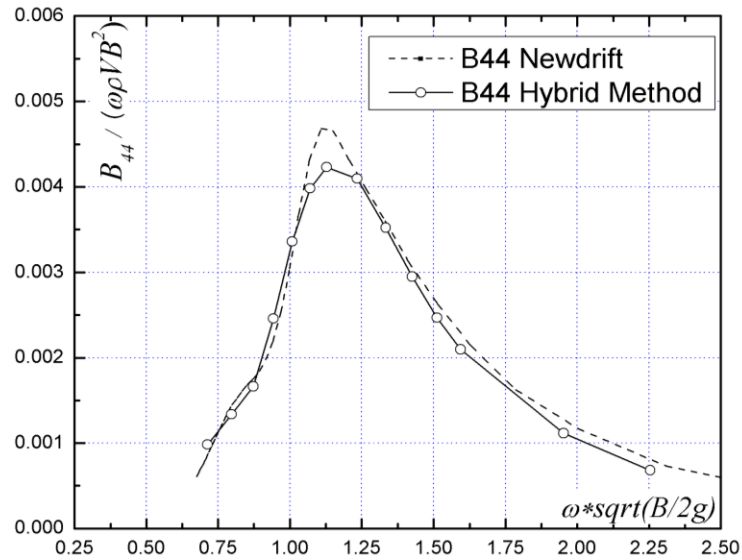


Figure 4.12 Roll added mass and damping coefficient of S175 ship, $F_n=0.0$

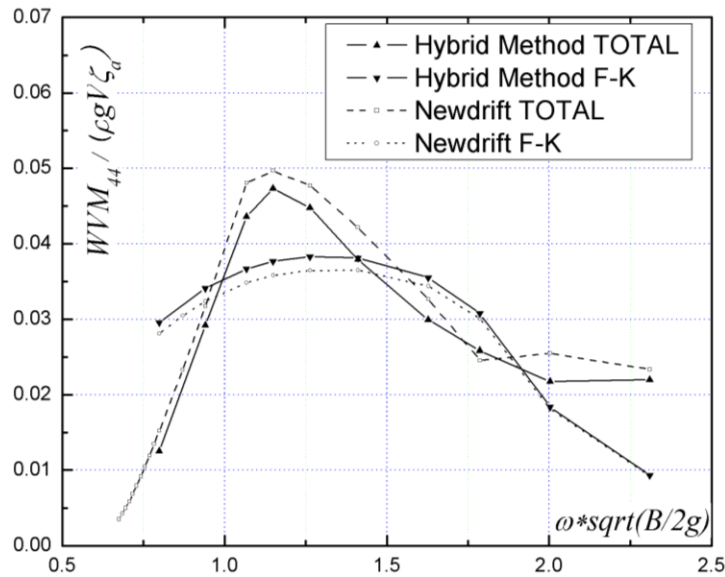


Figure 4.13 Froude-Krylov moment and wave exciting moment of S175 Ship, $F_n=0.0$

4.5 Motion Simulation under Small Amplitude Incident Waves

The waves excited small amplitude ship motions are studied and results thereof are shown in this section. As the wave excited motions are assumed small, hence the hydrodynamic forces are calculated up to ship's mean wetted surface and restoring forces are approximated by ship's geometric parameters.

4.5.1 Wigley Case, Head Seas Condition

The first set of results has been obtained for the two Wigley-hulls investigated by Journée (1992). The two hulls are mathematically defined as: $y/b = [1 - (2x/L)^2][1 - (z/D)^2][1 + 0.2(2x/L)^2]$,

where $2b/L=0.1$ for Wigley-III, $2b/L=0.2$ for Wigley-IV, and $D/L=0.0625$. The hulls' surfaces have been discretized by 256 panels in the port part, while 148 panels are used on the control surface. The free-surface has been discretized according to the incident wave length.

The numerical results of ship motions in head-sea are plotted in the following figures. Figure 4.14 and Figure 4.15 show the nondimensionalized time series of incident wave, heave motion and pitch motion at $\lambda/L=1.0$. Very stable results have been reached after two wave periods. Figure 4.16 and Figure 4.17 show the heave and pitch motion results, including amplitudes and phase angles for both hulls. A good agreement is observed for all the cases among the two numerical methods and most of the available experimental data, except for the pitch motion, for which some unexpected deviation at large wave lengths (quasi-static case) appears.

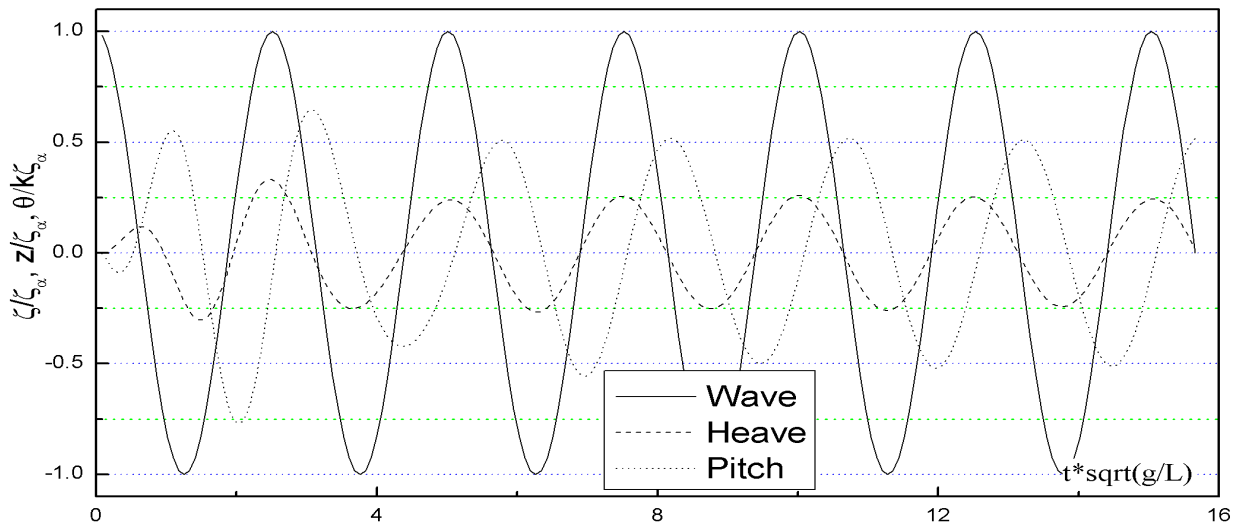


Figure 4.14 Motions' histories of Wigley III at zero speed, $\lambda/L=1.0$

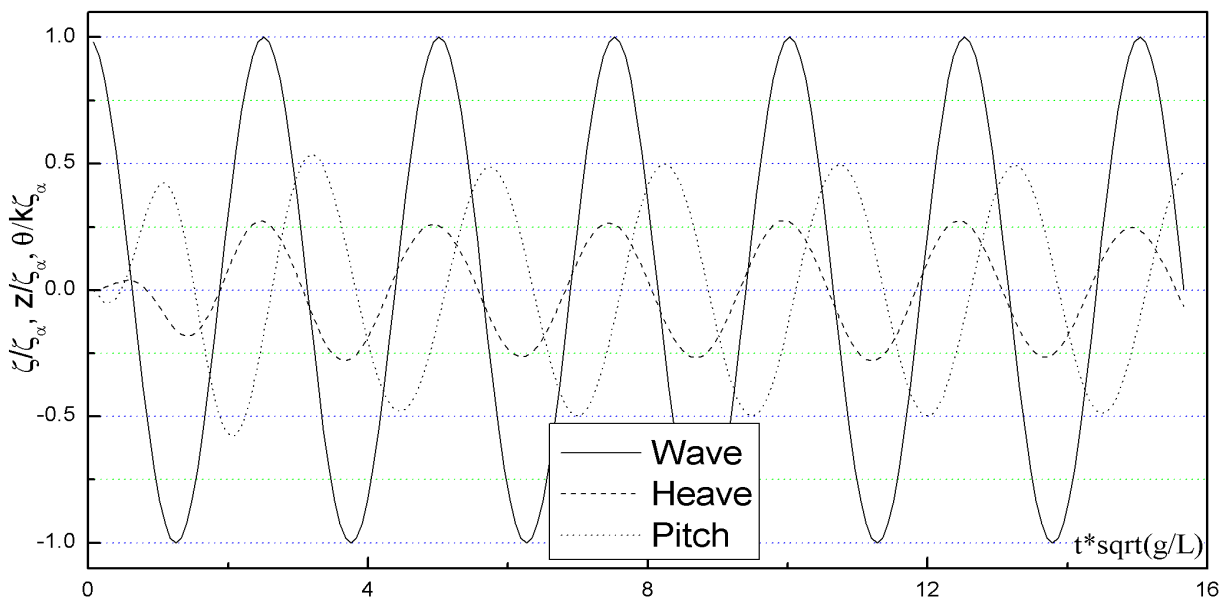


Figure 4.15 Motions' histories of Wigley IV at zero speed, $\lambda/L=1.0$

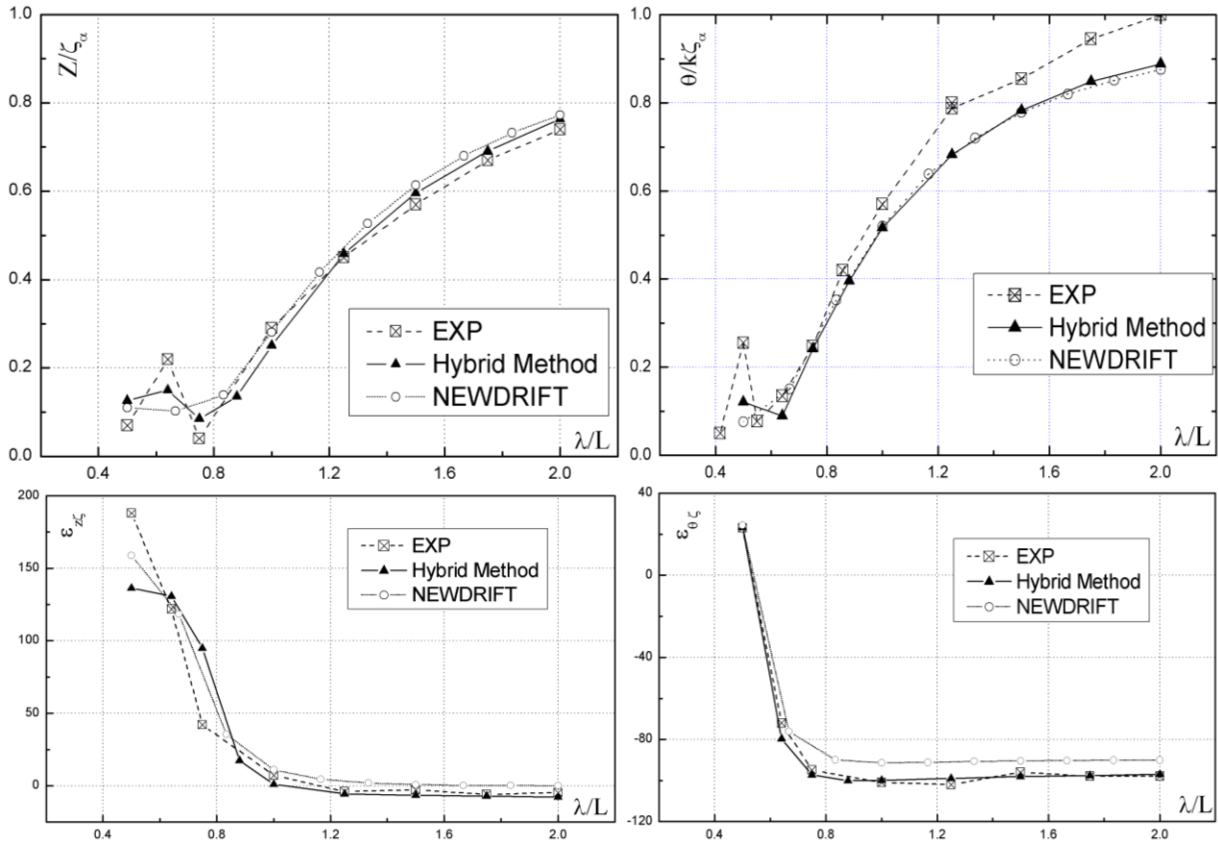


Figure 4.16 Prediction of heave and pitch motions of Wigley III at zero speed

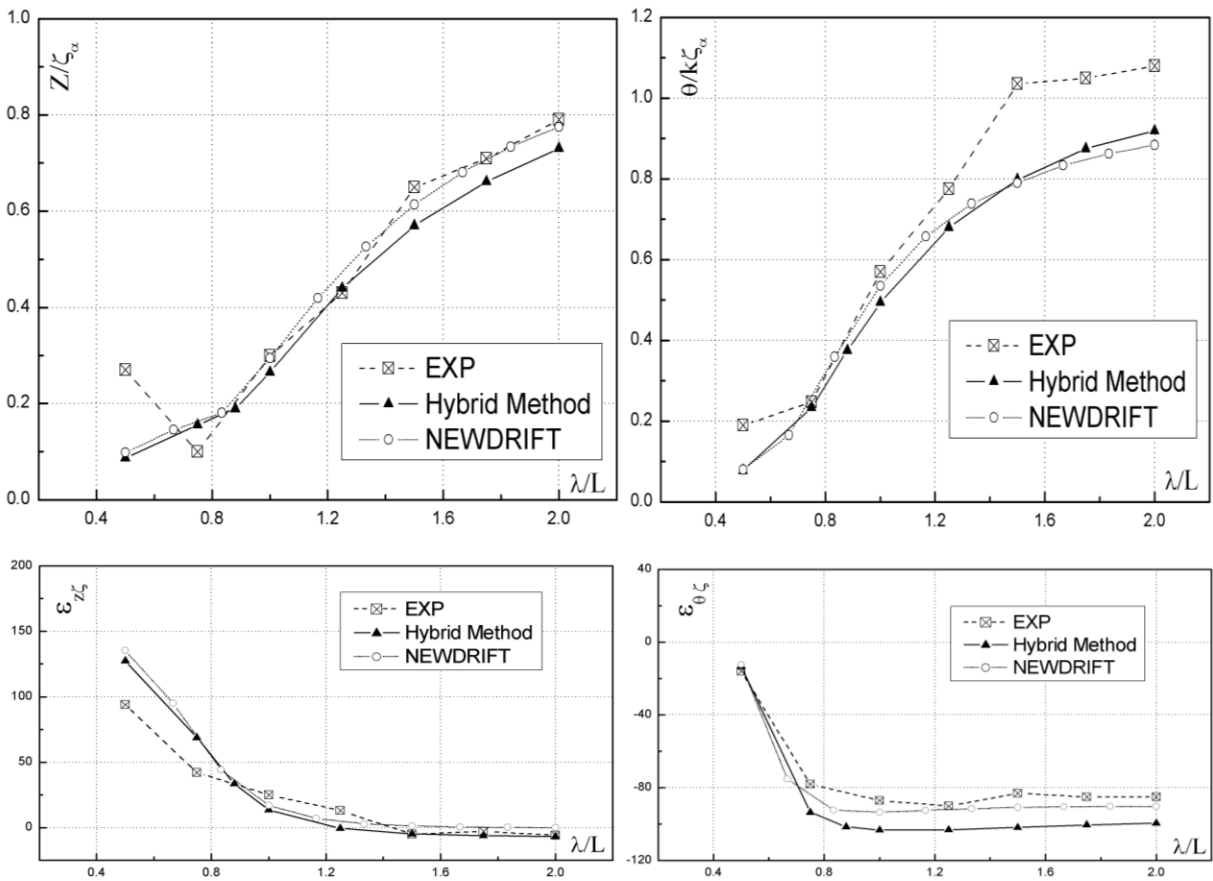


Figure 4.17 Prediction of heave and pitch motions of Wigley IV at zero speed

4.5.2 Series60 Case, Head Seas Condition

The second computational example refers to a Series 60 hull with block coefficient $C_b=0.6$ which has been also studied extensively by many researchers (e.g. Stefun, 1960). The hull's surface has been discretized into 363 panels on the port part, while 148 panels are used on the control surface. The free-surface has been discretized according to the wave length.

The numerical results for the motions in head-seas are plotted. Figure 4.18 shows the heave and pitch results, including amplitudes and phase angles. The plotted experimental data of heave and pitch amplitudes are reproduced from Fig 13&14 of Stefun's paper (1960). The phase angles for heave and pitch are taken from the same source (there from Fig 6 to Fig 12). A generally good agreement among different numerical methods and the experimental data is observed for all the cases, though some shift for the heave and pitch phase angles, which are very sensitive, is noted.

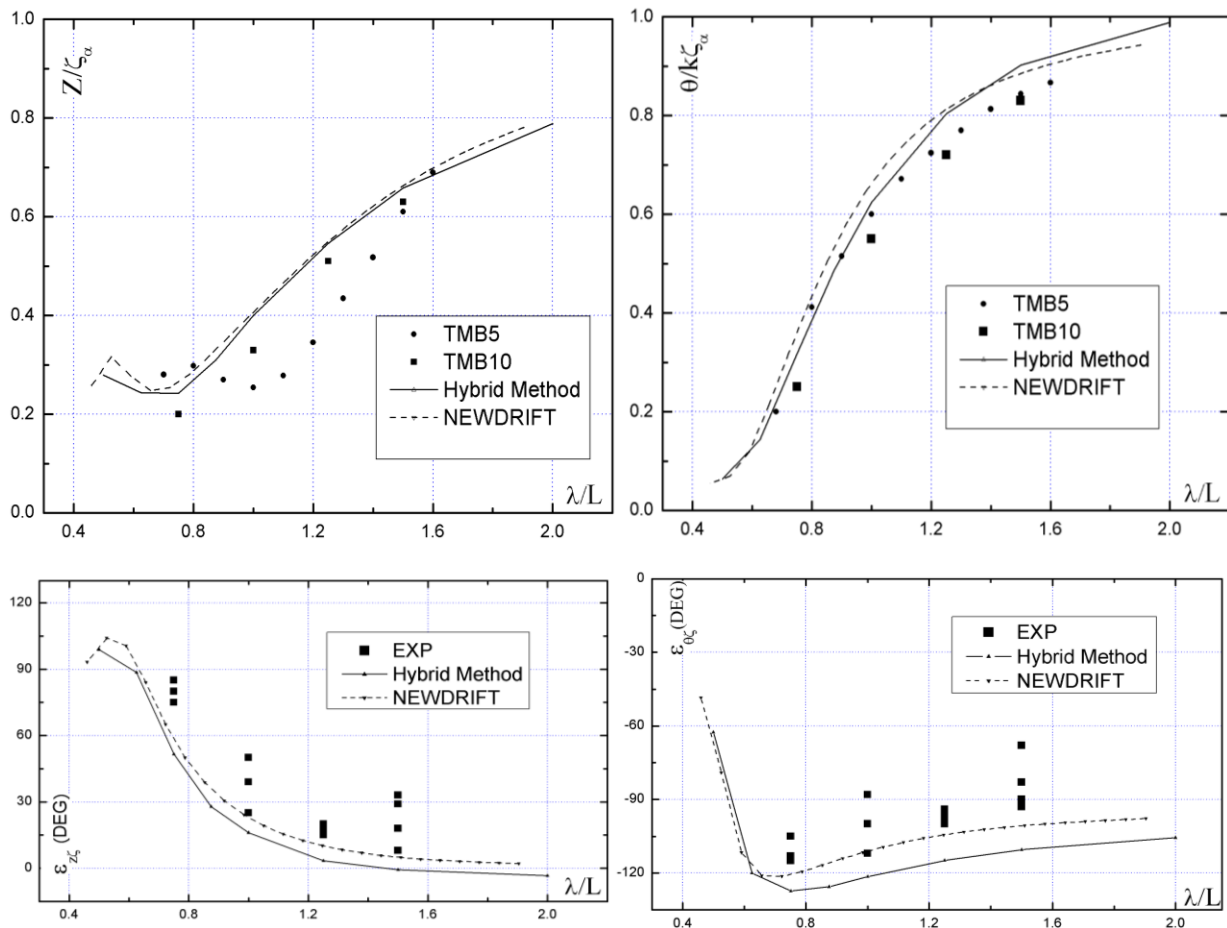


Figure 4.18 Comparison for heave and pitch motions of Series60 at zero speed

4.5.3 Roll Motion of a Barge

The barge, which was studied on diffraction and forced motion problems in the previous section, is chosen for the first application to roll motion simulation. Considering the characteristic

rectangular body type, some viscous damping should be actually introduced in the motion simulation. Lack of this treatment is expected to lead to deviations from experimental data and other numerical results which include viscous damping around the resonance region.

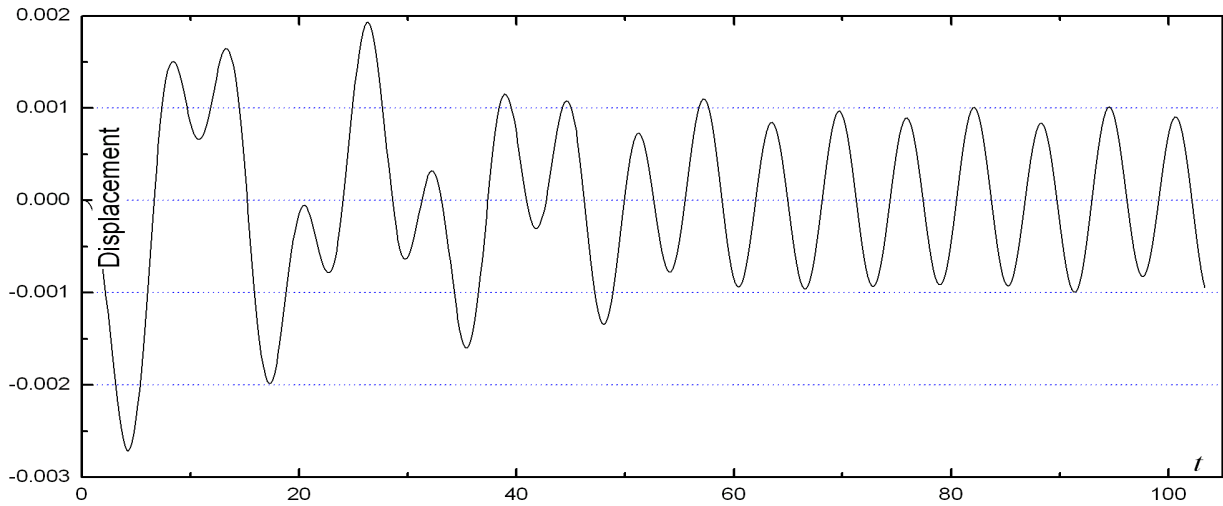


Figure 4.19 Linear motion history of the barge with an incident wave $\lambda=60\text{m}$

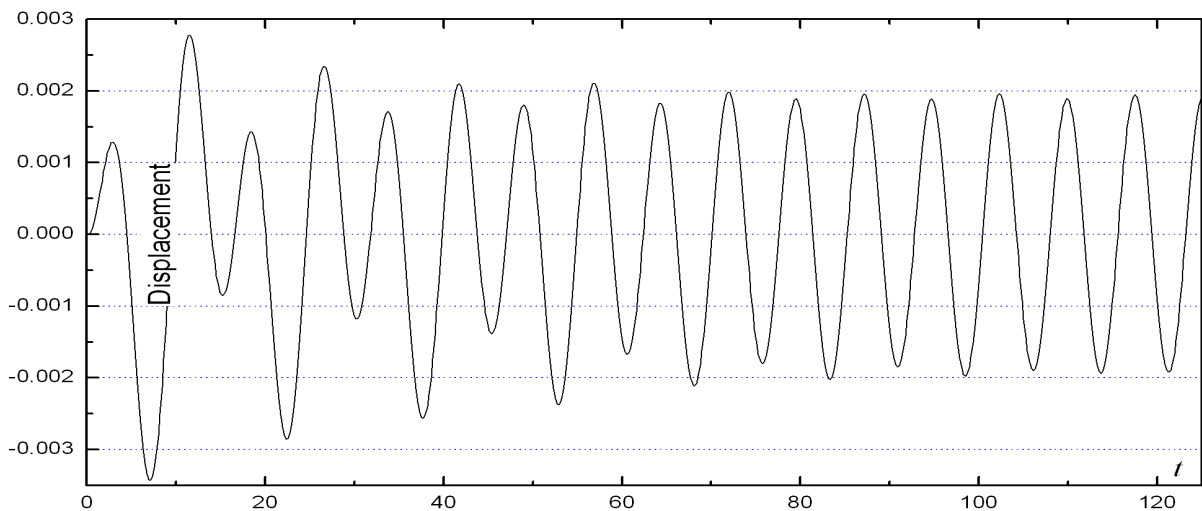


Figure 4.20 Linear motion history of the barge with an incident wave $\lambda=90\text{m}$

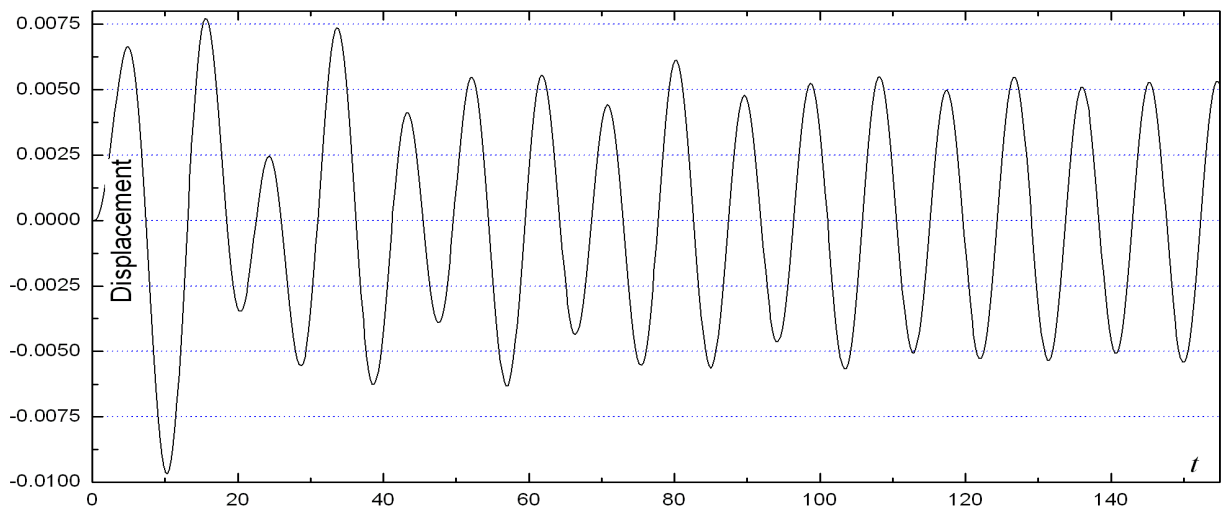


Figure 4.21 Linear motion history of the barge with an incident wave $\lambda=135\text{m}$

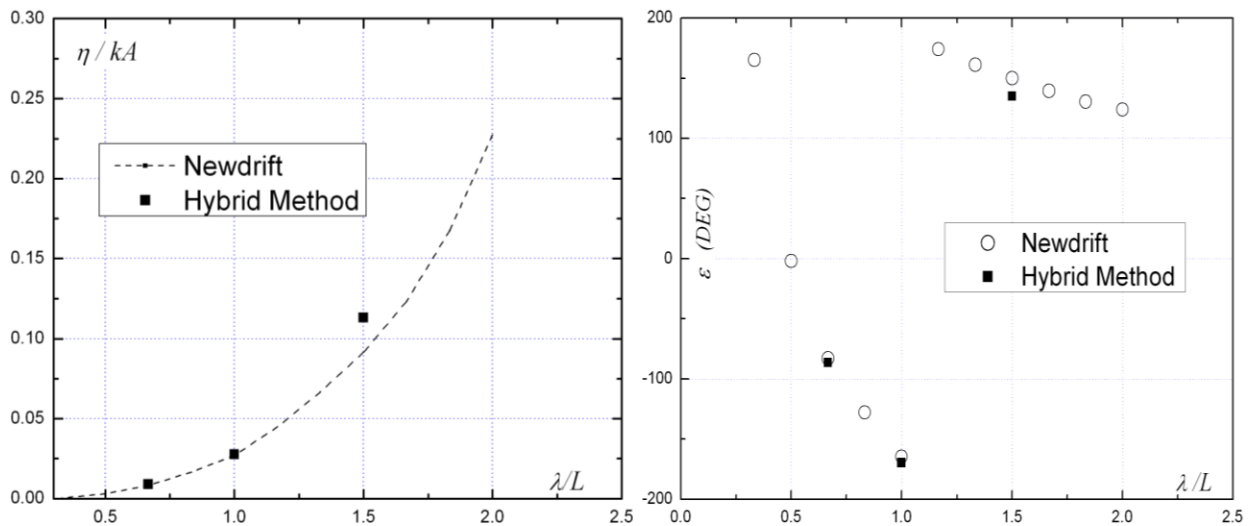


Figure 4.22 Linear motion results from NEWDRIFT and the hybrid method

It is observed that the roll motion of this barge takes much longer time to arrive at a steady state, if we leave the body completely free to respond to the incident wave. However, if we proceed with a preliminary estimation of the velocity amplitude and implement it in the initial conditions (noted as Condition 1 and 2 as following), the oscillation time to reach the steady state is reduced rapidly, as revealed in Figure 4.23. On the other hand, these results show the influence of initial conditions in a time domain simulation. In specific nonlinear problems, e.g. nonlinear roll motion problems, with different initial conditions, the motion may reach a different steady or even unsteady state (Spyrou and Thompson, 2000), at last.

Condition 1: $a(t=0)=\text{predicted value}$; $v(t=0)=0$; $\eta(t=0)=0$;

Condition 2: $a(t=0)=\text{predicted value}$; $v(t=0)=\text{predicted value}$; $\eta(t=0)=0$;

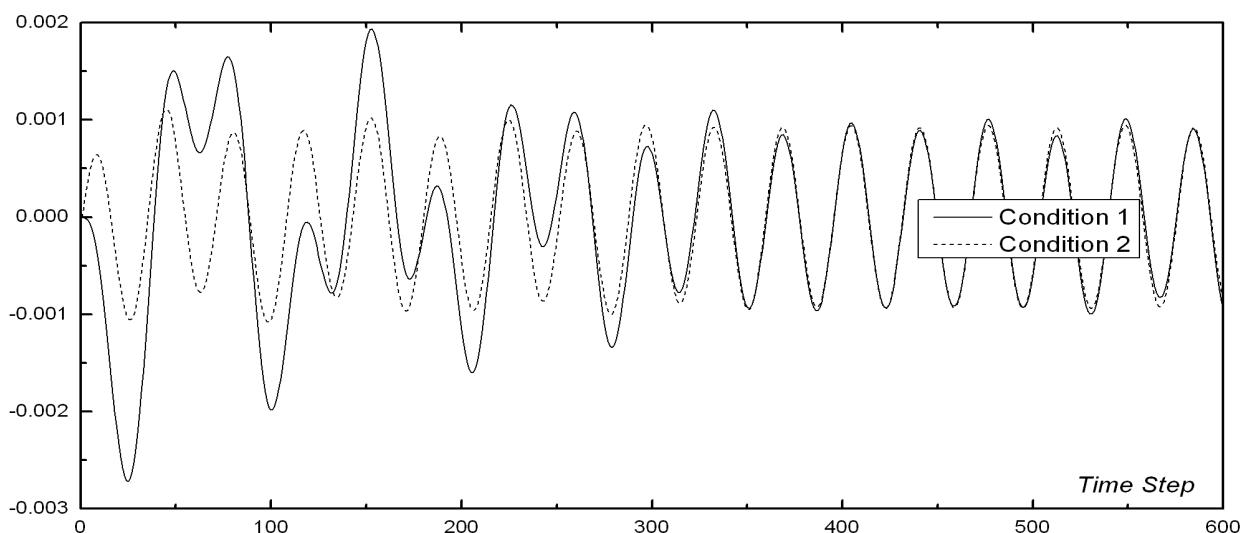


Figure 4.23 Displacement of the barge, small amplitude incident wave, $\lambda=60\text{m}$

4.5.4 S-175 Ship Case

The S-175 container ship, which has been investigated thoroughly by ITTC members in seakeeping benchmark studies since late 70ties (ITTC seakeeping committee, 1978, 1981, 1984), is chosen as another validation case. The ship's hull surface was discretized by 380 panels on the port side, while 148 panels are used on the control surface. For this zero speed case, only the numerical results from the panel code NEWDRIFT were available and have been plotted against the present HYBRID method results. The numerical results for the motions in head-seas are plotted in Figure 4.24. A good agreement is observed throughout the whole computational range, except for some slight deviation when the wave length is long (quasi-hydrostatic case).

For the S175 hull, using proper initial conditions and introducing the viscous damping correction by Ikeda and Himeno's method (1978), the roll motion can be predicted quite satisfactorily. Figure 4.25 and Figure 4.27 show the roll simulation under the excitation of different wave conditions. For the viscous damping correction, an iteration scheme is needed, which is time-consuming. If experimental data are available, this part can be simplified.

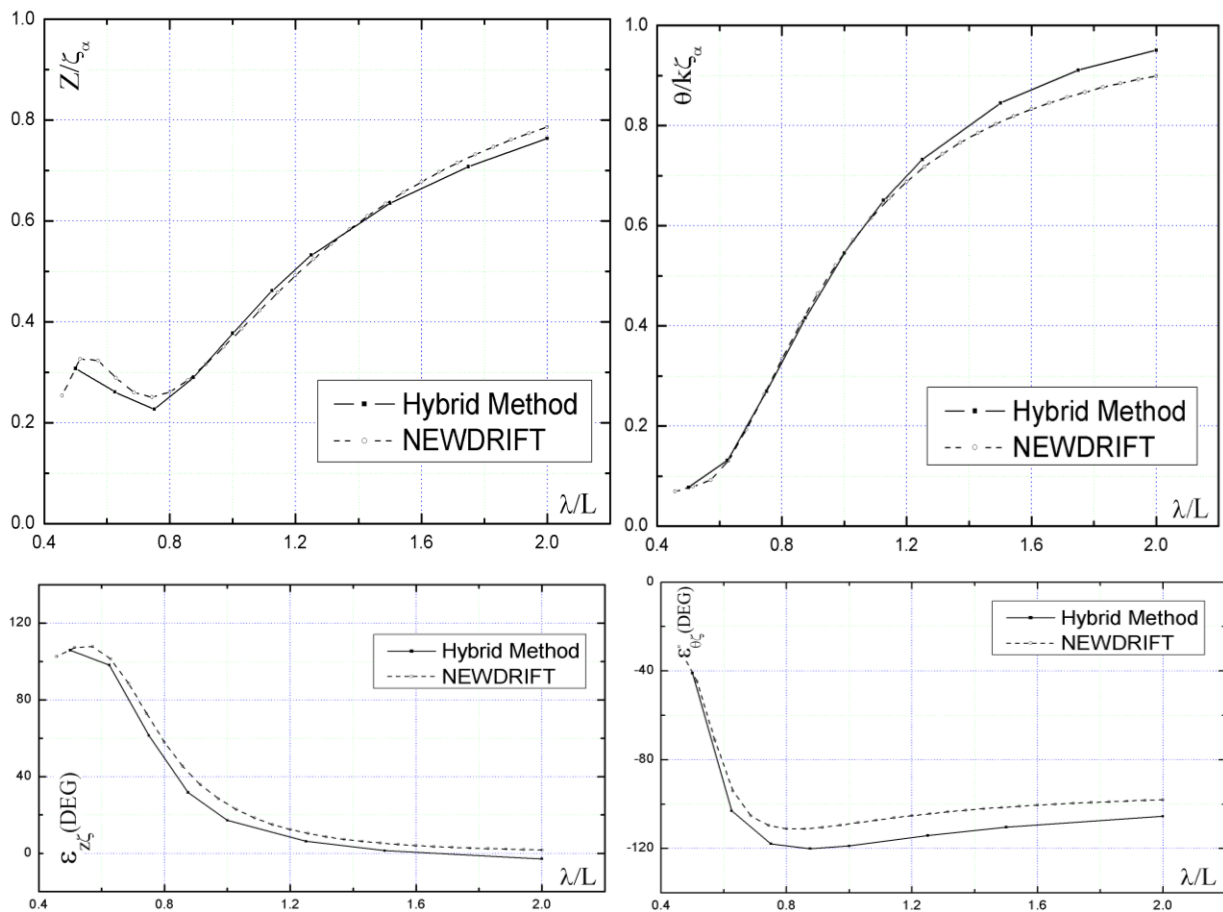


Figure 4.24 Prediction of heave and pitch motions of S175 ship at zero speed

For the case of $\lambda=169\text{m}$, an additional simulation has been carried out, i.e., replace the linear restoring moment with instantaneous restoring moment calculated on the actually wetted surface. Of course, under such a condition, the roll amplitude may become quite large so that the estimated viscous damping coefficient based on Ikeda & Himeno method may substantially deviate from the true value. It is, however, of interest to see how the time varying instantaneous restoring moment performs in a non-harmonic way, as shown in Figure 4.28.

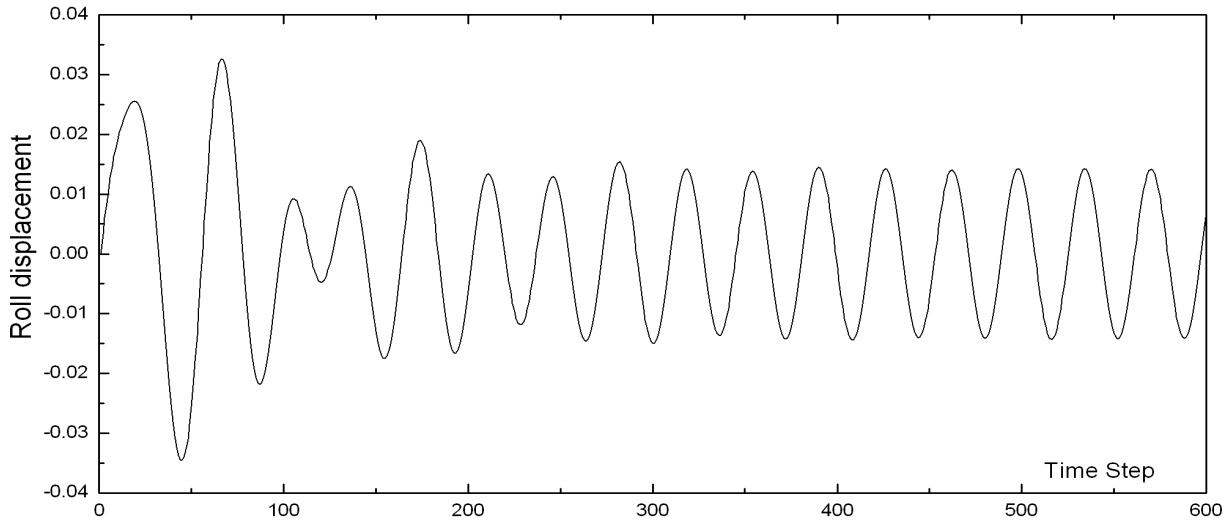


Figure 4.25 Roll displacement of S175 ship with an incident wave $\lambda=120\text{m}$

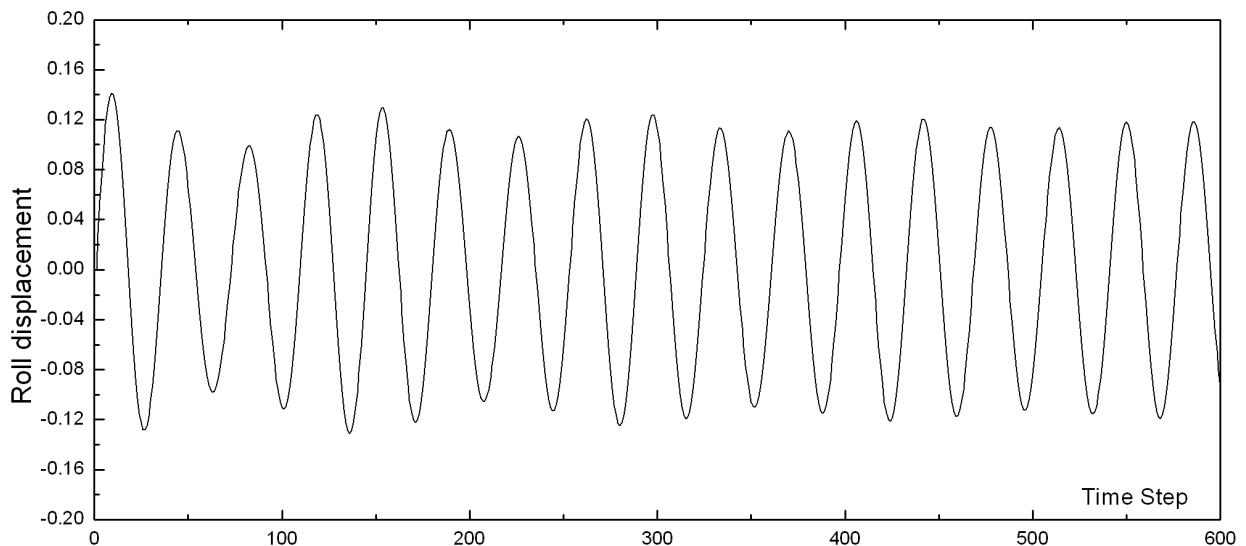


Figure 4.26 Roll displacement of S175 ship with an incident wave $\lambda=400\text{m}$

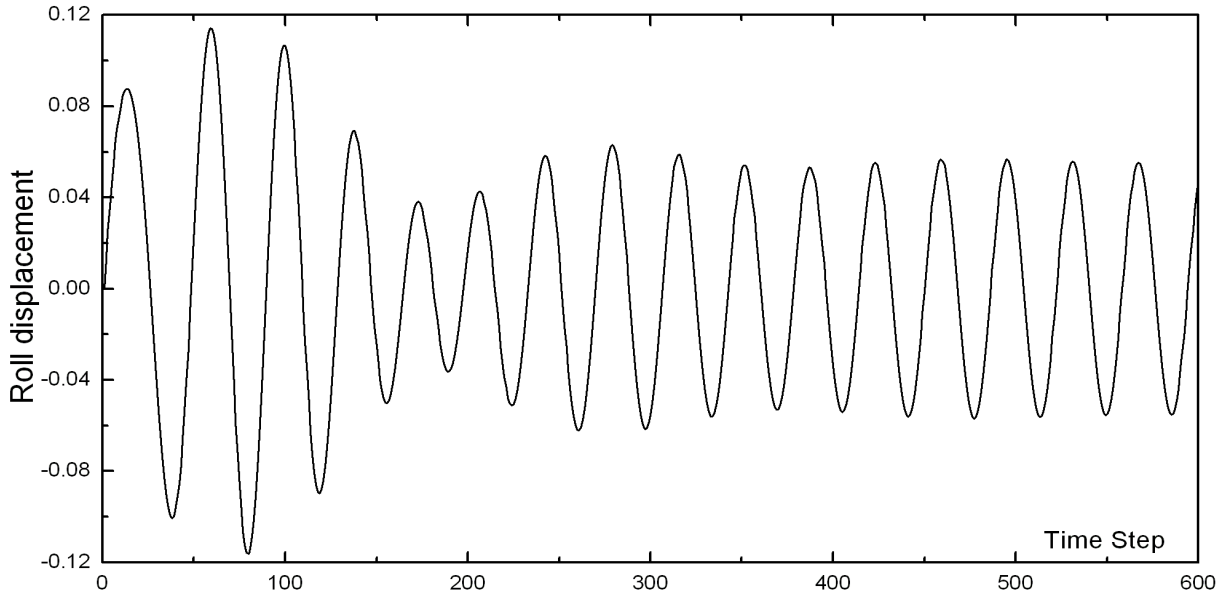


Figure 4.27 Roll displacement of S175 ship with an incident wave $\lambda=169\text{m}$

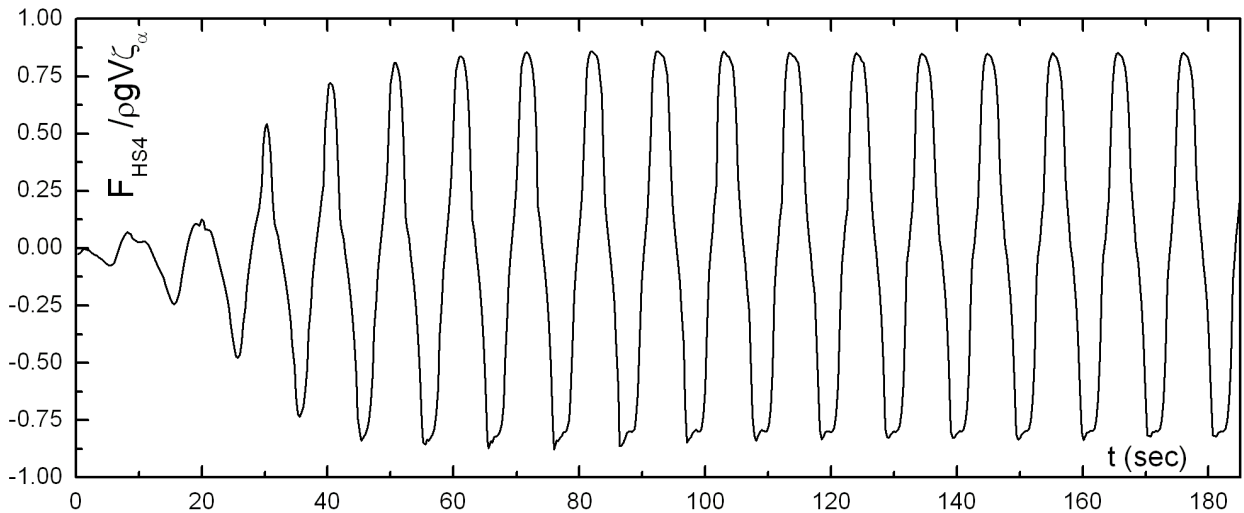


Figure 4.28 Nondimensional time varying restoring moment of S175 ship at beam seas, $\zeta_{\alpha}=0.02\lambda$, $\lambda=169\text{m}$

4.6 Large Amplitude Ship Motion Simulation in Head Seas

The large amplitude ship motions in waves are studied in this section. As the motion amplitude is assumed to be large, the following treatment will be necessary:

- 1) the incident wave forces and restoring forces should be exactly calculated;
- 2) the hydrodynamic forces should be also calculated up to ship's instantaneous wetted surface.

In the present study, we calculate the incident wave forces and restoring forces up to the non-disturbed incident wave profile, not the exact wave profile affected by diffraction and radiation, while the diffraction and radiation problems are calculated up to the mean wetted surface thus we can avoid re-panelization at each time instant. These assumptions are good for fast computation in potential flow framework.

4.6.1 Wigley Hull Case

The Wigley-hull which has been investigated by Journée(1992), is mathematically expressed as $y/b=[1-(2x/L)^2][1-(z/D)^2][1+0.2(2x/L)^2]$, where $2b/L=0.1$ for Wigley-III.

The hull surface was discretized by 256 panels in the port part while 148 panels are used on the control surface. The hydrostatic and Froude Krylov forces due to incident wave at different wave heights are calculated up to undisturbed incident wave profile; 3650 panels are used on half body, whereas 1393 panels are used to represent the *deck* closing the top of the ship above waterline. The deck height is set as $D_m/D=0.1/0.0625$. The panelization is shown in Figure 4.29. This hull surface panelization is independent and used for calculating Froude-Krylov force and hydrostatic force.

Figure 4.30 shows the numerical results of motion amplitudes and phase angles in head seas. It is noticed that for moderate sea state ($A/\lambda=0.008, 0.02$), the large amplitude simulating results are very close to the results based on small amplitude assumptions, which were obtained in previous study presented earlier. But for the high waves case, with $A/\lambda= 0.04$, the large amplitude computational results show a larger amplitude. One point which deserves our special attention is the excellent agreement with experimental data with respect to the phase angle. In the experiment, the nominal wave amplitude is $\zeta_a=0.02m$ for a $3m$ long model.

Figure 4.31 to Figure 4.34 show the nondimensionalized histories of heave and pitch motions for $\lambda/L=1.0&1.5$ under different wave excitation, namely, Froude-Krylov linear, Froude-Krylov exact with $A/\lambda=0.008, 0.02$ and 0.04 respectively. It is observed from these time histories that, as the wave amplitude increases, the nonlinearity becomes stronger, that means flatter wave trough and sharper wave crest.

During the simulation, it is observed that for long waves, the motion results become unstable and the simulation crashes after several wave periods. A similar phenomenon was noticed for shorter wave cases after longer time simulation. A deeper study showed that the fixed control surface is responsible for this error. As the wave length increases, the control surface should be placed deeper, say at least 0.5λ . Figure 4.35 shows a long time simulation for $\lambda/L=1.0$ case with the new setting. A stable performance is observed. But when simulating $\lambda/L=1.5$ case, it is observed that the computation becomes unstable after 30 wave periods (not shown here). Although the simulation eventually also crashed, a great improvement was observed. It is believed that if we increase the depth of the control surface, we will have better results for the state of longer waves.

The impulsive motion phenomenon of slamming, are not considered in the present simulation; however, the likely flooding of ship's deck is considered by forming the upper boundary of ship's hull; the resulting downward force and related moment are calculated by integrating the Bernoulli pressure. The instantaneous wetted surface used for the hydrostatic and Froude-Krylov force computations are shown in Figure 4.36 to Figure 4.39, noting that the motion data, or the actual ship position, is not revealed.

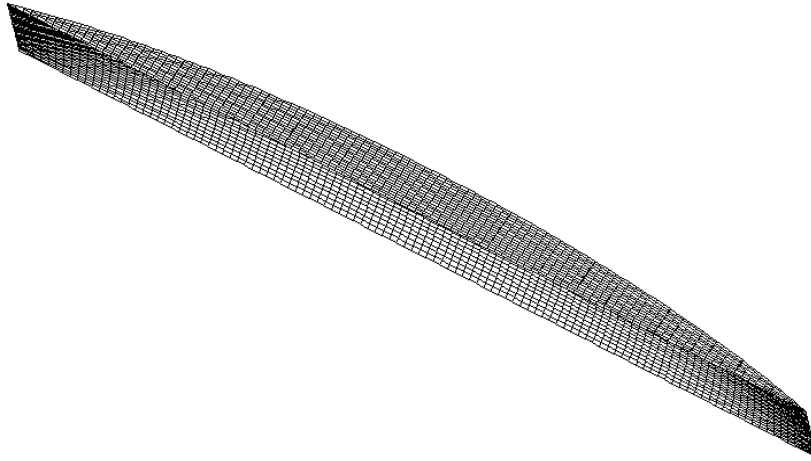


Figure 4.29 Panelization for Froude-Krylov force computation

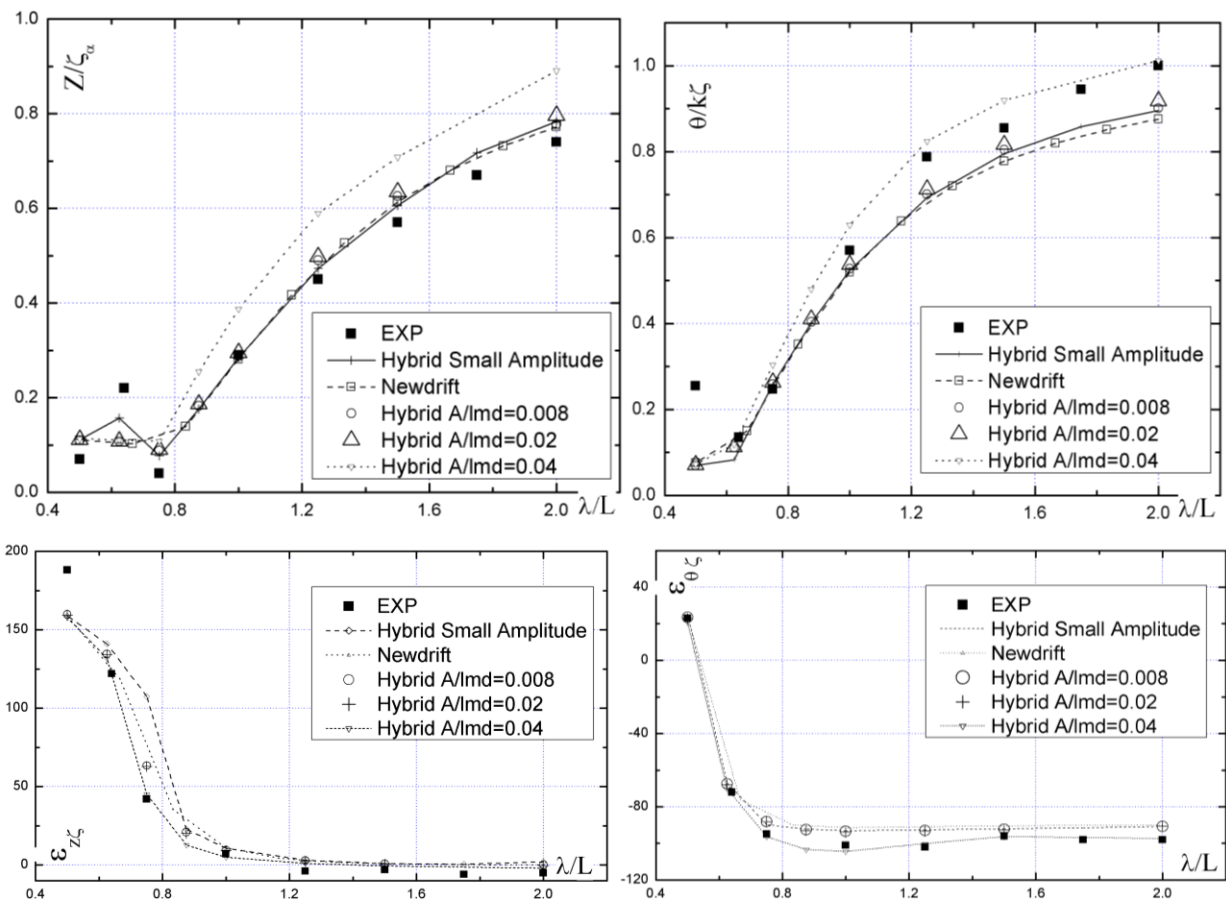


Figure 4.30 Results on heave and pitch motions of Wigley-III, $F_n=0.0$

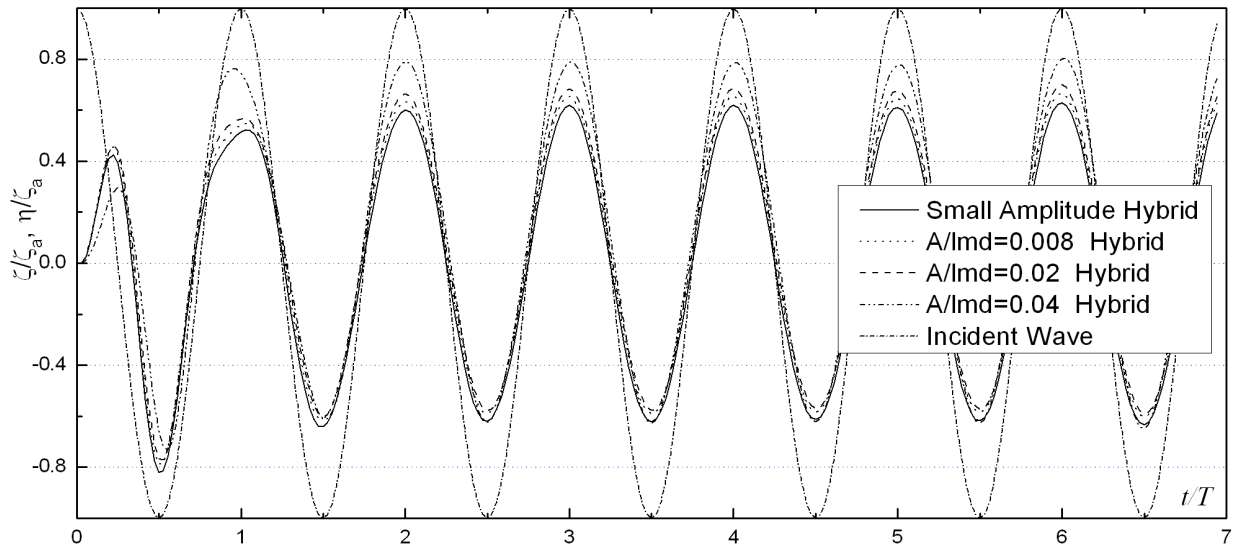


Figure 4.31 Nondimensionalized heave motion at $\lambda/L=1.5$ at different wave amplitudes

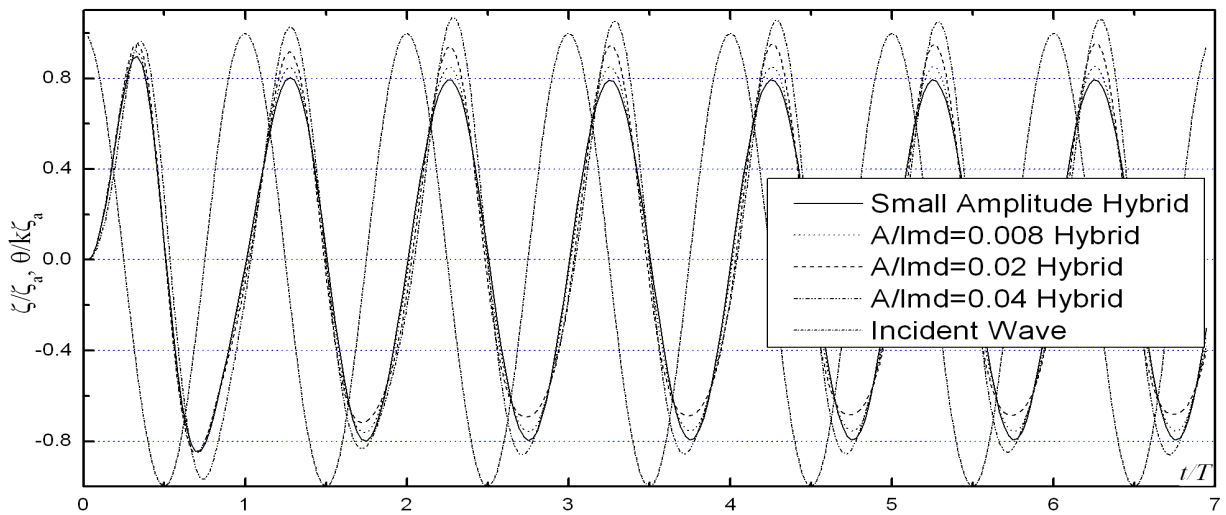


Figure 4.32 Nondimensionalized pitch motion at $\lambda/L=1.5$ at different wave amplitudes

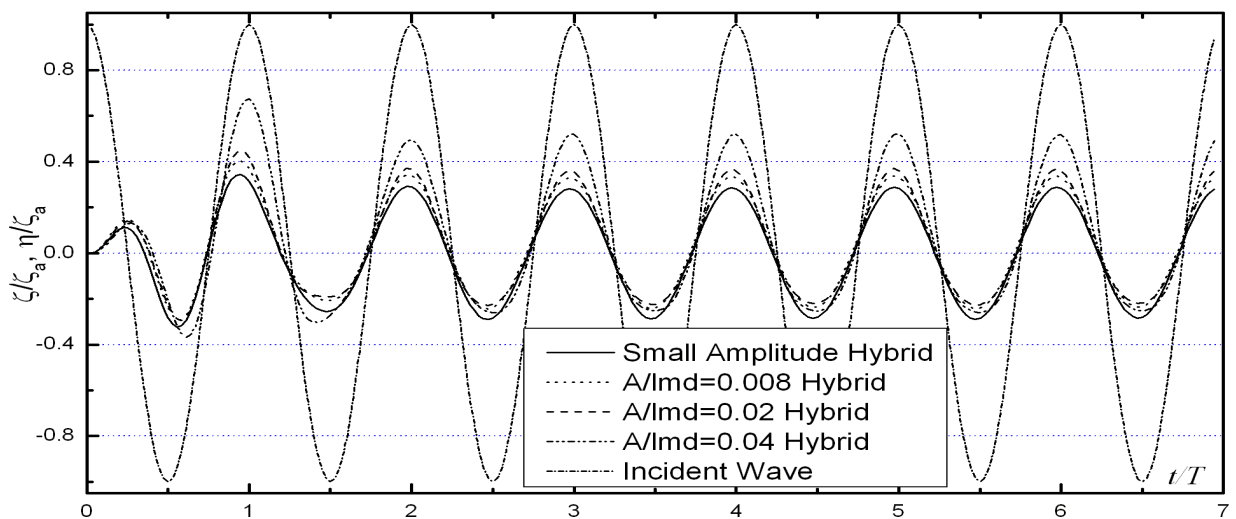


Figure 4.33 Nondimensionalized heave motion, $\lambda/L=1.0$, with different computation setting

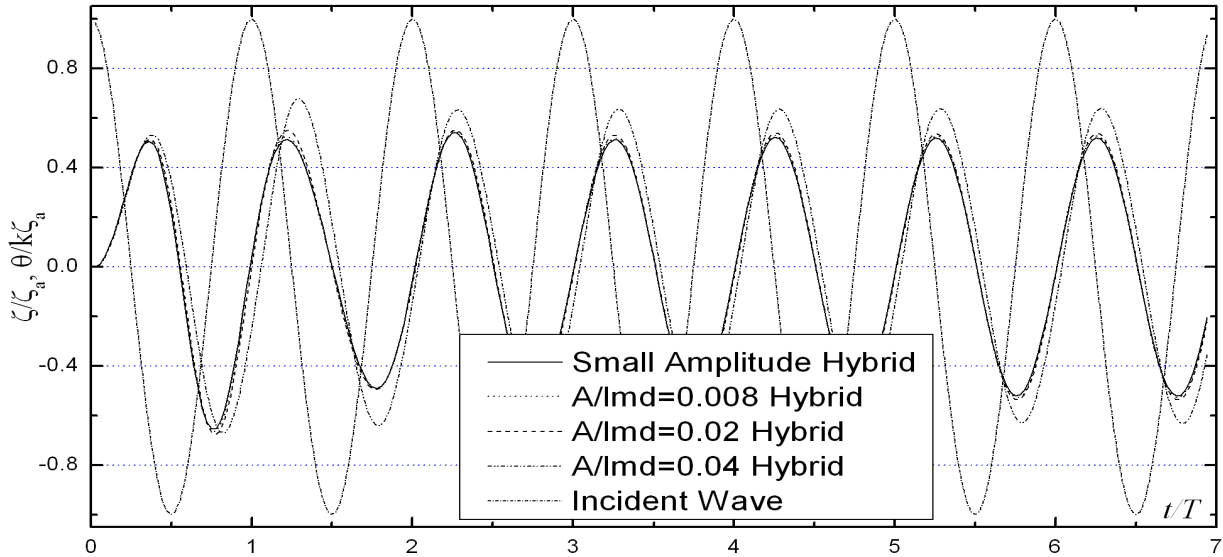


Figure 4.34 Nondimensionalized pitch motion, $\lambda/L=1.0$. with different computation setting

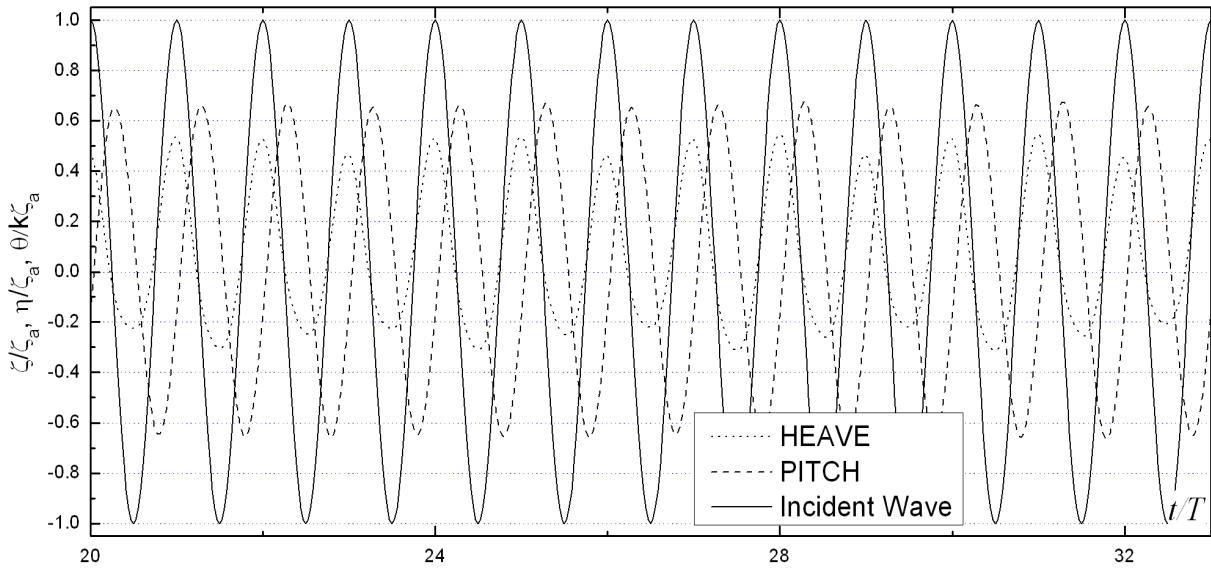


Figure 4.35 Nondimensionalized nonlinear heave and pitch motion, $\lambda/L=1.0, H/\lambda=0.04$

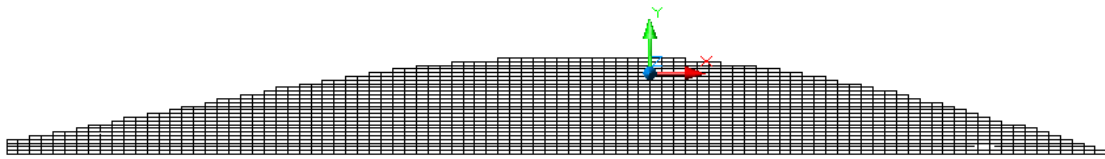


Figure 4.36 Wetted surface at $t/T=6$ for Froude-Krylov force calculation ($\lambda/L=1.5, H/\lambda=0.04$)

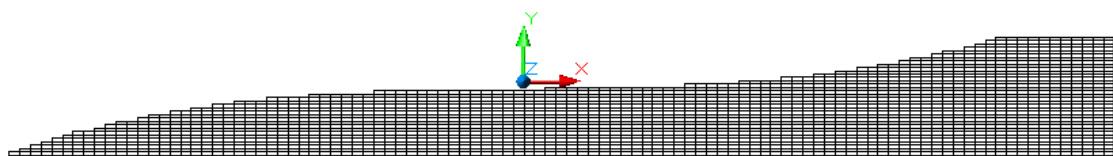


Figure 4.37 Wetted surface at $t/T=6.25$ for Froude-Krylov force calculation ($\lambda/L=1.5, H/\lambda=0.04$)

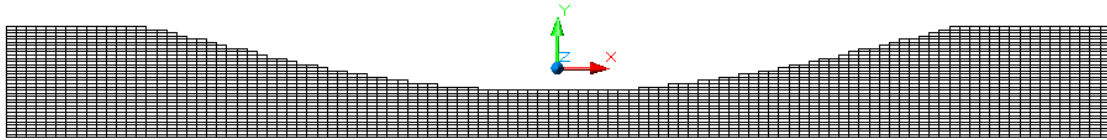


Figure 4.38 Wetted surface at $t/T=6.5$ for Froude-Krylov force calculation ($\lambda/L=1.5$, $H/\lambda=0.04$)

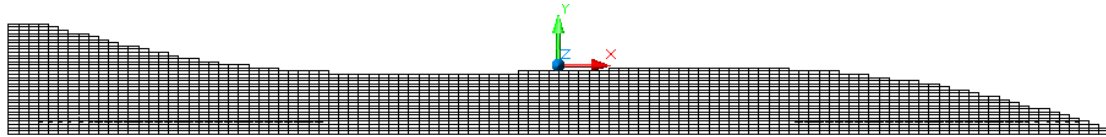


Figure 4.39 Wetted surface at $t/T=6.75$ for Froude-Krylov force calculation ($\lambda/L=1.5$, $H/\lambda=0.04$)

4.6.2 Series60 ($C_b=0.6$) Case

The large amplitude ship motion model has been applied to the Series 60 hull with block coefficient $C_b=0.6$. For comparison purposes, the same panelization as for the small amplitude motion simulation is used. The numerical results for the motions in head-seas, including amplitude and phase angle against the incident wave, are plotted in Figure 4.40. The plotted experimental data of heave and pitch amplitudes are reproduced from Fig 13&14 of Stefun's paper (1960). The phase angles for heave and pitch are taken from the same source (there from Fig6 to Fig 12). A good agreement among different numerical methods and the experimental data is observed for all the cases. What is more important, the agreement between experimental data and large amplitude computation is better than the agreement between experimental data and small amplitude computation. Figure 4.41 shows the nondimensionalized histories of incident wave, heave motion and pitch motion at $\lambda/L=1.0$. It is seen that for the zero speed case, heave and pitch motions arrive at a steady state after about 3 wave periods of excitement.

An interesting phenomenon was observed for the short wave range computation, as shown in Figure 4.42. It appears that the nonlinear pitch motion is around another position which is different from the upright position. It is confirmed by further analysis that at upright position, the trim moment due to hydrostatic pressure is non zero, but takes a quantity which will induce about 0.9° trim. This should be the actual mean position about which the pitch motion takes place. The trim is estimated by $\alpha=M_2/\rho g A_2^w$ (Assuming GM_L about equal BM_L). Here α is the trim angle, M_2 is the pitch moment. A_2^w is the corresponding moment of inertia about y -axis.

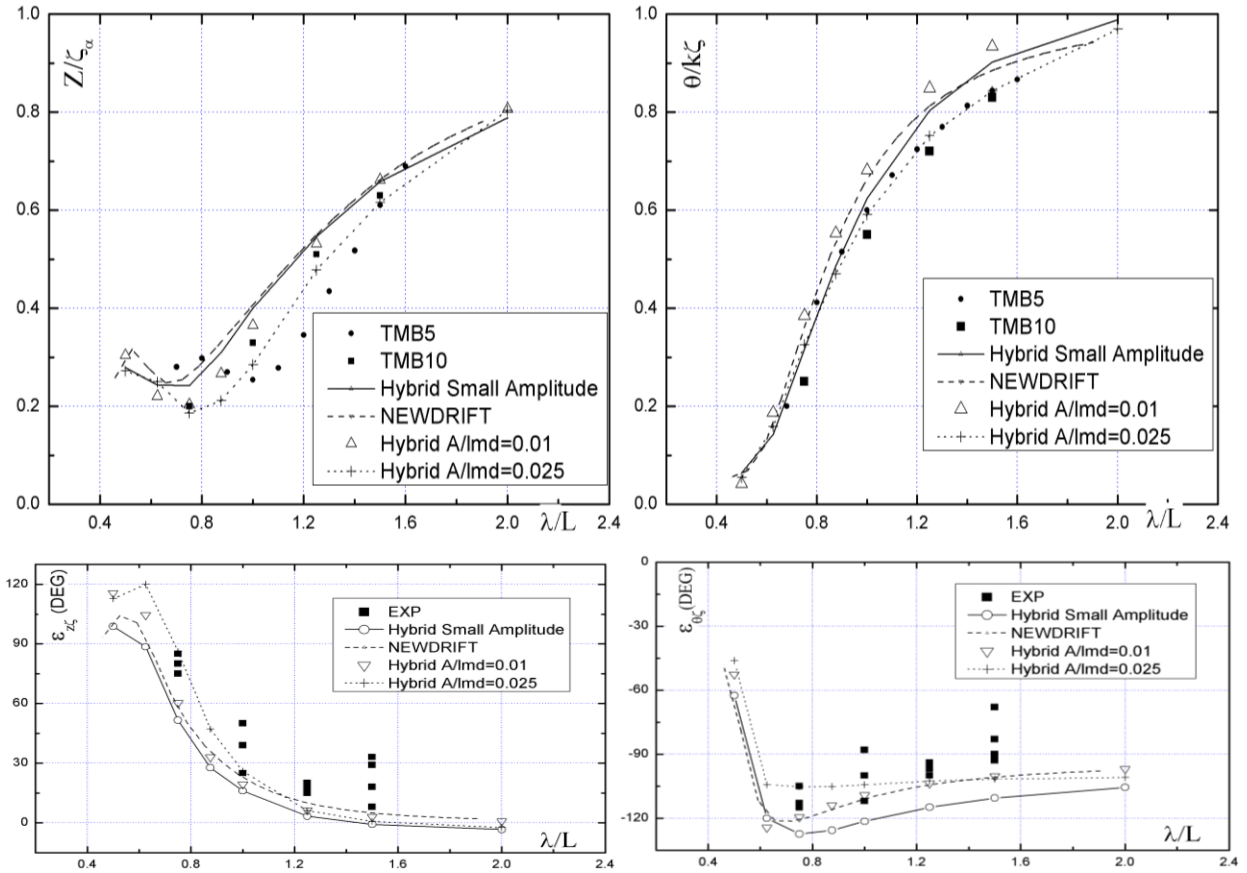


Figure 4.40 Results of Series60 heave and pitch motions at zero speed

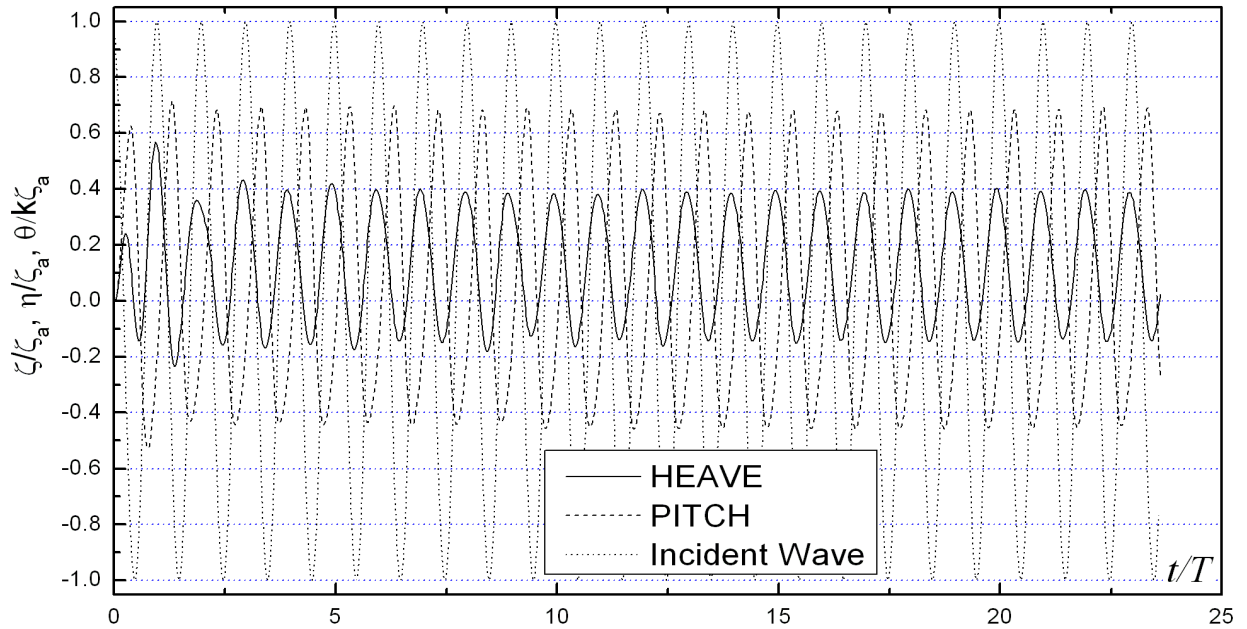


Figure 4.41 Nondimensionalized nonlinear heave and pitch motion at $\lambda/L=1.0$ with $H/\lambda=0.04$ by setting the bottom of control surface at $d/\lambda=0.9$

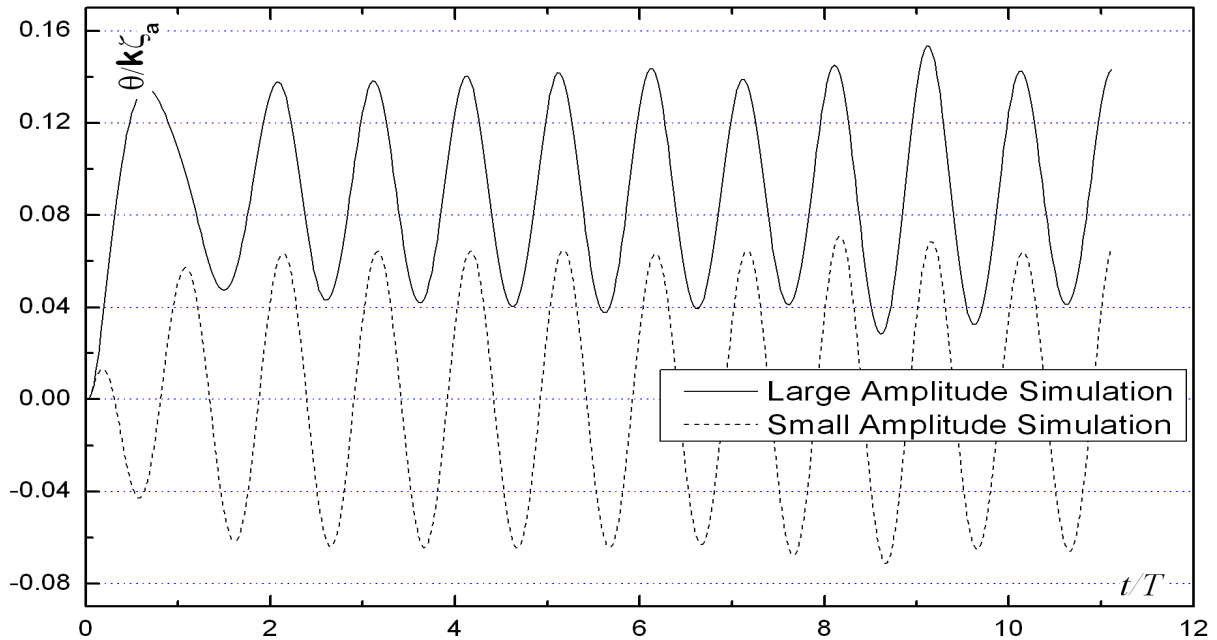


Figure 4.42 Series60 pitch motion in a wave $\lambda/L=0.5$, small amplitude and large amplitude with $A/\lambda=0.01$

4.6.3 S175 Ship Case

The S-175 container ship has been investigated in various benchmark studies by ITTC members since the late 70ties and until today it is still a very good model for validation purpose due to the richness of relevant data. The herein plotted numerical results include those from NEWDRIFT, HYBRID method linear simulation and HYBRID method large amplitude simulation. The numerical results for the motions in head-seas are plotted in Figure 4.43. Besides the good agreement between NEWDRIFT and the small amplitude HYBRID simulation, the results from large amplitude simulation show a significant decrease on motion amplitude response operator where the wave length is about the same as the ship length, especially for the heave. Unfortunately, for this zero speed case, we did not find experimental data for comparison.

Figure 4.44 shows the nondimensionalized histories of heave motion and pitch motion at $\lambda/L=1.25$, compared to the Hybrid method linear simulation results. It is observed that the nonlinear simulations' character is quite different from the linear simulations'. For this case, which corresponds to 250 steps in the code, for the linear simulation it took about 15 minutes on a regular PC hardware with Intel Core 2 QUAD CPU(Q8200 2.33GHz); the following 250 steps of nonlinear simulation, with the diffraction problem pre-solved, took about 14 minutes CPU time. This time record refers to the motion subroutine only, thus not including the entire calculation effort.

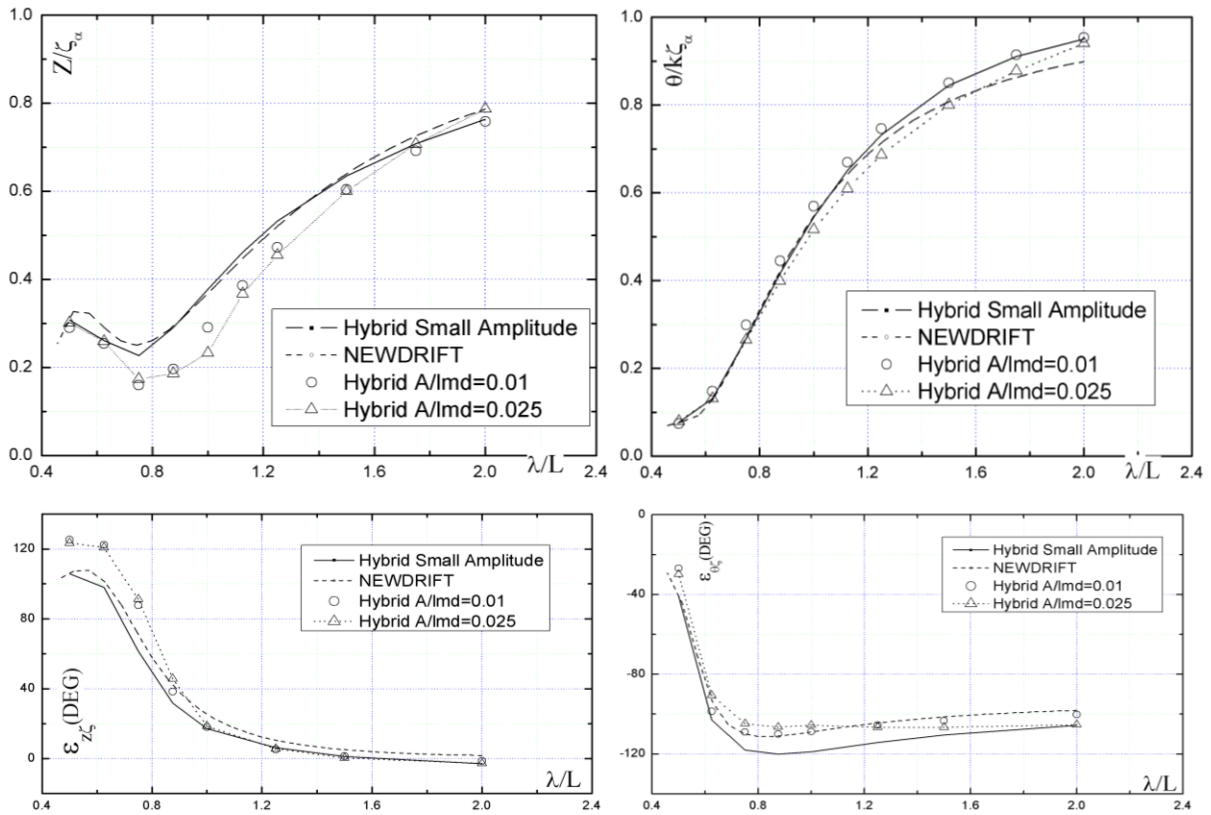


Figure 4.43 Comparison for heave and pitch motions of S175, $F_n=0.0$

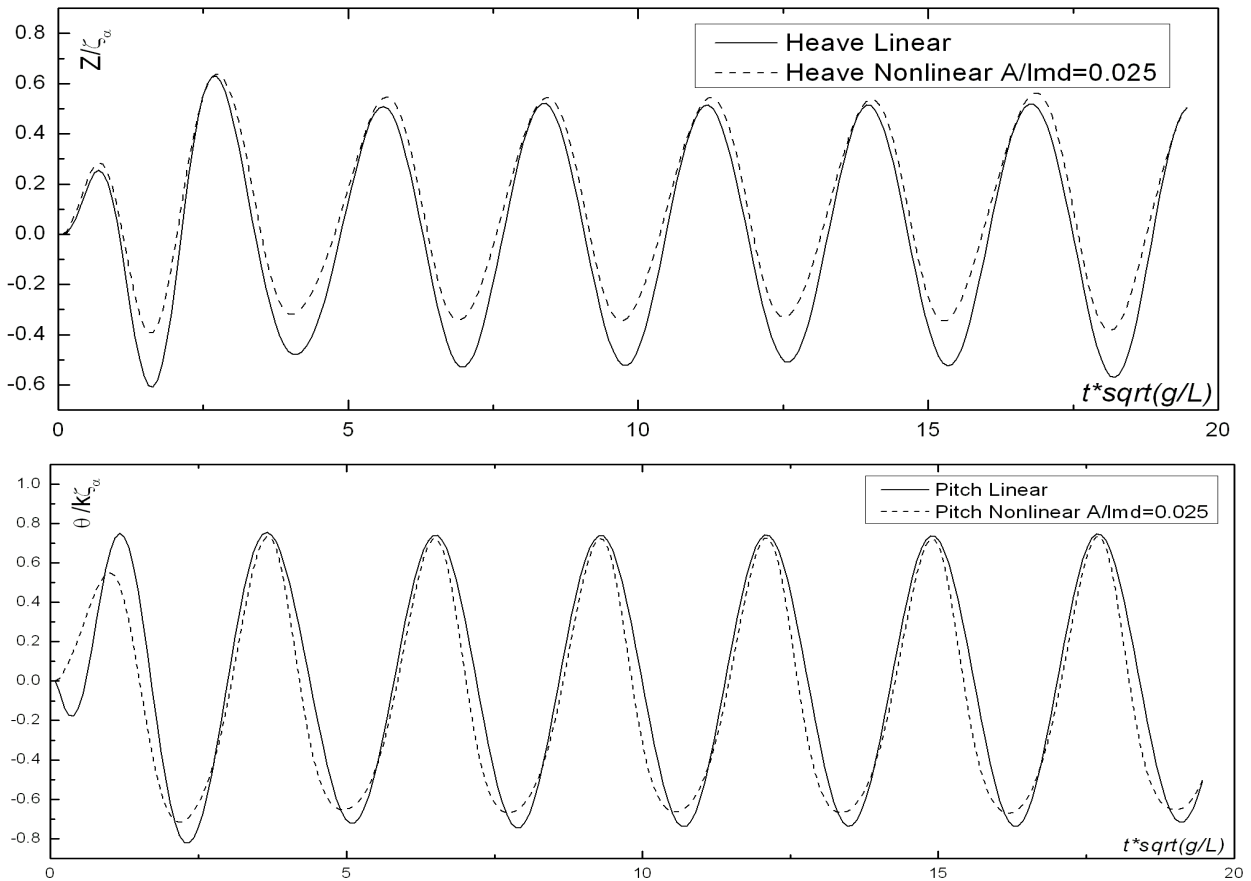


Figure 4.44 Nondimensionalized nonlinear heave and pitch motion at $\lambda/L=1.25$, head seas, $F_n=0.0$

4.6.4 Modified Wigley Hull Case

As shown in the previous studies, at different incident wave states, though the hydrodynamic forces are still taken into account up to the mean wetted surface, due to the fact that the Froude-Krylov and hydrostatic force computation include the effect of the actually wetted body surface, the predicted motions agree better with the experimental data than results based on small amplitude motion assumption. In other words, the large amplitude model is able to deal with the effect of the actual wetted-surface, though not entirely exactly. This capability allows us anyway to draw important conclusions about the effect of the above water hull shape, which is interesting both from the design and ship's operation point of view.

In this section, we apply the motion models to a *Modified Wigley III*, which has the same underwater geometry as the Wigley-III hull, but a *flared above-water hull shape*, as shown in Figure 4.45. The definition of the above water hull is as following:

$$\begin{aligned}
 x &= x_0(1+z) \quad (\text{for } z \geq 0) \\
 y &= \begin{cases} b \left(1 - \left(\frac{2x_0}{L} \right)^2 \right) \left(1 - \left(\frac{z}{D} \right)^2 \right) \left(1 + 0.2 * \left(\frac{2x_0}{L} \right)^2 \right) \left(1 + \left(\frac{2x_0}{L} \frac{z}{D_0 - D} \right)^2 \right) & z < 0 \\ b \left(1 - \left(\frac{2x_0}{L} \right)^2 \right) \left(1 + 0.2 * \left(\frac{2x_0}{L} \right)^2 \right) & z \geq 0 \end{cases}
 \end{aligned}$$

Heave and pitch motions' results are shown in Figure 4.46. From this comparison, it is clear that the motion amplitude of this modified hull shows a clear decrease when compared to the original, wall-sided hull, which is consistent with a common conclusion on the effect of the above-waterplane hull's flare; thus, the importance of the exact calculation of Froude-Krylov force and hydrostatic restoring force during motion simulation is confirmed.

During the simulations (the results of another hull which has more flare in the middle body but less flare on the ends are not shown here), the following phenomena are observed:

- 1) the nonlinearity is more obvious when the incident wave length is between $0.8L$ and $1.4L$, which corresponds to the region of ship's increased motion response due to heave-pitch resonance;
- 2) the nonlinearity is more obvious when the body has flare in the bow and stern area;
- 3) the nonlinearity is more obvious when the body does not have bow-stern symmetric shape.

The first observation is more related to the wave-body interaction while the other two points are more about above waterplane geometry's influence through the hydrostatic and Froude-Krylov forces' calculation. The heave and pitch motion histories of two hulls in head seas with $\lambda/L=1.0$

are shown in Figure 4.47. The motion amplitudes of the modified hull are smaller than those of the original hull. Furthermore, the motion histories of the modified hull, which features slight flares on the ends, have a more obvious nonlinear behavior.

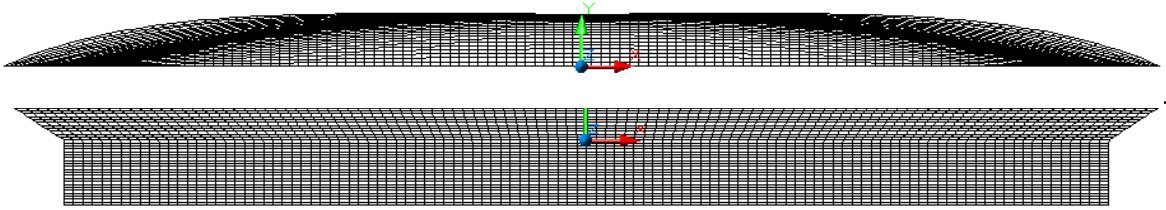


Figure 4.45 Body plan of the modified Wigley hull

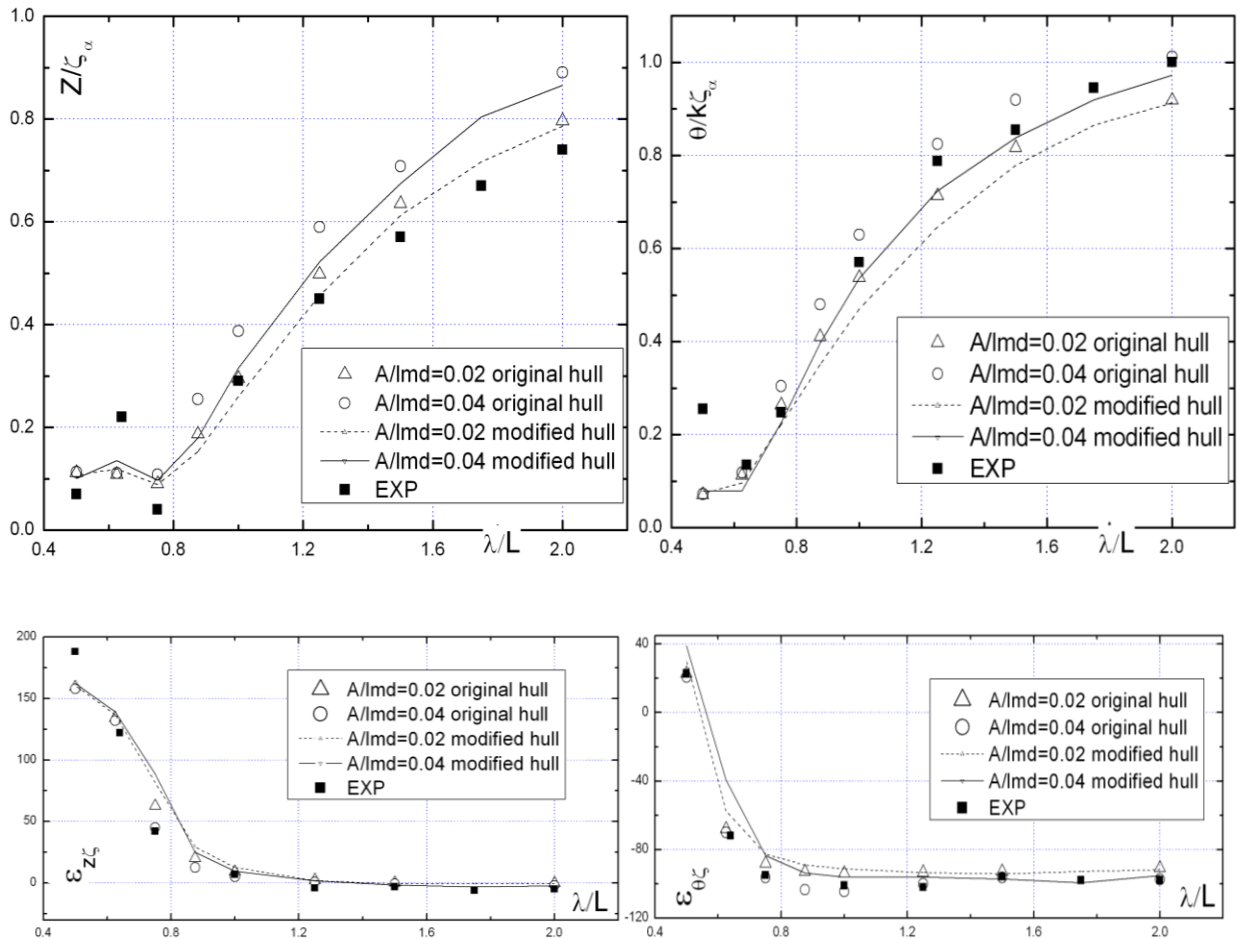


Figure 4.46 Comparison for heave and pitch motions of Modified Wigley Hull at zero speed

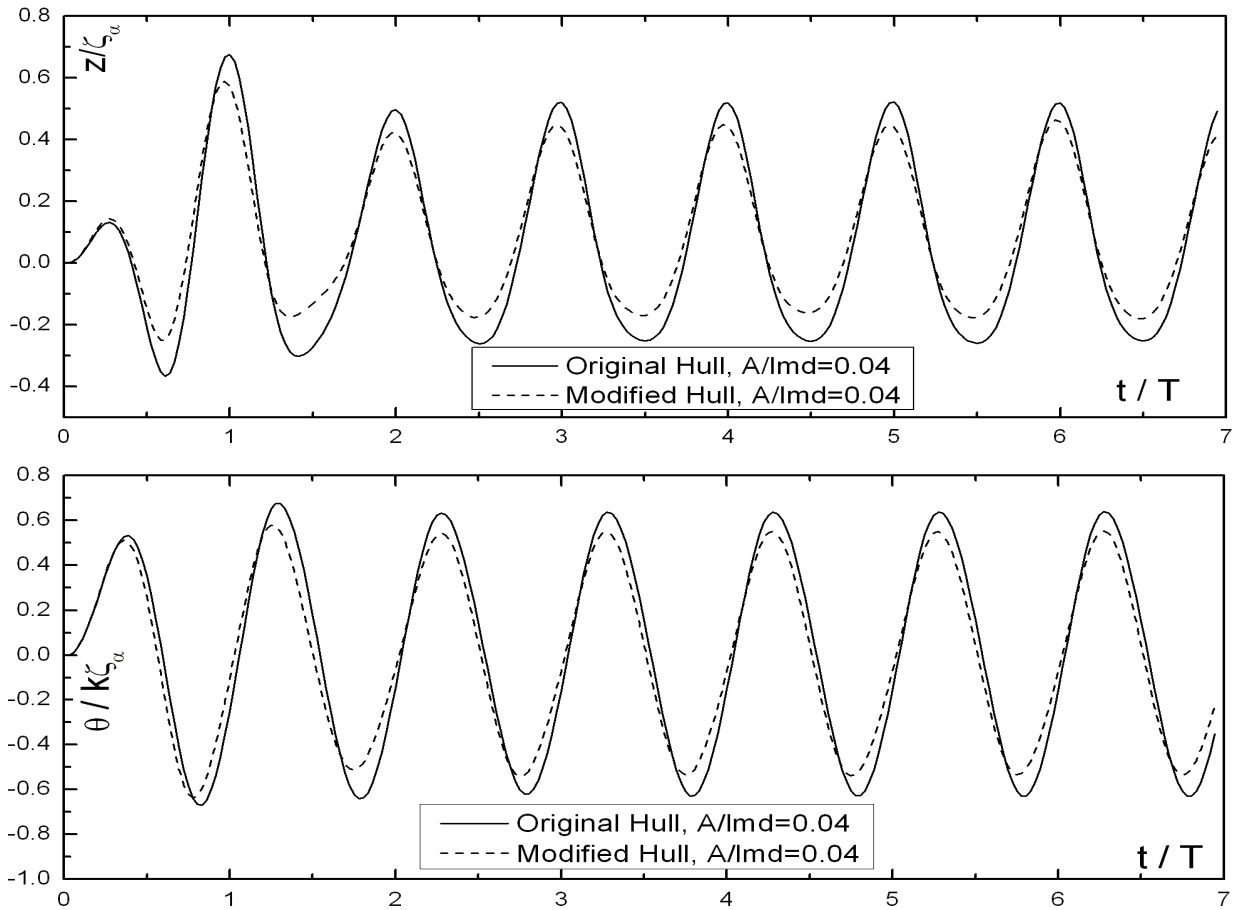


Figure 4.47 Nondimensionalized nonlinear heave and pitch motion at $\lambda/L=1.0$, head seas, $F_n=0.0$

4.7 Conclusions

The time domain hybrid method, which was formulated in the previous chapter, has been validated by extensive case studies on simulating hydrodynamic forces and ship motions at zero speed.

During these studies, a free-surface simulator which is based on the linear free-surface condition was adopted. Systematic studies show that it can yield good results. Based on the detailed study of a hemisphere, a general conclusion on choosing the size and paneling of the free-surface is achieved; subsequent successful applications to a variety of body cases prove the feasibility of the concluded concept.

Regarding the computational time, with 1000-2000 panels distributed on the boundary of the inner domain, it takes a few minutes to set up all the necessary influence matrices. Then during the time-marching simulation, a few seconds are needed for every time step, if the motion is prescribed (forced motion). Else, an iterative scheme is needed to arrive at a converged state,

thus more time will be consumed. For simulating the motion for about 10 wave periods at zero speed, it takes less than one hour on a regular PC hardware with Intel Core 2 QUAD CPU(Q8200 2.33GHz).

For the validation of motions, results for both small amplitude and large amplitude simulations are shown. In the large amplitude motion simulation, the hydrostatic and Froude-Krylov forces are calculated up to undisturbed wavy surface, while the hydrodynamic forces are calculated up to mean wetted surface so as to reduce the computational burden. According to the obtained results, these assumptions appear to be rational simplifications for fast computation in potential flow framework. On the other hand, the fully nonlinear computation is still not affordable, or the efficiency is questionable.

Obtained results include the added mass and damping coefficient of different bodies at different forced motion modes, diffraction force amplitude of different bodies, and ship motions by assuming small amplitude and large amplitude. Comparisons have been made between the results obtained by the present hybrid method, available experimental data, and other numerical methods. Good agreements are observed throughout the studies. When the large amplitude motion model is applied, nonlinear phenomena, either by checking the RAOs or the motion time history, are noted, compared to the prediction based on small amplitude assumptions. The present model proves to be capable of studying the above water hull shape's effect on ship motions.

The present hybrid method has been successfully applied to floating bodies which have flared sections, thus it overcomes one of the main shortcomings of the time-domain transient Green function method. Furthermore, it does not need so many panels in such a large area as the Rankine source method, since a stable boundary condition can be obtained on the control surface with the previously introduced Green function method in the outer fluid domain. That is to say, it inherits the advantages from both methods and becomes a more efficient solver.

Chapter 5 **Simulation of Motions of Ships Advancing in Waves by the Time-Domain Hybrid Method**

In this chapter, we will focus on the motion simulation of ships with constant forward speed. Only some specific points will be elaborated in this chapter, as the general formulation and numerical scheme have been explained in the previous chapters.

5.1 **Hydrodynamic Forces**

The unsteady pressure is given by Bernoulli's equation:

$$p = \rho \left(-\frac{\partial \Phi}{\partial t} - \frac{1}{2} \nabla \Phi \cdot \nabla \Phi - gz \right) \quad (5-1)$$

Integrating this equation over the wetted surface S_b we will obtain the forces acting on the body. Here, the unsteady term is evaluated as:

$$\frac{\partial \Phi}{\partial t} = \frac{D\Phi}{Dt} - \vec{v} \cdot \nabla \Phi \approx \frac{\Phi(t) - \Phi(t - \Delta t)}{\Delta t} - U_0 \frac{\partial \Phi}{\partial x} \quad (5-2)$$

For simulating small amplitude ship motions in response to small amplitude incident wave excitement, all the force terms in the motion equation will be calculated up to the mean wetted surface and the hydrostatic restoring forces are approximated by using the ship geometric parameters as shown in Section 4.1. For larger amplitude ship motions in response to large amplitude incident waves, Froude-Krylov forces and restoring forces will be calculated exactly over the wetted surface of the moving body up to the undisturbed incident wavy surface and transferred into the motion equations.

5.2 **Calculation of Added Resistance in Short Waves**

Before we proceed with the motion problem, we briefly address and discuss the solution of the quasi-nonlinear added resistance problem of ship advancing in waves. As elaborated in Section 2.4 and preliminarily validated in Section 2.6.8, the prediction of added resistance can be calculated by using Maruo's far field method. Extensive validations (Liu, et al. 2011) by using potential and motion results from NEWDRIFT have proved the method's simplicity and accuracy, though in the short wave range the numerical results are not very satisfactory. In this

section, two semi-analytical methods are introduced for the correction of added resistance in short wave range.

Faltinsen et al. (1980) derived the following asymptotic formula for the added resistance, assuming that the incident waves are perfectly reflected from the non-shaded part of the ship surface that is exposed to the waves:

$$F_1 = \int_L \vec{F}_n \sin \varphi dl \quad (5-3)$$

$$\text{where } \vec{F}_n = \frac{1}{2} \rho g \zeta_a^2 \left[\sin^2(\varphi - \chi) + \frac{2\omega_0 V}{g} [1 + \cos \varphi \cos(\varphi - \chi)] \right]$$

The integration in equation (14) is performed over the non-shaded part of the waterline.

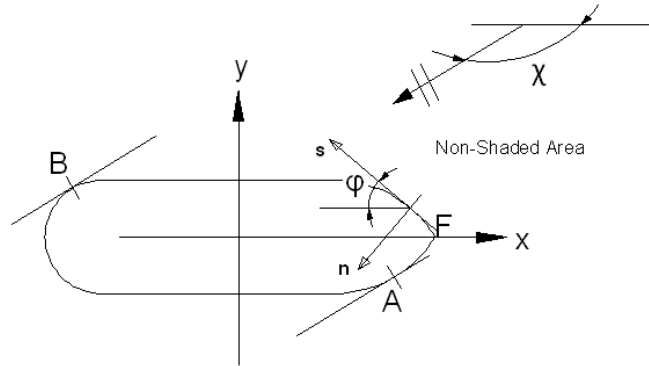


Figure 5.1 Coordinate system for the short waves range added resistance calculation methods

This expression yields good results for relatively full bodies; however, some poor results were obtained for fine hull forms like those of containerships. In order to improve this drawback, Kuroda et al. (2008) further investigated Fujii and Takahashi's semi-empirical method (1975) and proposed an improved expression for the added resistance in short waves, which takes the following form:

$$R_{AW} = \frac{1}{2} \rho g \zeta_a^2 \alpha_d (1 + \alpha_U) B B_f(\chi) \quad (5-4)$$

where:

$$B_f(\chi) = \frac{1}{B} \left[\int_I \sin^2(\varphi - \chi) \sin \varphi dl + \int_{II} \sin^2(\varphi + \chi) \sin \varphi dl \right]$$

$$\alpha_d = \frac{\pi^2 I_1^2(k_e d)}{\pi^2 I_1^2(k_e d) + K_1^2(k_e d)}$$

$$1 + \alpha_U = 1 + C_U F_n$$

$$k_e = k(1 + \Omega \cos \chi)^2$$

$$C_U = \max[10.0, -310B_f(\chi) + 68]$$

B and d are the beam and draught of the ship; B_f is the bluntness coefficient, α_d accounts for the effect of draught and frequency and $1 + \alpha_u$ for the effect of forward speed. The two integrals in $B_f(\chi)$ expression are calculated over the A-F section (integral *I*) and B-F (integral *II*) section of the non-shaded part of the waterline. I_1 is the first order modified Bessel function of the first kind and K_1 is the first order modified Bessel function of the second kind. Note that in the original proposal, the determination of C_U was more complicated and required the use of experimental data.

5.3 Consideration on Time Stepping and the Overlapping Grid Concept

As the ship is travelling in water, the intersection between the hull and the free surface will be moving accordingly. This will result in a time varying free-surface geometry. In order to solve the corresponding equations by the hybrid method, we need to update the influential matrices at every time step; to partly update the elements related to the panels which are disturbed by the moving hull and partly to update those elements related to the panels on the moving hull itself. For the panels on the free-surface, which are crossed or occupied by the moving hull, special attention is needed.

The herein applied gridding concept is explained in the following: the free-surface area is panelized by splitting it into *four* zones, as shown in Figure 5.2. Zone I to Zone III will not be disturbed by the moving hull so that the panelization will remain unchanged. For Zone IV, the so-called *Chimera grids concept* is introduced for accurate and efficient simulation.

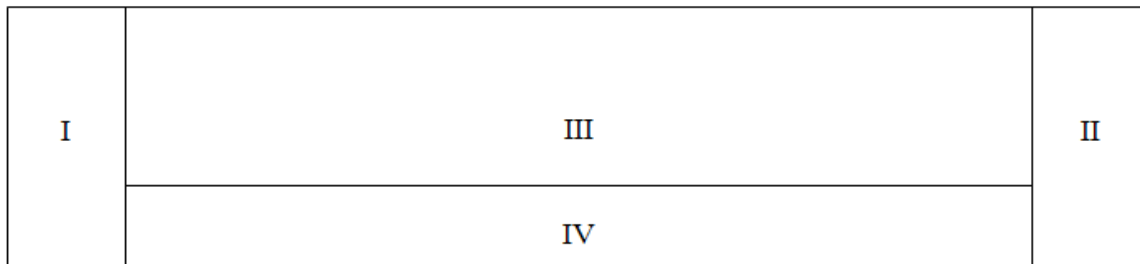


Figure 5.2 Overview of the different zones of free-surface panelization

The Chimera grids method is being widely used in aerodynamic engineering problems (Weatherill *et al.*, 1999). Generally, it involves panelization systems, which discretize the

domain boundary by separately generated but overlapping grids that exchange information between each other through certain interpolation scheme. This method has been previously used successfully in solving problems with dynamically moving bodies. In this thesis, a very simplified Chimera grid system is constructed to simulate the near-ship free-surface condition.

The Chimera grids system involves three major steps:

- 1) overlapping grids generation;
- 2) an algorithm for cutting holes;
- 3) to interpolate data in overlapping grid area.

A brief introduction and example can be found in J. Guerrero's paper (2006). Following this concept, two sets of panelization are created for the free-surface area Zone IV in the present program: the *Parent Panel System* and the *Sub Panel System*. The *parent panels* are in the same level of the panels in other zones so that they will participate in the influential matrices (not directly, as treatment is needed at every time instant). The *sub panels* have two functions. First, they are used to give a good representation of the area occupied by the hull. Secondly they are used as a bridge to find out proper information for their parent panels, as shown in Figure 5.3.

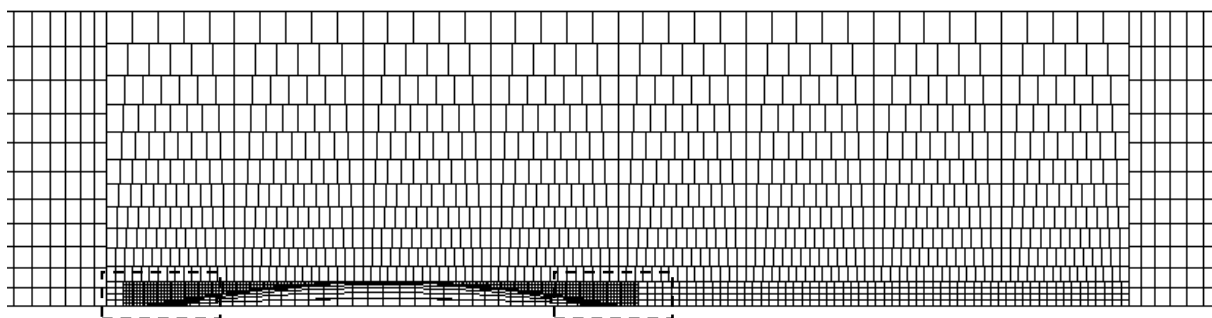


Figure 5.3 Example of free-surface panelization

At the beginning of the procedure, a control loop is conducted to check for all the sub panels whether they are inside or outside of the ship's waterline intersection, thus to *cut the hole*. Since the sub panels are in defined locations and the advancing speed is constant, it is possible to adjust the time interval so that the ship will pass one sub panel in x-direction during each time interval. Thus the occupied panels, or "the hole" geometry, can be captured/predicted. As the active sub panels are determined, the status of the parent panels can be classified as: 0, means occupied /passive; or 1, means free/active. Those marked as 0, they will not participate in the influential matrices; those marked as 1, they will take their original geometry information to participate in the computation. After this matrices' update, the influence matrices can be determined.

Regarding the free-surface condition of the parent panels: if a panel is marked as 0, it is passive so that we simply skip this panel; if it is marked as 1 and located behind of the hull, then we compute the free surface condition of *every sub panel* by using their historical information and store the average value (current *interpolation* scheme); if it is marked as 1 and located ahead of the hull, then we compute the free surface condition directly.

For the free-surface condition of sub-panels, if one is marked as 0, it is passive so that we simply skip this panel; if it is marked as 1 and located behind of the hull, then we compute the free surface condition by using their initial conditions when they became active and historical information since then; if it is marked as 1 and located ahead of the hull, then we compute the free surface condition by using their own historical information in recent steps and their parent panel's historical information in previous steps. Once the influence matrices and free surface condition are determined, Equation (3-33) in section 3.2 can be solved.

5.4 Numerical Scheme

As the detailed formulation has been interpreted in Chapter 3, here we recall directly the final equation for the velocity potential in the inner fluid domain:

$$\begin{aligned} \sum_{j,k=1}^{N^c} \left\{ -C_{ij} [A_{jk}]^{-1} [B_{kj}] - D_{ij} \right\} \Phi_{nj}^M + \sum_{j=N^c+1}^{N^c+N^f} (-D_{ij} \Phi_{nj}^M) + \sum_{j=N^c+N^f+1}^{N^c+N^f+N^b} C_{ij} \Phi_j^M \\ = - \sum_{j=1}^{N^c} C_{ij} \left\{ [A_{ij}]^{-1} [Memo_j]_o \right\} - \sum_{j=N^c+1}^{N^c+N^f} C_{ij} \Phi_j^M + \sum_{j=N^c+N^f+1}^{N^c+N^f+N^b} D_{ij} \Phi_{nj}^M \end{aligned} \quad (3-33)$$

As explained in Chapter 3, the Generalized Minimum Residual method (GMRES) is chosen to solve this equation. For nonzero speed problem, the panelization needs to be updated at every time step (by using Chimera grid system in this chapter), thus result in time-dependent matrices which need to be updated at every time instant.

For ship motion problem, we use in general about 200-600 panels to discretize ship's surface, about 400 panels on the control surface, and 3000 panels on the free surface. When addressing more refined nonlinear effects (like higher order forces, added resistance etc.) are investigated, more panels on the hull are needed. The free surface panelization is restricted between the body boundary and a control surface, which forms the border between the inner and outer domains. The extent of the discretized free surface depends on the wave length, ship speed, and target simulating time. Typically the size of the inner domain is $(5L-15L) \times (B/2+\lambda) \times \lambda/2$ for simulating 10-20 wave periods with moderate ship speed. The flowchart of the numerical procedure and implemented code is shown in Figure 5.4.

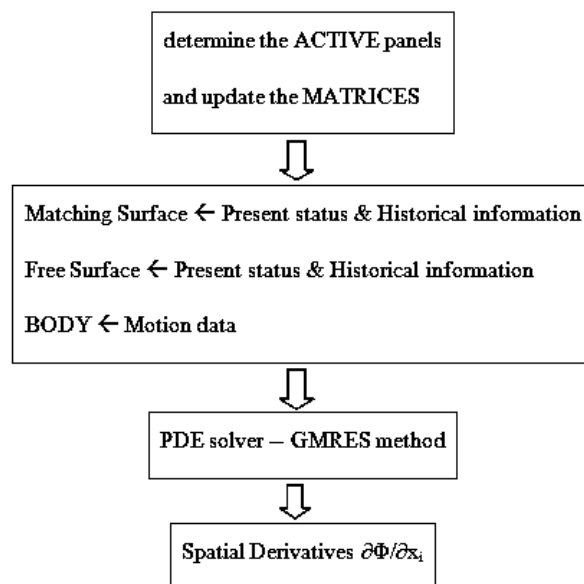


Figure 5.4 Flowchart of the HYBRID method program, with forward speed

5.5 Results and Discussions

The developed hybrid method has been numerically implemented as a computer code developed at the Ship Design Laboratory of NTUA. Some typical results are presented and discussed in the following.

5.5.1 Wave Resistance of a Wigley Hull

As a demonstration of the above procedure, the hybrid method together with the preliminary Chimera grid scheme is applied to the steady free-surface problem, namely the ship advancing at constant forward speed in calm water; herein, the calculated wave making resistance of a standard Wigley hull is presented and discussed. As stated (Shahshahan, et al., 1990), the Wigley model has no vortex system shed from the bottom because of its sharp keel and due to its sharp bow there is no wave-breaking resistance, either. Furthermore, it has been shown that there is no separation zone at the stern. Thus the total resistance may be considered to be composed exclusively of wave-making resistance and viscous-frictional resistance, free of vortex formation or separation (very small viscous-pressure resistance).

The studied Wigley hull is defined as $y/b=[1-(2x/L)^2][1-(z/H)^2]$, where $2b/L=0.1$ and $H/L=0.0625$. The Froude number is denoted by $Fn=U/\sqrt{gL}$. In the shown example, the panelization used in the computation includes in total about 3000 panels (Figure 5.5). The length of waves generated by ship's travelling is determined by $\lambda=2\pi U_0^2/g$. In the computation, we set

the travelling distance as about $(6-10)\lambda$ and it takes more than 8 hours to arrive some steady state for each point. The final value is evaluated as the average value of the last $8\pi U_0/g$ time interval.

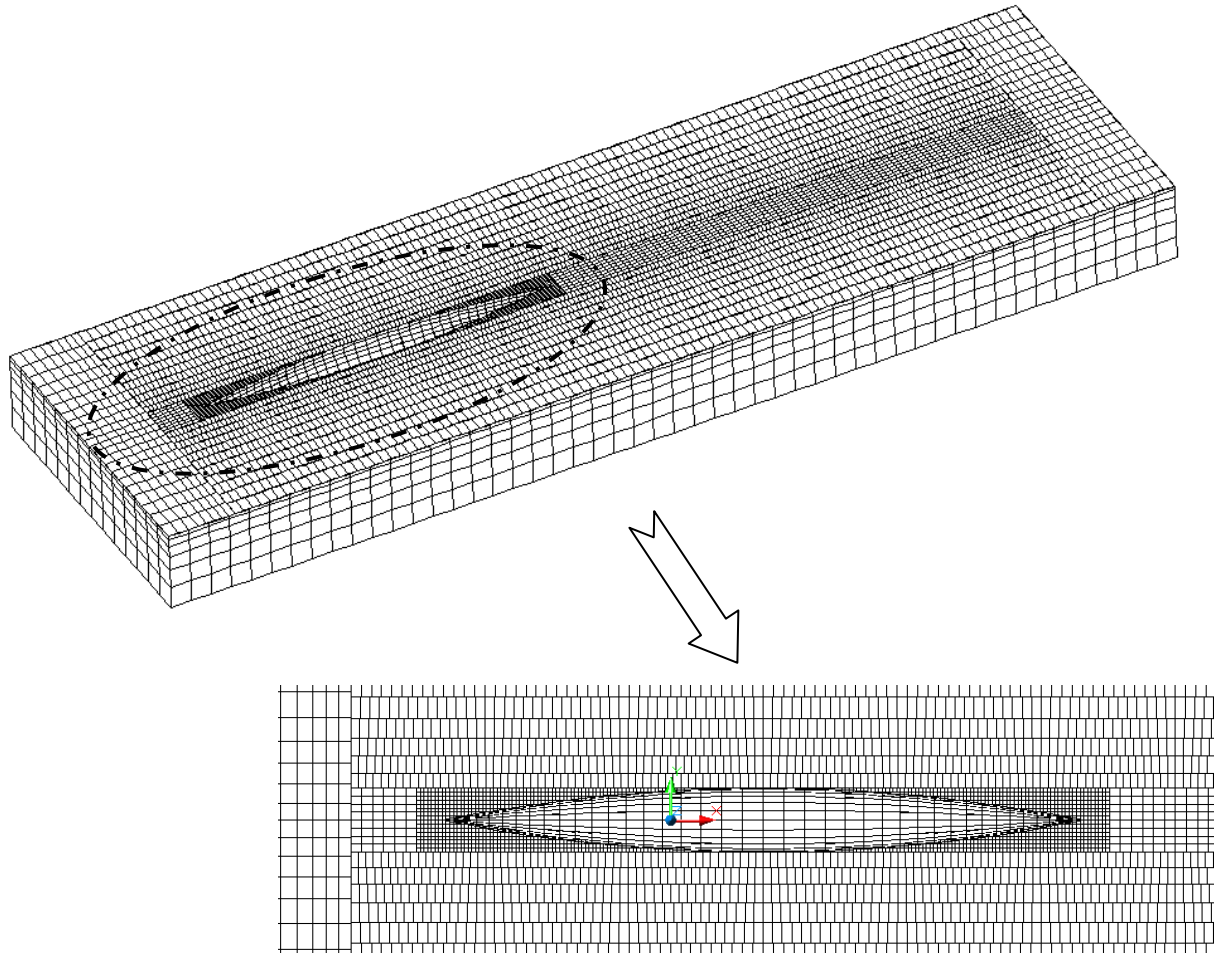


Figure 5.5 Example of runtime panelization

Figure 5.6 shows the solution of velocity potential Φ and boundary condition $\partial\Phi/\partial n$ on the downstream wetted free surface panels at the end of a simulation. The results appear to be stable and reasonable, despite some gap between results on the Parent Panel and Sub Panel, which can be readily improved by introducing some more advanced scheme *to interpolate data in the overlapping grid area*.

Figure 5.7 shows the results for the wave making resistance of the studied Wigley hull, without sinkage/trim correction. The comparison has been made with available experimental data (Chen *et al.*, 1983) and corresponding SHIPFLOW results (SHIPFLOW, 2005). A good agreement is observed, with respect to both the magnitude and the hump/hollow trend.

Recalling the results (Figure 2.16 and 2.17) obtained by the TDGF method in Chapter 2, it is observed that results from the present hybrid method do not have the highly oscillatory performance which is very common for results based on Green function methods. Instead, the results are quite smooth which is very similar to the Rankine source method based results. More

validation cases need to be done if we like to apply this method on wave making resistance evaluation.

After introducing the Chimera grid system, the time step can be set very small so that the saw-tooth-curve problem (e.g. Kataoka & Iwashita, 2004), which is very often observed, has been addressed. Furthermore, as the local panelization is very fine, it is relatively easy to calculate the spatial derivatives accurately. Figure 5.8 shows the time history of wave making resistance of this Wigley hull at $Fn=0.25$.

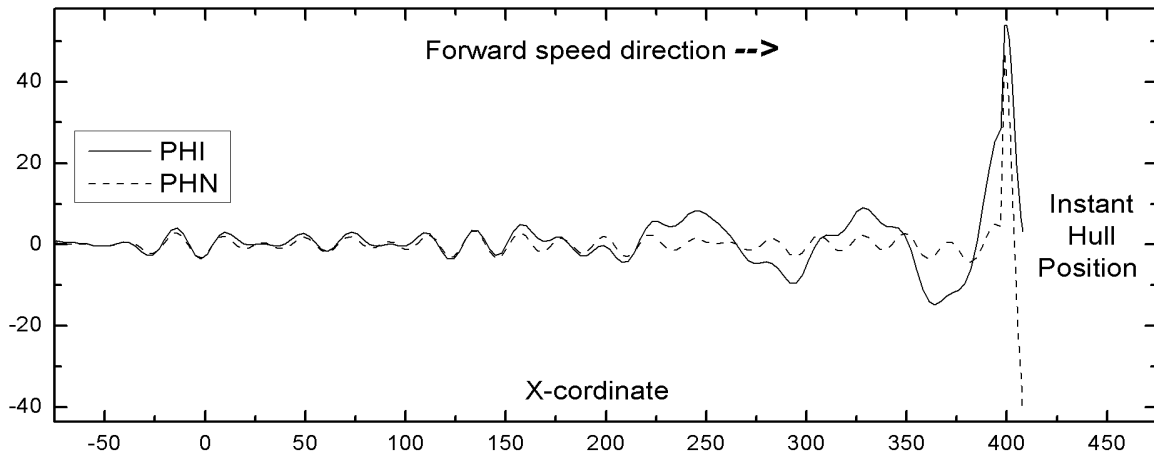


Figure 5.6 Downstream potential results along longitudinal direction, $Fn=0.275$

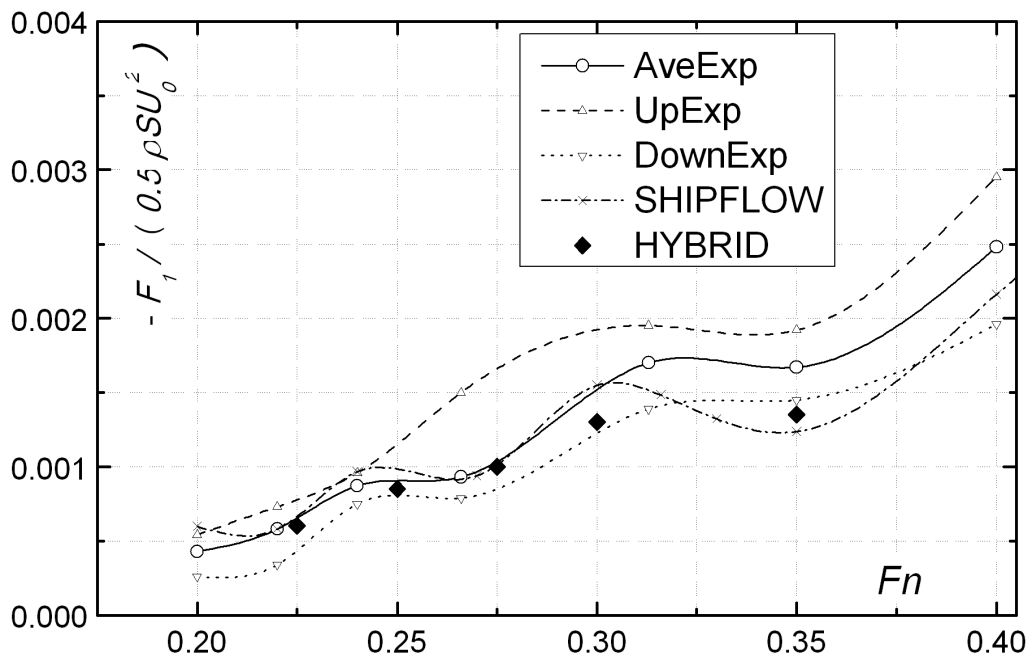


Figure 5.7 Wave making resistance of a Wigley hull, without sinkage/trim correction

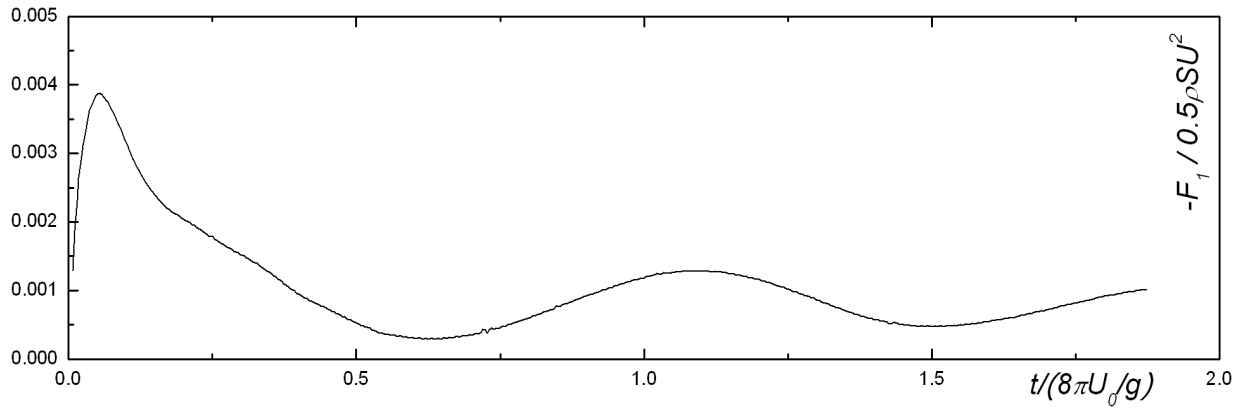


Figure 5.8 Time history of the wave making resistance of a Wigley hull, $Fn=0.25$

5.5.2 Diffraction Problem of S175 Ship at $Fn=0.275$

The diffraction problem of ITTC S175 hull is studied by present method. Figure 5.9 shows the wave exciting force/moment results compared with the results from the 3D frequency domain panel code NEWDRIFT. The agreement is overall very good, though the results from present method are slightly lower than those from NEWDRIFT. It should be noted that the NEWDRIFT code is based on the zero-frequency Green function method and forward speed effects are taken into account in an approximate way via slender-body theory assumptions.

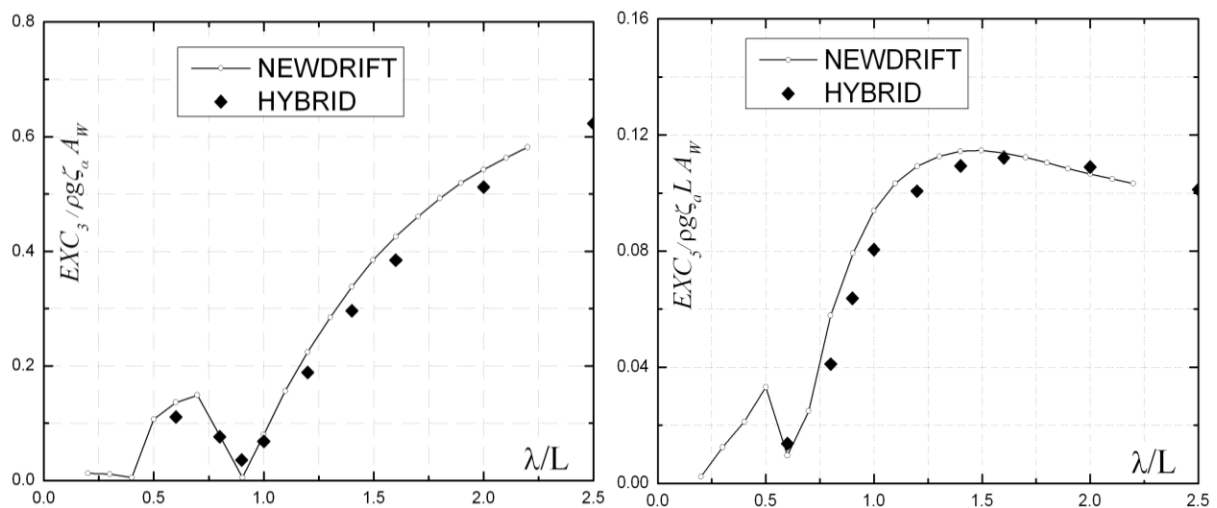


Figure 5.9 Wave exciting force of S175 ship at $Fn=0.275$

5.5.3 Motion Simulation of S175 Ship at $Fn=0.275$ with Different Wave Conditions

The present method has been applied to simulate ship motions, under both small amplitude and large amplitude assumptions. The Froude-Krylov and hydrostatic restoring forces/moments are

calculated dependent on the motion model. Figure 5.10 shows the comparison of results from the present hybrid method against available experimental data (15th ITTC, 1978) and results from 3D frequency domain panel code NEWDRIFT. For small amplitude incident wave simulation case, the present method gives some results lower than NEWDRIFT and is actually closer to experimental data. For large amplitude simulations, the incident wave steepness varies systematically, namely $A/\lambda=0.01, 0.02$ and 0.04 (noted as CS1, CS2 and CS3 respectively in the graph) where A is the wave amplitude. The motion amplitudes decrease gradually as the wave steepness increases. This is physically meaningful, considering the quickly increased damping and restoring due to the above water flared hull form of S175 ship. On the other side, for $A/\lambda=0.04$ the resulting peak values of heave and pitch motions are much lower than experimental results and the steepness of the RAO becomes smaller. For $A/\lambda=0.01$ case, in long wave range the heave motion is very close to experimental data while the pitch motion amplitude is higher. Considering that this wave is quite flat, the deviation of RAOs from results based on small amplitude motion assumption clearly shows the importance of using different models. It should be noted that the wave steepness of the experimental data, which was done for validation of the linear numerical methods then, is not known.

Interestingly, taking reference to another source (Ogawa, 2007), the experimental data of a similar container ship under different wave conditions are revealed (shown in the following as Fig.3 and Fig.9, reproduced from the original paper). When studying these data, it is observed that as the wave amplitude increases, especially when the amplitude is very large, there is in general, a trend of RAO's shift ('bending') to the longer wave' side and the amplitude decreases, which is similar to observations in the present study.

In this case study, the m_j terms based on Neumann-Kelvin assumption are used to account for the steady potential effect on the oscillatory motions.

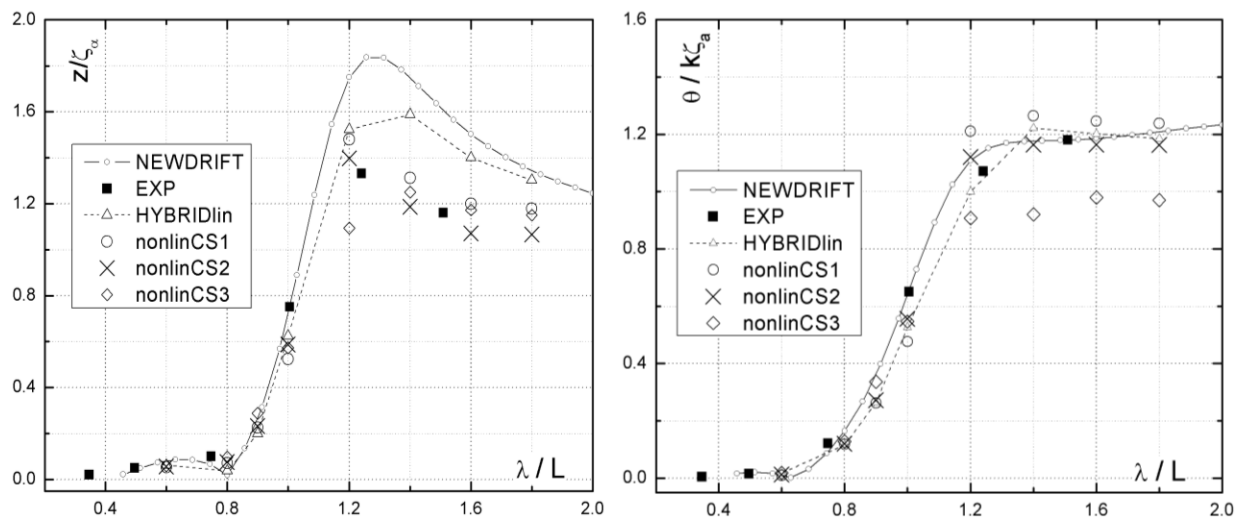


Figure 5.10 Motion amplitude of S175 ship at $F_n=0.275$

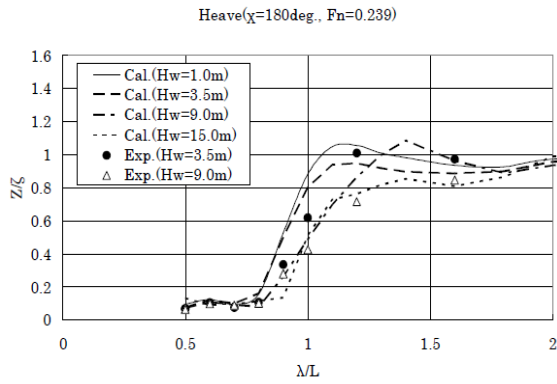


Fig. 3: The effect of wave height on the response amplitude operator of heave ($\chi=180\text{deg.}$, $F_n=0.239$)

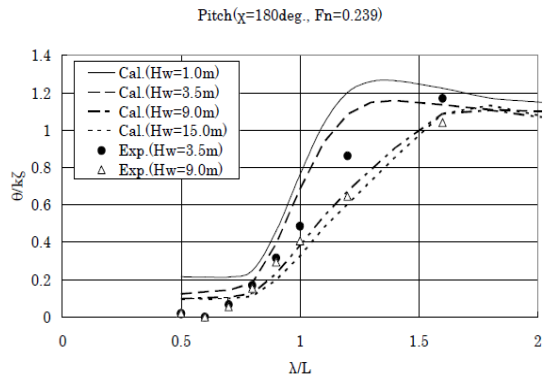


Fig. 9: The effect of wave height on response amplitude operator of pitch ($\chi=180\text{deg.}$, $F_n=0.239$)

5.5.4 Added Resistance of S175 Ship at $F_n=0.275$

The added resistance of the ITTC S175 ship in head seas was also calculated based on Maruo's far-field theory by using the potential and motion data obtained from present hybrid method (noted as HYBRID). Results calculated by the panel code NEWDRIFT (noted as NDfar) and short wave range corrections based on Faltinsen's formula and Kuroda & Tsujimoto's formula respectively are also shown in Figure 5.11 for comparison (noted as SW1 and SW2 respectively). The calculated results agree well with the experimental data (Takahashi, 1988) and other numerical result.

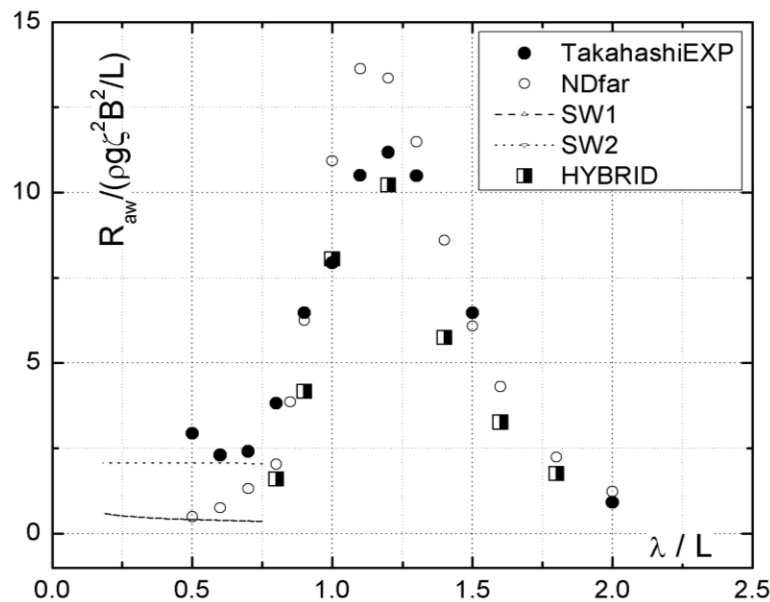


Figure 5.11 Added resistance on S-175 ship at $F_n=0.275$

5.6 Conclusions

The time domain hybrid method for simulating large amplitude motions of ships advancing in waves with constant forward speed has been validated in this chapter. Preliminary validation results include the estimation of wave making resistance, wave exciting forces, simulation of ship motions, either under small amplitude or large amplitude assumptions, and the estimation of ship's added resistance in head sea condition. Comparisons are made mainly with results of the code NEWDRIFT (Papanikolaou, 1985, 1992), which is a 3D constant panel method code based on frequency domain theory and available experimental data. Good agreements are observed for all case studies, which indicate that the present formulation and numerical scheme are correct and working properly.

During the conducted time domain simulations, a preliminary numerical scheme based on the Chimera grid concept is designed to reduce the computational burden and give accurate description of the near field free surface. Results come out satisfactorily, thus they show that the Chimera grid concept is indeed a feasible choice for extensive time domain simulation. In the future, further development of the Chimera grid concept appears recommendable. Also, during the simulation, as the near field panels and body panels are time-varying, at every time step, the corresponding influence matrices are to be set up and consume a lot of time. For a motion simulation of 10-15 wave periods, it takes 5-10 hours with about 4000 panels in total. Thus, in further development, the computational efficiency needs to be improved.

Finally, for the calculation of added resistance in short waves, the asymptotic method of Faltinsen and an improved derivative of it introduced recently by Kuroda et al. and Tsujimoto et al. are employed. The theoretical methods and implemented numerical procedure for the calculation of the added resistance in waves proved to be reliable and robust thus may be employed within a ship design optimization procedure as well within a ship operation assessment and routing optimization procedure (Papatzanakis, et al. 2011).

Chapter 6 Further Development of the Time Domain Hybrid Method

In the previous chapter, the ship motion problem was formulated in an earth-bound coordinate system and simulated by the developed hybrid method. Good results were achieved despite the quite time consuming procedure. Significant effort was devoted to the improvement of the efficiency of the developed approach by introducing the *Chimera grid concept*; however, in view of the nature of a forward speed problem formulation in an earth bound coordinate system, the influence matrices must be updated at every time instant, which is inevitably time consuming. Furthermore, one major advantage of a time domain method over a frequency domain method is its capability to study the instantaneous motion response to random sea conditions, which needs very long time simulation. However, due to the limitation on the panel numbers, it is not possible to do this kind of simulation by the hybrid method in an earth-fixed coordinate system, as the free surface area will be huge, so will be the number of panels.

In this chapter, we will formulate the same problem in a body-travelling coordinate system. The matching surface will be set at certain distance away from the hull and travelling with the body, thus the free surface area will be fixed, which is actually quite the same with what we did in Chapter 4 for zero speed problems; however, now the matching surface is travelling with the body at the same forward speed. Under such situation, the panelization will be fixed, thus there will not be any update of the influence matrices, so that the simulation time will be greatly reduced, making the simulation in random sea states also possible.

6.1 Free Surface Condition

The linearized free-surface condition can be expressed in the body-fixed coordinate system as:

$$\left(\frac{\partial}{\partial t} - U_0 \frac{\partial}{\partial x}\right)^2 \Phi + g \frac{\partial \Phi}{\partial z} = 0 \quad (6-1)$$

This expression can be rewritten as:

$$\frac{\partial^2 \Phi}{\partial t^2} - 2U_0 \frac{\partial^2 \Phi}{\partial x \partial t} + U_0^2 \frac{\partial^2 \Phi}{\partial x^2} = -g \frac{\partial \Phi}{\partial z} \quad (6-2)$$

It has been shown by Wang (2003) that by using Laplace transform, Φ can be expressed as following:

$$\begin{aligned} \Phi(x, y, 0, t) &= H\left(t - \frac{x_0 - x}{u}\right). \\ \left[\Phi\left(x_0, y, 0, t - \frac{x_0 - x}{u}\right) + \frac{x_0 - x}{u} \frac{\partial}{\partial t} \Phi\left(x_0, y, 0, t - \frac{x_0 - x}{u}\right) - (x_0 - x) \frac{\partial}{\partial x} \Phi\left(x_0, y, 0, t - \frac{x_0 - x}{u}\right) \right] \\ &+ \frac{g}{u^2} \int_x^{x_0} (x - \xi) \frac{\partial}{\partial n} \Phi\left(\xi, y, 0, t - \frac{\xi - x}{u}\right) H\left(t - \frac{\xi - x}{u}\right) d\xi \end{aligned} \quad (6-3)$$

where $H(t)$ is the *unit step function*. It should be noted that the initial conditions for panels located in the area that is free from disturbance/occupation of a sailing hull or not are different.

The above expression can be derived from the free surface condition expression (3-15) by carefully treating the corresponding term in the body-fixed coordinate system. For a point p, let $(X, Y, 0)$ be its coordinate in earth-fixed system and $(x, y, 0)$ be the coordinate in body-fixed system at time t , then we have $X = x + ut$.

In the body-fixed coordinate system, Equation (3-15) should be re-written as:

$$\begin{aligned} \Phi(p, t) &= \Phi(p_0, t_0) + \left(\frac{\partial \Phi(p, t)}{\partial t} - u \frac{\partial \Phi(p, t)}{\partial x} \right) \Big|_{t=t_0, p=p_0} (t - t_0) \\ &- g \int_{t_0}^t (t - \tau) \frac{\partial \Phi(p(x + u(t - \tau), y, 0, \tau), \tau)}{\partial n} d\tau \end{aligned} \quad (6-4)$$

For $x_0 = x + u(t - t_0)$, then

$$\begin{aligned} \Phi(x, y, 0, t) &= \Phi\left(x_0, y, 0, t - \frac{x_0 - x}{u}\right) + \frac{x_0 - x}{u} \frac{\partial}{\partial t} \Phi\left(x_0, y, 0, t - \frac{x_0 - x}{u}\right) \\ &- (x_0 - x) \frac{\partial \Phi}{\partial x}\left(x_0, y, 0, t - \frac{x_0 - x}{u}\right) \\ &- g \int_{t_0}^t (t - \tau) \frac{\partial \Phi(p(x + u(t - \tau), y, 0, \tau), \tau)}{\partial n} d\tau \end{aligned} \quad (6-5)$$

Let $\xi = x + u(t - \tau)$, i.e., $\tau = t - (\xi - x) / u$, then the free surface condition can be expressed as:

$$\begin{aligned} \Phi(x, y, 0, t) &= \Phi\left(x_0, y, 0, t - \frac{x_0 - x}{u}\right) + \frac{x_0 - x}{u} \frac{\partial}{\partial t} \Phi\left(x_0, y, 0, t - \frac{x_0 - x}{u}\right) \\ &- (x_0 - x) \frac{\partial \Phi}{\partial x}\left(x_0, y, 0, t - \frac{x_0 - x}{u}\right) \\ &+ \frac{g}{u^2} \int_x^{x_0} (x - \xi) \frac{\partial}{\partial n} \Phi\left(\xi, y, 0, t - \frac{\xi - x}{u}\right) d\xi \end{aligned} \quad (6-6)$$

This expression is valid only for the area behind the stern when $t > (x_0 - x) / u$. Thus the H-function should be included as in Equation (6-3).

6.2 Discretization of Free Surface Condition

In the body fixed coordinate system, the inner domain free surface is discretized as following:

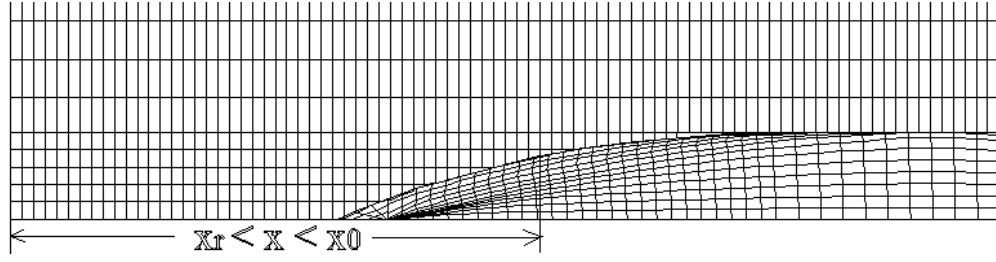


Figure 6.1 Wetted free surface panels' simulation

In the area that $x_r < x < x_0$ (shown in Figure 6.1) where x_r is the coordinate of the rear matching surface and x_0 the intersection of waterline and free surface; the center of each panel is marked as x_i and $x_i - x_{i+1} = \Delta x = u\Delta t$.

At time instant $t = t_n = n\Delta t$, the velocity potential of a point at $x = x_m$ is denoted as $\Phi_m^n = \Phi(x_m, y, 0, t_n)$

The first three terms on the right hand of Equation (6-3) can be discretized respectively as:

$$\Phi_0^{n-m} H[(n-m)\Delta t] = \begin{cases} 0 & n \leq m \\ \Phi_0^{n-m} & n > m \end{cases}$$

$$-m\Delta x \frac{\partial}{\partial x} \Phi_0^{n-m} H[(n-m)\Delta t] = \begin{cases} 0 & n \leq m \\ -m\Delta x \frac{\partial}{\partial x} \Phi_0^{n-m} & n > m \end{cases}$$

$$m\Delta t \frac{\partial}{\partial t} \Phi_0^{n-m} H[(n-m)\Delta t] = \begin{cases} 0 & n \leq m \\ m\Delta t \frac{\partial}{\partial t} \Phi_0^{n-m} & n > m \end{cases}$$

For the fourth term, there H-function is defined as $H[(n-(i-m))\Delta t] = H[(n+m-i)\Delta t]$,

where $\zeta = iu\Delta t$.

$$H[(n+m-i)\Delta t] = \begin{cases} 0 & n+m \leq i \\ 1 & n+m > i \end{cases}$$

For $n+m > i$, there are still two cases:

1) $n \leq m$, which means the initial effect at x_0 has not arrived x_m yet.

$$\begin{aligned} & \frac{g}{u^2} \int_x^{x_0} (x-\xi) \frac{\partial}{\partial n} \Phi \left(\xi, y, 0, t - \frac{\xi-x}{u} \right) H[(n+m-i)\Delta t] d\xi \\ &= \frac{g}{u^2} \int_x^{x+ut} (x-\xi) \frac{\partial}{\partial n} \Phi \left(\xi, y, 0, t - \frac{\xi-x}{u} \right) * 1 * d\xi + \frac{g}{u^2} \int_{x+ut}^{x_0} (x-\xi) \frac{\partial}{\partial n} \Phi \left(\xi, y, 0, t - \frac{\xi-x}{u} \right) * 0 * d\xi \\ &= \frac{g}{u^2} \int_x^{x+ut} (x-\xi) \frac{\partial}{\partial n} \Phi \left(\xi, y, 0, t - \frac{\xi-x}{u} \right) d\xi \end{aligned}$$

$$\xi - x = \xi_1$$

then the above expression will become

$$= \frac{g}{u^2} \int_0^{ut} (-\xi_1) \frac{\partial}{\partial n} \Phi \left(\xi_1 + x, y, 0, t - \frac{\xi_1}{u} \right) d\xi_1$$

$$\xi_1 = u\tau$$

$$= -g \int_0^{n\Delta t} \tau \frac{\partial}{\partial n} \Phi(u\tau + x, y, 0, t - \tau) d\tau$$

This expression can be discretized as

$$= -g (\Delta t)^2 \sum_{j=1}^{n-1} j \frac{\partial}{\partial n} \Phi_{m-j}^{n-j}$$

2) $n > m$, which means the initial effect at x_0 has arrived x_m .

$$\begin{aligned} & \frac{g}{u^2} \int_x^{x_0} (x - \xi) \frac{\partial}{\partial n} \Phi \left(\xi, y, 0, t - \frac{\xi - x}{u} \right) H[(n + m - i)\Delta t] d\xi \\ &= \frac{g}{u^2} \int_x^{x_0} (x - \xi) \frac{\partial}{\partial n} \Phi \left(\xi, y, 0, t - \frac{\xi - x}{u} \right) d\xi \end{aligned}$$

$$\xi - x = \xi_1$$

then the above expression will become

$$= \frac{g}{u^2} \int_0^{x_0 - x} (-\xi_1) \frac{\partial}{\partial n} \Phi \left(\xi_1 + x, y, 0, t - \frac{\xi_1}{u} \right) d\xi_1$$

$$\xi_1 = u\tau$$

$$= -g \int_0^{m\Delta t} \tau \frac{\partial}{\partial n} \Phi(u\tau + x, y, 0, t - \tau) d\tau$$

This expression can be discretized as

$$= -\frac{1}{2} g (\Delta t)^2 m \frac{\partial}{\partial n} \Phi_0^{n-m} - g (\Delta t)^2 \sum_{j=1}^{m-1} j \frac{\partial}{\partial n} \Phi_{m-j}^{n-j}$$

In short, the discretized form of the free surface condition is as following:

$$\Phi(x, y, 0, t) = \begin{cases} -g (\Delta t)^2 \sum_{j=1}^{n-1} j \frac{\partial}{\partial n} \Phi_{m-j}^{n-j} & n \leq m \\ \Phi_0^{n-m} - m\Delta x \frac{\partial}{\partial x} \Phi_0^{n-m} + m\Delta t \frac{\partial}{\partial t} \Phi_0^{n-m} & \\ \quad -\frac{1}{2} g (\Delta t)^2 m \frac{\partial}{\partial n} \Phi_0^{n-m} - g (\Delta t)^2 \sum_{j=1}^{m-1} j \frac{\partial}{\partial n} \Phi_{m-j}^{n-j} & n > m \end{cases} \quad (6-7)$$

6.3 Integral Equations

In the body fixed coordinate system, under the assumption that the motion is small, the velocity potential can be solved up to the mean wetted surface with either *mixed singularity model* or *source distribution model* as following:

$$\begin{aligned}
 2\pi\Phi_{II}(p, t) + \iint_{S_c} \left[\Phi_{II}(q, t) \frac{\partial}{\partial n_q} \left(\frac{1}{r_{pq}} - \frac{1}{r_{pq'}} \right) - \left(\frac{1}{r_{pq}} - \frac{1}{r_{pq'}} \right) \frac{\partial \Phi_{II}}{\partial n_q} \right] ds_q \\
 = \int_0^t d\tau \iint_{S_c} \left(\tilde{G} \frac{\partial \Phi_{II}}{\partial n_q} - \Phi_{II} \frac{\partial \tilde{G}}{\partial n_q} \right) ds_q \\
 + \frac{1}{g} \int_0^t d\tau \int_{wl} \left[U_0^2 \left(\tilde{G} \frac{\partial \Phi_{II}}{\partial \xi} - \Phi_{II} \frac{\partial \tilde{G}}{\partial \xi} \right) - U_0 \left(\tilde{G} \frac{\partial \Phi_{II}}{\partial \tau} - \Phi_{II} \frac{\partial \tilde{G}}{\partial \tau} \right) \right] d\eta
 \end{aligned} \tag{6-8}$$

$$\begin{aligned}
 \Phi(p, t) = \frac{1}{4\pi} \iint_{S_c} \sigma(q, t) \left(\frac{1}{r_{pq}} - \frac{1}{r_{pq'}} \right) ds_q + \\
 \frac{1}{4\pi} \int_0^t d\tau \left[\iint_{S_c} \sigma(q, \tau) \tilde{G}(p, t; q, \tau) ds_q + \frac{U_0^2}{g} \int_{wl} \sigma(q, \tau) \tilde{G}(p, t; q, \tau) n_1 d\eta \right]
 \end{aligned} \tag{6-9}$$

6.4 Numerical Results and Discussions

6.4.1 Forced Motion Problem of S175 Ship at $Fn=0.275$

Numerical experiments were carried out to determine the optimal size and paneling of the free surface area. Based on our experience, we change the width, depth and length of the solution domain systematically and compare the resulting added masses and damping coefficients. Finally we set the width as $\max(3B, 0.5\lambda)$, depth as $\max(5D, 0.4\lambda)$, and length $\max(3L, 2\lambda+L)$. With this setting, the following results are obtained (denoted as HYBRID II), as shown in Figure 6.2 and Figure 6.3. Also plotted are the results from the panel code NEWDRIFT (denoted by ND), a 3D body exact formulation (Zhang et al., 2010, results denoted by 3D B.E.) and the Hybrid method developed in last Chapter (denoted as HYBRID I). Obvious deviations among different methods have been observed in this study.

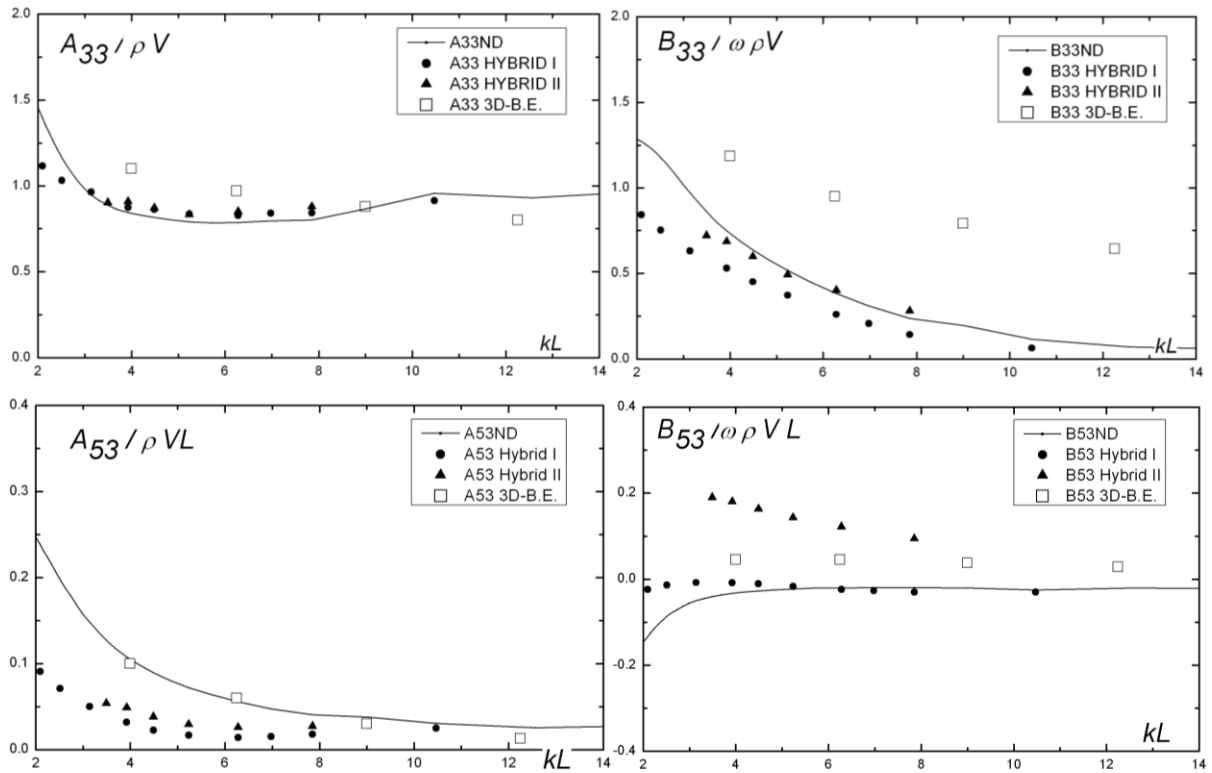


Figure 6.2 Added masses and damping coefficients due to forced heave motion, S175, $Fn = 0.275$

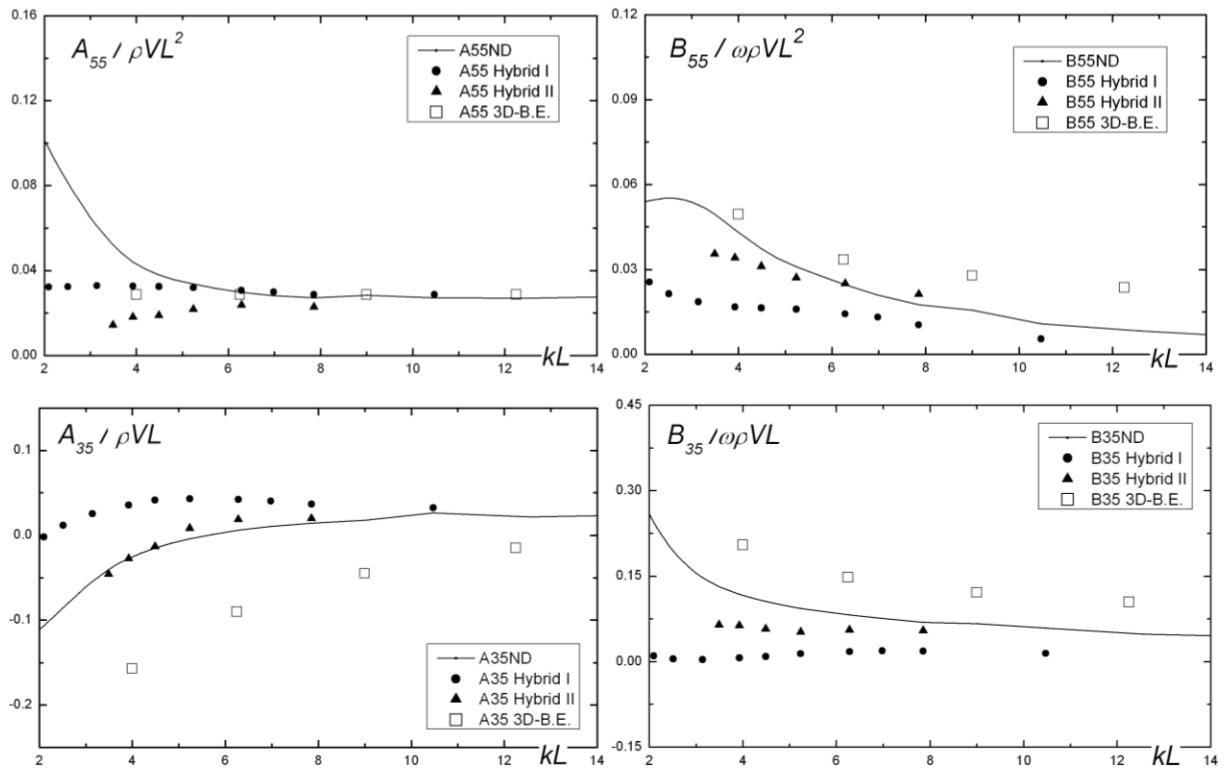


Figure 6.3 Added masses and damping coefficients due to forced pitch motion, S175, $Fn = 0.275$

6.4.2 Motion Simulation of S175 Ship at $F_n=0.275$ with Different Wave Conditions

The motion of the S175 container ship is again studied by using the present method. For small amplitude motion case, we assume the gravity (mass) centre is on the calm waterplane at the mid-ship, that is $x_c=0$ $z_c=0$, then the motion equation is reduced and all the forces are estimated about the assumed gravity center to obtain the motion prediction. For large amplitude motion case, we estimate the radiation and diffraction forces up to the mean wetted surface but the hydrostatic and Froude-Krylov part exactly about the actual gravity center to obtain the motion prediction. The m_j term is calculated either based on Neumann-Kelvin simplification or directly as elaborated in Section 3.4.

The numerical results on heave and pitch motions are shown in Figure 6.4 and Figure 6.5. During the simulation, the wave amplitude is set as constant $A/L=0.01$. By using a small amplitude model, with either m_j term computation, the heave motion is overestimated in long wave range. By using large amplitude model, which introduces the exact computation of Froude-Krylov force and restoring forces, the heave motion in long wave range is improved and get closer to experimental data. For m_j term, the effect is mainly around the peak range, which is also observed in others' computations (Bingham & Maniar, 1996). During the computation, it is confirmed that the m_j term estimation based on Neumann-Kelvin simplification is quite reasonable. Problem of present simulation is that, when compared to experimental data there is a shift in the range where λ is comparable to L and the shift appears in heave amplitude curve hasn't been improved by applying large amplitude model.

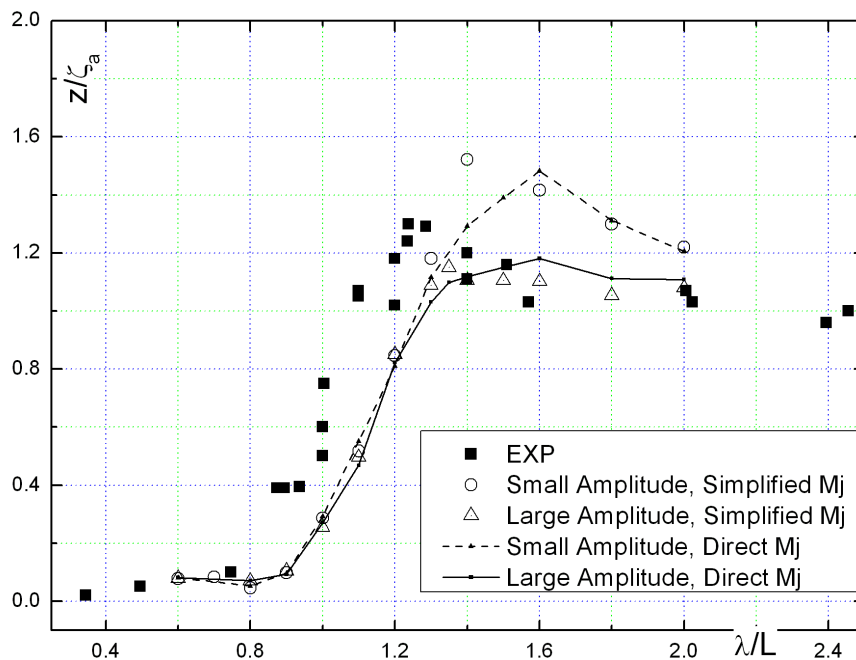


Figure 6.4 Heave motion amplitude calculation of S175 ship, $F_n=0.275$

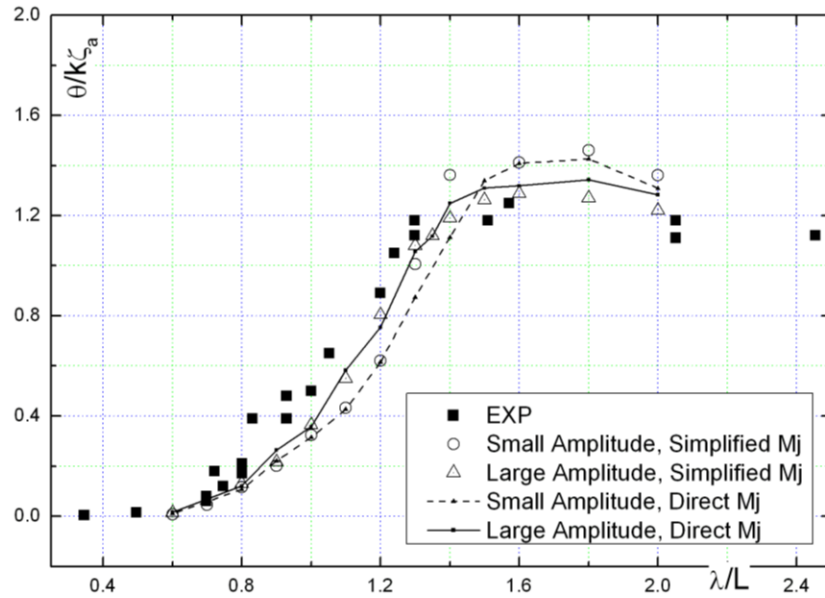
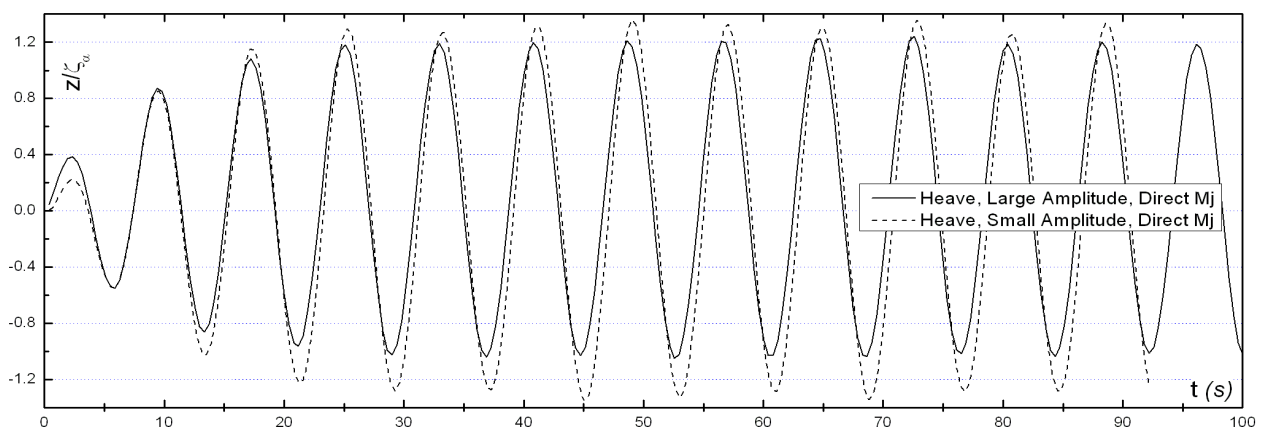


Figure 6.5 Pitch motion amplitude calculation of S175 ship, $F_n=0.275$

For pitch motion, when the small amplitude model is used, we observed some shift when compared to experimental data. The different m_j term assumptions appear to only affect the peak value. But by applying the large amplitude motion model, the pitch motion results were obviously improved, the shift becomes weak and the results in all the studied range closely match the experimental results. Furthermore, when the Froude-Krylov force and restoring forces are exactly calculated, it will introduce some serious differences, compared to the linear calculation in the small amplitude model, around bow and stern where the flare of sections is significant. This effect is more visible in the pitch response, thus it improved the prediction. Figure 6.6 shows the heave and pitch motion histories of the S175 ship with $\lambda/L=1.4$, either with small amplitude simulation or with large amplitude simulation. Due to the fact that the wave amplitude is small, $A/\lambda=0.01$, the nonlinearity is not strong. However, there are still obvious deviations between the two curves from different models. This indicates the importance of applying a more exact model even when the wave amplitude is small.



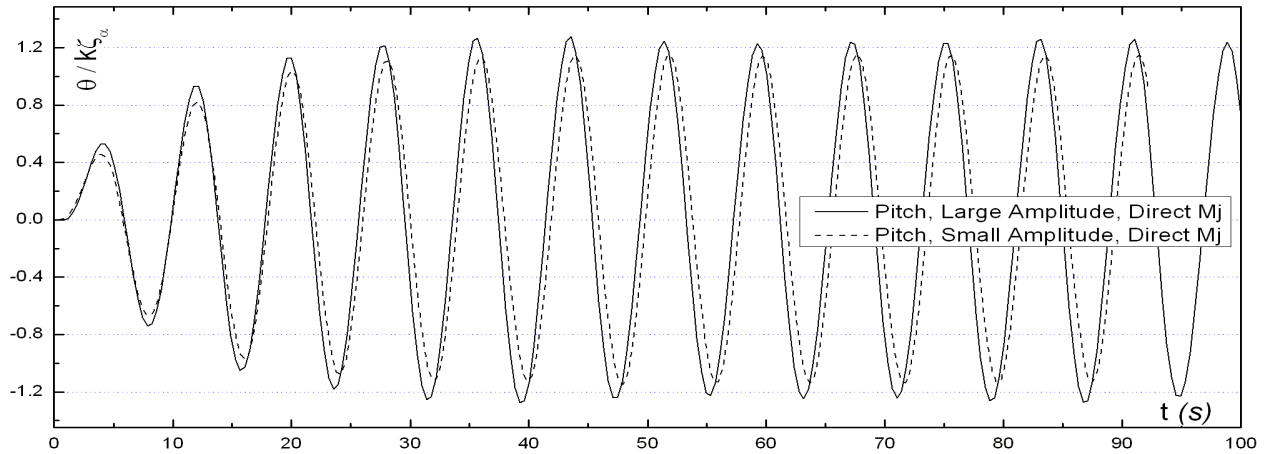


Figure 6.6 Heave and pitch motion histories calculation of S175 ship, $\lambda/L=1.4$, $Fn=0.275$

It is understood that around the resonance range, the hydrodynamic forces are comparable to the hydrostatic part and the interaction is quite complicated. When we drop the line-integral term in integral Equation (6-8), for sure some error will arise which cannot be estimated numerically. As shown in Chapter 2 in the calculation of the wave resistance of the Wigley hull, despite the highly oscillatory performance which is common to TDGF based calculation methods, there is a definite deviation from experimental data, which seems to be responsible for the present shift. And indeed although the calculated heave exciting force presented in the last chapter agrees pretty well with NEWDRIFT results, in the present exciting force calculation a shift shows up, as shown in Figure 6.7.

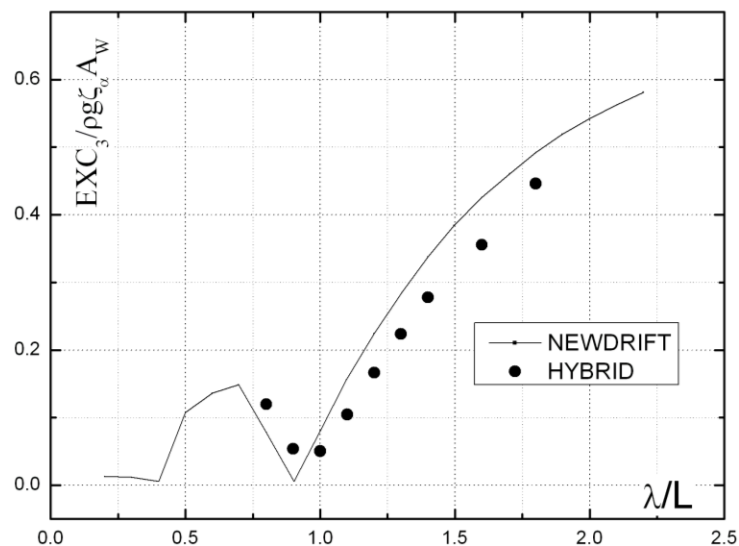


Figure 6.7 Wave exciting force in heave direction of S175 ship, $Fn=0.275$

Finally, as pointed out by Lin and Kuang (2009), the dissipating far field boundary condition is no longer suitable for strongly nonlinear cases. Since the ship generated wave energy is proportional to the Froude number, computational instabilities will occur if the far field boundaries do not accurately estimate the radiated ship wave energy for high Froude numbers. This may be also the reason for inaccuracies in the prediction of relevant phenomena.

6.4.3 Motion of a Wigley Hull with Different Above-Water Hull Shapes

From the previous studies, it is noted that the developed hybrid method is capable of studying the effect of above waterplane hull shape changes. This indicates its ability to be applied to the optimization of the design of ship's above water hull shape. In this section, we will apply the developed numerical method and computer code to the basic Wigley III hull, a second modified hull as used in Section 4.6, and a third modified hull (noted as V2) which is defined by the following expression:

$$x = x_0(1+z) \quad (x \leq 0, z \geq 0)$$

$$y = \begin{cases} b \left(1 - \left(\frac{2x_0}{L} \right)^2 \right) \left(1 - \left(\frac{z}{D} \right)^2 \right) \left(1 + 0.2 * \left(\frac{2x_0}{L} \right)^2 \right) \left(1 + \left(\frac{2x_0}{L} \frac{z}{D_0 - D} \right)^2 \right) & z < 0 \\ b \left(1 - \left(\frac{2x_0}{L} \right)^2 \right) \left(1 + 0.2 * \left(\frac{2x_0}{L} \right)^2 \right) & z \geq 0 \end{cases}$$

The heave and pitch motions in small amplitude incident head waves with forward speed are calculated and plotted in Figure 6.8. It is observed that for the heave motion there is a peak (indicating a resonance) point in the NEWDRIFT results and the motion amplitude decreases for larger wave lengths. For present hybrid method the main deviation is due to some shift, when compared to either NEWDRIFT or experiment data, despite some reasonable agreement between the two numerical methods. The shown experimental data of pitch motion are unexpectedly comparably very high and both numerical methods failed to predict the peak values. This phenomenon was also observed in the original report (Journée, 1992). One thing worthy of attention is that since this experiment was designed to validate a linear motion theory, the nominal wave height was set as a small constant value, which changes in terms of wave steepness with the various wave lengths.

Figure 6.9 shows the panelization of the modified Wigley hull V2, with some slight flare introduced in the bow/stern regions and a small over-hang at the stern, which is similar to a real ship. The hybrid method is applied to predict the heave and pitch motion of this hull and the results are shown in Figure 6.10 to Figure 6.13. Figure 6.10 and 6.11 show the heave and pitch motions at small wave steepness, $A/L=0.01$. At this condition, the results from applying the large amplitude model are almost identical to the results from the small amplitude model. The

results of both modified hulls slightly deviate from the results of the original hull, because the wave amplitude is small and the flare is also limited near the waterplane, so that the exact calculation of incident wave forces and restoring forces does not affect much the computation.

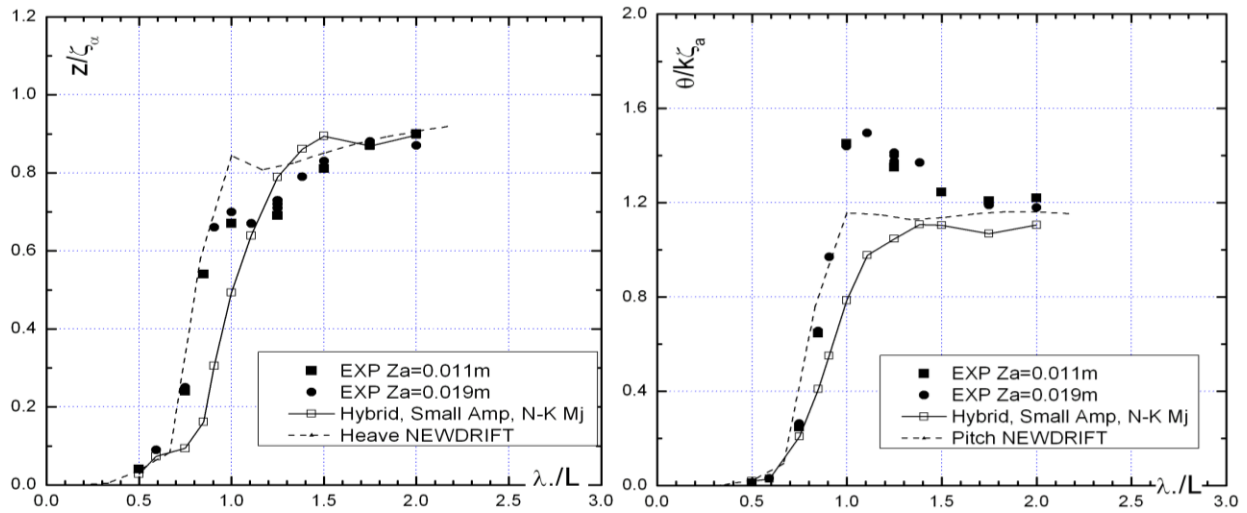


Figure 6.8 Heave and pitch motion of Wigley III hull, $Fn=0.2$, small amplitude

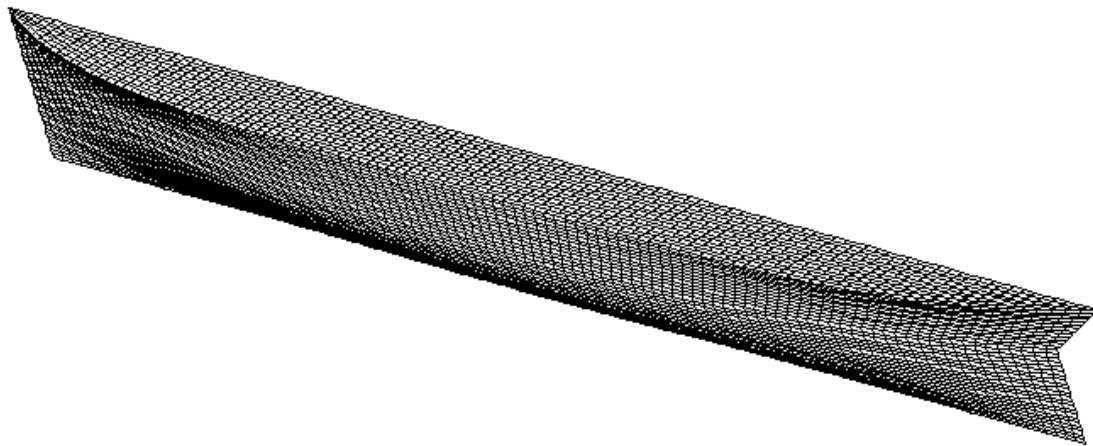


Figure 6.9 Panelization of the Modified Wigley III hull

At a steeper wave condition, $A/L=0.02$, more obvious deviations show up for both heave and pitch motions, as shown in Figure 6.12 and 6.13. For heave motion, the amplitude of the modified hull has decreased compared to the other two hulls due to its large projected area on the vertical direction. On the other hand, the pitch motion of the modified hull V2 is obviously smaller than for the other two hulls in the long wave range. These calculations, offer some valuable information regarding the applicability of these methods in the preliminary design stage. When considering the actual sea conditions encountered in ship's service route, we may be able to determine the optimal routine or even the optimal hull shape for specific routes.

We should keep in mind that all the three Wigley hulls are actually very narrow, with $L/B=10$, compared to actual shiplike forms and the introduced flares are also quite conservative compared to a real ship. Due to this reason, the m_j term based on Neumann-Kelvin simplification is employed. During these computations, the wave steepness was kept constant. If we use other settings, say constant wave height, the results will be of course different.

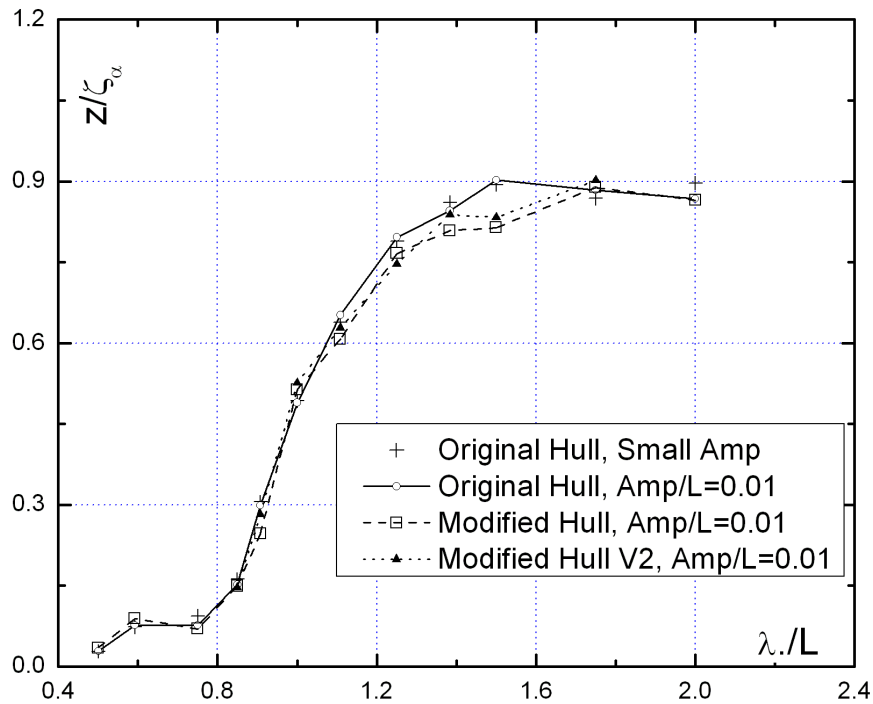


Figure 6.10 Heave amplitude of three different Wigley hulls, $F_n=0.2$, $\text{Amp}/L=0.01$

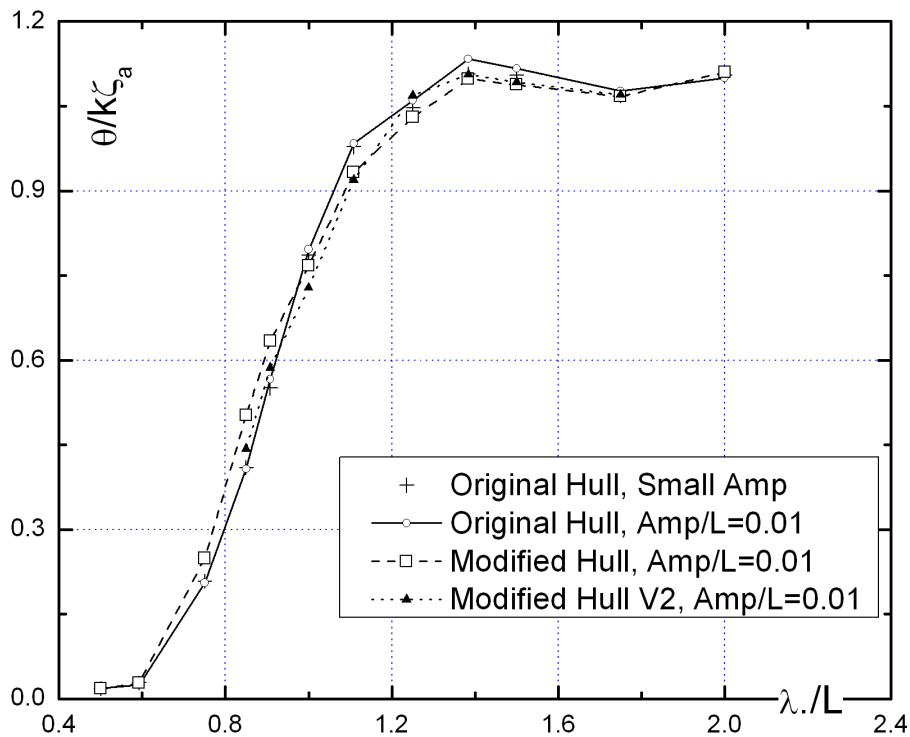


Figure 6.11 Pitch amplitude of three different Wigley hulls, $F_n=0.2$, $\text{Amp}/L=0.01$

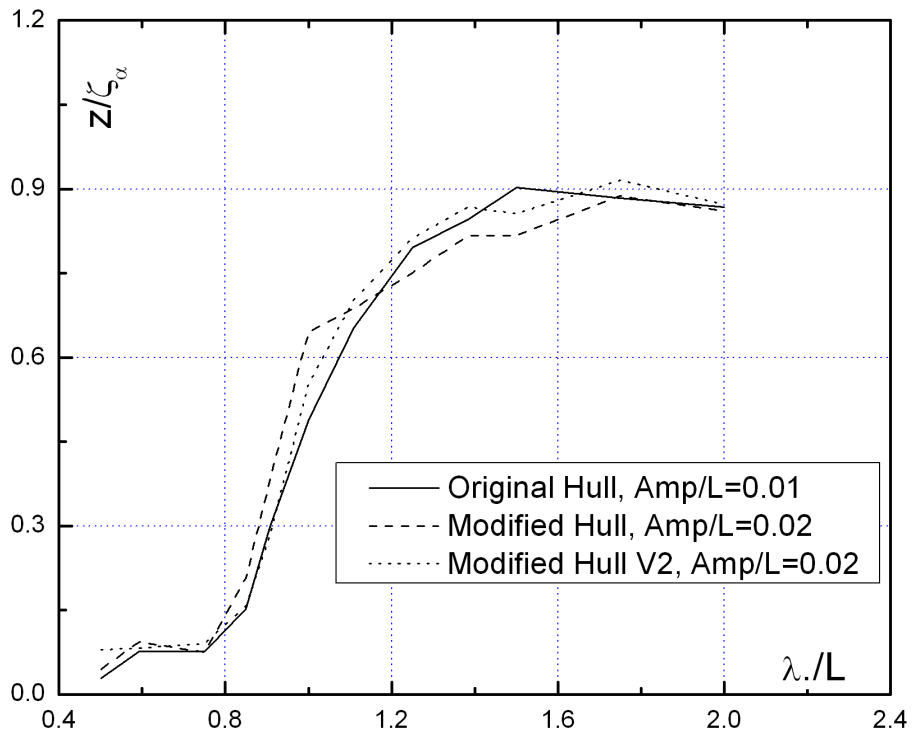


Figure 6.12 Heave amplitude of three different Wigley hulls, $F_n=0.2$, $Amp/L=0.02$

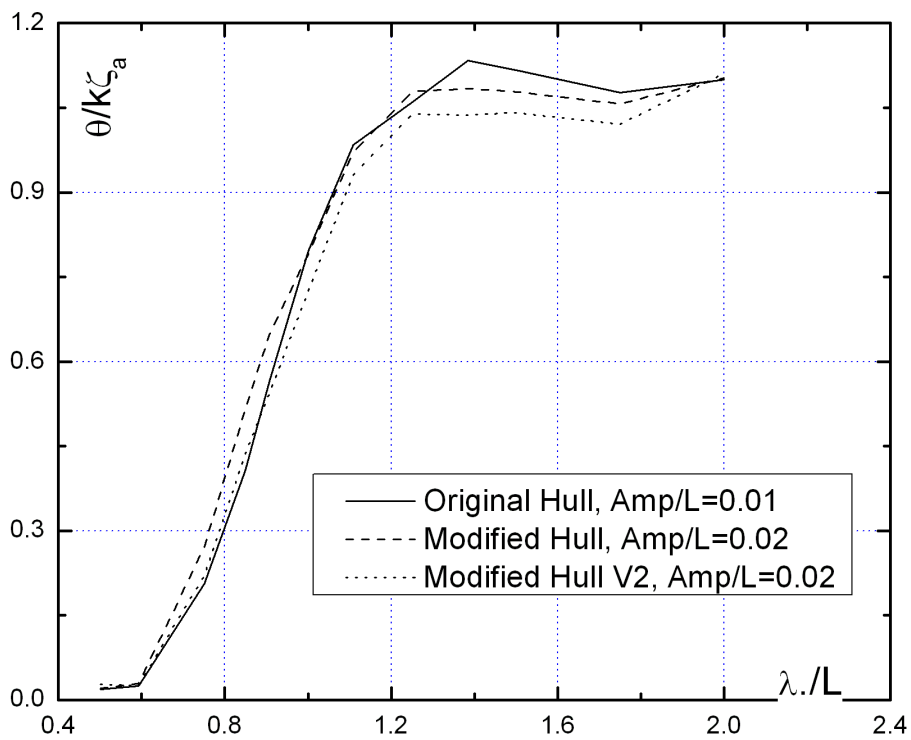


Figure 6.13 Pitch amplitude of three different Wigley hulls, $F_n=0.2$, $Amp/L=0.02$

6.5 Computational Time

An important aspect of this chapter's work refers to the computational efficiency. Looking backward at the work in this thesis, we started with a TDGF method for simulating the hydrodynamic forces. In that case, the most time-consuming parts of the work are:

- 1) to invert the influence matrices that correspond to the panels on body surface;
- 2) to calculate the memory part that is based on the historical information.

As the panel number on the body surface is limited, the first problem is not very serious. For the second aspect, as long as the linear problem is considered, this also does not pose serious problems.

When we proceed to the hybrid method, things change as following. For zero speed problems, the panelization is fixed and the matrices are pretty large, in the order of 2000×2000 ; however, we need to set up the matrices only once at the beginning. The main burden at each time step is to update the free surface condition and matching surface condition, followed by the effort in solving the equations by the GMRES method, which take a few seconds. In case of the motions problem, an iterative scheme is applied so that additional time is needed. In this case, if the partial derivatives need to be calculated, this is another few seconds' work. Thus, for a simulation of about 300 time steps (corresponding to 6-8 wave periods) it takes less than one hour to complete the simulation on a regular PC hardware with Intel Core 2 QUAD CPU(Q8200 2.33GHz).

In case of the forward speed problem, as shown in Chapter 5, the situation is very different. At every time step, the hull will be moving thus the free surface near the ship will also change, so that the influence matrices need to be updated at every time step. It takes about 30 seconds for preparing the matrices, depending on how complicated the problem is. After the *Chimera* grid concept is introduced, though the panels that are far away from the ship are fixed, thus do not need to be updated at every time step, due to the fact that near field panels are very small so that the number of panels that need to be updated is still quite large, there are still a considerable amount of data processing at each time step. For one simulation, it takes more than 5 hours for forced motion problem or even more than 10 hours for more complicated large amplitude motion problems. As a method that is based on potential flow theory, this is not efficient.

There are other possible ways for improving the simulation efficiency, e.g. Precorrected-FFT scheme (Kring, et al, 2000), but in the present study I did not try in that direction, instead I tried to formulate the problem in the body-fixed coordinate system, which results in a panelization system that is quite similar to the zero speed problem. By doing so, the efficiency has been

improved. For a typical motion simulation in head seas condition, it is possible to finish a run within 2 hours. But the now occurring problems are in two points:

- 1) the free surface condition update is complicate;
- 2) the matching surface condition update is not accurate due to the omission of the waterline integral term which appears in Equation (6-8) or Equation(6-9).

The second point also affects the first point internally through the solved integral equations. This is reflected in the results, where some shift shows up in the motions' RAOs. As pointed out before, recently other researchers argue on the effect of far field condition and propose some new type of far field condition.

Chapter 7 Summary of the Research and Recommendations for Future Development

In this thesis, for studying the seakeeping behavior of floating structures and ships in waves (at zero and nonzero forward speed), a time domain transient Green function method was developed, by formulating the basic hydrodynamic problem and by numerically solving it through the implementation of the theoretical method (new code development). During the systematic validations the developed method and numerical scheme proved to be quite robust. But when it was applied to practical shiplike forms (floating bodies) with flared section at the waterline, numerical problems arise, thus they prevent us from further practical numerical tests.

Due to this reason a *hybrid* method was formulated subsequently to overcome the problem. In the hybrid method the fluid domain is divided into two regions, namely the inner domain, where the Rankine source method is used, and the outer domain, in which the transient Green function method is employed to form a boundary/matching condition for the inner domain equation. In the hybrid method, part of the free surface is included in the inner domain thus it needs to be panelized and proper condition needs to be assigned. A double integration scheme is used to numerically simulate the linearized free-surface condition. In the numerical implementation of the developed approach, the normal constant panel method is used to solve the relevant boundary value problem of potential theory. The panelization is done for the whole domain leading to about 4000 panels in total. The resulting discretized integral equations are solved by using GMRES method at each time step. The simulation of the free surface condition by the adapted method proves quite satisfactory. Furthermore, a Chimera grid scheme has been developed to improve solution of near field velocity potentials and also give us flexibility on choosing the time interval, which is very important for a time domain simulation method.

Numerical results cover investigations of various hull forms (mathematical and ship-like hull forms) on the wave making resistance problem, forced motion problem, diffraction problem, heave, roll and pitch motions, either of small amplitude or large amplitude, either with zero speed or nonzero speed forward speed, and added resistance in waves. It can be seen from these validations that the hybrid method has been successfully applied to different type of bodies, either of simple geometry or real ships and different operational conditions.

In order to reduce the computational time, some further development was carried out so as to formulate the problem in a body-fixed coordinate system. The solution procedure is quite similar; however it is a more complicated procedure with respect to the simulation of the free surface condition and the matching surface condition. Numerical tests were carried out successfully

despite that some error shows up probably due to insufficient treatment of the outer domain solution, which internally affect the inner domain solution through the matching condition.

From a practical point of view the hybrid method overcomes the numerical difficulties met in time domain Green function method when studying real ship hulls with flared sections at the waterline. For the zero speed case, the results are very satisfactory with decent efficiency. With some further development it can be easily applied to offshore engineering problems. The hybrid method was also validated by studying the large amplitude motion problems of ships with constant forward speed, thus proved that it can be used as a valuable design tool for hull form assessment and optimization, as it is capable of studying the seakeeping characteristics of hulls with different possible above-water shape. A by-product of the present method is its capability to calculate the wave-making resistance to a good accuracy, even though some more systematic validation is herein needed.

For the solution in the body fixed coordinate system, some shift in the RAO curve is observed when predicting ship motions. This is perhaps due to the insufficient treatment of the outer domain solution when neglecting the tricky line integral term along the water-hull intersection line. Further developments may rely on an improved scheme to deal with the waterline integral term, or the formulation of another condition on the matching surface.

At present stage, in the motion simulation, Froude-Krylov forces and restoring forces are calculated exactly over the wetted body surface up to the undisturbed wave surface, while diffraction and radiation forces are calculated up to the mean wetted surface. For the former term, since the radiation and diffraction solutions are available, correction can be done so that the disturbed wave surface can be estimated at each time step, thus a better prediction can be expected. For the latter term, since to set up large scale time-varying influence matrices are quite time consuming and this almost eliminates the advantage of a potential theory based method, it is concluded that maybe other type methods, e.g. CFD methods, should be considered.

Bibliography

- Abkowitz M.A., "Stability and Control of Ocean Vehicles," MIT press, 1969.
- Ahahshahan A. and Landweber L., "Boundary-layer effects on wave resistance of a ship mode," J. Ship. Res. Vol.34, 1990, pp.29-37.
- Beck R.F. and Liapis S.J., "Transient motions of floating bodies at zero forward speed," J. Ship Research, Vol.31, No.3, 1987.
- Beck R.F. and Magee A.R., "Time domain analysis for predicting ship motions," Proc. IUTAM Symp., Dynamics of Marine Vehicles and Structures in Waves, 1990.
- Bingham, H. B. and Maniar, H. D., "Computing the double-body m-terms using a B-spline based panel method," 11th International Workshop on Water Waves and Floating Bodies, 1996.
- Chang M.S., "Computation of 3-D ship motions with forward speed," Proceedings 2nd International Conference on Numerical Ship Hydrodynamics, 1977, pp. 124-135.
- Chen C.Y. and Noblesse F., "Comparison between theoretical predictions of wave resistance and experimental data for the Wigley hull," J. Ship Research, Vol.27, 1983, pp.215-226.
- Chen X.B and Malenica S., "Nonlinear effects of the local steady flow on wave diffraction-radiation at low forward speed," Int. Offshore and Polar Engineering Conf., 1996.
- Chen X. B., Diebold L. and Doutreleau Y., "New green-function method to predict wave-induced ship motions and loads," Proc. 23rd Symposium on Naval Hydrodynamics, 2000.
- Cummins W.E., "The impulsive response function and ship motions," Schiffstechnik, Vol.9, 1962, pp.124-135.
- Duan W.Y., "Nonlinear Hydrodynamic Forces Acting on a Ship Undergoing Large Amplitude Motions," PhD Thesis, Harbin Engineering University, 1995.
- Duan W.Y. and Dai Y. S., "Time-domain calculation of hydrodynamic forces on ships with large flare," International Shipbuilding Progress, Vol.46, 1999, pp.223-232.
- Duan W.Y. and Price W.G., "A numerical method to solve the m-terms of a submerged body with forward speed," Int. J. Num meth in Fluids, Vol.40, 2002.
- Duan W.Y. and Dai Y. S., "Integration of the Time-Domain Green Function," IWWF22, 2007.
- Edward V. Lewis, "Principles of Naval Architecture," Volume III, Society of Naval Architects and Marine Engineers, 1988

- Faltinsen O. M., and Michelsen, F. C., "Motions of Large Structures in Waves at Zero Froude Number," Proceedings of the International Symposium on Dynamics of Marine Vehicles and Structures in Waves, 1974, pp.91-106.
- Faltinsen O. M., Minsaas K. J., Liapis N. and Skjördal S. O., "Prediction of resistance and propulsion of a ship in a seaway," Proc. 13th Symposium on Naval Hydrodynamics, 1980, pp. 505-529.
- Farell C., "On the wave resistance of a submerged spheroid," J. Ship Research, Vol.17, 1973, pp.1-11.
- Ferrant P., "A coupled time and frequency approach for nonlinear wave radiation," Proc. 18th Symposium on Naval Hydrodynamics, 1990, pp. 67-83.
- Finkelstein A., "The initial value problem for transient water waves," Comm. Pure App. Maths., Vol.10, 1957, pp.511-522.
- Fujii H. and Takahashi T., "Experimental study on the resistance increase of a ship in regular oblique waves," Proceeding of 14th ITTC, 1975, pp. 351-360.
- Gerritsma, J. and Beukelman W., "Analysis of the Modified Strip Theory for the calculation of ship motions and wave bending moments," International Shipbuilding Progress, 1967.
- Grim, O., "Berechnung der durch Schwingungen eines Schiffskörpers erzeugten hydrodynamischen Kräfte," STG-Jahrbuch, 1953, pp. 277-299.
- Hess J.L. and Smith A.M.O., "Calculation of nonlifting potential flow about arbitrary three-dimensional bodies," J. Ship. Res. Vol.8, 1964.
- Huang D. B., "Approximation of time-domain free surface function and its spatial derivatives", China shipbuilding, Vol.2, 1992, pp. 16-25.
- Hulme A., "The wave forces acting on a floating hemisphere undergoing forced periodic oscillations," J. Fluid Mech., 1982, pp. 443-463.
- Ikeda Y., Himeno Y. and Tanaka N., "Components of roll damping at forward speed," Trans. Japan Society of Naval Architects, Vol.143, 1978.
- Iafrafi A. and Campana E.F., "A domain decomposition approach to compute wave breaking (wave breaking flows)," Int. J. Numer. Meth. Fluids, 2003, 41, pp 419-445.
- Inglis R.B. and Price W.G., "A 3D ship motion theory comparison between theoretical prediction and experimental data of the hydrodynamic coefficients with forward speed," Trans. Roy. Inst. Nav. Arch., Vol.124, 1981.
- ITTC Seakeeping Committee, "Seagoing quantities of Ships," Proc. 9th ITTC proceedings, 1960.
- ITTC Seakeeping Committee, "Comparison of results obtained with compute programs to predict ship motions in six-degrees-of-freedom and associated responses," Proc. 15th ITTC, 1978, pp. 79-92.

- ITTC Seakeeping Committee, "Summary of results obtained with computer programs to predict ship motions in six degree of freedom and related response," 15th and 16th ITTC seakeeping committee comparative study on ship motion program (1976-1981), 1983.
- ITTC Seakeeping Committee, "Prediction of Added Resistance," Proc. 17th ITTC, 1984, pp. 500-503.
- Iwashita H. and M. Ohkusu, "The Green function method for ship motions at forward speed," *Schifftechnik*, Vol.39, 1992, pp. 3-21.
- Journée, J. M. J., "Experiments and calculations on 4 Wigley hull forms in head waves," Technical Report MEMT21, Delft University of Technology, 1992.
- Kashiwagi M., "Numerical seakeeping calculations based on the slender ship theory," *Ship Technology Research*, Vol.44, 1997, pp. 167-192.
- Kashiwagi M., "Impact of hull design on added resistance in waves – application of the enhanced unified theory," Proc. of 10th Int. Marine Design Conference, 2009, pp. 521-535.
- Kat J. O., "The numerical modeling of ship motions and capsizing in severe seas," *Journal Ship Research*, Vol.34, 1990.
- Kataoka S., Sueyoshi A., Arihama K., Iwashita H., and Takaki M., "A study on body nonlinear effects in the unsteady wave field," *Trans. of the West- Japan Society of Naval Architects*, No.103, 2002, pp.123-134.
- Kataoka S. and Iwashita H., "Estimations of hydrodynamic forces acting on ships advancing in the calm water and waves by a time-domain hybrid method," *J. of the Society of Naval Architects of Japan*, Vol.196, 2004, pp.123-138.
- Kataoka S. and Iwashita H., "Seakeeping estimations of ships by a time-domain hybrid method," *Inter. RIAM Symposium*, 2005.
- Kim B., "Some considerations on forward speed seakeeping calculations in frequency domain," *Int. J. Offshore and Polar Engineering*, Vol. 15, 2005.
- King B.K., Beck R.F. and Magee, A.R., "Seakeeping calculations with forward speed using time domain analysis," Proc. 17th Symp. Naval Hydro., 1988.
- Korsmeyer F.T., "The first and second order transient free-surface wave radiation problems," PhD Thesis, MIT, 1988.
- Korvin-Kroukovski B.V., "Investigation of ship motions in regular waves," *Trans. SNAME*, 1955, pp. 386-485.
- Kring D., Korsmeyer T., Singer J. and White J., "Analyzing mobile offshore bases using accelerated boundary-element methods", *Marine Structures*, Vol.13, July 2000, pp. 301-313.

- Kuroda M., Tsujimoto M., and Fujiwara T., "Investigation on components of added resistance in short waves," J. of the Japan Society of Naval Architects and Ocean Engineers, Vol. 8, 2008, pp. 171-176.
- Lewis E. V., "Principles of Naval Architecture," Volume III, the Society of Naval Architects and Marine Engineers, 1988.
- Liu S. K., "Time-domain Simulation of the Hydrodynamic Forces Acting on a Ship Advancing in Following Seas," Master Thesis, Harbin Engineering University, 2005.
- Liu S.K., "A time-domain hybrid method for simulating ship motions at zero speed," internal report, NTUA-SDL
- Liu S.K., Papanikolaou A., and Duan W.Y., "A time domain numerical simulation method for nonlinear ship motions," Proc. Int. Conference on Ship Design, Production & Operation, Harbin, China, 2007, pp. 177-185.
- Liu S.K. and Papanikolaou A., "A time-domain hybrid method for calculating hydrodynamic forces on ships in waves," 13th Inter. Congress of the Inter. Maritime Association of the Mediterranean, 2009.
- Liu S.K. and Papanikolaou A., "Time-domain hybrid method for simulating large amplitude motions of ships advancing in waves," ITTC Workshop on Seakeeping, 2010.
- Liu S.K., Papanikolaou A. and Zaraphonitis G., "Prediction of added resistance of ships in waves," Ocean Engineering, 2011.
- Lin R.Q and Kuang W.J., "A nonlinear method for predicting motions of fast ships," FAST 2009.
- Lin W.M., and Yue D., "Numerical Solutions for Large-Amplitude Ship Motions in the Time-Domain," Proc. 18th Symposium on Naval Hydrodynamics, 1990, pp. 41-66.
- Lin W.M., Meinhold M., Salvesen N., and Yue D.K.P., "Large-Amplitude Ship Motions and Wave Loads for Ship Design," Proc. 20th Symp. Naval Hydro., 1994.
- Lin W.M., Chen H., and Zhang S., "A hybrid numerical method for wet deck slamming on a high speed catamaran," 10th International Conference on Fast Sea Transportation, 2009.
- Maruo H., "The excess resistance of a ship in rough seas," International Shipbuilding Progress, Vol.4, No. 35, 1957.
- Maruo H., "The drift of a body floating on waves," J. Ship Research, Vol.4, No. 3, 1960, pp.1-10.
- Maruo, H., "Resistance in waves," 60th anniversary Series, The Society of Naval Architects of Japan, Vol.8, 1963, pp.67-102.
- Naito S., Yamamoto O., Takahashi T., "Effect of ship hull forms on resistance increase in waves," Proc. 5th Marine Dynamics Symposium, 1988, pp. 45-79.

- Naito S., "Propulsive performance of ships in actual seas," Proceedings of 7th Osaka Colloquium on Seakeeping and Stability, 2008.
- Nakos D.E. and Sclavounos P.D., "Ship motions by a three-dimensional Rankine panel method," Proc. 18th Symp. Naval Hydro. ,1990.
- Newman J.N., "Marine Hydrodynamics," MIT press, 1977.
- Ohkusu M., "Added resistance in waves of hull forms with blunt bow," Proc. 15th Symposium on Naval Hydrodynamics, 1985, pp. 135-147.
- Ogawa Y., "A Study on Nonlinear Wave Loads of a Large Container Carrier in Rough Seas," 10th International Symposium on Practical Design of Ships and Other Floating Structures, 2007.
- Papanikolaou, A., "On the Nonlinear Problem of a Vertically Oscillating Cylinder of Arbitrary Shape," Dr.-Ing. Thesis, Tech. Univ. of Berlin, 1977.
- Papanikolaou, A., and Nowacki, Z., "Second-Order Theory of Oscillating Cylinders in a Regular Steep Wave", Proc. 13th ONR Symp., Tokyo, 1980, pp. 303-333.
- Papanikolaou A., "On Integral-Equation-Methods for the Evaluation of Motions and Loads of Arbitrary Bodies in Waves," Journal Ingenieur - Archiv., Vol. 55,1985, pp.17-29.
- Papanikolaou A. and Liu S.K., "On the prediction of added resistance of ships in waves," William Froude Conference: Advances in Theoretical and Applied Hydrodynamics – Past and Future, 2010.
- Papanikolaou A. and Schellin Th., "A three dimensional panel method for motions and loads of ships with forward speed," Journal Schiffstechnik-Ship Technology Research, Vol. 39, No. 4, 1992, pp.147-156.
- Papanikolaou A. and Zaraphonitis G., "On an improved method for the evaluation of second-order motions and loads on 3D floating bodies in waves," Journal Schiffstechnik, Vol. 34, 1987, pp.170-211.
- Papanikolaou A. and Zaraphonitis G., "COMPUTER PROGRAM NEWDRIFT V.7", NTUA Internal Report, 2001.
- Papanikolaou A., Zaraphonitis G. and Schellin Th., "On a 3D Method for the Evaluation of Motions and Loads of Ships with Forward Speed in Waves," Proc. 5th Int. Congress on Marine Technology, IMAEM '90, 1990.
- Papatzanakis G., Papanikolaou A. and Liu S.K., "Optimization of Routing with Uncertainties," 14th Inter. Congress of the Inter. Maritime Association of the Mediterranean, 2011(accepted).
- Pinkster J.A. "Mean and low frequency wave drifting forces on floating structures," Ocean Engineering, Vol.6, 1979, pp. 593-615.

- Salvesen N., Tuck E. O. and Faltinsen O., "Ship motions and sea loads," *Trans. Soc. Nav. Arch. and Marine Eng.*, Vol. 78, 1970, pp. 250-287.
- Salvesen, N., "Second-order steady state forces and moments on surface ships in oblique regular waves," *Proc. Int. Symp. on Dynamics of Marine Vehicles and Structures in Waves*, Univ. College London, 1974, pp.212-226.
- Shin Y.S., Chung J.S., Lin W.M., Zhang S. and Engle A., "Dynamic loadings for structural analysis of fine form container ship based on a non-linear large amplitude motions and loads method," *Trans. SNAME*, Vol.105,1997, pp. 127-54.
- SHIPFLOW, "SHIPFLOW 3.0 examples manual," <http://www.flowtech.se/>, 2005.
- Song M. J., Kim K., and Kim Y., "Numerical analysis and validation of weakly nonlinear ship motions and structural loads on a modern containership," *Ocean Engineering*, Vol.38, 2011. pp. 77-87.
- Spanos D., "Simulation of the motions of a ship after flooding in waves and investigation of the survivability of ROPAX ships (in Greek)," PhD Thesis, National Technical University of Athens, Ship Design Laboratory, 2002.
- Spyrou K. J. and Thompson J. M. T., "The Nonlinear Dynamics of Ship Motions: A Field Overview and Some Recent Developments," *Philosophical Transactions: Mathematical, Physical and Engineering Sciences*, Vol. 358, No. 1771, 2000, pp. 1735-1760.
- Stefun G.P., "Comparative Seakeeping Tests at the David Taylor Model Basin, the Netherlands Ship Model Basin, and the Admiralty Experiment Works," *Proc. 9th ITTC proceedings*, 1960.
- Strøm-Tejsen, J., Yeh, H.Y.H. and Moran, D.D., "Added resistance in waves," *Transactions of the Society of Naval Architects and Marine Engineers*, Vol.81, 1973, pp.109-143.
- Sueyoshi M., Kihara H. and Kashiwagi M., "A hybrid technique using particle and boundary-element methods for wave-body interaction problems," *9th International Conference on Numerical Ship Hydrodynamics*, 2007.
- SWAN2, "Ship flow simulation in calm water and in waves", user manual, 2002
- Wang J.F., "Numerical Simulation of the Linear Free-Surface Condition," Master Thesis, Harbin Engineering University, 2003
- Weatherill N. P., Soni B. K. and Thompson J. F., "Handbook of Grid Generation," CRC Press, 1999.
- Wehausen J. V., "Effect of the initial acceleration upon the wave resistance of ship models," *J. Ship. Res.*, Vol.7, 1964, pp. 38-50.
- Wehausen J.V. and Laitone E.V., "Surface Waves, Handbuch der Physik," Springer-Verlag, 1960.

- Wu G. X. and Taylor R. E., "Radiation and diffraction of water waves by a submerged sphere at forward speed," Proc. R. Soc. Lond. A417, 1988, pp. 433-461.
- Wu G.X., "A numerical scheme for calculating the m_j -terms in wave-current-body interaction problem," Applied Ocean Research, Vol. 13, 1991.
- Yasukawa H., "Application of a 3-D Time Domain Panel Method to Ship Seakeeping Problems," 24th Symposium on Naval Hydrodynamics, 2003, pp. 376-392.
- Yeung R. W., "A Singularity-Distribution Method for Free-Surface Flow Problems with an Oscillating Body," California Univ. Berkeley, 1973.
- Zaraphonitis, G., "Second-order theory of motions and loads of arbitrarily shaped 3D bodies in waves" Dr.-Eng. Thesis, National Technical University of Athens, 1990.
- Zhang S., Lin W.M. and Weems K., "A hybrid boundary-element method for non-wall-sided bodies with or without forward speed," Proc 13th International Workshop on Water Waves and Floating Bodies, 1998.
- Zhang X., Bandyk P. and Beck R.F., "Time domain simulations of radiation and diffraction forces," J. Ship. Res., 2010.
- Zhao R. and Faltinsen O. M., "A discussion on the m_j -terms in the wave-current-body interaction problem," Proc 4th International Workshop on Water Waves and Floating Bodies, 1989.

Appendix-1 Time-domain hybrid method for radiation problems, with impulsive function

In hybrid method due to the difficulties in updating the instantaneous meshes on free-surface and body surface, its application is constrained in linear problems. As a matter of fact, the linear problem has been investigated in time domain by Beck following Cummins's pioneering work. In this theory, solution of the velocity potential due to an impulsive motion has been obtained. Then the potential due to any motion can be found by an integration of the impulsive potential. With this theory, the time-domain method can yield good results for linear cases with an efficiency comparative to frequency domain method.

In this section, we will introduce this idea into the hybrid method in hope for solving the radiation problems with a better efficiency.

A1.1 Radiation Problem

Here we concentrate on the radiate problem. By adopting the concept proposed by Cummins, the radiation potential due to a k -th direction impulse motion can be decomposed as:

$$\varphi_k(p, t) = \psi_k(p) \delta(t) + \chi_k(p, t) \quad (k = 1, 2, \dots, 6) \quad (\text{A1-1})$$

where ψ_k and χ_k meet the following conditions:

$$\left\{ \begin{array}{l} \nabla^2 \psi_k = 0 \\ \psi_k = 0 \quad (\text{on } S_f) \\ \frac{\partial \psi_k}{\partial n} = n_k \quad (\text{on } S_b) \end{array} \right. \quad \left\{ \begin{array}{l} \nabla^2 \chi_k(p, t) = 0 \\ \frac{\partial^2 \chi_k}{\partial t^2} + g \frac{\partial \chi_k}{\partial z} = 0 \quad (\text{on } S_f) \\ \frac{\partial \chi_k}{\partial n} = 0 \quad (\text{on } S_b) \\ \chi_k|_{t=0} = 0, \quad \frac{\partial \chi_k}{\partial t}|_{t=0} = -g \frac{\partial \psi_k}{\partial z} \quad (\text{on } S_f) \end{array} \right. \quad (\text{A1-2})$$

ψ_k and χ_k can be physically interpreted as a radiation potential, an instantaneous effect, by the impulse motion and a subsequent diffraction potential, a memory effect, by the body due to the initial impulse.

Since the hybrid will be used here to solve the problem, the same concept which has been explained in Chapter 3 will be adopted without any further explanation. Substituting the expression (A1-1) into equation and gathering terms proportional to $\delta(t)$ separately, we will get two sets of equations:

$$\left\{ \begin{array}{l} \iint_{S_c + S_b + S_f} \left\{ \psi_I(q) \frac{\partial}{\partial n_q} \left(\frac{1}{r_{pq}} \right) - \frac{1}{r_{pq}} \frac{\partial \psi_I(q)}{\partial n_q} \right\} ds_q = -2\pi \psi_I(p) \quad (p \in S_I) \\ \iint_{S_c + S_b + S_f} \left\{ \chi_I(q, t) \frac{\partial}{\partial n_q} \left(\frac{1}{r_{pq}} \right) - \frac{1}{r_{pq}} \frac{\partial \chi_I(q, t)}{\partial n_q} \right\} ds_q = -2\pi \chi_I(p, t) \quad (p \in S_I) \end{array} \right. \quad (\text{A1-3})$$

$$\left\{ \begin{array}{l} 2\pi \psi_{II}(p) + \iint_{S_c} \left[\psi_{II}(q) \frac{\partial}{\partial n_q} \left(\frac{1}{r_{pq}} - \frac{1}{r_{pq'}} \right) - \left(\frac{1}{r_{pq}} - \frac{1}{r_{pq'}} \right) \frac{\partial \psi_{II}(q)}{\partial n_q} \right] ds_q = 0 \quad (p \in S_{II}) \\ 2\pi \chi_{II}(p, t) + \iint_{S_c} \left[\chi_{II}(q, t) \frac{\partial}{\partial n_q} \left(\frac{1}{r_{pq}} - \frac{1}{r_{pq'}} \right) - \left(\frac{1}{r_{pq}} - \frac{1}{r_{pq'}} \right) \frac{\partial \chi_{II}(q, t)}{\partial n_q} \right] ds_q = \int_0^t d\tau \iint_{S_c} \tilde{G} \frac{\partial \chi_{II}(q, \tau)}{\partial n_q} ds_q \\ - \int_0^t d\tau \iint_{S_c} \chi_{II}(q, \tau) \frac{\partial \tilde{G}}{\partial n_q} ds_q + \iint_{S_c} \tilde{G}(p, t; q, 0) \frac{\partial \psi_{II}(q)}{\partial n_q} ds_q - \iint_{S_c} \psi_{II}(q) \frac{\partial \tilde{G}(p, t; q, 0)}{\partial n_q} ds_q \quad (p \in S_{II}) \end{array} \right. \quad (\text{A1-4})$$

Combining the equations for ψ and χ respectively, we get the equations to be solved as:

$$\left\{ \begin{array}{l} \iint_{S_c + S_b + S_f} \left\{ \psi_I(q) \frac{\partial}{\partial n_q} \left(\frac{1}{r_{pq}} \right) - \frac{1}{r_{pq}} \frac{\partial \psi_I(q)}{\partial n_q} \right\} ds_q = -2\pi \psi_I(p) \quad (p \in S_I) \\ 2\pi \psi_{II}(p) + \iint_{S_c} \left[\psi_{II}(q) \frac{\partial}{\partial n_q} \left(\frac{1}{r_{pq}} - \frac{1}{r_{pq'}} \right) - \left(\frac{1}{r_{pq}} - \frac{1}{r_{pq'}} \right) \frac{\partial \psi_{II}(q)}{\partial n_q} \right] ds_q = 0 \quad (p \in S_{II}) \end{array} \right. \quad (\text{A1-5})$$

$$\left\{ \begin{array}{l} \iint_{S_c + S_b + S_f} \left\{ \chi_I(q, t) \frac{\partial}{\partial n_q} \left(\frac{1}{r_{pq}} \right) - \frac{1}{r_{pq}} \frac{\partial \chi_I(q, t)}{\partial n_q} \right\} ds_q = -2\pi \chi_I(p, t) \quad (p \in S_I) \\ 2\pi \chi_{II}(p, t) + \iint_{S_c} \left[\chi_{II}(q, t) \frac{\partial}{\partial n_q} \left(\frac{1}{r_{pq}} - \frac{1}{r_{pq'}} \right) - \left(\frac{1}{r_{pq}} - \frac{1}{r_{pq'}} \right) \frac{\partial \chi_{II}(q, t)}{\partial n_q} \right] ds_q \\ = \int_0^t d\tau \iint_{S_c} \tilde{G}(p, t; q, \tau) \frac{\partial \chi_{II}(q, \tau)}{\partial n_q} ds_q - \int_0^t d\tau \iint_{S_c} \chi_{II}(q, \tau) \frac{\partial \tilde{G}(p, t; q, \tau)}{\partial n_q} ds_q \\ + \iint_{S_c} \tilde{G}(p, t; q, 0) \frac{\partial \psi_{II}(q)}{\partial n_q} ds_q - \iint_{S_c} \psi_{II}(q) \frac{\partial \tilde{G}(p, t; q, 0)}{\partial n_q} ds_q \quad (p \in S_{II}) \end{array} \right. \quad (\text{A1-6})$$

On the control surface, the matching conditions are expressed as:

$$\begin{aligned} \psi_I &= \psi_{II}, \quad \frac{\partial \psi_I}{\partial n} = -\frac{\partial \psi_{II}}{\partial n} \quad (\text{on } S_c) \\ \chi_I &= \chi_{II}, \quad \frac{\partial \chi_I}{\partial n} = -\frac{\partial \chi_{II}}{\partial n} \quad (\text{on } S_c) \end{aligned} \quad (\text{A1-7})$$

Solve the above equations we will get ψ and χ ; then the velocity potential due to arbitrary motion in k -th direction may be obtained by the superposition of the impulse response function, which can be written as an integration:

$$\begin{aligned} \Phi_k &= \int_0^t \varphi_k(p, \tau) \dot{\zeta}_k(t - \tau) d\tau \\ &= \psi_k(p) \dot{\zeta}_k(t) + \int_0^t \chi_k(p, \tau) \dot{\zeta}_k(t - \tau) d\tau \quad (k = 1, 2, \dots, 6) \end{aligned} \quad (\text{A1-8})$$

The forces exerting on the body are calculated by substituting the above expression into linear Bernoulli's equation. Thus we get the forces in j -th direction due to k -th direction motion as:

$$\begin{aligned} F_{jk}(t) &= -\rho \ddot{\zeta}_k(t) \iint_{S_b} \psi_k \bar{n}_j ds - \rho \int_0^t \frac{\partial}{\partial t} [\dot{\zeta}_k(t-\tau)] \iint_{S_b} \chi_k(p, \tau) \bar{n}_j ds d\tau \\ &= -\mu_{jk} \ddot{\zeta}_k(t) - \int_0^t K_{jk}(\tau) \dot{\zeta}_k(t-\tau) d\tau \end{aligned} \quad (A1-9)$$

where

$$\begin{aligned} \mu_{jk} &= \rho \iint_{S_b} \psi_k \bar{n}_j ds \\ K_{jk}(t) &= \rho \iint_{S_b} \chi_k(p, t) \bar{n}_j ds \end{aligned}$$

It is clear that μ_{jk} and $K_{jk}(t)$ are functions of the body geometry and time while they are independent of the history of the motion. For a given hull, they can be calculated once only and be used later wherever or whenever in need. From Wehausen's formulation, μ_{jk} and $K_{jk}(t)$ are related to the frequency domain added mass and damping coefficients by a Fourier transform:

$$\begin{aligned} A_{jk}(\omega) &= \mu_{jk} + \int_0^\infty d\tau K_{jk}(\tau) \cos \omega \tau \\ B_{jk}(\omega) &= \omega \int_0^\infty d\tau K_{jk}(\tau) \sin \omega \tau \end{aligned} \quad (A1-10)$$

where $A_{jk}(\omega)$ & $B_{jk}(\omega)$ are the added mass and damping coefficients in the frequency domain.

A1.2 Free-surface Condition

The linearized free-surface condition for $\chi(t)$ is:

$$\frac{\partial^2 \chi}{\partial t^2} + g \frac{\partial \chi}{\partial z} = 0$$

This expression can be rewritten as:

$$\frac{\partial^2 \chi}{\partial t^2} = -g \frac{\partial \chi}{\partial z}$$

Integrating the above equation with respect to time t twice and taking into account the initial condition for χ on free surface, we will get the free-surface condition as:

$$\begin{aligned} \frac{\partial \chi_k(p, t)}{\partial t} &= -g \int_0^t d\tau \left. \frac{\partial \chi_k(p, \tau)}{\partial n} + \frac{\partial \chi_k(p, \tau)}{\partial \tau} \right|_{\tau=0} \\ \frac{\partial \chi_k(p, t)}{\partial t} &= -g \int_0^t d\tau \frac{\partial \chi_k(p, \tau)}{\partial n} - g \frac{\partial \psi(p)}{\partial z} \end{aligned}$$

$$\int_0^t d\tau \frac{\partial \chi_k(p, \tau)}{\partial \tau} = \int_0^t d\tau \left[-g \int_0^t d\tau \frac{\partial \chi_k(p, \tau)}{\partial n} - g \frac{\partial \psi(p)}{\partial z} \right]$$

$$\chi_k(p, t) = -g \int_0^t (t - \tau) \frac{\partial \chi_k(p, \tau)}{\partial n} d\tau - \frac{\partial \psi_k(p)}{\partial n} g t \quad (\text{A1-11})$$

A1.3 Numerical Scheme

The panel method is used to solve the equations (A1-5) and (A1-6). The domain boundary, which consists of the body boundary S_b , the free-surface boundary S_f and the control surface S_c , is divided into N^b, N^f, N^c plane quadrilateral elements.

From the second equation in (A1-5) we find:

$$\psi_j = [A_{ij}]^{-1} [B_{ij}] \psi_{nj} \quad (i = 1, 2, 3, \dots, N^c) \quad (\text{A1-12})$$

where

$$A_{ij} = \begin{cases} 2\pi + \iint_{\Delta s_j} \frac{\partial}{\partial n_j} \left(-\frac{1}{r_{ij}} \right) ds_j & (i = j) \\ \iint_{\Delta s_j} \frac{\partial}{\partial n_j} \left(\frac{1}{r_{ij}} - \frac{1}{r_{ij}'} \right) ds_j & (i \neq j) \end{cases} \quad B_{ij} = \iint_{\Delta s_j} \left(\frac{1}{r_{ij}} - \frac{1}{r_{ij}'} \right) ds_j$$

The discretized form of the first equation is:

$$\sum_{j=1}^{N^c + N^f + N^b} (C_{ij} \psi_j - D_{ij} \psi_{nj}) = 0 \quad (i = 1, 2, 3, \dots, N^c + N^f + N^b) \quad (\text{A1-13})$$

$$\text{where } C_{ij} = \begin{cases} 2\pi & i = j \\ \int_{\Delta s_j} \frac{\partial}{\partial n_j} \left(\frac{1}{r_{ij}} \right) ds_j & i \neq j \end{cases} \text{ and } D_{ij} = \int_{\Delta s_j} \left(\frac{1}{r_{ij}} \right) ds_j.$$

On the body boundary $\frac{\partial \psi_k}{\partial n}$ is known; on the free surface ψ_k is known as zero; from the former equation set we have got the relationship between ψ_k and $\frac{\partial \psi_k}{\partial n}$ on the control surface; Noticing the matching condition in (A1-7), we will have the following equations:

$$\sum_{j=1}^{N^c} \left\{ -C_{ij} [A_{jk}]^{-1} [B_{kj}] - D_{ij} \right\} \psi_{nj} - \sum_{j=N^c+1}^{N^c+f} D_{ij} \psi_{nj} + \sum_{j=N^c+f+1}^{N^c+f+b} C_{ij} \psi_j = \sum_{j=N^c+f+1}^{N^c+f+b} D_{ij} \psi_{nj} \quad (\text{A1-14})$$

$$(i = 1, 2, 3, \dots, N^c+f+b)$$

Solve the equations set we will get the unknowns on control surface, wetted surface and free surface.

As to χ part, we have to solve equation (A1-6). From the second equation we find that:

$$\sum_{j=1}^{N^c} A_{ij} \chi_j^M = Memo_i + \sum_{j=1}^{N^c} B_{ij} \chi_{nj}^M \quad (i=1,2,\dots,N^c)$$

$$\text{where } A_{ij} = \begin{cases} 2\pi + \iint_{\Delta s_j^M} \frac{\partial}{\partial n_j} \left(-\frac{1}{r_{ij}} \right) ds_j & (i=j) \\ \iint_{\Delta s_j^M} \frac{\partial}{\partial n_j} \left(\frac{1}{r_{ij}} - \frac{1}{r_{ij}'} \right) ds_j & (i \neq j) \end{cases} \quad B_{ij} = \iint_{\Delta s_j^M} \left(\frac{1}{r_{ij}} - \frac{1}{r_{ij}'} \right) ds_j$$

$$\text{and } Memo_i = \Delta t \sum_{m=1}^{M-1} \varepsilon_m \sum_{j=1}^{N^c} \left(\chi_{nj}^m \iint_{\Delta s_j^m} \tilde{G}_j^m ds_j - \chi_j^m \iint_{\Delta s_j^m} \tilde{G}_{nj}^m ds_j \right) + \iint_{\Delta s_j} \tilde{G}_j^M \psi_{knj} ds_j - \iint_{\Delta s_j} \psi_{kj} \tilde{G}_{nj}^M ds_j$$

Thus we have

$$\chi_j^M = [A_{ij}]^{-1} \left[Memo_i + \sum_{j=1}^{N^c} B_{ij} \chi_{nj}^M \right] \quad (i=1,2,\dots,N^c) \quad (\text{A1-15})$$

In the inner domain the discretized form of the linearized free-surface is:

$$\chi_j^M = -g(\Delta t)^2 \sum_{m=1}^{M-1} (M-m) \frac{\partial \chi_j^m}{\partial n_j} - gM\Delta t \frac{\partial \psi_j}{\partial n_j} \quad (j=1,2,3,\dots,N_f) \quad (\text{A1-16})$$

Here j is the free-surface panel index while $M\Delta t$ and $m\Delta t$ denote for the present moment t and

the historical moment τ respectively, $\frac{\partial \chi_j^m}{\partial n_j}$ is $\frac{\partial \chi_k}{\partial n}$ on panel j at time τ .

The discretized form of the integral equation in the inner domain is:

$$\sum_{j=1}^{N^{c+f+b}} (C_{ij} \chi_j^M - D_{ij} \chi_{nj}^M) = 0 \quad (i=1,2,3,\dots,N^{c+f+b}) \quad (\text{A1-17})$$

$$\text{where } C_{ij} = \begin{cases} 2\pi & i=j \\ \int_{\Delta s_j} \frac{\partial}{\partial n_j} \left(\frac{1}{r_{ij}} \right) ds_j & i \neq j \end{cases} \text{ and } D_{ij} = \int_{\Delta s_j} \left(\frac{1}{r_{ij}} \right) ds_j. \text{ The boundary condition is}$$

known on body boundary; from the free-surface condition we know that χ_f is a function of $\frac{\partial \chi_f}{\partial n}$;

from (A1-15) we have the relationship between χ_c and $\frac{\partial \chi_c}{\partial n}$; then for the inner domain integral

equation, we will have $N^c + N^f + N^b$ unknowns and $N^c + N^f + N^b$ equations. Taking into account the matching condition on the control surface and substituting the former conditions into the above equation we will get:

$$\sum_{j,k=1}^{N^c} \left\{ -C_{ij} [A_{jk}]^{-1} [B_{kj}] - D_{ij} \right\} \chi_{nj}^M + \sum_{j=N^c+1}^{N^{c+f}} (-D_{ij} \chi_{nj}^M) + \sum_{j=N^{c+f}+1}^{N^{c+f+b}} C_{ij} \chi_j^M = \quad (A1-18)$$

$$- \sum_{j=1}^{N^c} C_{ij} \left\{ [A_{ij}]^{-1} [Memo_j]_o \right\} - \sum_{j=N^c+1}^{N^{c+f}} C_{ij} \chi_j^M + \sum_{j=N^{c+f}+1}^{N^{c+f+b}} D_{ij} \chi_{nj}^M \quad (i=1,2,\dots,N^{c+f+b})$$

where the subscript o indicates “outer domain”. Solve the equations set we will get the velocity potential result on control surface, free-surface and mean wetted surface.

A1.4 Summary

If this method can be fully validated, it can serve as a fast time domain code for linear radiation problem, which is useful for preliminary investigations. More research into the theory is needed.

Curriculum Vitae

Shukui LIU was born on April 15, 1982, in Henan province, P. R. China. After his graduation in October 2005 with a master of engineering degree in naval architecture from the College of Shipbuilding Engineering of Harbin Engineering University (P. R. China), he entered the PhD post-graduate programme of the School of Naval Architecture and Marine Engineering at the National Technical University of Athens (NTUA) in the frame of the EU funded ASIA LINK collaborative project of NTUA with Harbin Engineering University.

Education

Oct. 2005 - Apr. 2011	PhD	School of Naval Architecture and Marine Engineering, Ship Design Laboratory, NTUA
Sep. 2003 - Oct. 2005	Master Eng.	College of Shipbuilding Engineering, HEU
Sep. 1999 - Jul. 2003	Bachelor Eng.	College of Shipbuilding Engineering, HEU

List of Publications

1. Liu S.K., Papanikolaou A., Duan W.Y., "A time domain numerical simulation method for nonlinear ship motions", Journal of Harbin Engineering University, Vol.27, 2006, pp.177-185
2. Liu S.K. and Papanikolaou A., "A time-domain hybrid method for calculating hydrodynamic forces on ships in waves," 13th Inter. Congress of the Inter. Maritime Association of the Mediterranean, Istanbul, 2009.
3. Liu S.K. and Papanikolaou A., "Time-domain hybrid method for simulating large amplitude motions of ships advancing in waves", Proceeding of ITTC benchmark study and workshop on seakeeping, Seoul, 2010; accepted for republication at the Journal of the Korean Society of Naval Architects and Ocean Engineers.
4. Liu, S.K., Papanikolaou, A., Zaraphonitis, G., "Prediction of added resistance of ships in waves", Ocean Engineering, 2011.
5. Liu S.K. and Papanikolaou A., "Nonlinear time-domain hybrid method for simulating ship motions in waves", 5th Int. Water Waves Workshop, Berlin, 2010
6. Papanikolaou A. and Liu S.K., "On the prediction of added resistance of ships in waves", The William Froude Conference: Advances in Theoretical and Applied Hydrodynamics, Portsmouth, 2010

7. Liu S.K. and Papanikolaou A., "Application of Chimera grid concept to simulation of the free-surface boundary condition," 26th International Workshop on Water Waves and Floating Bodies, Athens, 2011.
8. Liu S.K. and Papanikolaou A., "A time-domain hybrid method for calculating hydrodynamic forces on ships in waves," 14th Inter. Congress of the Inter. Maritime Association of the Mediterranean, Genoa, 2011(accepted).
9. Papatzanakis G., Papanikolaou A. and Liu S.K., "Optimization of Routing with Uncertainties," 14th Inter. Congress of the Inter. Maritime Association of the Mediterranean, 2011, Genoa, (accepted).